Advances in Electroanalytical Chemistry



A Thesis for the Degree of Doctor of Philosophy

in Physical and Theoretical Chemistry by

Yijun Wang

St. John's College

University of Oxford

Supervisor: Professor Richard G. Compton

Trinity Term 2012

Abstract

This thesis concerns several advances in electroanalytical chemistry which are separated into four parts: the electrochemical investigation of diffusional behaviour, the mechanistic and kinetic study of electrochemistry with room temperature ionic liquids (RTILs), the study of weakly-supported electrochemistry and a comparison of the Butler-Volmer and Marcus-Hush kinetic theories of electron transfer.

A study of the diffusional behaviour of electroactive species is essential for further studies, especially in the case when electrochemistry is complicated through ion-pairing interactions between the electroactive species and other electrolytes. In Part II of this thesis, the possibility of the ferricenium ion-paired with perchlorate and hexafluorophosphate in acetonitrile was discussed firstly employing chronoamperometric technique. Afterwards, the hexaammineruthenium III/II couple supported by chloride, nitrate and sulfate respectively was studied by a similar method.

In order to avoid unwanted ion-pairing effects, room temperature ionic liquids can be applied as solvent, which provide high conductivity by their own ionic nature so that experiments can be conducted without adding additional supporting ions. Because of RTILs have distinctive properties, for example, high viscosity, high conductivity and ionic nature, electrochemistry could be greatly changed compared to those in conventional solvents. Part III of this thesis gives a detailed description of this topic. First, a study of the reduction of 1,4-benzonquinone in 1-ethyl-3-methylimidazolium bis(trifluoromethanesulfonyl)imide is presented to show the new mechanistic insight into comproportionation in a electrochemical process. Second, a discussion of the oxidation of hydroquinone in the same RTIL is introduced to suggest a possible ECE scheme which was never reported before.

The interest of weakly supported electrochemistry is also well-established, which not only provides another alternative strategy to avert ion-pairings but also offers more physical insights into electrochemical processes. Quantitative methods analysing voltammetries without an excess amount of supporting electrolyte are developed by introducing a migration term into the mass transport equation. In Part IV, new mechanistic insights into the reduction of 2-nitrobromobenzene and the dimerisation

of 2,6-diphenylpyrylium in acetonitrile were provide by using weakly-supported cyclic voltammetry. Also, pulse techniques was also adopted to investigate the reduction of cobaltocenium and cobalt(III) sepulchrate, giving an alternative way for electrochemical analysis.

A major application of electroanalytical chemistry is investigating electrochemical kinetics. Two kinetic models mostly concerned by electrochemists are Butler-Volmer and Marcus-Hush formalisms. The classic phenomenological model, Butler-Volmer formalism successfully describes most common electron transfer kinetics but shows little reference with nature of the involved species, solution and electrode material, while a more physically insightful theory, the Marcus-Hush formalism, takes species natural properties, for instance, a change of distances or geometry in the solvation or coordination shells of the redox, into account although it requires more complex formulations. Comparative studies of these two theories are presented in Part V in order to improve our understanding of the electron transfer kinetics under different circumstances. First, comparison of cyclic voltammograms of the reduction of europium(III) and 2-methyl-2-nitropropane at mercury microhemispherical electrodes was carried out. Second, square wave and differential pulse voltammetric techniques were also employed to further discriminate the two kinetic models. These studies all find that the symetric Marcus-Hush theory assuming the reactants and products have identical force constant dose not satisfactorily agree with the experimental results. Hence, the introduction of asymmetric Marcus-Hush theory was presented considering different oxidative and reductive reorganization energies, which gives reasonable agreement with experiments and makes this theory more insightful.

Acknowledgments

I would like to thank:

Professor Richard Compton, for accepting me as his D.Phil student and his kind guidance and support during my doctoral studies at Oxford.

Dr. Emma Rogers, Dr. Juan Limon-Petersen and Dr. Eduardo Laborda, for making me understand the beauty of electrochemistry. This thesis would never has been accomplished without their help.

Dr. Ian Cutress, Stephen Belding, Martin Henstridge and Eddy Barnes, for providing their amazing simulation software used in this thesis.

All Compton Group members, who are like a family. Life with them is always full of fun, friendship and happiness. Particularly to **Yige Zhou, Yao Meng, Jane Panchompoo, Barbara Kozub, Ying Wang**.

St. John's College, for generously providing me financial support through a Lamb and Flag Studentship. The Lamb and Flage is a great pub with great Guinness and lemonade.

My parents, who are not scientists and have no idea about what I am writing (in English). Their support gives me the biggest courage to overcome any difficulty.

Contents

Abstract iii

Acknowledgments iii

Contents iv

Part I Introduction 1

1 Introduction to Electrochemistry 2

1.1 The Electrode/Solution Interface 2

1.1.1 Structure of the Interface 2

1.1.2 Charge Exchange Processes 3

1.2 Mass Transport 4

1.2.1 Diffusion 4

1.2.2 Migration 6

1.2.3 Convection 8

1.3 Heterogeneous Electron Transfer 8

1.3.1 The Butler-Volmer (BV) Theory 9

1.3.2 The Marcus-Hush (MH) Theory 11

1.4 Homogeneous Processes 16

1.4.1 EC Mechanism 16

1.4.2 ECE Mechanism 17

1.4.3 CE Mechanism 17

References 18

2 Introduction to Electroanalytical Techniques 20

2.1 Electrochemical Equipments 20

2.1.1 Electrodes 21

2.1.2 Potentiostat 23

2.1.3 Faraday cage 23

2.2 Electrochemical Methods 24

2.2.1 Potential Step Chronoamperometry 24

2.2.2 Cyclic Voltammetry 26

2.2.3 Pulse Voltammetry 31

2.3 Simulating Electrochemical Processes 33

2.4 General Information for Experiments 34

2.4.1 Instrumentation 34

2.4.2 Calibration of Electrodes 34

2.4.3 Making Mercury Hemispherical Electrodes 35

2.4.4 Determination of Diffusion Coefficients by Double Step Chronoamperometry . 35

References 36

Part II Electrochemical Investigation of Diffusional Behaviour 39

3 The Measurement of the Diffusion Coefficients of Ferrocene and Ferricenium and their Temperature Dependence in Acetonitrile using Double Potential Step Microdisc Electrode Chronoamperometry 40

3.1 Introduction 41

3.2 Experimental 46

3.2.1 Chemical Reagents 46

3.2.2 Instrumental 46

3.3 Results and discussion 47
3.3.1 Cyclic Voltammetry 47
3.3.2 Double Potential Step Chronoamperometry 48
3.4 Conclusions 52
References 54

4 Measurement of the Diffusion Coefficients of $[Ru(NH_3)_6]^{3+}$ and $[Ru(NH_3)_6]^{2+}$ in Aqueous Solution using Microelectrode Double Potential Step Chronoamperometry 57

4.1 Introduction 58
4.2 Experimental 59
4.3 Results and Discussion 60
4.3.1 Cyclic Voltammetry 60
4.3.2 Potential Step Chronoamperometric Experiments 61
4.4 Conclusions 66
References 67

Part III Mechanistic and Kinetic Study of Electrochemistry in Room Temperature Ionic Liquids 70

5 The Electrochemical Reduction of 1,4-Benzoquinone in 1-Ethyl-3-methylimidazolium bis(trifluoromethanesulfonyl)imide, $[C_2mim][NTf_2]$: A Voltammetric Study of the Comproportionation between Benzoquinone and the Benzoquinone Dianion 71

5.1 Introduction 72
5.2 Experimental 75
5.2.1 Chemical Reagents 75
5.2.2 Instrumental 75
5.3 Theory 75

5.3.1 Potential Step Chronoamperometric Experiments 76
5.3.2 Cyclic Voltammetric Simulation Techniques 76
5.4 Results and Discussion 77
5.4.1 Reduction of BQ to $BQ^{\bullet-}$ 77
5.4.2 Reduction of BQ to $BQ^{\bullet-}$ and BQ^{2-} 84
5.5 Conclusions 89
References 91

6 A Kinetic and Mechanistic Study of the Electrochemical Oxidation of Hydroquinone in 1-Ethyl-3-methylimidazolium bis(trifluoromethanesulfonyl)imide, [C_2mim][NTf_2] 94

6.1 Introduction 95
6.1.1 Electro-oxidation of Hydroquinone in Aqueous Solutions 95
6.1.2 Electro-oxidation of Hydroquinone in Acetonitrile 98
6.1.3 Electro-oxidation of Hydroquinone in Other Solutions 100
6.2 Experimental 101
6.2.1 Chemical Reagents 101
6.2.2 Instrumental 101
6.3 Theory 102
6.3.1 Suggested Mechanism 102
6.3.2 Cyclic Voltammetric Simulation Techniques 102
6.4 Results and Discussion 103
6.4.1 Cyclic Voltammetry 103
6.4.2 Chronoamperometry 105
6.4.3 Interpreting and Simulating the Cyclic Voltammetry 106
6.5 Conclusions 110
References 112

Part IV Study of Weakly-supported Electrochemistry 115

7 Voltammetry in the Absence of Excess Supporting Electrolyte - ECE-DISP1 Reactions: the Electrochemical Reduction of 2-Nitrobromobenzene in Acetonitrile Solvent 116

7.1 Introduction . . . 117

7.1.1 The ECE/DISP1 problem . . . 117

7.1.2 Weakly Supported Voltammetry . . . 118

7.2 Experimental . . . 119

7.2.1 Chemical Reagents . . . 119

7.3 Results and Discussion . . . 119

7.3.1 Experiments under full support . . . 119

7.3.2 Experiments under weak support . . . 123

7.4 Conclusions . . . 126

References . . . 127

8 New Chemical Insights Using Weakly Supported Voltammetry: Ion Pairing in the EC_2 Reduction of 2,6-Diphenylpyrylium in Acetonitrile 130

8.1 Introduction . . . 130

8.2 Experimental . . . 131

8.2.1 Chemical Reagents . . . 131

8.2.2 Instrumental . . . 131

8.3 Results and discussion . . . 132

8.4 Conclusion . . . 138

References . . . 139

9 Differential Pulse Techniques in Weakly Supported Media. Changes in the Kinetics and Thermodynamics of Electrode Processes Resulting from the Supporting

Electrolyte Concentration **141**

9.1 Introduction . . . 142

9.2 Experimental . . . 143

9.2.1 Chemical Reagents . . . 143

9.2.2 Instrumental and Solutions . . . 144

9.2.3 Determination of diffusion coefficients . . . 144

9.2.4 Voltammetric studies . . . 144

9.3 Theory . . . 146

9.3.1 Normalised Parameters . . . 148

9.3.2 Boundary Conditions . . . 149

9.3.3 Numerical Methods . . . 151

9.4 Results and Discussion . . . 152

9.4.1 Theoretical results . . . 152

9.4.2 Experimental results . . . 158

9.5 Conclusions . . . 166

References . . . 168

Part V Comparative Study of Butler-Volmer and Marcus-Hush Kinetics **172**

10 An Experimental Comparison of the Marcus-Hush and Butler-Volmer Descriptions of Electrode Kinetics Applied to Cyclic Voltammetry. the One Electron Reductions of Europium (III) and 2-Methyl-2-Nitropropane Studied at A Mercury Microhemisphere Electrode **173**

10.1 Introduction . . . 173

10.2 Experimental Methods . . . 176

10.3 Experimental Results . . . 176

10.3.1 Quantifying quality of fit . . . 176

10.3.2 The one electron reduction of Eu(III) . . . 177
10.3.3 The one electron reduction of 2-methyl-2-nitropropane (MeNP) . . . 180
10.4 Conclusions . . . 184
References . . . 186

11 Quantitative Weaknesses of the Marcus-Hush Theory of Electrode Kinetics Revealed by Reverse Scan Square Wave Voltammetry: the Reduction of 2-Methyl-2-Nitropropane at Mercury Microelectrodes 190

11.1 Introduction . . . 190
11.2 Experimental . . . 193
11.2.1 Chemical reagents . . . 193
11.2.2 Instrumental . . . 193
11.2.3 Square wave voltammetry experiments . . . 193
11.2.4 Simulation details . . . 194
11.3 Characterisation of the electrode kinetics by SWV . . . 194
11.4 Conclusions . . . 200
References . . . 202

12 The Use of Differential Pulse Voltammetries to Discriminate Between the Butler-Volmer and the Simple Marcus-Hush Models for Heterogeneous Electron Transfer: The Electro-reduction of Europium (III) in Aqueous Solution 204

12.1 Introduction . . . 205
12.2 Experimental . . . 209
12.2.1 Chemical Reagents . . . 209
12.2.2 Instrumental and Solutions . . . 210
12.2.3 Determination of diffusion coefficients by double potential step chronoamperometry . . . 211

12.2.4 Voltammetric kinetic studies . . . 211
12.3 Results and discussion . . . 213
12.4 Conclusions . . . 218
References . . . 220

13 Giving Physical Insight into the Butler-Volmer Model of Electrode Kinetics: Application of Asymmetric Marcus-Hush Theory to the Study of the Electroreductions of 2-Methyl-2-Nitropropane, Cyclooctatetraene and Europium(III) on Mercury Microelectrodes 224

13.1 Introduction . . . 225
13.2 Experimental . . . 227
13.2.1 Chemical Reagents . . . 227
13.3 Instrumental . . . 227
13.3.1 Experiments . . . 228
13.3.2 Fitting details . . . 229
13.4 Results and discussion . . . 229
13.5 Conclusions . . . 240
References . . . 242

Part VI Overall Conclusions 244

Appendices I

Appendix I: Theory for Chapter 5 II

Appendix II: Theory for Chapter 6 VIII

Appendix III: Theory for Chapter 7 XIII

Appendix IV: Theory and UV Experiments for Chapter 8 XXVIII

Appendix V: Theory for Chapter 10 **XL**

Appendix VI: Theory for Chapter 13 **XLVI**

Part I Introduction

Chapter 1 Introduction to Electrochemistry

Electrochemistry is the science dedicated to the study of chemical reactions taking place at the interface between an electrode (normally an electronic conductor like ReO_3 or semiconductor like WO_3) and a charge donor/accepter(electroactive species) in a media containing ionic species (electrolyte). The rest of this chapter gives a brief introduction to electrochemistry. More details can be found in several classic textbooks [1–6].

1.1 The Electrode/Solution Interface

The electron transfer process at the interfacial region is commonly considered as a function of the potential applied on electrode. When a potential difference is applied at the interface, charge will transfer between the electrode and the electroactive species or the electrolyte which induces a current. By monitoring the change of this current, kinetic, thermodynamic and mechanistic information of the process can be obtained. Before any further explanation is given, an understanding of interfacial region structure where the chemistry happens is essential.

1.1.1 Structure of the Interface

When an electrode is immersed into a medium (usually a solution), a charge separation between them will develop a potential different across the interface. To keep thermodynamical stability and electroneutrality, ions near the electrode will rearrange themselves rapidly. Therefore, ions of the same charge are repelled while those of opposite charge are more likely to stay around the vicinity of the electrode. Then an electric field gradient is formed in a zone which is called the 'Double Layer'.

The first theoretical model of the 'Double Layer' was introduced by Helmholtz [7, 8], indicating

that the charge at the electrode is confined near the surface and is evenly counter-balanced by a layer of oppositely charged solvated ions. This layer also contains some solvent molecules and is named as the Inner Helmholtz Plane (IHP). Its outside region with counter-balancing solvated ions is called the Outer Helmholtz Plane (OHP). Gouy and Chapman [9, 10] made significant improvement of the theory by introducing a diffuse layer in which the potential decreases approximately exponentially (rather than linearly as suggested by Helmholtz) from the electrode. Stern [11] combined the two models and developed a more commonly used theory called the Gouy-Chapman-Stern model, which is shown in Figure 1.1.

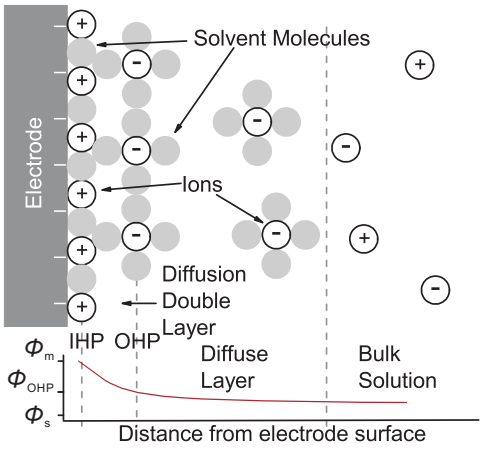


Figure 1.1: A schematic diagram of the structure of the Stern Double Layer model and the change of electrical potential versus the distance from the electrode surface. ϕ_m is potential at the surface of the metal electrode, ϕ_{OHP} is potential in the Outer Helmholtz Plane, and ϕ_{S} is potential in the bulk solution.

1.1.2 Charge Exchange Processes

There are two kinds of processes that charge exchanges between electrode and electrolyte interface. The first is named 'Faradaic' process after Sir Michael Faraday [12]. Faradaic current is generated by electro-oxidation/reduction of electroactive species. Its magnitude is proportional to the amount of charge exchanged. One mole of passed electrons gives 96485.4 C (known as the Faraday Constant, F) of charge.

The other type are non-Faradaic processes, which occurs when the potential applied on the electrode changes without leading to an oxidation or reduction of the species. Processes such as adsorption/desorption or interfacial structural changes, e.g. Ohmic drop variation caused by the concen-

tration profile changes in the electrode surface, may produce non-Faradaic current. This current I_c (called the charging current or the capacitative current) is described as follows assuming a homogeneous electrode surface:

$$I_c = AC_{dl}\frac{dE}{dt} = AC_{dl}\nu \tag{1.1}$$

where A is the electrode surface area, C_{dl} is the double layer capacitance, $\frac{dE}{dt}$ is the variation in potential with time which is equal to ν, the scan rate of voltammetry.

Although both the Faradaic and non-Faradaic processes contribute to the total current, the non-Faradaic current is not desirable for most electrochemical experiments; therefore conditions are usually designed to minimise its influence. For example, microelectrodes which have a small (mostly micrometer-scale) diameter are employed in the present thesis to reduce the surface area term A in Equation 1.1. Also, high scan rates (above 1,000 $V\ s^{-1}$) are usually avoided. This thesis mainly concerns the Faradaic current, which is typically determined by the mass transport, heterogeneous electron transfer kinetics as well as homogeneous chemical reactions processes in electrochemistry. These topics are covered in the following sections.

1.2 Mass Transport

Mass transport in an electrochemical experiment brings in a fresh supply of electroactive species to the interfacial region and moves the product away from the surface. There are three major types of mass transport, diffusion, migration and convection involved in electrochemical processes.

1.2.1 Diffusion

Diffusion is the movement of molecules caused in order to maximise the entropy and balance the concentration gradient (degree of randomness or disorder of the system is maximised) as shown in Figure 1.2. The electroactive species is consumed in the interfacial region, making a lower concentration compared to the bulk solution. The concentration difference drives fresh reactants to resupply the

consumed ones. This phenomenon was mathematically described by Adolf Fick by Fick's laws [13, 14]:

$$J = -D\nabla c \tag{1.2}$$

$$\frac{\partial c}{\partial t} = D\nabla^2 c \tag{1.3}$$

where J is the flux of the species, D is the diffusion coefficient, c is the concentration and t is time. Fick's first law (Equation 1.2) indicates that the diffusional flux is proportional to the concentration gradient, and the second law (Equation 1.3) shows that the variation of concentration is proportional to the spatial flux gradient.

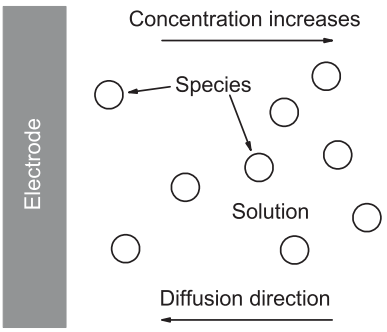


Figure 1.2: A schematic diagram of diffusion in an electrochemical system.

The diffusion coefficient value (D) is of importance for further quantitative analysis, which is normally determined experimentally (see Part I). Theoretically, the Stokes-Einstein model is commonly used for the estimation of unknown D values [15]:

$$D = \frac{k_{\mathrm{B}}T}{6\eta\pi a} \tag{1.4}$$

where k_{B} is the Boltzmann constant, T is the temperature, η is the viscosity of the solution, and a is the hydrodynamic radius of the species, which encompasses the radius of the molecule and its solvation shell. As inferred from this theory, the diffusion coefficient is temperature-dependent, which

can also be described through an Arrhenius equation [2]:

$$D = D_\infty \exp\left(\frac{-E_{a,D}}{RT}\right) \tag{1.5}$$

where D_∞ is a constant corresponding to the hypothetical diffusion coefficient at infinite temperature, R is the universal gas constant (8.314 J K^{-1} mol^{-1}), and $E_{a,D}$ is the diffusional activation energy of the electroactive species.

In a quiescent electrochemical system containing neutral electroactive species, or charged species with a high concentration of supporting electrolyte (normally chemically and electrochemically 'inert'), diffusion is considered as the sole mass transport contributor. However, if the charged species is not fully supported, the flux can also be effected by electric migration which is introduced in the following section.

1.2.2 Migration

Electric migration is defined as the mass transport of charged molecules from or to the electrode interface brought by the external electric field at the electrode, which is shown in Figure 1.3.



Figure 1.3: A schematic diagram of migration in an electrochemical system with (a) a positively charged electrode and (b) a negatively charged electrode.

In the present of an electric field gradient, any charged species will experience an electric field

force. This force is described by Coulomb's law:

$$\vec{F} = q\vec{E} \tag{1.6}$$

where $\vec{F}$ is the electric field force vector, q is the charge of the species and $\vec{E}$ field vector. The migration flux of species i is given as:

$$\vec{J_{\mathrm{i}}} = -z_{\mathrm{i}} u_{\mathrm{i}} c_{\mathrm{i}} \nabla\phi \tag{1.7}$$

where $\vec{J_{\mathrm{i}}}$ is the flux vector, z_{i} is the charge, u_{i} is the mobility, c_{i} is the concentration, and $\nabla\phi$ is the electric field gradient. The relationship between ionic mobility and the diffusion coefficient was suggested by Einstein [16] as:

$$u_{\mathrm{i}} = \frac{RTD_{\mathrm{i}}}{F} \tag{1.8}$$

where R, T, and F are the gas constant, temperature and the Faraday constant.

The net flux consists of both diffusion and migration terms as presented by the Nernst-Planck equation as:

$$\vec{J_{\mathrm{i}}} = -D_{\mathrm{i}}\nabla c_{\mathrm{i}} - z_{\mathrm{i}} D_{\mathrm{i}} c_{\mathrm{i}} \frac{F}{RT}\nabla\phi \tag{1.9}$$

Poisson equation suggests a way to calculate the electric field as:

$$\nabla^2\phi = -\frac{\rho}{\epsilon_{\mathrm{r}}\epsilon_0} \tag{1.10}$$

where ϵ_{r} and ϵ_0 are the dielectric constant and the permitivity of the solution, and the charge density ρ can be estimated by:

$$\rho = F\sum_i z_{\mathrm{i}} c_{\mathrm{i}} \tag{1.11}$$

Traditionally, an excessive amount of supporting electrolyte will be added into an electrochemical system in order to balance the electric field, decrease the IR drop and reduce the migration flux to a negligible level. However, in many cases, supporting electrolytes are not completely 'inert' which

will cause unwanted electrochemical and chemical reactions, e.g. SO_4^{2-} as supporting ions may have ion-pairing effect with electroactive hexaammineruthenium ions in water. Also, the solubility of the electrolyte sometimes not high enough. Therefore, studies of the migration effect is getting more concerned by electrochemists.

1.2.3 Convection

Convection is the movement of ensembles of molecules caused by mechanical or natural means. 'Forced convection' (*e.g.* stirring or shaking) and 'natural convection' (*e.g.* thermal or density gradients caused by long time current) are the two major types. In a quiescent system, convection normally has very little influence on the experimental results if experimental time is not long (normally less than 10 s), so it is little considered in the present thesis compared to diffusion and migration.

1.3 Heterogeneous Electron Transfer

Apart from mass transport, the Faradaic current can also be controlled by the rate of heterogeneous electron transfer. To explain, we consider a simple one electron reduction as an example:

$$\mathrm{O} + \mathrm{e}^- \underset{k_{\mathrm{ox}}}{\overset{k_{\mathrm{red}}}{\rightleftharpoons}} \mathrm{R} \tag{1.12}$$

where k_{red} and k_{ox} are the reduction and oxidation rate constants for the heterogeneous electron transfer. The electronic flux is the sum of both reduction and oxidation fluxes (J_{red} and J_{ox}):

$$J = J_{\mathrm{red}} + J_{\mathrm{ox}} = k_{\mathrm{red}} c_{\mathrm{R}} - k_{\mathrm{ox}} c_{\mathrm{O}} \tag{1.13}$$

where c_{R} and c_{O} are the concentration of the species R and O. Then the current can be presented as:

$$I = JAF = AF(k_{\mathrm{red}} c_{\mathrm{R}} - k_{\mathrm{ox}} c_{\mathrm{O}}) \tag{1.14}$$

where A is the electrode surface area and F is the Faraday constant. There are many methods to determine the kinetics (k_f and k_b). The two major theories, Butler-Volmer and Marcus-Hush, are introduced as follows.

1.3.1 The Butler-Volmer (BV) Theory

Butler and Volmer developed a fundamental electrode kinetic model for further electrochemical studies [17, 18]. The BV model is based on the Transition State Theory [19, 20], which dictates that overcoming of an activation energy barrier ($\Delta G^\ddagger$) between the reactants and products is required to drive the reactant to a transition state ($\ddagger$) with an Gibbs free energy of $G^\ddagger$ as shown in Figure 1.4. The kinetics then is related to the activation energy according to the Arrhenius equation:

$$k = Ae^{-\Delta G^\ddagger/RT} \tag{1.15}$$

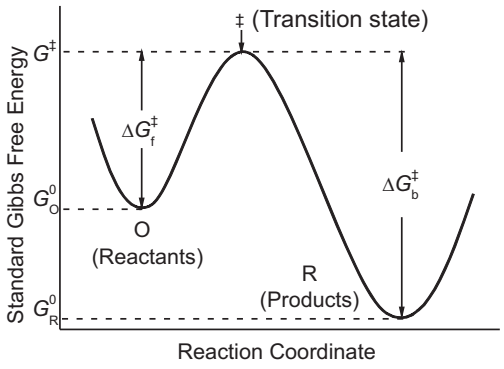


Figure 1.4: A schematic diagram of the Transition State Theory. G^0_O, $G^\ddagger$ and G^0_R are the standard Gibbs Energy for the species R, the transition state intermediate and the species R.

where A is a constant, $\Delta G^\ddagger$ is the activation energy which equals the standard Gibbs energy differences between the transition state and O ($\Delta G^\ddagger_\mathrm{c} = G^\ddagger$ - G^0_O) for the cathodic process (forward reaction), and between the transition state and R ($\Delta G^\ddagger_\mathrm{a} = G^\ddagger$ - G^0_R) for the anodic process (backward reaction).

When the electrode potential is set at a reference point, *e.g.* the formal potential, the cathodic

and anodic activation energies are called the formal activation energies, $\Delta G^{\ddagger}_{0,\mathrm{c}}$ and $\Delta G^{\ddagger}_{0,\mathrm{a}}$. When the electrode potential differs from the formal potential, the electron energy will be increased or lowered by a value of:

$$-F(E - E^{0'}) \tag{1.16}$$

where $E - E^{0'}$ is the difference between the applied and the formal potential, which is also known as the overpotential. Assuming there is a positive overpotential, the activation energy difference ($\Delta G^{\ddagger}_{0,\mathrm{c}}$-$\Delta G^{\ddagger}_{\mathrm{c}}$) is a fraction of the $F(E - E^{0'})$ value as shown in Figure 1.5. The BV model introduces an unitless parameter, the transfer coefficient (α) is defined to present this fraction. Its value is normally between 0 and 1 and typically around 0.5. Hence the applied cathodic activation energy becomes:

$$\Delta G^{\ddagger}_{\mathrm{c}} = \Delta G^{\ddagger}_{0,\mathrm{c}} - \alpha F(E - E^{0'}) \tag{1.17}$$

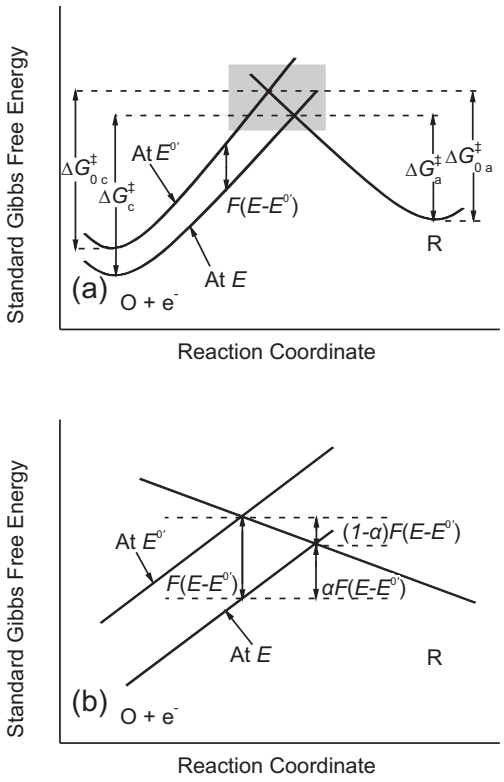


Figure 1.5: A schematic diagram of the changes of standard free energies of activation for the Transition State Theory. The lower figure shows a magnified illustration of the boxed area in the upper figure.

Now we can obtain the rate constants for the reduction and backward reactions according to Equation 1.15 as:

$$k_{\mathrm{f}} = A\exp\left(\frac{\Delta G^{\ddagger}_{0,\mathrm{c}}}{RT}\right)\exp\left(\frac{-\alpha F(E-E^{0'})}{RT}\right) = k^{0}_{\mathrm{f}}\exp\left(\frac{-\alpha F(E-E^{0'})}{RT}\right) \tag{1.18}$$

$$k_{\mathrm{b}} = A\exp\left(\frac{\Delta G^{\ddagger}_{0,\mathrm{a}}}{RT}\right)\exp\left[\frac{(1-\alpha)F(E-E^{0'})}{RT}\right] = k^{0}_{\mathrm{b}}\exp\left[\frac{(1-\alpha)F(E-E^{0'})}{RT}\right] \tag{1.19}$$

When in equilibrium, reduction and backward reactions have the same rate constant, which is defined as the standard electrochemical rate constant, k^{0}_{BV}. The total current then can be expressed as:

$$I = FAk^{0}_{\mathrm{BV}}\left\{\exp\frac{-\alpha F(E-E^{0'})}{RT}c_{\mathrm{O}} - \exp\left[\frac{(1-\alpha)F(E-E^{0'})}{RT}\right]c_{\mathrm{R}}\right\} \tag{1.20}$$

where c_{O} and c_{R} are the concentrations for oxidasing and reducing agents.

1.3.2 The Marcus-Hush (MH) Theory

Although the BV model has proven greatly successful in the analysis of electron transfer processes and is widely used by researchers, it does have defects, for example, it predicts an electron transfer rate dependent on the overpotential *ad infinitum*. Moreover, because of the phenomenological nature, its physical insight is very limited. By contrast, Marcus first suggested an alternative way to present the electron transfer kinetics [21–25] which was then improved by Hush [26, 27]. It was originally established to study outer sphere electron transfer reactions (when only electron exchange happens and no molecule structure change is caused), and further developed to take inner sphere electron transfer contributions into account which involved structural changes in solvation and coordination shells. The introduction of the 'reorganization energy' gives this kinetic model an microscopic insight into the electrochemical system.

The classic Frank-Condon electron transfer principle states that because the electron 'tunneling' from one molecule is a such fast process, that the external environment does not have enough time to change. After the electron transfers, the newly formed ions are surrounded by a 'foreign' environment

(e.g. the nearby dipolar solvent molecular environment) that is favoured by their predecessor. This causes a 'solvation energy' barrier that can determine the rate of electron transfer. However, directly applied this principle would have a defect that when reactions happen, the energy would not be conserved. To clarify, we take the oxidation from $Fe(H_2O)_6^{3+}$ to $Fe(H_2O)_6^{2+}$ in an aqueous solution as an example. As shown in Figure 1.6, the tunneling electron transfer from the ground state to the product state with the activation energy obtained from thermal activation via collision with solvent molecules. Electron transfer occurs when $Fe(H_2O)_6^{3+}$ ions are at the transition state (‡) to form $Fe(H_2O)_6^{2+}$. At this point of intersection, the energy of reactants and products are the same. To make the whole process happen, the energy obtained from thermal activation must match the energy to make the bond lengths/angles of the reactant and its solvation shell become stretched, compressed and/or distorted to the transitions state level. Further studies of the probability of the 'electron jump' were carried out by Hush [26–28], which relate the rate of electron transfer to the energy we described above. Details can be found in a series of classic books of electrochemistry [2, 3].

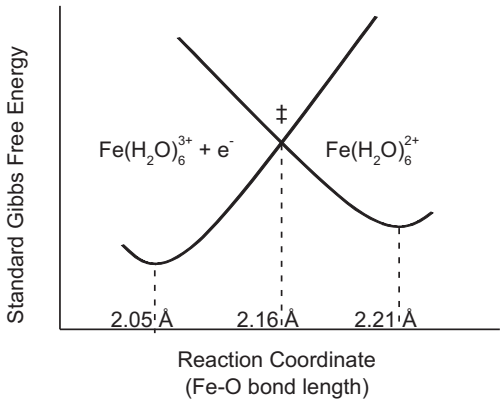


Figure 1.6: A schematic diagram of the electron transfer from $Fe(H_2O)_6^{3+}$ to $Fe(H_2O)_6^{3+}$.

To conduct the mathematical description of the Gibbs energy changes in an electrode reaction, we introduce a new reaction coordinate (q), which is determined by the vibrational motions in O and R and fluctuations in the orientation and position of the solvent molecules. Two basic assumptions for this model are that (1) the position (relative to the electrode) of the reactant molecules are fixed and (2) the Gibbs energies depend quadratically on the the reaction coordinate. Expressions of the

standard Gibbs energy for O and R are:

$$G_{\mathrm{O}}^{0} = (k/2)(q - q_{\mathrm{O}})^2 \tag{1.21}$$

$$G_{\mathrm{R}}^{0} = (k/2)(q - q_{\mathrm{R}})^2 + \Delta G^0 \tag{1.22}$$

where G_{O}^{0} and G_{R}^{0} are the standard Gibbs energies for O and R, k is a constant (e.g. the force constant for a chemical bonding), $q - q_{\mathrm{O}}$ and $q - q_{\mathrm{R}}$ are the changes in the reaction coordinate for O and R (e.g. changes in bond lengths), and ΔG^0 is the Gibbs energy change which equals $F(E - E^{0\prime})$ as shown in Figure 1.7.

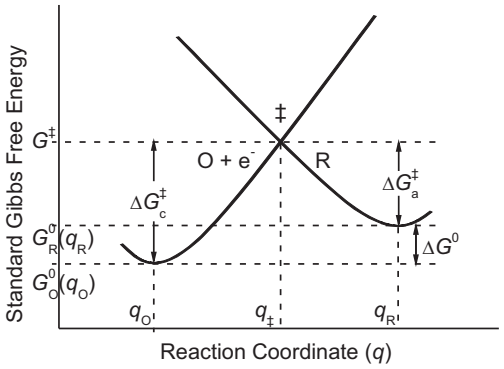


Figure 1.7: A schematic diagram of the changes in Gibbs free energies of activation suggested by the Marcus-Hush Theory.

Similar to the BV model, we assume that the electron transfer occurs at the transition state, where $q = q^{\ddagger}$, $G_{\mathrm{O}}^{0}(q^{\ddagger})$ and $G_{\mathrm{R}}^{0}(q^{\ddagger})$ are given by:

$$G_{\mathrm{O}}^{0}(q^{\ddagger}) = (k/2)(q^{\ddagger} - q_{\mathrm{O}})^2 \tag{1.23}$$

$$G_{\mathrm{R}}^{0}(q^{\ddagger}) = (k/2)(q^{\ddagger} - q_{\mathrm{R}})^2 + \Delta G^0 \tag{1.24}$$

Since when $q = q^{\ddagger}$, $G^0_{\mathrm{O}}(q^{\ddagger}) = G^0_{\mathrm{R}}(q^{\ddagger})$, $q^{\ddagger}$ is then obtained as,

$$q^{\ddagger} = \frac{q_{\mathrm{O}} + q_{\mathrm{R}}}{2} + \frac{\Delta G^0}{k(q_{\mathrm{O}} + q_{\mathrm{R}})} \tag{1.25}$$

The Gibbs energy of activation is then given by:

$$\Delta G^{\ddagger}_{\mathrm{c}} = G^0_{\mathrm{O}}(q^{\ddagger}) - G^0_{\mathrm{R}}(q^{\ddagger}) = \frac{k(q_{\mathrm{R}} - q_{\mathrm{O}})^2}{8}\left[1 + \frac{2\Delta G^0}{k(q_{\mathrm{R}} - q_{\mathrm{O}})^2}\right]^2 \tag{1.26}$$

Defining $\lambda = (k/2)(q_{\mathrm{R}} - q_{\mathrm{O}})^2$, the Equation 1.26 is changed to:

$$\Delta G^{\ddagger}_{\mathrm{c}} = \frac{\lambda}{4}\left(1 + \frac{\Delta G^0}{\lambda}\right)^2 = \frac{\lambda}{4}\left(1 + \frac{F(E - E^{0\prime})}{\lambda}\right)^2 \tag{1.27}$$

λ is named as the 'reorganization energy', representing the necessary energy to turn the nuclear configurations in the reactant and solvent to the product state. It consists of both the inner term (λ_{i}) from the reorganization of reactants and the outer term (λ_{o}) from the solvent

$$\lambda = \lambda_{\mathrm{i}} + \lambda_{\mathrm{o}} \tag{1.28}$$

$\Delta G^{\ddagger}_{\mathrm{c}}$ is the energy needed to bring the O and R species from their usual environment to the state for electron transfer. Also, the additional energy of ion-pairing and the electrostatic work are required to reach the reactive positions, which are named as the work terms w_{O} and w_{R}, and added into Equation 1.27 as:

$$\Delta G^{\ddagger}_{\mathrm{c}} = \frac{\lambda}{4}\left(1 + \frac{\Delta G^0 - w_{\mathrm{O}} + w_{\mathrm{R}}}{\lambda}\right)^2 = \frac{\lambda}{4}\left(1 + \frac{F(E - E^{0\prime}) - w_{\mathrm{O}} + w_{\mathrm{R}}}{\lambda}\right)^2 \tag{1.29}$$

To determine the λ_{i} value, a classic model of harmonic vibration for a molecule over the range of distortion is used, which gives:

$$\lambda_{\mathrm{i}} = \sum_j \frac{1}{2} k_{\mathrm{j}}(q_{\mathrm{O,j}} - q_{\mathrm{R,j}})^2 \tag{1.30}$$

where k_{j} is force constant for j (for example, a bond force constant), $q_{\mathrm{O,j}}$ and $q_{\mathrm{R,j}}$ are the displacements in the normal mode coordinates (for example, a bond length). To get the λ_{o} value, we assume the solvent is a dielectric continuum and O has a spherical geometry, and then λ_{o} is represented as:

$$\lambda_0 = \frac{e^2}{8\pi\epsilon_0}\left(\frac{1}{a_{\mathrm{O}}} - \frac{1}{R}\right)\left(\frac{1}{\epsilon_{op}} - \frac{1}{\epsilon_{\mathrm{s}}}\right) \tag{1.31}$$

where ϵ_0 is the permitivity of the solvent, ϵ_{op} and ϵ_{s} are the optical and static dielectric constants, R is twice as the distance between the centre of the molecule and the electrode which is normally set to be infinity.

To relate the BV and MH models, α can be calculated from:

$$\alpha = \frac{1}{F}\frac{\partial G_{\mathrm{c}}^{\ddagger}}{\partial E} = \frac{1}{2} + \frac{F(E - E^{0'}) - (w_{\mathrm{O}} - w_{\mathrm{R}})}{2\lambda} \tag{1.32}$$

Referring to the BV model, the kinetics can be calculated by a standard Arrhenius relationship:

$$k = A\exp\left(\frac{-\Delta G_{\mathrm{c}}^{\ddagger}}{k_{\mathrm{B}}T}\right) \tag{1.33}$$

where A is a prefactor that depends on the nature of electron transfer process, k_{B} is the Boltzmann constant, and T is the absolute temperature. A commonly used term of MH formalism for electrode kinetics (detailed assumptions and derivation of these equations can be found in [28]) is presented as:

$$I = FAk_{\mathrm{MH}}^{0}\left[f_{\mathrm{red}}(\Lambda,\eta)c_{\mathrm{A}} - f_{\mathrm{ox}}(\Lambda,\eta)c_{\mathrm{B}}\right] \tag{1.34}$$

where $\eta = \frac{F}{RT}(E - E^{0'})$, f is a function of the applied potential and the reorganization energy (λ):

$$f_{\mathrm{red/ox}}(\Lambda,\eta) = \frac{I_{\mathrm{red/ox}}(\Lambda,\eta)}{I_{\mathrm{red/ox}}(\Lambda,0)} \tag{1.35}$$

$$\Lambda = \frac{F\lambda}{RT} \tag{1.36}$$

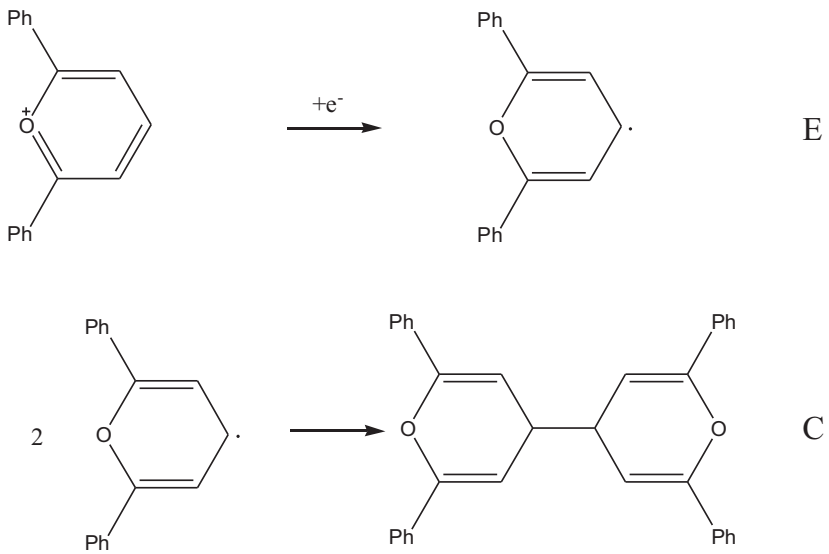
$$I_{\mathrm{red/ox}}(\Lambda,\eta)=\int_{-\infty}^{+\infty}\frac{\exp\left[-\Delta G_{\mathrm{c}}^{\ddagger}(\epsilon)\right]}{1+\exp\left[\mp\epsilon\right]}d\epsilon \tag{1.37}$$

1.4 Homogeneous Processes

Besides heterogeneous electron transfer processes, chemical processes without heterogeneous charge exchanges are also involved in electrochemical mechanisms which is called as homogeneous processes. These chemical steps can have significant influences on the voltammetry. Testa and co-workers introduced a notification system which relates an electron transfer step to the letter 'E' and a homogeneous step to 'C' [29], and combines the letters in the reaction order. The letters are combined in the order of the processes happening at the electrode surface. Three types of mechanisms, EC, ECE and CE are presented in this section.

1.4.1 EC Mechanism

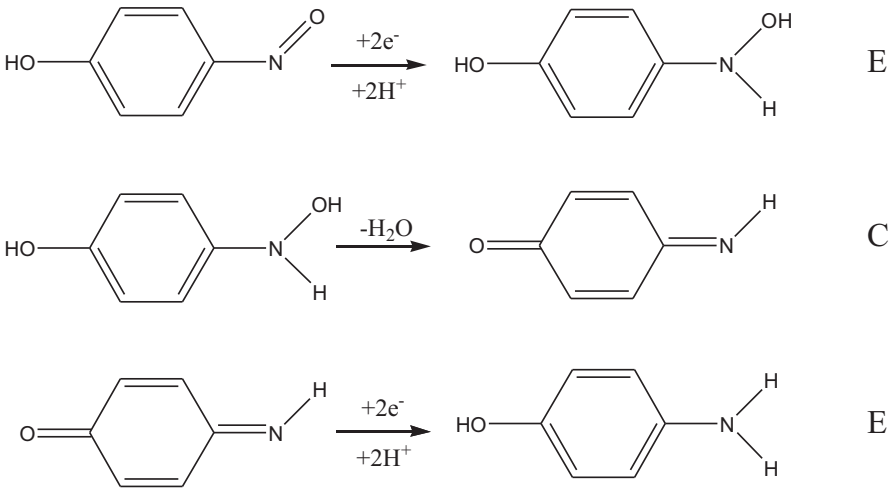
An EC mechanism includes an electron transfer step followed by a chemical step. An example of this mechanism is the electro-reduction of 2,6-diphenylpyrylium cation (DPP^{+}) in acetonitrile [30]:



DDP^+ ions are reduced first, forming reactive $DDP^\bullet$ radicals, which combine together rapidly by a dimerisation process. Since the C step is a second-order reaction, this mechanism is also named as an EC_2 scheme.

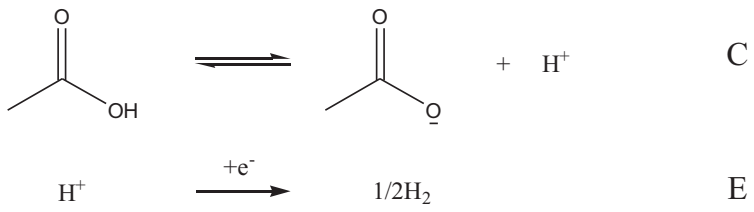
1.4.2 ECE Mechanism

An ECE mechanism has an additional E step after an EC scheme. The reduction of 4-nitrosophenol in aqueous solution is taken as an example:



1.4.3 CE Mechanism

A CE mechanism represents an electron transfer step following a chemical step. An example for this type is the reduction of acetic acid [31]:



References

[1] R.G. Compton, G.H.W. Sanders, Electrode Potentials, Oxford University Press, Oxford, 1998.

[2] R.G. Compton, C.E. Banks, Understanding Voltammetry, 2nd edn., Imperial College Press, London, 2011.

[3] A.J. Bard, L.R. Faulkner, Electrochemical Methods, Fundamentals and Applications, John Wiley & Sons, New York, 2001.

[4] P.H. Rieger, Electrochemistry, 2nd edn., Chapman and Hall, Inc., New York, 1994.

[5] C.M.A. Brett, A.M.O. Brett, Electrochemistry: Principles, Methods and Applications, Oxford University Press, Oxford, 1994.

[6] A.M. Bond, Broadening Electrochemical Horizons, Oxford University Press, Oxford, 2002.

[7] H.L.F. von Helmholtz, Ann. Physik. 165 (1853) 211–233.

[8] H.L.F. von Helmholtz, Ann. Physik. 243 (1879) 337–382.

[9] G. Gouy, Compt. Rend. Chimie. 149 (1900) 654.

[10] D.L. Chapman, Phil. Mag. 25 (1913) 475.

[11] O. Stern, Z. Elektrochem. Angew. Phys. Chem. 30 (1924) 508–516.

[12] M. Faraday, Experimental Researches in Electricity, Bernard Quaritch, London, 1839.

[13] A. Fick, Poggendorff's Annel. Physik. 94 (1855) 59–86.

[14] A. Fick, Phil. Mag 10 (1855) 30–39.

[15] A. Einstein, Ann. Phys. 17 (1905) 549–560.

[16] J. Goodisman, Electrochemistry: Theoretical foundations, Wiley, New York, 1987.

[17] J.A.V. Butler, Trans. Faraday Soc. 19 (1924) 729–733.

[18] T. Erdey-Gruz, M. Volmer, Z. Physik. Chem. 150 (1930) 203–213.

[19] P.W. Atkins, Physical Chemistry, 6th edn., Oxford University Press, Oxford, 1998.

[20] R. Berry, S.A. Rice, J. Ross, Physical Chemistry, Wiley, New York, 1980.

[21] R.A. Marcus, J. Chem. Phys. 24 (1956) 966–978.

[22] R.A. Marcus, J. Chem. Phys. 24 (1956) 979.

[23] R.A. Marcus, J. Chem. Phys. 26 (1957) 867.

[24] R.A. Marcus, Annu. Rev. Phys. Chem. 15 (1964) 155.

[25] R.A. Marcus, J. Chem. Phys. 43 (1965) 679–701.

[26] N.S. Hush, J. Chem. Phys. 28 (1958) 962–972.

[27] N.S. Hush, Trans. Faraday Soc. 57 (1961) 557.

[28] N.S. Hush, J. Electroanal. Chem. 470 (1999) 170–195.

[29] A.C. Testa, W.H. Reinmuth, Anal. Chem. 33 (1961) 1320–1324.

[30] E.O. Barnes, Y. Wang, S.R. Belding, R.G. Compton, ChemPhysChem 13 (2012) 92–95.

[31] R.S. Stojanovic, A.M. Bond, Anal. Chem. 65 (1993) 56–64.

Chapter 2 Introduction to Electroanalytical Techniques

After understanding the theoretical knowledge of electrochemistry from the previous chapter, an introduction of one important application, electroanalytical techniques, is presented in this chapter, which are a class of approaches that investigate an analyte by measuring the potential or current in an electrochemical cell [1, 2]. Fundamental principles and methodologies regarding to this area are explained. First, a series of key equipments including electrodes, potentiostat and Faraday cage are introduced respectively. Then several major methods of how to use these equipments to obtain interested information - potential step chronoamperometric, cyclic voltammetric and pulse voltammetric techiquies are described in detail. In addition, a mathematical simulation of experimental findings is the way applied in this thesis to gain informative insights into electroanalytical chemistry from experiments. Last but not least, general experimental details are given in the final section of this chapter, which provides information of the employed equipments, preparation and calibration of electrodes and making hemispherical electrodes.

2.1 Electrochemical Equipments

Electrochemical experiments are normally carried out in electrochemical cells, which are the devices either driving chemical reactions using electric energy or obtaining energy from electrochemical reactions. A typical electrochemical cell, called a 'three-electrode system', normally consists of an electrolyte solution containing species to be studied, a working electrode, a counter electrode, a reference electrode, and a potentiostat. The electrodes are immersed into the solution, and connected to the potentiostat as shown in Figure 2.1. In some cases, a 'quasi-reference electrode' which works as both a counter and a reference electrode is introduced when an accurate determination of the working

electrode potential is not the main research interest.

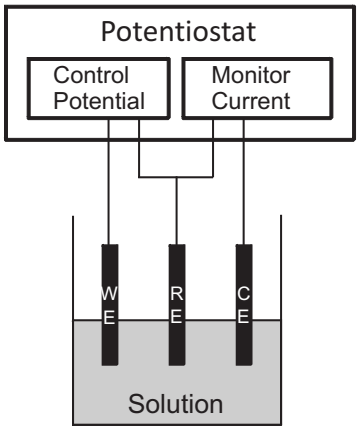


Figure 2.1: An illustration of a typical three-electrode setup. WE is the working electrode, CE the counter electrode and RE the reference electrode.

2.1.1 Electrodes

A complete electrochemical cell reaction can be divided into two half-cell parts, the electron-gaining and electro-losing electrode processes. When we are interested in a certain half-cell process in an electrochemical cell, a 'working electrode' (WE) is employed where interfaces for electron interchange are provided and the current or potential is monitored. We can classify WEs by geometry into several types, but disk and hemispherical electrodes are mostly employed in general electrochemical studies and experiments reported in this thesis. To complete a circuit, a 'counter electrode' (CE) is introduced which plays a role to balance the injection of charge into the cell at the WE. An additional electrode, the 'reference electrode' (RE), is usually added into the cell. Then a voltage added to the WE can be determined relative to the RE. A good RE normally has a fixed potential throughout the measurement, therefore the applied potential (E_{app}) can be expressed as:

$$E_{\mathrm{app}} = E_{\mathrm{WE}} - E_{\mathrm{RE}} - IR_{\mathrm{s}} \tag{2.1}$$

where E_{WE} and E_{RE} are the potentials on the WE and RE respectively, I is the current, and R_{s} is the uncompensated resistance of the media in the cell. The combined term IR_{s} is named 'Ohmic drop' which can make the voltammetry stretched or distorted. However, Ohmic drop can be reduced

to a negligible level compared to the potential difference between WE and RE by adding a high concentration of supporting electrolyte, reducing the distance between WE and RE or using a small working electrode ($I \propto r_0^2$, $R_\mathrm{s} \propto r_0^{-1}$, so $IR_\mathrm{s} \propto r_0$).

Macro- and Micro- Electrodes

In common electrochemical experiments, a working electrode normally has a diameter greater than 100 μm. This type of electrode is call the 'marcroelectrode', which is easy to fabricate and can be purchased cheaply. However, thanks to the fast progress of small electrode fabrication techniques, the use of micro-electrodes (which have a micron-scale diameter) has been widely encouraged. Microelectrodes have a large number of advantages compared to marcoelectrodes [3–5]. First, the potential difference at the interfacial region is obtained at a shorter timescale, which is particularly important in measuring fast electron transfer processes [5, 6]. Second, as mentioned before, the Ohmic drop is proportional to the radius of working electrode, meaning IR_s value could be minimised by employing microelectrodes. Third, as suggested by Equation 2.2, a small electrode surface area also leads to a smaller double layer capacitance, which is favorable for most electrochemical experiments considering the Faradaic process only.

$$C_\mathrm{dl} = \epsilon_\mathrm{r}\epsilon_0 A d^{-1} \tag{2.2}$$

where C_dl, ϵ_r, ϵ_0, A, and d are the electrode double layer capacitance, the relative static permittivity, the electric constant and the thickness of the double layer

The differences between macro- and micro- electrodes mainly come from their distinct diffusional patterns at the electrode surface, which are shown in Figure 2.2.

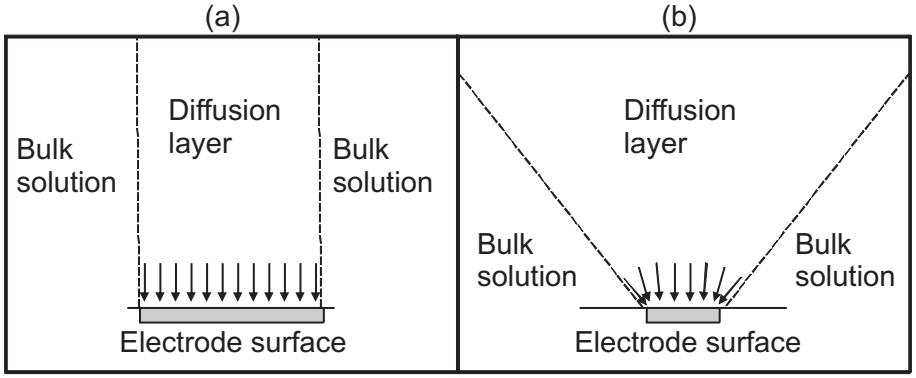


Figure 2.2: A comparison of the diffusional pattern at (a) a macroelectrode and (b) a microelectrode. The volume of diffusion layer for macroelectrodes is confined within the expanding area of the electrode surface. For microelectrodes, the diffusion layer is relatively larger because it could be stretched divergently into the bulk solution.

Since the diffusion layer is much smaller than the size of a macroelectrode, the diffusion is mainly planar. Microelectrodes have a convergent diffusion, which dominates when the voltammetric scan rate is moderately slow.

2.1.2 Potentiostat

Potentiostat is an instrument that imposes the potential difference between working and reference electrodes, and monitor the current response between working and counter electrodes. A potentiostat is usually controlled by a computer, on which researchers can input programs designating certain potential waveforms and kept a watch on the results of experiments.

2.1.3 Faraday cage

All electrochemical experiments were undertaken within a Faraday cage, which is an enclose made of conducting materials that blocks external static and non-static electric fields. This can reduce the external electric interference for more stable measurements. Because the temperature inside the cage may not meet the required experimental condition (298±1K unless otherwise stated), a thermometer was equipped in the Faraday cage to monitor the temperature, and an automatic heater was also

introduced to compensate the temperature loss when it was below the wanted value.

2.2 Electrochemical Methods

Electrochemical experiments are carried out by a controlling potentiostat which can apply a fixed potential or systematically varying potentials at the working electrode surface and record the change of current. Some common methods employed along with this thesis are presented in this section including potential step chronoamperometry, cyclic voltammetry and pulse voltammetry

2.2.1 Potential Step Chronoamperometry

Potential step chronoamperometric techniques step the potential to an expected value and maintain it for a certain period of time. The current variation in time is recorded. To explain the observed response, we consider a simple one electron reduction process reducing O to R. An example of chronoamperometry is shown in Figure 2.3.

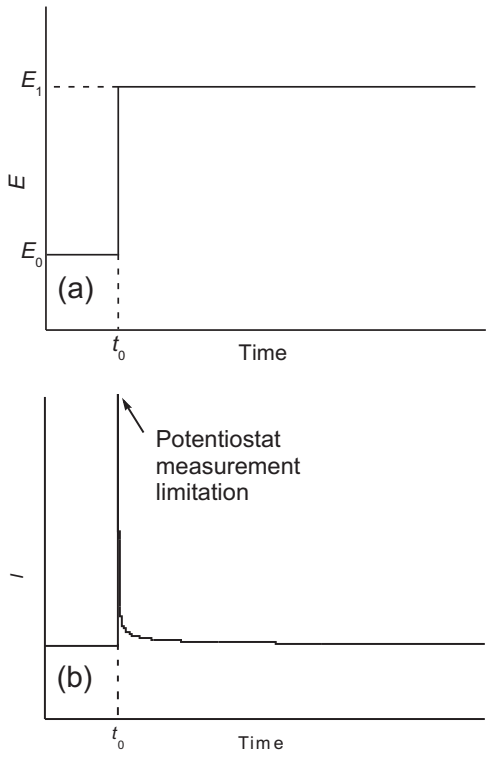


Figure 2.3: A schematic demonstration of chronoamperometry. (a) shows a varying pattern of the potential applied on the working electrode. The potential is set as an initial value, E_0, then stepped to and held at a preset value, E_1 from time t_0. (b) is the corresponding response of the current varying with time. The current is zero before t_0, then increases instantaneously to the measurement limitation of current, and decays systematically with time.

At macroelectrodes, a mathematical description of chronoamperometry is given by the Cottrell equation [7]:

$$I_{\mathrm{d}} = \frac{nFAD^{\frac{1}{2}}c}{\pi^{\frac{1}{2}}t^{\frac{1}{2}}} \tag{2.3}$$

where I_{d} is the current response, n is the number of electron transferred, F is the Faraday constant, A is the surface area of the electrode, D is the diffusion coefficient, c is the concentration of the electroactive species and t is the time. The current is varying linearly versus the $\frac{1}{\sqrt{t}}$ value, and has a limit of zero when the time approaches infinity. However, it is important to note that this is hard to achieve in practical experiments because that long-time current may cause undesired natural convection.

With respect to microdisk electrodes, a semi-empirical description was developed by Shoup and

Szabo [8], which has a maximum error of 0.6 % over the entire time domain:

$$I = 4nFDcr_{\mathrm{d}}f(\tau) \tag{2.4}$$

$$f(\tau) = 0.7854 + 0.8863\tau^{-\frac{1}{2}} + 0.2146\exp(-0.7823\tau^{-\frac{1}{2}}) \tag{2.5}$$

where r_{d} is the radius of the microdisk and the dimensionless time parameter, τ is given by:

$$\tau = \frac{4Dt}{{r_{\mathrm{d}}}^2} \tag{2.6}$$

Multiple step chronoamperometry is also commonly used. An analytical method studying the second step is developed by Klymenko [9] by introducing an exponentially expanding time grid. Further steps can also be simulated using the same methodology.

2.2.2 Cyclic Voltammetry

Cyclic voltammetry involves a linearly varying potential from a value where there is no Faradaic current (E_0) to a point that the electron transfer process is purely diffusion controlled (E_1) and then back to the initial position as shown in Figure 2.4.

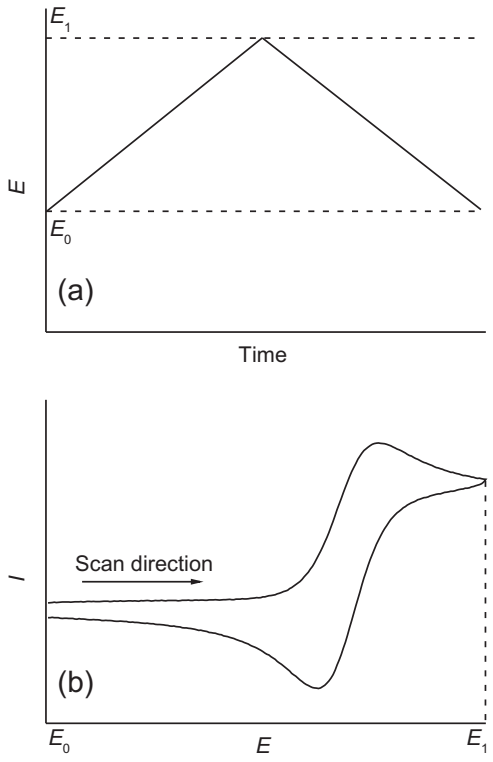


Figure 2.4: A schematic demonstration of cyclic voltammetry. (a) shows the varying the potential applied on the working electrode versus time. (b) the corresponding current response versus potential.

Cyclic voltammetry is one of the most widely applied electroanalytical methods. Its peak heights, shapes and positions can be used to determine a series of physical, kinetic and thermodynamic paramenters (e.g. concentrations of electroactive species, diffusion coefficients, standard rate constants and formal potentials).

Examples of voltammograms of a one electron reduction process with different kinetics (k_0) at a marcro-electrode are shown in Figure 2.5, where $E_{\mathrm{p}}^{\mathrm{red}}$, $E_{\mathrm{p}}^{\mathrm{ox}}$, and E_{f} are the reduction peak, oxidation peak and formal potentials, $I_{\mathrm{p}}^{\mathrm{red}}$ and $I_{\mathrm{p}}^{\mathrm{ox}}$ are the reduction peak and oxidation peak currents. Different kinetics result in various voltammetric responses. Figure 2.5a shows a reversible reaction with a fast electron transfer rate ($k_0 > 0.3\,\nu^{\frac{1}{2}}$ cm s^{-1}, where ν is the scan rate in V s^{-1}). The initial potential does not lead to a significant current, but when the potential is scanned towards the position that electron transfer occurs, the current increases approximately exponentially. If the potential keeps rising, the current begins to drop due to the limitation of mass transport to the electrode, leading to a peak in

the voltammogram which is very useful for qualitative and quantitative analysis. The Randles-Ševčík equation [10, 11] based on BV kinetics is used to calculate the peak height (I_p) at 298K:

$$I_\mathrm{p} = 2.69 \times 10^{-5} n^{\frac{3}{2}} A D^{\frac{1}{2}} c_\mathrm{bulk} \nu^{\frac{1}{2}} \tag{2.7}$$

where n is the number of electrons transfered (*e.g.* n= 1 for the $Fe^{2+}|Fe^{3+}$ redox couple, since one electron transfers from Fe^{2+} to form Fe^{3+}), A is the electrode surface area, D is the diffusion coefficient, c_bulk is the contration of the bulk solution, and ν is the scan rate. The peak to peak separation ($|E_\mathrm{p}^\mathrm{red}$ - $E_\mathrm{p}^\mathrm{ox}|$) is $2.20\frac{RT}{F}$ (56 mV at 298 K). In this type of reaction, if the diffusion coefficients for the redox couple are similar, the half-wave potential ($E_{\frac{1}{2}}$ defined as the mid-point between $E_\mathrm{p}^\mathrm{red}$ and E_p^ox) is around the same with the formal potential ($E^{0'}$).

Voltammograms for quasi-reversible and irreversible reactions with relatively slow kinetics ($0.3\ \nu^{\frac{1}{2}}$ cm $s^{-1} > k_0 > 2 \times 10^{-5}\nu^{\frac{1}{2}}$ cm s^{-1}, and $k_0 < 2 \times 10^{-5}\nu^{\frac{1}{2}}$ cm s^{-1} respectively). As can be seen in Figure 2.5a and 2.5b, the waves are broader and smaller than the reversible one. In these cases, the peak current is not only determined by the diffusional property of the electroactive species; the α value in the Butler-Volmer model can also influence the current. Then the Randles-Ševčík equation is changed accordingly to [12]:

$$I_\mathrm{p} = 2.99 \times 10^{-5} (n\alpha)^{\frac{1}{2}} A D^{\frac{1}{2}} c_\mathrm{bulk} \nu^{\frac{1}{2}} \tag{2.8}$$

This variation reflects different electrode kinetics. For reversible processes, both k_f and k_b are fast, resulting in that the concentration ratio of reactants and products is in equilibrium as predicted in Nernst equation, while for irreversible ones, the back reaction is relatively slow.

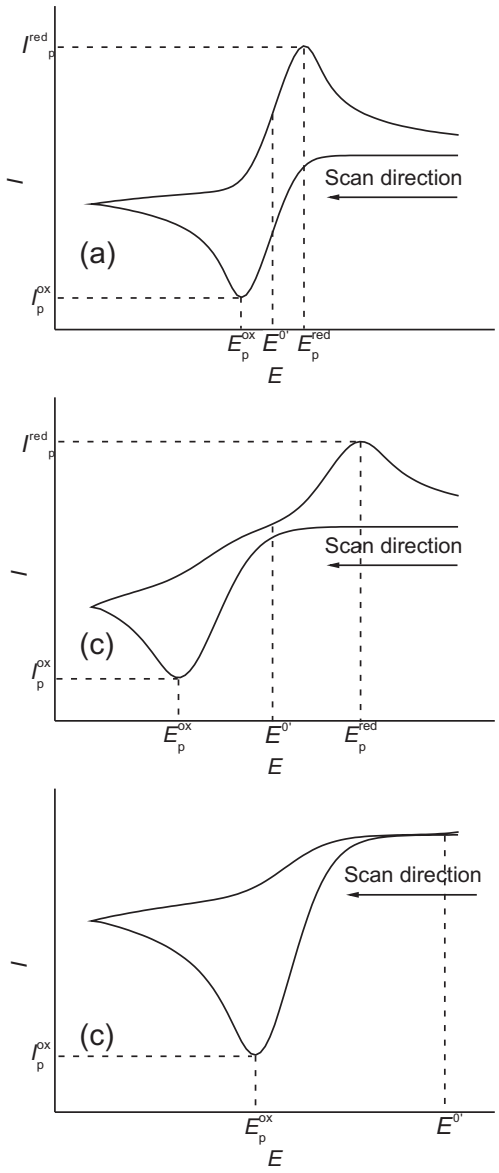


Figure 2.5: Cyclic voltammograms for one electron reduction reactions at a macroelectrode for (a) a reversible reaction with a fast kinetics ($k_0 > 0.3\ \nu^{\frac{1}{2}}$ cm s^{-1}), (b) a quasi-revisable reaction with a medium kinetics ($0.3\ \nu^{\frac{1}{2}}$ cm s$^{-1} > k_0 > 2 \times 10^{-5}\nu^{\frac{1}{2}}$ cm s^{-1}), and (c) a irreversible reaction with a slow kinetics ($k_0 < 2 \times 10^{-5}\nu^{\frac{1}{2}}$ cm s^{-1}).

At microelectrodes, when moderate scan rates are applied, convergent diffusion dominates the electron transfer process, and the waves have a plateau shape with a limiting current other than a peak-shaped current curve. This difference against macroelectrodes is due to distinct diffusion patterns at the electrode surface. At macroelectrodes, dominatinglinear diffusion means that only the solution above the electrode surface can contribute to the diffusion of electroactive species towards the electrode. Therefore, as the time increases, there will not be enough species compensating those

consumed at the electrode, and the thickness of diffusion layer will become larger, leading to smoother concentration gradient and smaller current. In contrast, at microelectrodes, the diffusion is convergent, meaning the diffusion layer is expanded divergently into the bulk solution unlike a confined volume at macroelectrodes. As a result, the lose of concentration gradient can be rapidly recovered and the current can be maintained at a maximum level. This status is named as the 'steady-state', at which the diffusion of reactants is fast enough to compensate those consumed at the electrode surface. An example of voltammetry at microelectrodes is shown in Figure 2.6, where I_{ss} is the steady-state limiting current.

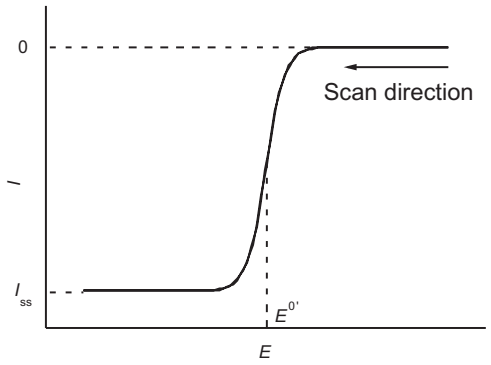


Figure 2.6: Cyclic voltammogram for one electron reduction reactions at a microelectrode. A steady-state limiting current I_{ss} can be achieved when rapid diffusion can compensate the consumed electroactive species.

The limiting current can be used to calibrate the radius (r_d) of a microdisk electrode by the following equation:

$$I_{ss} = 4nFDc_{bulk}r_d \tag{2.9}$$

It should also be noted that the concentration depletion can also occur at a microelectrode at high scan rates when the time given for the recovery of lost species is limited, or the diffusion coefficient is not high to make the replenishment faster than the consumption (*e.g.* as happens in highly viscous room temperate ionic liquids).

2.2.3 Pulse Voltammetry

Pulse voltammetry is another common electroanalytical method which is employed in many chapters of this thesis. Compared to cyclic voltammetry, pulse voltammetric techniques employ pulse-shaped waveforms instead of a linear one. The potential is held at an initial value (E_0) where no Faradaic process occurs and then stepped progressively to a purely diffusion-controlled value. Examples of the waveforms and current responses for four types of pulse voltammetric techniques, sampled current polarography (SCP), normal pulse voltammetry (NPV), differential pulse voltammetry (DPV), and square wave voltammetry (SWV) are shown in Figure 2.7. Sampled current polarography has varying potentials in a series of steps, with the current sampled at the end of each step. Normal pulse voltammetry consists of a series of pulses of increasing amplitude, with the potential returning to the initial value after each pulse. Differential pulse voltammetry and square wave voltammetry are similar. They both have small pulses of a preset amplitude added on a staircase. Unlike NPV, there are two sample periods, before (reverse) and at the end of each pulse period (forward) respectively, as shown in Figure 2.7, and the current difference of these two periods is recorded for display.

There are two major advantages using pulse techniques, especially DPV and SWV. First, the charging current can be better discriminated, for example, it can be subtracted out by superimpositing the reverse and forward currents. Second, even at steady-state, peak-shaped curves can still be obtained for analysis other than a flat line in a cyclic voltammogram. Therefore the interest in kinetic and mechanistic studies using pulse techniques [13–22] is well established, which are insightfully important for accurate measurements of kinetic and thermodynamic parameters.

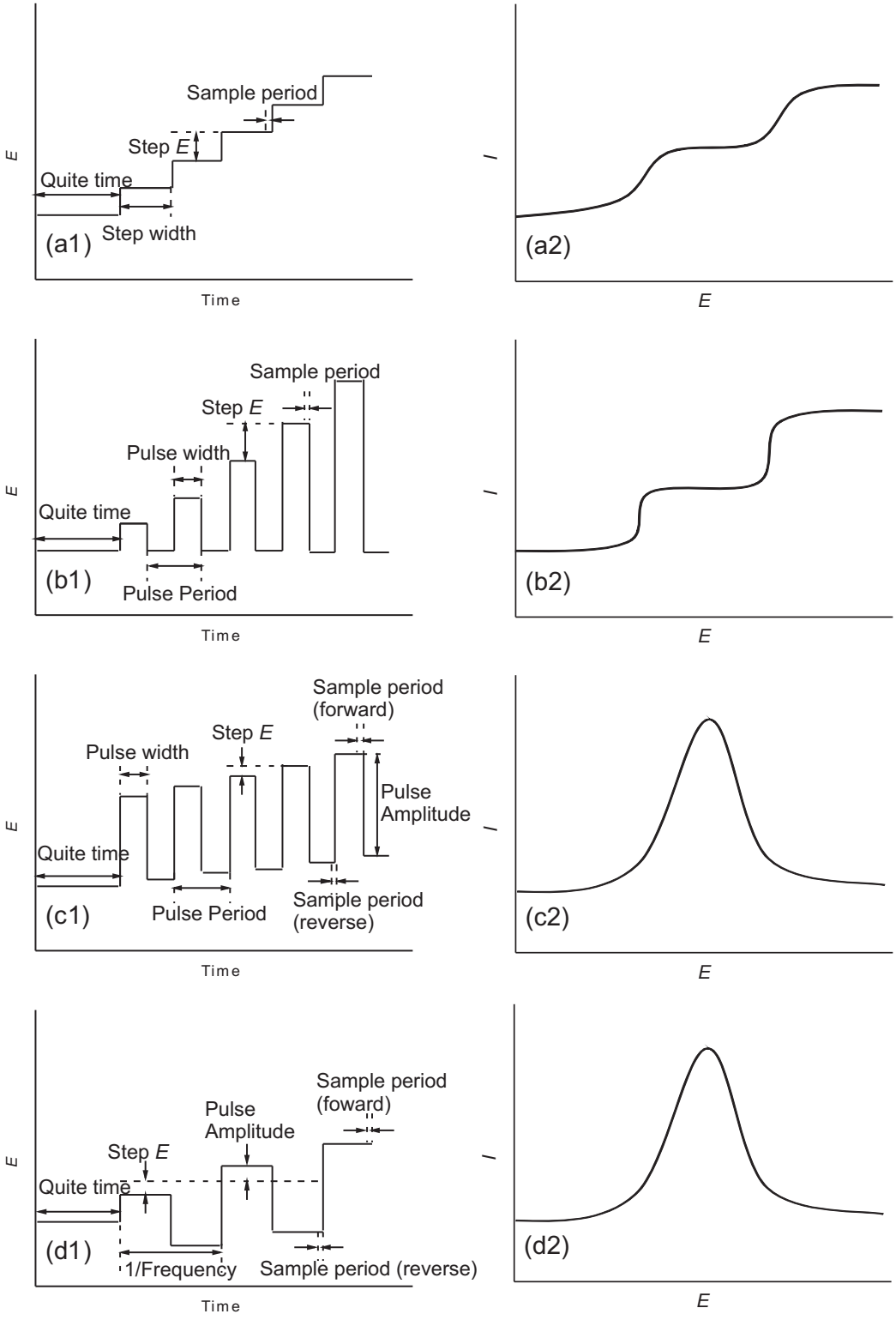


Figure 2.7: A schematic demonstration of pulse voltammetry. (a1), (b1), (c1) and (d1) are the waveforms for sampled current polarography, normal pulse voltammetry, differential pulse voltammetry, and square wave voltammetry. (a2), (b2), (c2) and (d2) are the typical corresponding current responses correspondingly.

2.3 Simulating Electrochemical Processes

After electrochemical experiments are carried out using electrochemical methods mentioned in the previous section, theoretical analysis is the following step that can provide a wealth of informative parameters. Although mathematical models cannot give exact descriptions of the voltammograms because the disability of simulating a real consecutive system, many strategies have been developed which approximate the result using well optimized discrete models [23–28]. One commonly used methodology, the 'Fast Implicit Finite Difference' approach is introduced in this section, which is also the fundamental of the commercial voltammetric simulation software *Digisim* (version 3.0, BAS Technicol, USA [27, 29–31]) and the bespoke programs utilized within this thesis. This method solves the partial differential equations (normally with a couple of space and time variables) associated with mass transport, electrode kinetics and homogeneous rates or equilibria. The continuous space and time are separated into finite spatial dimensions. For a one dimensional case, the space coordinate x and time coordinate t are divided into discrete points with intervals of Δx and Δt between each two points as shown in Figure 2.8.

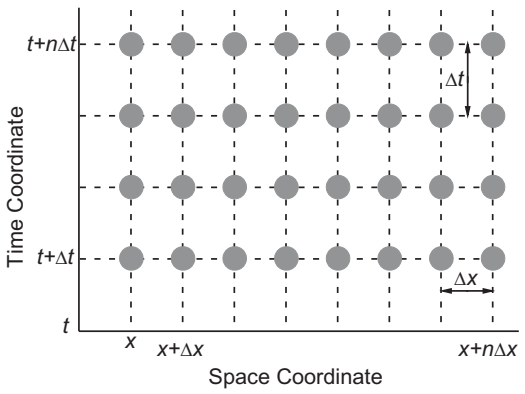


Figure 2.8: A schematic demonstration modeling voltammograms using the 'Fast Implicit Finite Difference' approach

In the grid, concentrations of relevant species at adjacent points are assumed varying linearly, which provides approximate boundary conditions for solving the partial differential equations. Hence, a concentration profile at each time point is gained, which enables electrochemists to generate a

simulated time-dependent current curve. Fitting simulated curves to the experimental data is realised by varying concerned unknown parameters (e.g. c, k_0 or α values). Hence, a best-fit theoretical voltammograms can allow the quantitative deterimination of kinetic and thermodynamic properties of electrode processes.

2.4 General Information for Experiments

2.4.1 Instrumentation

All the electrochemical experiments unless otherwise stated were carried out by a computer-controlled μ-Autolab potentiostat (Eco-Chemie, Netherlands). The working electrodes were a 10 μm diameter gold (Au) microdisk electrode (Cypress Systems Ltd, ESA Biosciences, Massachusetts), a 10 μm diameter platinum (Pt) microdisk electrode (Cypress Systems Ltd, ESA Biosciences, Massachusetts), and three home-made platinum microdisk electrodes with radius of 7.5, 25 and 50 μm respectively using 99.99 % pure platinum wires (Goodfellow Cambridge Ltd, Cambridge). A gold goil was introduced for the counter electrodes. For experiments in aqueous solutions, a saturated calomel elctrode (SCE, Radiometer, Cobenhagen) or a silver|silver chloride electrode (Radiometer, Cobenhagen) was used as reference electrode, while in non-aqueous solutions, a 0.5 mm silver wire was employed as a quasi-reference electrode.

2.4.2 Calibration of Electrodes

Calibration of the size of working electrodes was carried out prior to each experiment because it was a key input value for all the simulation programs used in this thesis. First, working electrodes were polished using 1.0, 0.3 and 0.01 μm alumina-water slurry on soft lapping pads (Buehler, Illinois). Then the diameters of electrodes were calibrated by an electrochemical measurement of the steady-state limiting current of a 2 mM ferrocene (Fc) acetonitrile solution with 0.1 M TBAP at 293 K, using a literature diffusion coefficient of 2.3×10^{-9} m^2 s^{-1}. The radius r_d could be determined using Equation2.9, where r_d is the only unknown value.

2.4.3 Making Mercury Hemispherical Electrodes

Microdisk electrodes required two-dimensional models with two space variables for simulation which made computing unnecessarily complicated and time-consuming, especially for sophisticated electrochemical processes. Therefore, in some cases, mercury hemispherical electrodes were employed as working electrode because they made the space one-dimensional and thus required less computing.

The mercury hemisphere was electrochemically deposited from a 10 mM $Hg_2(NO_3)_2$ solution (acidified by 0.5% of HNO_3) directly onto the Pt electrode surface [32]. To reduce Hg(I), the potential was stepped to -0.25 V vs. Ag wire. The size of the hemispherical drop was controlled by the amount of charge put on the surface, which, for example, was 213 μC corresponding to 2.21 nmol for a 25 μm radius electrode.

2.4.4 Determination of Diffusion Coefficients by Double Step Chronoamperometry

Besides the size of working electrodes, the diffusion coefficients for both electroactive and electrogenerated species are of importance for further quantitative analysis. The electrochemical measurement of diffusion coefficients employed in this thesis was mainly double potential step chronoamperometry. The technique was undertaken using a sample time of 0.01 s. The sample was pre-treated by holding the potential at a point corresponding to zero Faradaic current for 20 s, after which the potential was stepped to a position after the peak and the current measured for 5 s. The potential was then stepped back to the initial value and the current measured for a further 5 s. The time-dependent current response obtained on the first step was analysed by the Shoup and Szabo method [8] (Equation 2.4-2.6) using a nonlinear curve fitting function available in OriginPro 7.5 (Microcal Software Inc.). The fit between experimental and theoretical data was optimised by inputting a value for r_d and instructing the software to iterate through various D and nc values until the standard deviation became minimal.

References

[1] A.J. Bard, L.R. Faulkner, Electrochemical Methods, Fundamentals and Applications, John Wiley & Sons, New York, 2001.

[2] C.G. Zoski, Handbook of Electrochemistry, Elsevier Science, Amsterdam, 2007.

[3] S. Pons, M. Fleischmann, Anal. Chem. 59 (1987) A1391–A1399.

[4] K. Aoki, Electroanalysis 5 (1993) 627–639.

[5] R.J. Forster, J. Chem. Soc. Rev. 23 (1994) 289–297.

[6] P. Andrieux, C. P. Hapiot, J.M. Saveant, Chem. Rev. 90 (1990) 723–738.

[7] F.G. Cottrell, Z. Physik. Chem. 42 (1903) 385–431.

[8] D. Shoup, A. Szabo, J. Electroanal. Chem. Interfacial Electrochem. 140 (1982) 237–245.

[9] O.V. Klymenko, R.G. Evans, C. Hardacre, I.B. Svir, R.G. Compton, J. Electroanal. Chem. 571 (2004) 211–221.

[10] J. Randles, Trans. Faraday Soc. 44 (1948) 327–338.

[11] A. Ševčík, Coll. Czech. Chem. Comm. 3 (1948) 349.

[12] C.M.A. Brett, A.M.O. Brett, Electrochemistry: Principles, Methods and Applications, Oxford University Press, Oxford, 1994.

[13] V. Mirčeski, Š. Komorsky-Lovrić, M. Lovrić, Square-Wave Voltammetry: Theory and Application, Springer, 2007.

[14] R. Gulaboski, V. Mirčeski, M. Lovrić, I. Bogeski, Electrochem. Commun. 7 (2005) 515–522.

[15] V. Pavlova, V. Mirčeski, S. Komorsky-Lovrić, S. Petrovska-Jovanović, B. Mitrevski, Anal. Chim. Acta 512 (2004) 49–56.

[16] D. Jadreško, M. Zelić, M. Lovrić, J. Electroanal. Chem. 645 (2010) 103–108.

[17] F. Garay, M. Lovrić, J. Electroanal. Chem. 518 (2002) 91–102.

[18] F. Garay, M. Lovrić, J. Electroanal. Chem. 527 (2002) 85–92.

[19] A. Molina, C. Serna, F. Martinez-Ortiz, J. Electroanal. Chem. 486 (2000) 9–15.

[20] J.J. O'Dea, J. Osteryoung, R.A. Osteryoung, J. Phys. Chem. 87 (1983) 3911–3918.

[21] A. Molina, J. Gonzalez, E. Laborda, Y. Wang, R.G. Compton, Phys. Chem. Chem. Phys. 13 (2011) 16748–16755.

[22] Y. Wang, E.O. Barnes, E. Laborda, A. Molina, R.G. Compton, J. Electroanal. Chem. 673 (2012) 13–23.

[23] J.C. Myland, K.B. Oldham, C.G. Zoski, J. Electroanal. Chem. Interfacial. Electrochem. 182 (1985) 221–234.

[24] H.J. Lee, C. Beriet, R. Ferrigno, H.H. Girault, J. Electroanal. Chem. 502 (2001) 138–145.

[25] K. Ludwig, B. Speiser, J. Electroanal. Chem. 588 (2006) 74–87.

[26] K.B. Oldham, J.C. Myland, Electrochim. Acta 56 (2011) 10612–10625.

[27] M. Rudolph, J. Electroanal. Chem. 314 (1991) 13–22.

[28] M. Rudolph, D.P. Reddy, S.W. Feldberg, Anal. Chem. 66 (1994) 589A–600A.

[29] M. Rudolph, J. Electroanal. Chem. 338 (1992) 85–98.

[30] M. Rudolph, D.P. Reddy, S.W. Feldberg, Anal. Chem. 66 (1994) 589A–600A.

[31] M. Rudolph, J. Electroanal. Chem. 375 (1994) 89–99.

[32] J. Mauzeroll, E.A. Hueske, A.J. Bard, Anal. Chem. 75 (2003) 3880–3889.

Part II Electrochemical Investigation of Diffusional Behaviour

Understanding the diffusional behaviour of species is fundamental for electroanalytical studies. This part of thesis reports three examples with respect to this topic. First, possible ion-pairing interactions between ferricenium ions and supporting electrolytes in acetonitrile were investigated. These methods were subsequently employed to study the hexaammineruthenium III/II redox couple in aqueous solution.

Chapter 3 The Measurement of the Diffusion Coefficients of Ferrocene and Ferricenium and their Temperature Dependence in Acetonitrile using Double Potential Step Microdisc Electrode Chronoamperometry

The work presented in this chapter has been published in:

Y. Wang, E.I. Rogers, R.G. Compton, J. Electroanal. Chem. 648 (2010) 15–19

As introduced in Chapter 2, the calibration of working electrodes in this thesis was mostly determined by a chronoamperommetric analysis of a ferrocene standard solution. Using this method, a good understanding of the diffusional behaviour of ferrocene is necessary because an accurate diffusion coefficient is needed as the input of the Shoup and Szabo model. This chapter is an introduction of the basic methodology regarding to the measurements of its diffusional behaviour. The ferrocene/ferricenium ($Fc|Fc^+$) redox couple is usually used in electrochemistry not only for calibration of microelectrodes, but also as an 'internal standard' for the translation of measured potentials with respect to an arbitrary reference electrode to a 'standard' redox couple.

However, there had been a divergence of views about the possibility of ferricenium ion ion-paired with some supporting electrolytes, which means the electrogererated cation may have intermolecular attractions with the anion of the supporting electrolyte, especially when the ions have high polarity. The ion-pair normally has a larger size compared to the initial ion, therefore it may cause variations of the diffusion coefficient according to the Stokes-Einstein Equation 1.4, and shifts of the half-wave potential. To clarify the fact, a rigorous study of the possible ion-pairing effect was undertaken in ferrocene solutions supported by the two most commonly used supporting electrolytes - tetra-*n*-butylammonium perchlorate (TBAP) which is believed to have no ion-pairing effect due to the low

polarity of perchlorate, and tetra-*n*-butylammonium hexafluorophosphate ($TBAPF_6$) which is more likely to pair with ferricenium.

The diffusion coefficients for both ferrocene and ferricenium in acetonitrile containing 0.1 M TBAP or 0.1 M $TBAPF_6$ are reported, determined using the technique of double potential step chronoamperometry at a microdisk electrode. Activation energies of diffusion, $E_{a,D}$ are calculated for both redox species in each system. Diffusion coefficient ratios of the diffusion coefficients of Fc compared to that of Fc^+ in each case were found to be very close to 1. Activation energies of diffusion, $E_{a,D}$, for ferrocene and ferricenium in the acetonitrile/perchlorate system were determined as 6.5 ($\pm$ 0.2) and 7.2 ($\pm$ 0.5) kJ mol^{-1}, respectively. Similar values were determined for the acetonitrile/hexafluorophosphate system: 7.1 ($\pm$ 0.1) kJ mol^{-1} for Fc and 7.4 ($\pm$ 0.3) kJ mol^{-1} for Fc^+. Cyclic voltammograms were recorded for ferrocene oxidation in both acetonitrile/electrolyte systems and it was observed that the $E_{\frac{1}{2}}$ values were similar and independent of the electrolyte used.

3.1 Introduction

Ferrocene, or bis-cyclopentadienyl iron(II) – a common metallocene – is a sandwich-type structure in which an iron molecule is sandwiched between two cyclopentadienyl (C_5H_5) rings. Ferrocene (Fc) has high thermal stability and is highly soluble in organic media [1]. It exhibits reversible redox behaviour, according to the process:

$$Fc - e^- \rightleftharpoons Fc^+ \tag{3.1}$$

(where Fc^+ is the ferricenium ion), and the chemical reversibility [2] of the $Fc|Fc^+$ redox couple advocates its use as an internal standard, recommended by IUPAC (International Union of Pure and Applied Chemistry) [3], as a means of electrode potential calibration in organic solvent media [4, 5]. Typically, 0.5–2.0 mM ferrocene is dissolved in the test solution and the voltammetry of the redox species to be examined is recorded versus the potential of the $Fc|Fc^+$ redox couple. To this end, the redox behaviour of the model $Fc|Fc^+$ system has been subject of many electrochemical reports. The electrochemical oxidation of ferrocene to the monocation ferricenium, has been investigated in

numerous solvents, including ethanol, propylenecarbonate, dimethylformamide [6, 7], methanol [8], nitrobenzene, tetrahydrofuran, pyridine, benzonitrile [5], chloroform [9], dimethylsulfoxide [6], acetone [10] and commonly, acetonitrile [4, 6, 10–14]. The majority of these studies have been undertaken at room temperature, with the exception of that by Crooks *et al.*, who studied the system at temperatures between 298 and 573 K [13]. Literature concerning the effect of temperature on the behaviour of ferrocene in organic media is somewhat scarce.

When the $Fc|Fc^+$ couple is used as an internal reference standard the formal potential, E_f°, of the couple corresponds to the potential mid-way between the anodic and cathodic peaks in cyclic voltammetry corrected by the term $\frac{RT}{F}\ln\left(\frac{D_{Fc}}{D_{Fc^+}}\right)$ [15–17]. Accordingly, knowledge of the diffusion coefficients of both Fc and Fc^+ is important in the area of voltammetry [18]. Many of the literature papers report the diffusion coefficients of ferrocene, although very few measure and report the corresponding values for the ferricenium species, and those that do report diffusion coefficients for both the parent and product species are in wide disagreement. Most commonly, the ratio of the charged and neutral diffusion coefficients is measured and values ranging between 0.80 [15, 19–21] to 0.95 [18] have been reported, and in some cases, equal diffusion coefficients are assumed [14, 22, 23]. Rogers *et al.* investigated the redox behaviour of the $Fc|Fc^+$ couple in room temperature ionic liquids (RTILs) using the technique of double potential step chronoamperometry at microdisk electrodes [24]. These solvents, composed entirely of cations and coordinating anions are shown to give ratios much less than 1, due to Coulombic interactions between the charged species and the composing anions of the solvent. In such media, ratios ranging between 0.76 and 0.53 were determined, with values as low as 0.13 also observed in highly viscous liquids. Table 3.1 summarises the literature reports that quote values for both Fc and Fc^+ in various solvent|electrolyte systems, along with the method of measurement. Wang *et al.* addressed the issue of neutral parent molecules and radical cations and anions in various solvents [25]. In acetonitrile, the diffusion coefficients of a sample of benzoquinone species, phenothiazine and tris(4-bromophenyl)amine, for example, were shown to be virtually identical to that of the charged ion species, also for the $TMPD|TMPD^{\bullet+}$ couple, it was reported that $D_{TMPD^{\bullet+}} \approx$

D_{TMPD}. Ferricyanide, $[\mathrm{Fe(CN)_6}]^{3-}$, was measured to diffuse more slowly through acetonitrile media than ferrocyanide, $[\mathrm{Fe(CN)_6}]^{4-}$, with a diffusion coefficient ratio of between 0.8 and 0.9 [25, 26].

Table 3.1: Review of literature reporting diffusion coefficient values for both ferrocene and ferricenium.

Author	D_{Fc} /m^2 s^{-1}	D_{Fc^+} /m^2 s^{-1}	D_{Fc^+}/D_{Fc}	Solvent System[a]	Method of Measurement
Bond *et al.* [14]	2.60×10^{-9}	2.60×10^{-9}	1.00	MeCN + 0.1 M $TBAPF_6$	CV simulation
Hyk *et al.* [18]	2.11×10^{-9}	2.02×10^{-9}	0.96	MeCN + 0.2 M TBAP	Double-potential step chronoamperometry
	2.12×10^{-9}	2.02×10^{-9}	0.95	MeCN + 0.2 M TBAP	Double-potential step chronoamperometry
Martin *et al.* [19]	2.00×10^{-9}	1.60×10^{-9}	0.80	MeCN + 0.1 M TBAP	SECM chronoamperometry
Martin *et al.* [20]	2.15×10^{-9}	1.72×10^{-9}	0.80	MeCN + 0.1 M TBAP	Chronoamperometry
Rogers *et al.* [24]	2.36×10^{-11}	1.80×10^{-11}	0.76	$[C_4mim][OTf]$	Double-potential step chronoamperometry
	3.77×10^{-11}	2.65×10^{-11}	0.70	$[C_4mim][NTf_2]$	Double-potential step chronoamperometry
	5.90×10^{-12}	3.10×10^{-12}	0.53	$[C_4mim][PF_6]$	Double-potential step chronoamperometry
	8.60×10^{-12}	1.10×10^{-12}	0.13	$[P_{14,6,6,6}][FAP]$	Double-potential step chronoamperometry

[a] MeCN = acetonitrile, TBAP = tetrabutylammonium perchlorate, $TBAPF_6$ = tetrabutylammoniumhexafluorophosphate, $[C_4mim]^+$ = 1-butyl-3-methylimidazolium, $[OTf]^-$ = trifluoromethanesulfonate, $[NTf_2]^-$ = bis(trifluoromethanesulfonyl)imide, $[P_{14,6,6,6}]^+$ = tris(*n*-hexyl)tetradecylphosphonium and $[FAP]^-$ = trifluorotris(pentafluoroethyl)phosphate.

Slower diffusion of a charged species in solution may result from ion-pairing interaction with the supporting electrolyte species. In a report by Klymenko *et al.*, the effect of varying the supporting electrolyte in acetonitrile solvent was investigated using the TMPD|$TMPD^{\bullet+}$ redox couple (where TMPD is *N*,*N*,*N*′,*N*′-tetramethylphenylenediamine) [27]. It was observed that the diffusion coefficient of the radical cation species decreased in the electrolyte order TBAP > $TBAPF_6$ > $TBABPh_4$ (where TBA^+ is tetrabutylammonium, with the anions perchlorate ($[ClO_4]^-$), hexafluorophosphate and tetraphenylborate, respectively), suggesting a greater interaction between $TMPD^{\bullet+}$ and $[BPh_4]^-$ than with $[ClO_4]^-$.

The presence of supporting electrolyte has been considered likely to have an effect on the voltammetry of the ferrocene oxidation process by way of interaction between the electrogenerated Fc^+ species and the supporting electrolyte anions, for example, $[PF_6]^-$ and $[ClO_4]^-$. Ion-pairing interactions can be determined by measurement of $E_{\frac{1}{2}}$ values, with increased ion-pairing leading to a more negative potential shift in the voltammetry, or by measurement of the diffusion coefficients and calculation of diffusional activation energies, $E_{a,D}$, where slower diffusion of ferricenium (smaller D_{Fc^+}) and a changed activation energy for diffusion of Fc^+ results from temperature-dependent ion-pairing. Numerous articles report the ion-pairing effect of perchlorate in acetonitrile and the formation of the $[Fc^+ClO_4^-]$ ion-pair, following the process shown below (Equation (3.2)) in acetonitrile [15, 28–30].

$$Fc^+ + ClO_4^- \rightleftharpoons [FcClO_4] \tag{3.2}$$

Ion-pairing between Fc^+ and $[PF_6]^-$ has also been reported, following the process in Equation (3.3) in both acetonitrile [30] and tetrahydrofuran [31, 32].

$$Fc^+ + PF_6^- \rightleftharpoons [FcPF_6] \tag{3.3}$$

The contrasting diffusion coefficient ratio values, explained above, and reported in Table 3.1 suggest that measurement of diffusion coefficients for Fc and Fc^+ is presently unclear. Stojek *et al.* [18] present

a set of very carefully measured data to yield the diffusion coefficient ratio of 0.95, although the value of 0.80 reported by Unwin *et al.* [19, 20] is also a possibly plausible result due to the high volume of literature reporting ion-pairing, suggesting slower Fc^+ diffusion. The current chapter aims to determine the extent of interaction and ion-pairing (if any) between Fc^+ and the solvent by studying the $Fc|Fc^+$ redox couple in acetonitrile containing either 0.1 M TBAP or $TBAPF_6$, and measuring the diffusion coefficients of both ferrocene and ferricenium, utilising the technique of double potential step chronoamperometry. Diffusional activation energies ($E_{a,D}$) can be measured from diffusion coefficient data as a function of temperature. Some articles report $E_{a,D}$ values of Fc (or publish data from which they can be calculated) [13, 33–35], although to the best of the authors knowledge, no-one has reported corresponding values for Fc^+. In this chapter, D_{Fc}, D_{Fc^+} and D_{Fc^+}/D_{Fc} ratio values are reported at several temperatures allowing calculation of the diffusional activation energy of both ferrocene and ferricenium.

3.2 Experimental

3.2.1 Chemical Reagents

Ferrocene ($Fe(C_5H_5)_2$, Aldrich, 98 %), tetra-*n*-butylammonium perchlorate (TBAP, > 99 %, Fluka), tetra-*n*-butylammonium hexafluorophosphate ($TBAPF_6$, 98 %, Aldrich), silver nitrate ($AgNO_3$, ≥ 99 %, Sigma-Aldrich) and acetonitrile (MeCN, Fischer scientific, dried and distilled, > 99 %) were used as received, without further purification.

3.2.2 Instrumental

For cyclic voltammetric experiments, a $Ag|Ag^+$ reference electrode was utilised, consisting of an Ag wire (0.5 mm diameter) immersed in a glass tube containing a solution of 10 mM $AgNO_3$ and 0.1 M TBAP in MeCN, which was separated from the bulk test solution by means of a porous Vycor frit. A stock solution of ferrocene was first prepared in acetonitrile to a known concentration (2 mM), which was then purged with nitrogen (BOC Gases, Guildford, UK) for 5 min prior to any measurements and

for the duration of the experiment thereafter.

3.3 Results and discussion

3.3.1 Cyclic Voltammetry

The cyclic voltammetry of 2 mM ferrocene in four different acetonitrile systems containing different electrolytes, namely 0.1 M TBAP, 0.2 M TBAP, 0.1 M of both TBAP and $TBAPF_6$, and 0.1 M $TBAPF_6$ was measured, and the half-wave potential, $E_{\frac{1}{2}}$ *vs* $Ag|Ag^+$ in each system determined. The potential was scanned from -0.3 to +0.4 V and back to -0.3 V. Figure 3.1 shows the CVs recorded at 298 K and 100 mV s^{-1}, and the measured $E_{\frac{1}{2}}$ values are given in Table 3.2. On a microdisk electrode, the half-wave potentials were all very similar in each case. The lack of a potential shift in any of the systems suggest either that interaction between the electrogenerated cation and the supporting electrolyte anion does not occur to any significant extent and electrogenerated Fc^+ exists predominantly as free-ions, or, that Fc^+ produced during the oxidation of Fc exists as [FcX] ion-pairs, where in this case, X^- is $[ClO_4]^-$ or $[PF_6]^-$, with ion-pairing occurring with a similar binding constant in the presence of either supporting electrolyte.

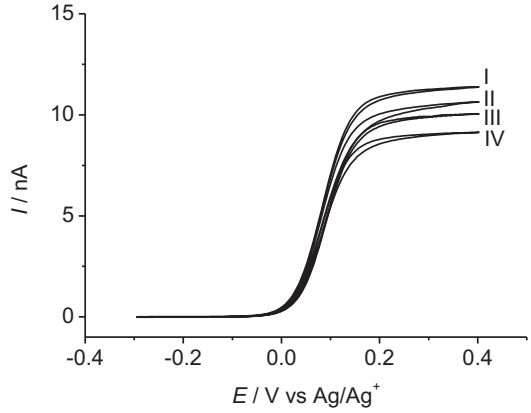


Figure 3.1: Cyclic voltammograms for the oxidation of 2 mM ferrocene in acetonitrile with (I) 0.2 M $TBAPF_6$, (II) 0.2 M TBAP, (III) 0.1 M TBAP, (IV) 0.1 M $TBAPF_6$ + 0.1 M TBAP, *vs* $Ag|Ag^+$, from which the half-wave potentials ($E_{\frac{1}{2}}$) for the redox couple were determined (Table 3.2).

Table 3.2: Half-wave potentials for the $Fc|Fc^+$ redox couple in various acetonitrile systems.

Electrolyte	$E_{\frac{1}{2}}$ /V *vs* $Ag|Ag^+$
0.1 M $TBAPF_6$	0.08
0.2 M TBAP	0.08
0.1 M TBAP	0.08
0.1 M TBAP + 0.1 M $TBAPF_6$	0.08

3.3.2 Double Potential Step Chronoamperometry

Double potential step chronoamperometry was performed to determine the diffusion coefficients of both Fc and Fc^+ in acetonitrile, containing either 0.1 M TBAP or $TBAPF_6$. Initially, a cyclic voltammogram was recorded to determine the position of the redox signal (voltammetry not shown). The potential was scanned from 0.0 to 0.9 V, and the redox couple was observed at a $E_{\frac{1}{2}}$ of 0.54 V *vs* Ag for both TBAP and $TBAPF_6$. Then, chronoamperometry was utilised, as detailed in Section 2.2; the potential was stepped from 0.0 V to 0.9 V and back to 0.0 V and the current measured for 5 seconds for both the forward and backward step. This was undertaken at 298, 303 and 308 K, and the experimental transients at each temperature are shown in Figure 3.2(I), (III) and (III) respectively. The limiting currents of the first step increase systematically, and the decay of the second step becomes slightly less steep as the temperature increases. Step 1 of the experimental transient was analysed with the Shoup and Szabo expression (Equations (2.4)–(2.6)) to calculate the diffusion coefficient of the neutral parent molecule, ferrocene. Step 2 of the transient was simulated using a program by Klymenko *et al.* (described in Section 2.2), and the diffusion coefficient of the oxidised species, ferricenium, was determined. An example of an experimental (–) and best-fit theoretical (∘) chronoamperometric transient for the $Fc|Fc^+$ redox couple in MeCN is shown in Figure 3.3, and the values are reported in Table 3.3.

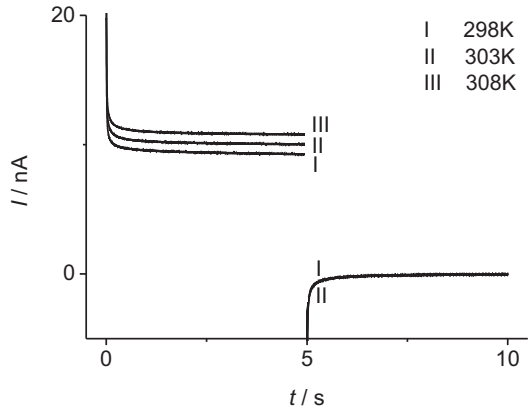


Figure 3.2: Experimental double potential step chronoamperometric transients for the $Fc|Fc^+$ system at temperatures of (I) 298, (III) 303 and (III) 308 K. The potential was stepped from 0.0 to 0.9 and back to 0.0 V.

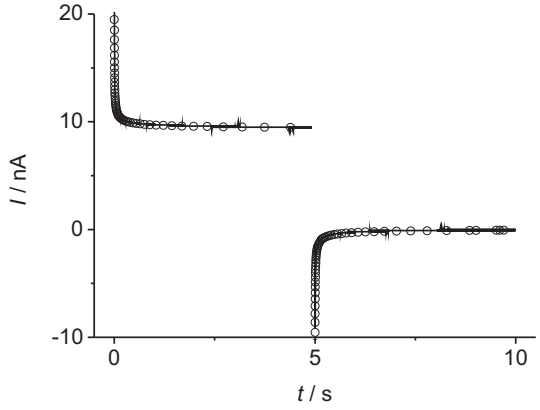


Figure 3.3: Experimental (–) and best-fit theoretical (○) double potential step chronoamperometric transients for the $Fc|Fc^+$ system at a temperature of 298 K in MeCN with 0.1 M $TBAPF_6$ supporting electrolyte. The potential was stepped from 0.0 to 0.9 and back to 0.0 V.

Table 3.3: Diffusion coefficients for ferrocene, Fc, and ferricenium, Fc^+, in acetonitrile at temperatures of 298, 303 and 308 K[a].

Electrolyte	T /K	$D_{Fc} \times 10^{-9}$ /m^2 s^{-1}	$D_{Fc^+} \times 10^{-9}$ /m^2 s^{-1}	D_{Fc^+}/D_{Fc}
TBAP	298	2.43 (± 0.02)	2.36 (± 0.06)	0.972
	303	2.54 (± 0.03)	2.48 (± 0.07)	0.977
	308	2.64 (± 0.03)	2.59 (± 0.05)	0.979
$TBAPF_6$	298	2.24 (± 0.03)	2.16 (± 0.08)	0.964
	303	2.35 (± 0.02)	2.27 (± 0.08)	0.967
	308	2.46 (± 0.03)	2.38 (± 0.08)	0.968

[a] D_{Fc} values were determined using the Shoup and Szabo [36] fitting function for chronoamperometric data. D_{Fc^+} were achieved by simulation of experimental chronoamperometric transients.

The best-fit diffusion coefficients of ferrocene reported are comparable with those found in literature: 2.30×10^{-9} m^2 s^{-1} at 20 °C [2], $2.37 (\pm 0.1) \times 10^{-9}$ m^2 s^{-1} at 24 °C [34], 2.40×10^{-9} m^2 s^{-1}

at 25 °C [2, 5], 2.51 (± 0.1) × 10^{-9} m^2 s^{-1} at 30 °C and 2.72 (± 0.1) × 10^{-9} m^2 s^{-1} at 40 °C [34]. An increase in D_{Fc} (and D_{Fc^+}) with increasing temperature was also observed, consistent with a decrease in the viscosity of the medium ($D \propto 1/\eta$ from Stokes-Einstein equation) [37]. The ratio of diffusion coefficients is comparable with the value of *ca.* 0.95, reported by Hyk *et al.* [18], which gives confidence in our results. This result contrasts with the value of 0.8 reported by Martin and co-workers [19, 20], which is more consistent with values reported in room temperature ionic liquids, where the solvent media is composed entirely of ions and strong Coulombic interactions between Fc^+ and the composing anion leads to D_{Fc^+}/D_{Fc} ratios much less that 1, usually between 0.5 and 0.8 [24].

To calculate the diffusional activation energy, the diffusion coefficients were analysed in terms of the Arrhenius equation [37]:

$$D = D_\infty \exp\left(\frac{-E_{a,D}}{RT}\right) \tag{3.4}$$

where D is the diffusion coefficient of the electroactive species, D_∞ is a constant corresponding to the hypothetical diffusion coefficient at infinite temperature, R is the universal gas constant (8.314 J K^{-1} mol^{-1}), and $E_{a,D}$ is the diffusional activation energy of the electroactive species. Plots of ln D *vs* T^{-1} for Fc and Fc^+ are shown in Figure 3.4 and values of $E_{a,D}$ = 6.5 (± 0.2) and 7.2 (± 0.5) kJ mol^{-1} were achieved, respectively, from the gradient of the best-fit line ($R^2 > 0.999$). The $E_{a,D}$(Fc) value can be compared with that reported in literature, 6.9 (± 0.7) kJ mol^{-1} [34], and an activation energy of viscosity, $E_{a,\eta}$ of 6.5 kJ mol^{-1} for acetonitrile, which was calculated from viscosity/temperature measurements reported in the literature [38]. As the activation energy values are very similar for both Fc and Fc^+, it can be said that Fc^+ either fully ion-paired with the perchlorate anion, or exists as free-ions, with no interaction between the oxidation species and the electrolyte occurring in this system.

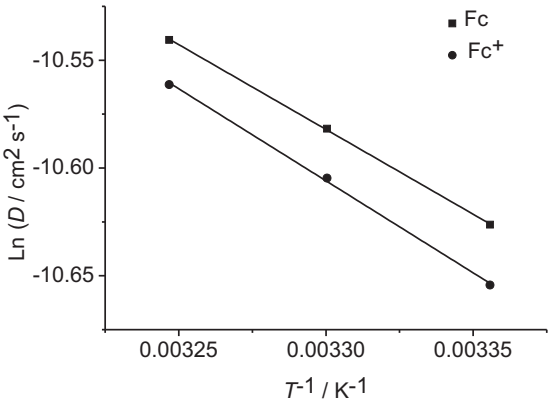


Figure 3.4: Arrhenius plots of ln D *vs* T^{-1} for Fc and Fc^+ in acetonitrile containing 0.1 M TBAP. Diffusion coefficients were obtained from chronoamperometric analysis following the Shoup and Szabo [36] expression and simulation techniques [27].

The fact that the activation energies for diffusion (minimal energy required to drive the diffusion) are similar for Fc and Fc^+, and to that of the solvent viscosity, suggests consistency with the Stokes – Einstein equation and that the ratio D_{Fc^+}/D_{Fc} will be essentially temperature independent. The activation energies allow D_{Fc^+} and D_{Fc} to be calculated as a function of temperature.

The double potential step chronoamperometry experiments were repeated for 2 mM Fc in MeCN with 0.1 M $TBAPF_6$ supporting electrolyte at 298, 303 and 308 K. Again, the potential was stepped from 0.0 V to 0.9 V and back to 0.0 V. Analysis of the experimental transients using the Shoup and Szabo expression and simulation techniques allowed determination of D_{Fc} and D_{Fc^+}, and these, as well as the D_{Fc^+}/D_{Fc} ratio, are given in Table 3.3. It can be noted that the values for both Fc and Fc^+ are slightly smaller than those reported earlier in acetonitrile solution containing 0.1 M TBAP, although the D_{Fc} values compare well with literature in the same acetonitrile/hexafluorophosphate system (2.24 $\times$ 10^{-9} m^2 s^{-1} at 25 °C [33]). The diffusion coefficient ratios are similar to those determined for the $Fc|Fc^+$ couple in the presence of TBAP, which again suggests that there is no interaction between Fc^+ and $[PF_6]^-$. The diffusion coefficients were plotted as a function of temperature (see Figure 3.5) and the diffusional activation energies calculated. Values of $E_{a,D}$ were determined from the gradient of the best-fit line ($R^2 \approx 1$) as 7.1 ($\pm$ 0.1) kJ mol^{-1} for Fc and 7.4 ($\pm$ 0.3) kJ mol^{-1} for Fc^+. A diffusional activation energy value of 7.0 kJ mol^{-1} for Fc in acetonitrile with $TBAPF_6$ supporting electrolyte has

been reported in literature [35], which compares well with the value determined in the current study.

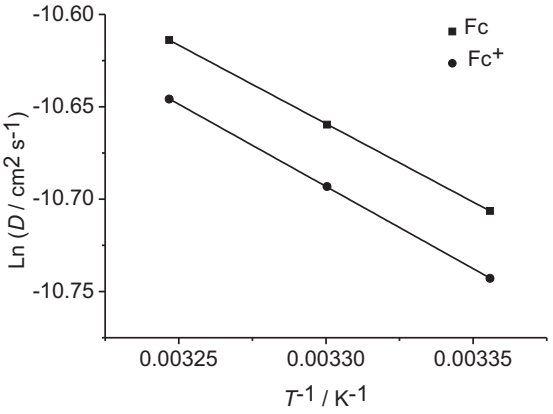


Figure 3.5: Arrhenius plots of ln D *vs* T^{-1} for Fc and Fc^+ in acetonitrile containing 0.1 M $TBAPF_6$. Diffusion coefficients were obtained from chronoamperometric analysis following the Shoup and Szabo [36] expression and simulation techniques [27].

3.4 Conclusions

Cyclic voltammetry was recorded for the $Fc|Fc^+$ redox couple in acetonitrile at a platinum microdisk, and half-wave potentials were determined to be similar in the presence of both TBAP and $TBAPF_6$. Double potential step chronoamperometric techniques were performed and the diffusion coefficients for both species were determined at temperatures of 298, 303 and 308 K. The effect of supporting electrolyte on the ratio of diffusion coefficients of the charged and neutral species was investigated and values of *ca.* 0.97 and 0.96 were determined for $Fc|Fc^+$ in MeCN with TBAP or $TBAPF_6$ respectively, consistent with that determined by Stojek *et al.* [18]. The diffusional activation energies were calculated for both Fc and Fc^+ in both systems. The activation energies were found to be similar and close to that for the solvent viscosity implying consistency with the Stokes – Einstein equation. The data in this study permit the inference of both diffusion coefficients as a function of temperature.

This chapter solved the historical argument about the ion-pairing effect between electrogenerated Fc^+ and PF_6^- in acetonitrile. The result assured the fact that the ion-pairing effect was not significant. This conclusion was confirmed by similar D_{Fc^+} and D_{Fc} values, diffusional activation energies with agreement of theoretical values and identical half-wave potentials for solutions with different supporting electrolytes. Further studies using $Fc|Fc^+$ redox couple to calibrate electrodes or to reference

potentials can base on the findings of this chapter.

References

[1] D. Xiang, G. Gao, H. Shao, H. Li, H.L. Zhang, H.Z. Yu, J. Phys. Chem. C 114 (2010) 617–621.

[2] M. Sharp, Electrochim. Acta 28 (1983) 301–308.

[3] G. Gritzner, J. Kuta, Pure Appl. Chem. 56 (1984) 461–466.

[4] R.G. Gagńe, C.A. Koval, G.C. Lisensky, Inorg. Chem. 19 (1980) 2855–2856.

[5] K.M. Kadish, J.Q. Ding, T. Malinski, Anal. Chem. 56 (1984) 1741–1744.

[6] J.W. Diggle, A.J. Parker, Electrochim. Acta 18 (1973) 975–979.

[7] A.J. Zara, S.S. Machado, L.O.S. Bulhões, A.V. Benedetti, T. Rabockai, J. Electroanal. Chem. 221 (1987) 165–174.

[8] T. Saji, Y. Maruyama, S. Aoyagui, J. Electroanal. Chem. 86 (1978) 219–222.

[9] M.H. Pournaghi-Azar, R. Ojani, Electrochim. Acta 39 (1994) 953–955.

[10] N.G. Tsierkezos, U. Ritter, J. Appl. Electrochem. 40 (2010) 409–417.

[11] G.N. Kamau, T.M. Saccucci, G. Gounili, A.E.F. Nassar, J.F. Rusling, Anal. Chem. 66 (1994) 994–1001.

[12] J. Daschbach, D. Blackwood, J.W. Pons, S. Pons, J. Electroanal. Chem. 237 (1987) 269–273.

[13] R.M. Crooks, A.J. Bard, J. Electroanal. Chem. 243 (1988) 117–131.

[14] A.M. Bond, K.B. Oldham, G.A. Snook, Anal. Chem. 72 (2000) 3492–3496.

[15] J. Redepenning, E. Castro-Narro, G. Venkataraman, E. Mechalke, J. Electroanal. Chem. 498 (2001) 192–200.

[16] J. Wang, Analytical Electrochemistry., VCH Publishers, Inc., 1994.

[17] R. Wibowo, L. Aldous, E.I. Rogers, S.E. Ward Jones, R.G. Compton, J. Phys. Chem. C 114 (2010) 3618–3626.

[18] W. Hyk, A. Nowicka, Z. Stojek, Anal. Chem. 74 (2002) 149–157.

[19] R.D. Martin, P.R. Unwin, J. Electroanal. Chem. 439 (1997) 123–136.

[20] R.D. Martin, P.R. Unwin, Anal. Chem. 70 (1998) 276–284.

[21] I. Haruko, K. Mitsuhiro, Denki Kaguki Oyobi Kogyo Butsuri Kaguku 69 (2001) 34–36.

[22] P.R. Birkin, S. Silva-Martinez, Anal. Chem. 69 (1997) 2055–2062.

[23] F. Scholz (Ed.) Electroanalytical Methods: a Guide to Experiments and Applications., Springer-Verlag, Berlin Heidelberg, 2002.

[24] E.I. Rogers, D.S. Silvester, D.L. Poole, L. Aldous, C. Hardacre, R.G. Compton, J. Phys. Chem. C 112 (2008) 2729–2735.

[25] R.L. Wang, K.Y. Tam, R.G. Compton, J. Electroanal. Chem. 434 (1997) 105–114.

[26] A.C. Fisher, et al., J. Phys. Chem. 95 (1991) 7538–7542.

[27] O.V. Klymenko, R.G. Evans, C. Hardacre, I.B. Svir, R.G. Compton, J. Electroanal. Chem. 571 (2004) 211–221.

[28] G.K. Rowe, S.E. Creager, J. Phys. Chem. 98 (1994) 5500–5504.

[29] T. Kondo, M. Okamura, K. Uosaki, J. Organomet. Chem. 637–639 (2001) 841–844.

[30] E.S. Yang, M.S. Chan, A.C. Wahl, J. Phys. Chem. 84 (1980) 3094–3099.

[31] C.A. Paddon, R.G. Compton, Electroanalysis 17 (2005) 1919–1923.

[32] R. Baron, N.M. Kershaw, T.J. Donohoe, R.G. Compton, J. Phys. Org. Chem. 22 (2009) 1136–1141.

[33] N.G. Tsierkezos, J. Solution Chem. 36 (2007) 289–302.

[34] S.R. Jacob, Q. Hong, B.A. Coles, R.G. Compton, J. Phys. Chem. B 103 (1999) 2963–2969.

[35] B.A. Coles, M.J. Moorcroft, R.G. Compton, J. Electroanal. Chem. 513 (2001) 87–93.

[36] D. Shoup, A. Szabo, J. Electroanal. Chem. Interfacial Electrochem. 140 (1982) 237–245.

[37] R.G. Compton, C.E. Banks, Understanding Voltammetry, World Scientific, Singapore, 2007.

[38] M.d.C. Grande, M. Garćia, C.M. Marschoff, J. Chem. Eng. Data 54 (2009) 652–658.

Chapter 4 Measurement of the Diffusion Coefficients of $[Ru(NH_3)_6]^{3+}$ and $[Ru(NH_3)_6]^{2+}$ in Aqueous Solution using Microelectrode Double Potential Step Chronoamperometry

The work presented in this chapter has been published in:

Y. Wang, J.G. Limon-Petersen, R.G. Compton, J. Electroanal. Chem. 652 (2011) 13–17.

Just like ferrocene/ferricenium being widely used as a standard reversible redox couple in acetonitrile and other organic solvents, $[Ru(NH_3)_6]^{3+}/[Ru(NH_3)_6]^{2+}$ is frequently used in electrochemical studies in aqueous solution due to its chemical and electrochemical reversibility [1–4]. However, unlike in a non-polarised solution, the strong polarity of water may increase the possibility of the formation of ion-pairs. Therefore, there is an ongoing interest in investigating this phenomena, especially for the commonly used and highly charged hexaaammineruthenium(III/II) couple.

Currently, there is little literature on the ratio of the diffusion coefficients of oxidised and reduced species, or even about the possibility of either species forming ion-pairs with electrolyte. Hence, it is important to measure the diffusion coefficients of the two ions and study their interaction with different amount of supporting electrolytes. This chapter reports diffusion coefficients for hexaammineruthenium ions, finding as expected a dependence of $D_{\mathrm{HexRu(III)}}$ and $D_{\mathrm{HexRu(II)}}$ on the concentration of supporting electrolyte. Moreover, different common supporting electrolytes were studied revealing ion-pairing effects in the presence of K_2SO_4.

4.1 Introduction

Hexaammineruthenium III/II (HexRu(III)|HexRu(II)) couple is a much used electrochemical redox couple [1–4]. In aqueous solutions it exhibits chemically and electrochemically reversible redox behaviour, and has been widely used for comparisons between models and experiment in theoretical studies of mass transport [5]. There has been a vast amount of work which reported the diffusion coefficient for $[Ru(NH_3)_6]^{3+}$ [1, 2, 5], although very few studies have been concentrated with $[Ru(NH_3)_6]^{2+}$ [6, 7].

In the framework of the classic Stokes-Einstein (S-E) equation, the diffusion coefficients of the two species corresponding to a redox couple should be the same, if there is no great change in their sizes. This is widely observed. It was reported that for the ferrocene|ferricenium ($Fc|Fc^+$) couple in acetonitrile solutions supported by either tetra-*n*-butylammoniumperchlorate (TBAP) or tetra-*n*-butylammoniumhexafluorophosphate ($TBAPF_6$), the diffusion coefficient ratio of the reductive and oxidative species was found to be between 0.96 and 1.00 by different research groups [8–10]. Georges also estimated this ratio in aqueous solutions using the Stokes-Einstein relationship and suggested a value of 1.00, although the solubility of Fc in water is as low as 5×10^{-5} M [11]. Wang and co-workers studied a series of species including *N*,*N*,*N*',*N*'-tetramethyl-*p*-phenylenediamine (TMPD), 2,3,5,6-tetrabromo-1,4-benzoquinone (TBBQ), 2,3,5,6-tetrachloro-1,4-benzoquinone (TCBQ), phenothiazine (PTZ) and their oxidised species in acetonitrile. They suggested that all the couples studied had a diffusion coefficient ratio close to unity. In addition, they also found that in an aqueous solution of TMPD with 0.2 M KCl, the ratio was about 0.96 [12]. Ikeuchi measured the $Ru(acac)_3|[Ru(acac)_3]^+$ couple in acetonitrile solutions with TBAP and $TBAPF_6$ separately, and found that the ratios were 0.99 and 1.01 respectively [13].

However, it has also been reported that in some cases the diffusion coefficients of the two compounds of a redox couple can differ substantially. Many studies were carried out employing room-temperature ionic liquids (RTILs), in which charged species may interact strongly with counter ions of the solvent via Coulombic forces and so diffuse more slowly. For example, Rogers reported diffusion coefficient

ratios of 0.13-0.76 for the $Fc|Fc^+$ couple and 0.33-0.77 for the $Cc^+|Cc$ couple in various ionic liquids [14] where Fc^+ diffuses more slowly than Fc. Evans studied the behaviour of TMPD in a range of ionic liquids at 323K and found that the diffusion coefficient ratio of $TMPD^{+\bullet}|TMPD$ was between 0.54 and 0.57, and the ratio of $TMPD^{2+}|TMPD^{+\bullet}$ was around 0.33 [15]. Similarly, the two ratios for *N*,*N*-dimethyl-*p*-phenylenediamine (DMPD), $D_{DMPD^{+\bullet}|DMPD}$ and $D_{DMPD^{2+}|DMPD^{+\bullet}}$, in the ionic liquid $[C_4mim][BF_4]$ was found to vary between 0.55 and 0.64 [16]. Wang *et al*. studied the reduction of benzoquinone in the ionic liquid $[C_2mim][NTf_2]$, and the diffusion coefficient ratios of $BQ^{-\bullet}|BQ$ and $BQ^{2-}|BQ^{-\bullet}$ couples were 0.39 and 0.85 [17]. An extreme example was reported by Buzzeo that in ionic liquids, the diffusion coefficient ratio of $O_2^{\bullet-}|O_2$ could be as small as 0.03 [18]. Redox couples may also exhibits different diffusional behaviours as function of solvent. Klymenko *et al*. suggested that the $TMPD^{+\bullet}|TMPD$ couple had a ratio of 0.78 in a ethanol solution with 0.1 M TBAP [19]. Ji studied benzoquinone in a propylene carbonate (PC) solution and found the ratios were 0.48 and 0.60 for $BQ^{-\bullet}|BQ$ and $BQ^{2-}|BQ^{-\bullet}$ respectively [20]. For benzoquinone in acetonitrile solutions, a $BQ^{-\bullet}|BQ$ ratio of 0.70 was measured by Unwin and his group [21]. Belding *et al*. found that for *para*-quaterphenyl (PQ) THF solutions, the two ratios for $PQ^{-\bullet}|PQ$ and $PQ^{2-}|PQ^{-\bullet}$ were 0.45 and 0.59 [22]. Similar situations were also found in aqueous systems. Fisher measured the $[Fe(CN)_6]^{4-}|[Fe(CN)_6]^{3-}$ couple in a water solution with 0.1 M KCl, the diffusion coefficient ratio was found to be 0.85 [23]. Also, Baticle found that the ratio for the $Fe^{2+}|Fe^{3+}$ couple was 1.24 in a H_2SO_4 solution [24]. One possible reason was that charged species may form ion-pairs with supporting electrolyte, which was widely cited in related researches [19, 25–28]. Counter ions of electrolyte may associate with charged redox species, and the total size of these species becomes larger. Therefore, according to the Stokes-Einstein equation, the diffusion coefficients for them may also decrease.

4.2 Experimental

Hexaammineruthenium(III) chloride ($[Ru(NH_3)_6]Cl_3$, Aldrich, 98 %), potassium chloride (KCl, Aldrich, > 99 %), potassium nitrate (KNO_3, Aldrich, > 99 %), potassium sulphate (K_2SO_4, AnalaR, 99.5 %),

ferrocene ($Fe(C_5H_5)_2$, Aldrich, 98 %), tetra-*n*-butylammonium perchlorate (TBAP, Fluka, > 99 %), acetonitrile (MeCN, Fischer scientific, dried and distilled, > 99 %), and nitrogen (N_2, BOC, high purity oxygen free) were used directly, without further purification.

2mM hexaammineruthenium(III) chloride solutions were made with ultrapure water with resistivity > 18.2 MΩ cm^{-1}, with various supporting electrolytes species (KCl, KNO_3 and K_2SO_4) in a range of concentrations of 0.1, 0.3 and 0.5 M. All the solutions were degassed for 30 min with N_2 before each experiment, and the temperature was controlled at 298 K using a thermostatted Faraday Cage.

4.3 Results and Discussion

4.3.1 Cyclic Voltammetry

Cyclic voltammograms were first recorded at a scan rate of 500 mV s^{-1}, at solutions containing 2 mM hexaammineruthenium (III) chloride, with different supporting species (KCl, KNO_3 and K_2SO_4) at various concentrations (0.1, 0.3 and 0.5 M) at a 25 μm radius platinum (Pt) microdisk electrode. The recorded voltammograms are presented as examples in Figure 4.1 for a concentration of 0.1 M of the supporting electrolytes in each case. The cyclic voltammograms obtained from the solutions containing KCl and KNO_3 are undistinguishable within experimental error, therefore, both the formal potential and diffusion coefficients of the electroactive couple are almost equal. However, the curve recorded using K_2SO_4 as supporting electrolyte shows that both the reduction and oxidation peaks are significantly smaller compared to the cases using KCl and KNO_3, which is a possible indication of a decrease of diffusion coefficients of both species, $[Ru(NH_3)_6]^{3+}$ and $[Ru(NH_3)_6]^{2+}$. Also, a shift in the half wave potential of -0.05 V is observed for K_2SO_4 in comparison with the other supporting electrolytes. These features are an indication that the sulfate anions affect the behaviour of the electrochemical couple. Next a more detailed experimental procedure was employed in order to obtain accurately the diffusion coefficients for both compounds of the electroactive couple.

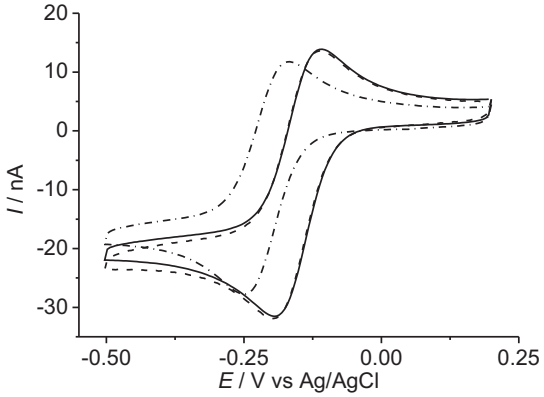


Figure 4.1: The cyclic voltammograms for 2 mM hexaammineruthenium(III) chloride solutions supported by 0.1 M KCl (solid), KNO_3 (dash) and K_2SO_4 (dash dot) respectively. The potential was stepped from 0.2 to -0.5 and back to 0.2 V vs Ag|AgCl.

4.3.2 Potential Step Chronoamperometric Experiments

Double potential step chronoamperometry at a 25 μm radius platinum (Pt) microdisk electrode was employed to quantitatively determine the diffusion coefficients for the hexaammineruthenium(III) cation as well as the hexaammineruthenium(II) cation. The sampling time was 0.005 s. The potential was stepped from 0 V vs Ag|AgCl (where there was no Faradaic current) to a potential of -0.4 V vs Ag|AgCl, assuring that the potential step was to potentials where the reduction is diffusion controlled. The chronoamperometric step was measured for 5 s. Then the potential was stepped back to a potential of 0.1 V vs Ag|AgCl and measured for 5 s.

An example of the experimental chronoamperometric transients is shown in Figure 4.2, which presents the choroamperometric response of 2 mM $[Ru(NH_3)_6]^{3+}$ solutions with different concentrations of KCl as supporting electrolyte. For the first step, the limiting currents decrease systematically as the concentration of KCl increases, while the decay of the second step becomes less steep. All transients were fitted by the Shoup and Szabo method (for the first step, Equations (2.4)–(2.6)) and a program based on the Klymenko method described in Section 2.2 (for the second step). An example of the fitting of experimental (–) and theoretical (○) transients is shown in Figure 4.3, which is for the KCl system. Diffusion coefficients for $[Ru(NH_3)_6]^{3+}$ and $[Ru(NH_3)_6]^{2+}$ in different systems from the best-fit are shown in Table 4.1.

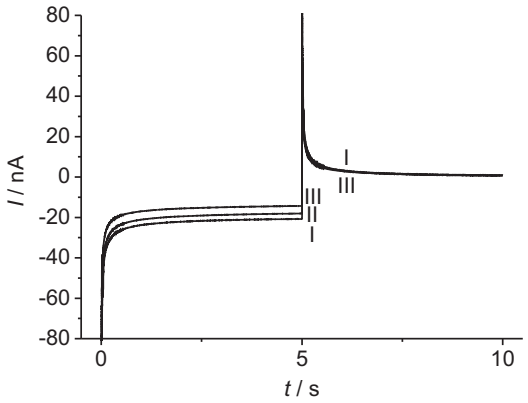


Figure 4.2: The chronoamperometric transients for 2 mM hexaammineruthenium(III) chloride solutions with (I) 0.1 M, (II) 0.3 M and (III) 0.5 M KCl respectively. The potential was stepped from 0 to -0.4 and back to 0.1 V vs Ag|AgCl.

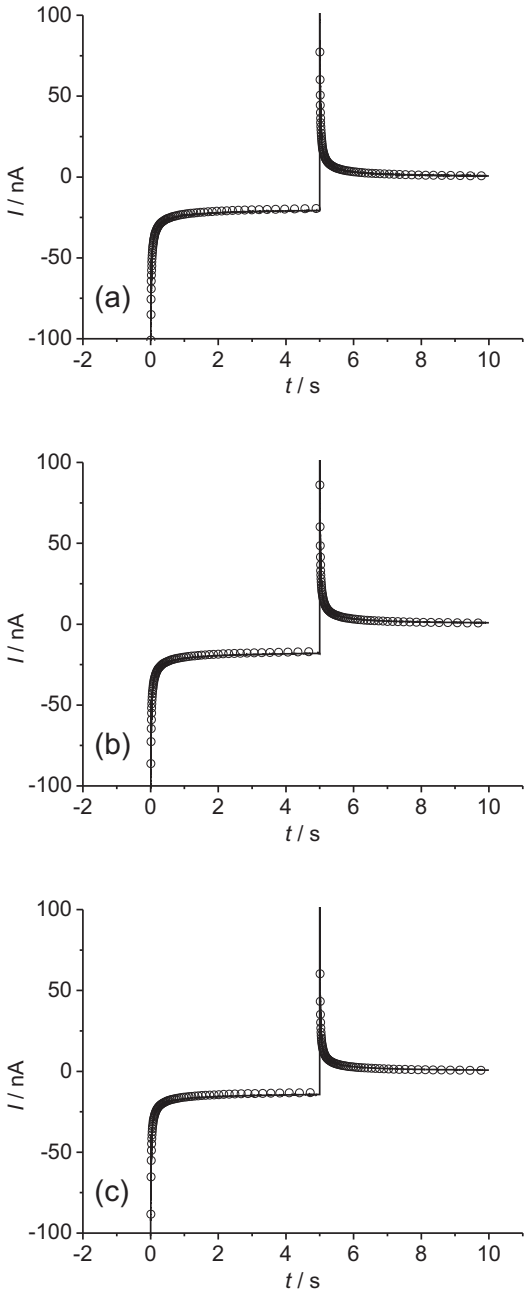


Figure 4.3: Examples of the fitting of experimental (–) and theoretical (○) transients. This fitting is for 2 mM hexaammineruthenium(III) chloride solutions with (a) 0.1 M , (b) 0.3 M and (c) 0.5 M KCl as supporting electrolyte respectively. The potential was stepped from 0.2 to -0.5 and back to 0.2 V vs Ag|AgCl.

Table 4.1: Diffusion coefficients for hexaammineruthenium(III) cation, $D_{\text{HexRu(III)}}$, and hexaammineruthenium(II) cation, $D_{\text{HexRu(II)}}$[a], in aqueous solutions with different concentrations (0.1 M, 0.3 M and 0.5 M) of KCl, KNO_3 and K_2SO_4 as supporting electrolyte at 298 K[b].

Electrolyte	c_{sup} (M)	$D_{\text{HexRu(III)}} \times 10^{-10}$ (m^2 s^{-1})	$D_{\text{HexRu(II)}} \times 10^{-9}$ (m^2 s^{-1})	$D_{\text{HexRu(III)}}/D_{\text{HexRu(II)}}$
KCl	0.1	8.43 (± 0.03)	1.19 (± 0.01)	0.708
	0.3	6.64 (± 0.04)	0.92 (± 0.01)	0.722
	0.5	5.47 (± 0.12)	0.77 (± 0.01)	0.710
KNO_3	0.1	8.00 (± 0.03)	1.11 (± 0.01)	0.721
	0.3	6.48 (± 0.04)	0.91 (± 0.01)	0.712
	0.5	5.32 (± 0.08)	0.73 (± 0.01)	0.729
K_2SO_4	0.1	5.71 (± 0.01)	0.88 (± 0.01)	0.649
	0.3	5.37 (± 0.21)	0.82 (± 0.03)	0.655
	0.5	4.96 (± 0.03)	0.75 (± 0.01)	0.661

[a] Error bars were calculated from the standard deviation of the best theoretical fits from several repeat potential step chronoamperograms.

[b] $D_{\text{HexRu(III)}}$ values were determined by the Shoup and Szabo method. $D_{\text{HexRu(II)}}$ were obtained by simulation of experimental chronoamperometric transients.

The diffusion coefficient value, $D_{\text{HexRu(III)}}$, determined in a solution with 0.1 M KCl was 8.43 ± 0.03 × 10^{-10} m^2 s^{-1}, which compares well to the literature values which range from 8.5 × 10^{-9} to 9.1 × 10^{-10} m^2 s^{-1} [29–31]. For all concentrations of supporting electrolyte (C_{sup}), KCl and KNO_3 systems yielded similar values of $D_{\text{HexRu(III)}}$ and $D_{\text{HexRu(II)}}$ values, which indicates that this couple had similar diffusional behaviour, and most probably there are no ion-pairing interactions in these two systems. A possible reason for the differences between the diffusion coefficients for $[Ru(NH_3)_6]^{3+}$ and $[Ru(NH_3)_6]^{2+}$ is that these two cations carry different charges which may change the diffusion coefficient by altering the hydrodynamic radii. In the K_2SO_4 system, the diffusion coefficients were all much smaller than in the other systems (for example $D_{\text{HexRu(III)}}$ was 5.17 × 10^{-10} m^2 s^{-1} when C_{sup} was 0.1 M, compared to 8.43 × 10^{-10} m^2 s^{-1} for the KCl system). This decrease in diffusion coefficients is likely caused by ion-pairing interaction between both $[Ru(NH_3)_6]^{3+}$ and $[Ru(NH_3)_6]^{2+}$ with SO_4^{2-}. When the species cations are associated with the supporting electrolyte anion, their size becomes larger than their 'normal size', and as a result, their transport is slower according to Stokes-Einstein theory [32, 33]. These observations agree with the earlier voltammetric inferences regarding the formation of complexes. Evidence of the formation of the ion-pair of $[Ru(NH_3)_6]^{3+} \cdot SO_4^{2-}$ has been previously reported by Yao *et al.* using the quartz crystal microbalance to measure the weight

of adsorbed species at an electrode surface [34].

It can be observed from Table 4.1 that in all three systems, both $D_{\mathrm{HexRu(III)}}$ and $D_{\mathrm{HexRu(III)}}$ values decreased as the increase of C_{sup}. Decay trends for the three systems are shown in Figure 4.4 (a for $D_{\mathrm{HexRu(III)}}$ and b for $D_{\mathrm{HexRu(II)}}$). The explanation of these phenomena is that the ionic strength of the solution influences the diffusion coefficients of the electroactive couple [35], probably in part through changed viscosity of the electrolyte solutions. The diffusion coefficient is inversely proportional to the viscosity of the solution according to the Stokes-Einstein equation.

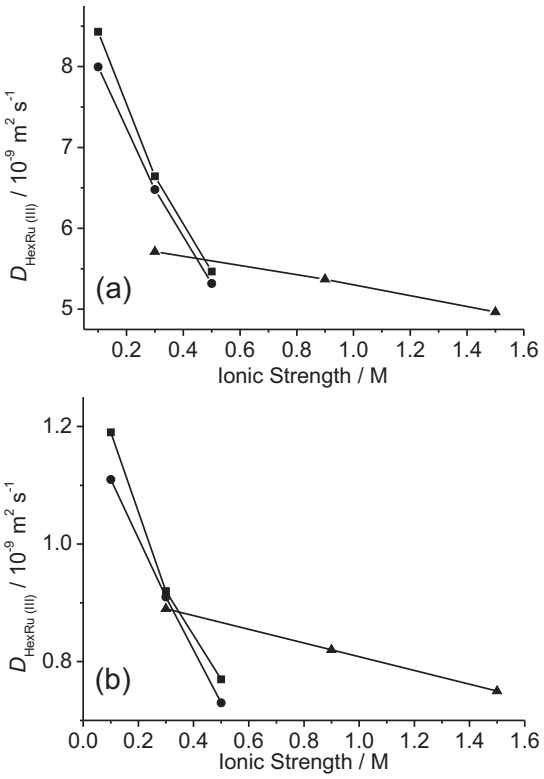


Figure 4.4: The changes of (a) $D_{\mathrm{HexRu(III)}}$ and (b) $D_{\mathrm{HexRu(II)}}$ varying the ionic strength of solution, for the supporting species KCl, KNO_3 and K_2SO_4.

In addition, in both KCl and KNO_3 systems, the ratios of $D_{\mathrm{HexRu(III)}}/D_{\mathrm{HexRu(II)}}$ are around 0.71, however, in the case of K_2SO_4 this ratio decreases to around 0.65, which means, the decrease of $D_{\mathrm{HexRu(II)}}$ is relatively smaller than $D_{\mathrm{HexRu(III)}}$. $[Ru(NH_3)_6]^{3+}$ probably has a stronger ion-pair with SO_4^{2-} than $[Ru(NH_3)_6]^{2+}$, which agrees to the cyclic voltammetric observations (negatively shifted reduction peak).

4.4 Conclusions

Double potential step chronoamperometry was recorded for the $[Ru(NH_3)_6]^{3+}$ and $[Ru(NH_3)_6]^{2+}$ couple in aqueous solutions with various supporting electrolytes (KCl, KNO_3 and K_2SO_4) at different concentrations (0.1 M, 0.3 M, and 0.5 M). The chronoamperometric transients were used to quantitatively determine the values of the diffusion coefficients, $D_{\mathrm{HexRu(III)}}$ and $D_{\mathrm{HexRu(II)}}$. It was observed that the diffusion coefficients of the electroactive couple are very similar for the cases where either KCl or KNO_3 was used as supporting electrolyte. Whereas, in the presence of K_2SO_4 as supporting electrolyte, smaller diffusion coefficients were found. Also, the ratios of $D_{\mathrm{HexRu(III)}}/D_{\mathrm{HexRu(II)}}$ were found at *ca.* 0.71 in both of the KCl and the KNO_3 cases, which were independent of the concentration of supporting electrolyte. However, in the case of K_2SO_4 this ratio was determined at *ca.* 0.65. Therefore, the SO_4^{2-} anion probably has an ion-pairing interaction with the $[Ru(NH_3)_6]^{3+}$ and $[Ru(NH_3)_6]^{2+}$, which leads to lower diffusion coefficients. Moreover, the indication of ion-pairing effect was further confirmed by comparing cyclic voltammograms using different supporting species, finding that SO_4^{2-} anions influence the half wave potential of the electroactive couple, the reduction peak was negatively shifted by *ca.* 0.05 V in the K_2SO_4 case in comparison with the other supporting species.

References

[1] J.G. Limon-Petersen, N.V. Rees, I. Streeter, A. Molina, R.G. Compton, J. Electroanal. Chem. 623 (2008) 165–169.

[2] J.G. Limon-Petersen, J.T. Han, N.V. Rees, E.J.F. Dickinson, I. Streeter, R.G. Compton, J. Phys. Chem. C 114 (2010) 2227–2236.

[3] R.G. Compton, C.E. Banks, Understanding Voltammetry, World Scientific, Singapore, 2007.

[4] A.J. Bard, L.R. Faulkner, Electrochemical Methods, Fundamentals and Applications, John Wiley & Sons, New York, 2001.

[5] E.J.F. Dickinson, J.G. Limon-Petersen, N.V. Rees, R.G. Compton, J. Phys. Chem. C 113 (2009) 11157–11171.

[6] A. Molina, E. Laborda, E.I. Rogers, F. Martinez-Ortiz, C. Serna, J.G. Limon-Petersen, N.V. Rees, R.G. Compton, J. Electroanal. Chem. 634 (2009) 73–81.

[7] T.L. Ferreira, T.R.L.C. Paixao, O.A. Richter, E. M. amd El Seoud, M. Bertotti, J. Phys. Chem. B 111 (2007) 12478–12484.

[8] A.M. Bond, K.B. Oldham, G.A. Snook, Anal. Chem. 72 (2000) 3492–3496.

[9] Y. Wang, E.I. Rogers, R.G. Compton, J. Electroanal. Chem. 648 (2010) 15–19.

[10] W. Hyk, A. Nowicka, Z. Stojek, Anal. Chem. 74 (2002) 149–157.

[11] J. Georges, S. Desmettre, Electrochim. Acta 29 (1984) 521–525.

[12] R.L. Wang, K.Y. Tam, R.G. Compton, J. Electroanal. Chem. 434 (1997) 105–114.

[13] H. Ikeuchi, K. Naganuma, M. Ichikawa, H. Ozawa, T. Ino, M. Sato, H. Yonezawa, S. Mukaida, A. Yamamoto, T. Hashimoto, J. Solution Chem. 36 (2007) 1243–1259.

[14] E.I. Rogers, D.S. Silvester, D.L. Poole, L. Aldous, C. Hardacre, R.G. Compton, J. Phys. Chem. C 112 (2008) 2729–2735.

[15] R.G. Evans, O.V. Klymenko, C. Hardacre, K.R. Seddon, R.G. Compton, J. Electroanal. Chem. 556 (2003) 179–188.

[16] E.O. Barnes, A.M. O'Mahony, S.R. Belding, R.G. Compton, J. Chem. Eng. Data 55 (2010) 2219–2224.

[17] Y. Wang, E.I. Rogers, S.R. Belding, R.G. Compton, J. Electroanal. Chem. 648 (2010) 134–142.

[18] M.C. Buzzeo, O.V. Klymenko, J.D. Wadhawan, C. Hardacre, K.R. Seddon, R.G. Compton, J. Phys. Chem. A 107 (2003) 8872–8878.

[19] O.V. Klymenko, R.G. Evans, C. Hardacre, I.B. Svir, R.G. Compton, J. Electroanal. Chem. 571 (2004) 211–221.

[20] X.B. Ji, C.E. Banks, D.S. Silvester, A.J. Wain, R.G. Compton, J. Phys. Chem. C 111 (2007) 1496–1504.

[21] R.D. Martin, P.R. Unwin, J. Electroanal. Chem. 439 (1997) 123–136.

[22] S.R. Belding, R. Baron, E.J.F. Dickinson, R.G. Compton, J. Phys. Chem. C 113 (2009) 16042–16050.

[23] A.C. Fisher, R.G. Compton, J. Phys. Chem. 95 (1991) 7538–7542.

[24] A.M. Baticle, F. Perdu, P. Vennereau, Electrochim. Acta 16 (1971) 901–912.

[25] J. Redepenning, E. Castro-Narro, G. Venkataraman, E. Mechalke, J. Electroanal. Chem. 498 (2001) 192–200.

[26] G.K. Rowe, S.E. Creager, J. Phys. Chem. 98 (1994) 5500–5504.

[27] T. Kondo, M. Okamura, K. Uosaki, J. Organomet. Chem. 637–639 (2001) 841–844.

[28] E.S. Yang, M.S. Chan, A.C. Wahl, J. Phys. Chem. 84 (1980) 3094–3099.

[29] C.E. Banks, R.G. Compton, A.C. Fisher, I.E. Henley, Phys. Chem. Chem. Phys. 6 (2004) 3147–3152.

[30] C.E. Banks, N.V. Rees, R.G. Compton, J. Electroanal. Chem. 535 (2002) 41–47.

[31] F. Marken, J.C. Eklund, R.G. Compton, J. Electroanal. Chem. 395 (1995) 335–338.

[32] A. Moreno, P.S. Pregosin, L.F. Veiros, A. Albinati, S. Rizzato, Chem. Eur. J. 15 (2009) 6848–6862.

[33] F. Hallberg, L. Furo, P. Stilbs, J. Am. Chem. Soc. 13 (2009) 13900–13901.

[34] K. Yao, K. Shimazu, M. Nakata, A. Yamagishi, J. Electroanal. Chem. 442 (1998) 235–242.

[35] R.A. Robinson, R.H. Stokes, Electrolyte Solutions, Butterworths Scientific: London, 1955.

Part III Mechanistic and Kinetic Study of Electrochemistry in Room Temperature Ionic Liquids

An alternative way to eliminate unwanted ion-pairing effects is using room temperature ionic liquids (RTILs) as solvents. Since RTILs are exclusively composed of ions, they usually show high intrinsic conductivity. This property can usefully decrease the Ohmic drop and enable experiments without supporting electrolyte. However, electrochemistry in RTILs can be significantly different compared to that in conventional solvents but our understanding of their electrochemical properties is still limited. This part of the thesis shows two examples of exploration of electroanalysis in RTILs.

Chapter 5 The Electrochemical Reduction of 1,4-Benzoquinone in 1-Ethyl-3-methylimidazolium bis(trifluoromethanesulfonyl)imide, $[C_2mim][NTf_2]$: A Voltammetric Study of the Comproportionation between Benzoquinone and the Benzoquinone Dianion

The work presented in this chapter was carried out in collaboration with

- **S.R. Belding** (for the theory and modelling parts)

and has been published in:

Y. Wang, E.I. Rogers, S.R. Belding, R.G. Compton, J. Electroanal. Chem. 648 (2010) 134–142

As introduced in the previous part, supporting electrolytes may cause the problem of unwanted ion-pairing effect into an electrochemical process. In some other cases, supporting electrolytes can also be undesirable because they increase the cost of experiments heavily and are no easy to recycle. Therefore there is an ongoing interest in studying alternative solvents that do not need additional supporting electrolyte, for instance, RTILs. RTILs are liquid salts at room temperature, which normally consist of long-chain non-polar organic cations and small polar inorganic anions. They exhibit exclusively high intrinsic conductivity, low vapor pressure and chemical stability. However, the high viscosity and charged nature also make their electrochemical behavious different from conventional solvents, so their application is still under investigation. This chapter, an introduction of the two-electron reduction of 1,4-benzoquinone, shows an example of employing RTILs in electrochemical analysis.

The two step electrochemical reduction of 1,4-benzoquinone, BQ, was investigated on a microdisk electrode (10 μm diameter Au) in the room temperature ionic liquid 1-ethyl-3-methylimidazolium bis(trifluoromethanesulfonyl)imide, $[C_2mim][NTf_2]$, over a wide range of scan rates. Two reduction

peaks were observed, corresponding to the reduction of BQ to the radical anion, $BQ^{\bullet-}$, at a peak potential, E_p of approximately -0.50 V, followed by reduction to the dianion, BQ^{2-} at more negative potentials ($E_p \approx$ -0.89 V):

$$BQ + e^- \rightleftharpoons BQ^{\bullet-} \tag{5.1}$$

$$BQ^{\bullet-} + e^- \rightleftharpoons BQ^{2-} \tag{5.2}$$

The technique of potential step chronoamperometry was used to measure the diffusion coefficients of each of the three reaction species, BQ, $BQ^{\bullet-}$ and BQ^{2-}, and values of 4.73 ($\pm$ 0.10) $\times$ 10^{-11}, 1.73 ($\pm$ 0.08) $\times$ 10^{-11} and 1.55 ($\pm$ 0.15) $\times$ 10^{-11} m^2 s^{-1} were determined, respectively, at 298 K. This technique, together with cyclic voltammetric simulations, allows elucidation of the kinetic and thermodynamic parameters for both reduction processes and the following homogeneous comproportionation process:

$$BQ^{2-} + BQ \rightleftharpoons 2\ BQ^{\bullet-} \tag{5.3}$$

including the Gibbs energy, ΔG°_{comp}, for the reaction, where a value of -38.3 kJ mol^{-1} suggests that the comproportionation of BQ^{2-} and BQ, to form $BQ^{\bullet-}$ is thermodynamically downhill.

5.1 Introduction

Many studies involving the reduction of 1,4- benzoquinone, BQ, have been undertaken in both aqueous [1–9] and non-aqueous [10–21] media. In aqueous media, it has long been established that quinones, Q, undergo reduction to form hydroquinone, H_2Q, in the following process [1]:

$$Q + 2H^+ + 2e^- \rightleftharpoons H_2Q \tag{5.4}$$

and a comproportionation reaction between electrogenerated H_2Q and parent Q leads to generation of the Q radical anion [1, 2]:

$$H_2Q + Q \rightleftharpoons 2Q^{\bullet-} + 2H^+ \tag{5.5}$$

In aprotic media, quinones can undergo two step reductions, as denoted below, to form both $Q^{\bullet-}$ and the dianion species, Q^{2-},

$$Q + e^- \rightleftharpoons Q^{\bullet-} \tag{5.6}$$

$$Q^{\bullet-} + e^- \rightleftharpoons Q^{2-} \tag{5.7}$$

as both $Q^{\bullet-}$ and Q^{2-} are stable. If the transfer of the second electron is more thermodynamically difficult than the first, comproportionation is favoured:

$$Q^{2-} + Q \rightleftharpoons 2Q^{\bullet-} \tag{5.8}$$

where the electrogenerated dianion reacts with the parent molecule to regenerate the intermediate radical anion [22].

For a given process, electrochemical methods, including cyclic voltammetry, have proved to be experimentally simple and accurate routes for the quantitative measurement of kinetic and thermodynamic data. For systems featuring two step electron transfer reactions, such as the EE systems denoted in Equations (5.6) and (5.7), that exhibit two separate voltammetric features relating to each reduction step, it is possible, at least in principle, to infer kinetic information about the comproportionation reaction. It has been established that for electrochemically reversible electrode reactions of the EE type that proceed with the absence of other chemical reactions, where mass transport occurs by diffusion only and species A, B and C (where A is the parent species, B is the radical anion and C is the dianion, in the scheme above) have equal diffusion coefficients, the effect of comproportionation on the voltammetry obtained is unobservable [22–25]. For systems where one or more of these conditions are not met, the comproportionation reaction will exert an effect on the voltammetry obtained. Ji *et al*. [16] looked at the reduction of 1,4-benzoquinone in propylene carbonate (PC) on a glassy carbon electrode and reported voltammetry for a two step reduction of BQ to $BQ^{\bullet-}$ and BQ^{2-}, although they observed that, upon reversing the second reductive wave, the oxidation wave, corresponding to the re-oxidation of BQ^{2-} to $BQ^{\bullet-}$, was absent, suggested to result from the fast comproportionation

of the dianion with the neutral species. Unlike, dimethyl formamide (DMF) and acetonitrile (MeCN), where generally, the ratio of the diffusion coefficients of a radical ion to its parent species is close to unity [16, 21, 26], a value of 0.48 was calculated for the diffusion coefficient ratio, $D_{BQ^{\bullet-}}/D_{BQ}$, that is, the radical anion species diffuses more slowly than the neutral molecule.

This unequal diffusion coefficient effect is common when using room temperature ionic liquids, RTILs, as solvents [27–32]. Numerous reports have shown discrepancies in diffusion coefficients in various ionic liquid media. For example, Rogers *et al*. reported ratios of 0.76–0.13 for the $Fc|Fc^+$ redox couple (where Fc is ferrocene), and 0.77–0.33 for $Cc^+|Cc$ (where Cc is cobaltocene) in a range of ionic liquids with different viscosities [33]. Diffusion coefficients of the neutral parent and corresponding radical cation were also found to differ significantly for the $TMPD|TMPD^{+\bullet}$ redox couple (where TMPD is *N*,*N*,*N*′,*N*′-tetramethylphenylenediamine), with the charged molecule diffusing more slowly through the 1-ethyl-3-methylimidazolium bis(trifluoromethanesulfonyl)imide, [C_2mim][NTf_2], ionic liquid solvent [34, 35]. An extreme illustration of differing diffusion coefficients is noticeable for the $O_2|O_2^{\bullet-}$ redox couple, where the diffusion coefficients were found to differ by more than an order of magnitude and a $D_{O_2^{\bullet-}}/D_{O_2}$ ratio as small as 0.03 was reported [36]. We are unaware of any literature reporting the diffusion coefficient ratio for the $BQ|BQ^{\bullet-}$ couple in RTIL solvents. Islam *et al*. studied the $BQ|BQ^{\bullet-}$ redox behaviour in 1-ethyl-3-methylimidazolium tetrafluoroborate, [C_2mim][BF_4], as well as dimethylsulfoxide (DMSO). They measured the mid-point potentials for both the $BQ|BQ^{\bullet-}$ and $BQ^{\bullet-}|BQ^{2-}$ redox processes (from the average of anodic and cathodic peak potentials) and calculated the Gibbs energy, ΔG°_{comp}, for the comproportionation reaction [37].

The current study reports the two step electrochemical reduction of 1,4-benzoquinone, BQ, in the room temperature ionic liquid 1-ethyl-3-methylimidazolium bis(trifluoromethanesulfonyl)imide, [C_2mim][NTf_2], on a 10 μm diameter Au microelectrode. Potential step chronoamperometry techniques are used to determine the diffusion coefficients of all three species involved in the reduction process, and these values are used, along with voltammetric simulation techniques to elucidate parameters relating to the kinetics and thermodynamics of the reaction process, including compropor-

tionation.

5.2 Experimental

5.2.1 Chemical Reagents

1,4-Benzoquinone (BQ, Sigma-Aldrich, 98 %), ferrocene ($Fe(C_5H_5)_2$, Aldrich, 98 %), tetra-*n*-butylammonium perchlorate (TBAP, > 99 %, Fluka), acetonitrile (MeCN, Fischer scientific, dried and distilled, > 99 %) and nitrogen (N_2, BOC Gases) were used as received, without further purification. 1-Ethyl-3-methylimidazolium bis(trifluoromethanesulfonyl)imide ([C_2mim][NTf_2]) was prepared following standard literature procedures [38].

5.2.2 Instrumental

A two electrode arrangement was utilized in a T-cell [39]. The microdisk electrode was modified with a small section of disposable pipette tip to form a cavity above the electrode surface, into which microlitre quantities of RTIL solution was placed. The microdisk was inserted into the bottom of the T-cell and the circuit completed by introduction of a 0.5 mm diameter silver (Ag) wire quasi-reference electrode through the top of the cell. Benzoquinone solutions were prepared to a known concentration (*ca.* 5 mM) by dissolving a small amount of solid directly in the RTIL, and stirred for *ca.* 2 hours in sealed vials. 20 μL of this solution was placed in the T-cell and placed under vacuum, to remove atmospheric oxygen and water impurities, for at least 90 minutes prior to measurements being taken. In some cases, nitrogen was flowed over the liquid to 'blanket' the solution while measurements were being taken.

5.3 Theory

We consider a two step electrochemical reduction and additional comproportionation reaction at a microdisk electrode:

$$A + e^- \rightleftharpoons B \quad k^0{}_{A|B},\ E^{0\prime}_{A|B} \tag{5.9}$$

$$B + e^- \rightleftharpoons C \quad k^0{}_{B|C},\ E^{0'}_{B|C} \tag{5.10}$$

$$C + A \rightleftharpoons 2B \quad k_{comp}, k_{disp} \tag{5.11}$$

where A is benzoquinone (BQ), B is the radical anion ($BQ^{\bullet -}$) and C is the dianion (BQ^{2-}), $k^0{}_{A|B}$ and $k^0{}_{B|C}$ are the heterogeneous rate constants for Equations (5.9) and (5.10), respectively, k_{comp} and k_{comp} are the rate constants for the comproportionation and disproportionation reactions (Equation (5.11)), $E^{0'}_{A|B}$ and $E^{0'}_{B|C}$ are the formal potentials for the corresponding reactions. The equilibrium constant for comproportionation, $K_{eqm} = k_{comp}/k_{disp}$, where k_{disp} is the rate constant for disproportionation. Also, $\Delta G^{\circ}_{comp} = -RT\ln K_{eqm} = -F(-E^{0'}_{B|C} + E^{0'}_{A|B})$.

5.3.1 Potential Step Chronoamperometric Experiments

Quadruple (A–B–C–B–A) Potential Step Chronoamperometry

This technique was undertaken to determine the diffusion coefficients of BQ, $BQ^{\bullet -}$ and BQ^{2-} simultaneously. The potential was stepped from a 0.00 V to a potential after reduction peak 1 (-0.65 V), corresponding to the reduction process BQ → $BQ^{\bullet -}$, and then to a potential after the second reduction peak (-0.9 V), corresponding to $BQ^{\bullet -}$ → BQ^{2-}, where it was reversed and stepped back to -0.60 V (after oxidation peak 2, corresponding to the reoxidation of BQ^{2-}) and then to 0.00 V (after oxidation peak 1, corresponding to the reoxidation of $BQ^{\bullet -}$). The theory used to simulate the resulting chronoamperometric transients is given in Appendix II.

5.3.2 Cyclic Voltammetric Simulation Techniques

Again, we consider the mechanism denoted in Equations (5.9)–(5.11).

The first reduction process (Equation (5.9)) was simulated using a program based on an E mechanism, developed and described by Klymenko *et al.* [36]. The program allows input of a wide range of measured and fixed parameters, including scan rate (v), potential (E_{min} and E_{max}), diffusion coefficient of species A (D_A), concentration of species A (c_A) and electrode radius (r_d). The fit between the experimental and theoretical voltammetry is optimised manually by varying parameters for the

standard heterogeneous rate constant ($k^0{}_{\mathrm{A|B}}$), the transfer coefficient ($\alpha_{\mathrm{A|B}}$) and the formal electrode potential ($E^0_{\mathrm{f,A|B}}$) of the A|B redox couple.

A second simulation technique, described in recent publications [24, 25] was used to model the stepwise two electron reduction (Equations (5.9) and (5.10)), allowing for an additional comproportionation step, shown in Equation (5.11). Values for experimental parameters, such as v, potential range (E_{start} and E_{end}) and r_{d} are input, including initial estimates for kinetic and thermodynamic parameters for both the A|B and B|C redox couples, including, k^0, E^0_{f}, α and k_{comp}, as well as concentration (c_{A}) and diffusion coefficients (D_{A}, D_{B} and D_{C}), and the values optimised until the best fit between experimental and theoretical voltammograms were achieved over a range of scan rates.

5.4 Results and Discussion

5.4.1 Reduction of BQ to $BQ^{\bullet-}$

Cyclic Voltammetry

Figure 5.1 shows typical cyclic voltammetry for the reduction of 5 mM 1,4-benzoquinone in [C_2mim][NTf_2] on a 10 μm diameter Au microdisk electrode at scan rates from 10–1000 mV s^{-1}. The potential is typically scanned from 0.00 to -0.65 V *vs* a 0.5 mm diameter Ag wire quasi-reference. BQ is reduced by one electron to the radical anion, $BQ^{\bullet-}$, at a peak potential of -0.49 V *vs* Ag (at 1000 mV s^{-1}), and oxidised back to BQ at a potential of -0.42 V *vs* Ag (at 1000 mV s^{-1}), corresponding to the following process:

$$\mathrm{BQ} + \mathrm{e}^- \rightleftharpoons \mathrm{BQ}^{\bullet-} \tag{5.12}$$

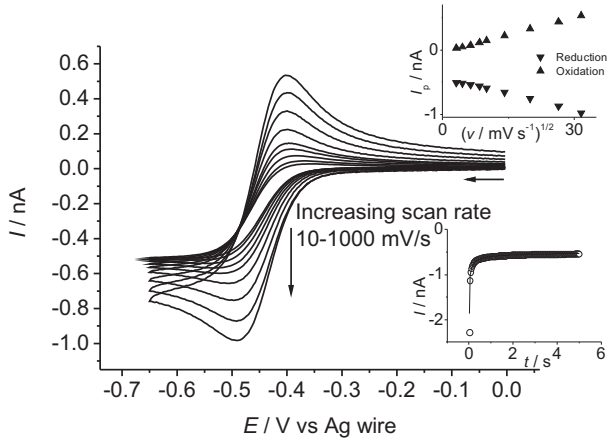


Figure 5.1: Cyclic voltammetry for the reduction of BQ to $BQ^{\bullet-}$ in [C_2mim][NTf_2] on a Au microdisk (10 μm diameter) at varying scan rates (10, 20, 40, 70, 100, 200, 400, 700 and 1000 mV s^{-1}) in the potential range 0.00 to -0.65 V. Upper inset: The plots of the reduction peak current and the oxidation peak current for BQ against the square root of scan rates (10 to 1000 mV s^{-1}). Lower inset: The experimental (—) and best-fit theoretical (○) single potential step chronoamperometric transient for the BQ|$BQ^{\bullet-}$ redox couple in the same potential range.

The shape of the peaks suggest that the electrode process shows relatively fast electrode kinetics, and the difference between the reductive and oxidative peaks, ΔE_p, of approximately 70 mV (at 1000 mV s^{-1}), is very close to that for a system displaying Nernstian behaviour (59 mV) at 298 K, under conditions of pure linear diffusion. The peak separation decreases with increasing scan rate, as a transition from steady-state behaviour at slower scan rates to more transient behaviour at faster scan rates occurs. Also, the peak current, i_p, increases systematically with scan rate, v; the expected dependency changes from v^0 to $v^{1/2}$ as the scan rate increases from values corresponding to convergent diffusion to those for linear diffusion (shown in upper inset in Figure 5.1) as is typical for RTILs. In this RTIL at a 10 μm diameter Au electrode, steady-state behaviour is only expected at scan rates much less than 5 mV s^{-1}, assuming $D = 4.81 \times 10^{-11}$ m^2 s^{-1} (determined from chronoamperometry, see later), $T = 298$ K and $r_d = 5$ μm, and using the inequality below,

$$v << \frac{RTD}{nFr_d{}^2} \tag{5.13}$$

where R is the universal gas constant (8.314 J K^{-1} mol^{-1}), T is the temperature, D is the diffusion coefficient, n is the number of electrons, F is the Faraday constant (96485 C mol^{-1}) and r_d is the radius of the disk electrode. Considering the inequality given in Equation (5.13), and given the slower

diffusion of BQ in the more viscous RTIL media, it can be suggested that the voltammetry obtained is intermediate of the micro/macro electrode region.

Potential Step Chronoamperometry

Next, potential step chronoamperometry was performed on the BQ|$BQ^{\bullet-}$ system, to determine the diffusion coefficients of both BQ and $BQ^{\bullet-}$ species. Initially, the potential was stepped from 0.00 V to -0.65 V. The resulting experimental chronoamperometric transient (—) for the reduction of BQ to $BQ^{\bullet-}$ is shown as an inset to Figure 5.1, along with the best theoretical fit (∘) to the Shoup and Szabo equation (Equations (2.4)–(2.6)). Then, double potential step chronoamperometry was undertaken. The potential was stepped from 0.00 V to -0.65 V (reduction of BQ to $BQ^{\bullet-}$) and back to 0.00 V (oxidation of $BQ^{\bullet-}$ to BQ), and the experimental (—) transient obtained is shown in Figure 5.2. The first step was analysed as before, to determine D_{BQ} and c_{BQ}, using the Shoup and Szabo expression, and the second step was simulated using the program described in Section 2.2, to determine $D_{\mathrm{BQ}^{\bullet-}}$. Table 5.1 reports the results from chronoamperometric fitting on a Au microdisk. The diffusion coefficient values for BQ in this system are approximately 1–2 orders of magnitude smaller than those obtained in more conventional solvents, such as acetonitrile (2.0 (± 0.24) × 10^{-9} m^2 s^{-1} [21], 2.4 (± 0.30) × 10^{-9} m^2 s^{-1} [40] and 2.7 (± 0.05) × 10^{-9} m^2 s^{-1} [41]) and propylene carbonate (4.2 (± 0.20) × 10^{-10} m^2 s^{-1} [16]), which is reasonable considering the higher viscosity of [C_2mim][NTf_2] (34 cP) [38] compared to acetonitrile (0.34 cP) and propylene carbonate (2.5 cP) [42], all at 298 K. Also included in the table for comparison are c_{BQ}, D_{BQ} and $D_{\mathrm{BQ}^{\bullet-}}$ values measured on a Pt microdisk electrode. These are in good agreement with those determined for Au, giving confidence in our results. It is important to note the value of $c_{\mathrm{BQ}} = 5.22$ mM from fitting of the chronoamperometric transient is in good agreement with the value $c_{\mathrm{BQ}} \approx 5$ mM used in this study.

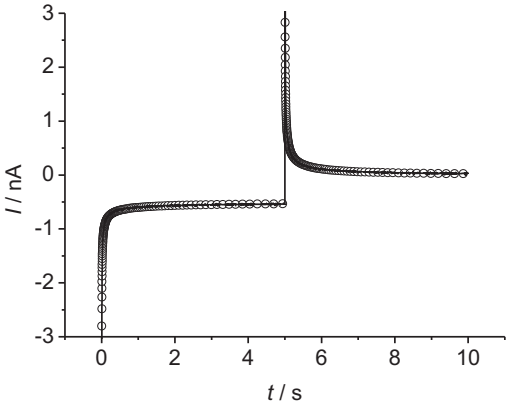


Figure 5.2: Experimental (—) and best-fit theoretical (∘) double potential step chronoamperometric transient measured for the BQ|$BQ^{\bullet-}$ redox couple in [C_2mim][NTf_2] on a 10 μm diameter Au microelectrode at room temperature. The potential was stepped from 0.00 to -0.65 V and back to 0.00 V.

Table 5.1: Single and double potential step chronoamperometric data[a] for BQ in [C_2mim][NTf_2] on Au and Pt microdisk electrodes (10 μm diameter).

Electrode	$c_{BQ}^{b,c}$ /mM	D_{BQ}[b] /m^2 s^{-1}	$D_{BQ^{\bullet-}}^{d}$ /m^2 s^{-1}
Au	5.22 (± 0.08)	4.81 (± 0.08) × 10^{-11}	1.70 × 10^{-11}
Pt	5.22 (± 0.03)	4.67 (± 0.05) × 10^{-11}	1.70 × 10^{-11}

[a] Error bars were calculated from the standard deviation of the best theoretical fits from several repeat potential step chronoamperograms.

[b] c_{BQ} and D_{BQ} values were determined using the Shoup and Szabo fitting function for chronoamperometric data.

[c] Note that the value of $c_{BQ} = 5.22$ mM from fitting of the chronoamperometric transient is in good agreement with the value $c_{BQ} \approx 5$ mM used in this study.

[d] $D_{BQ^{\bullet-}}$ values were achieved by simulation of experimental chronoamperometric transients.

It was determined, when simulating the double potential step chronoamperometric transients, that the ratio of diffusion coefficients, $D_{BQ^{\bullet-}}/D_{BQ} \neq 1$ (0.35 for Au and 0.36 for Pt), suggesting that the charged radical anion species, $BQ^{\bullet-}$, diffuses more slowly through the IL media than the neutral BQ species. As mentioned previously, this discrepancy in diffusion coefficients has also been reported for ferrocene|ferrocenium ($Fc|Fc^+$) [33, 43] and cobaltocenium|cobaltocene ($Cc^+|Cc$) [33] redox couples, as well as for molecules such as *N*,*N*,*N*′,*N*′-tetramethylphenylenediamine (TMPD|$TMPD^{+\bullet}$) [26, 35], and *N*,*N*-dimethylphenylenediamine (DMPD|$DMPD^+$) [24], in various RTILs, thought to result from increased electrostatic interactions between the charged species and ions of the IL compared to those between the neutral species and the IL.

Simulation of BQ Reduction CV

The next step was to elucidate the kinetic and thermodynamic parameters of the BQ|$BQ^{\bullet-}$ redox couple by means of cyclic voltammetric simulation techniques. The mathematical model utilised for the simulation of CV for the simple one-electron reduction of BQ was based on that developed by Klymenko *et al.* [36], which considers a simple E mechanism. The pre-determined values of D_{BQ}, $D_{BQ^{\bullet-}}$ and c_{BQ} were input into the program and values of ${k^0}_{BQ|BQ^{\bullet-}}$, $\alpha_{BQ|BQ^{\bullet-}}$ and $E^0_{f,BQ|BQ^{\bullet-}}$ (where ${k^0}_{BQ|BQ^{\bullet-}}$ is the standard heterogeneous electron transfer rate constant, $E^0_{f,BQ|BQ^{\bullet-}}$ is the formal electrode potential, and $\alpha_{BQ|BQ^{\bullet-}}$ is the transfer coefficient, for the BQ|$BQ^{\bullet-}$ couple) were varied until the best fit between experimental and theoretical CVs were achieved. The plots are shown in Figure 5.3 at (a) 10, (b) 100 and (c) 1000 mV s^{-1}. The reliability of the fitting procedure was ensured by simulating the voltammetry over a wide range of scan rates, and the parameters, which gave a very good fit over the scan rate range used, are reported in Table 5.2. Again, comparable values are reported for voltammetric fitting on a 10 μm diameter Pt microdisk. The parameters determined from simulation of cyclic voltammetry on both electrodes match well with those determined from chronoamperometry, giving confidence in the fits presented. The rate constant measured for the first electron transfer, that is for the process $BQ + e^- \rightleftharpoons BQ^{\bullet-}$, is electrochemically reversible on the time scale of the experiment (${k^0}_{BQ|BQ^{\bullet-}} \geq 3 \times 10^{-4}$ m s^{-1}). Figure 5.4 shows the experimental (—) and theoretical CVs for the first reduction process of BQ, using the parameters listed in Table 5.2, with varying values of ${k^0}_{BQ|BQ^{\bullet-}}$. While it is observed that a value of 0.007 m s^{-1} (○) provides the best-fit to the experimental CV, a value of 3×10^{-4} m s^{-1} (□) also provides an adequate fit to the data, therefore a rate constant for the process is determined to be larger than 3×10^{-4} m s^{-1}. When the rate constant decreases below this value, the fit becomes less satisfactory, especially when decreased below 5×10^{-5} m s^{-1} (▽).

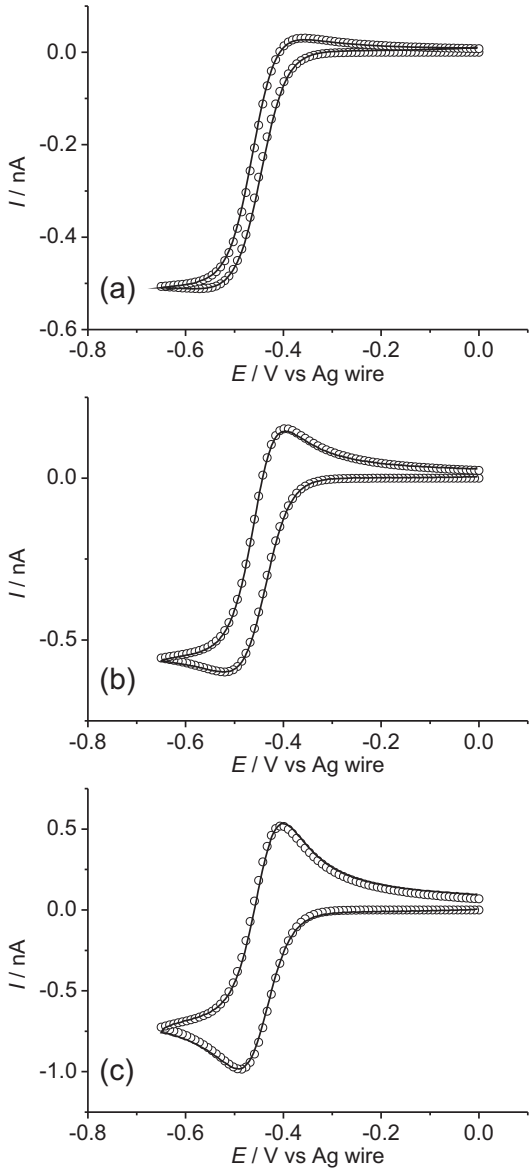


Figure 5.3: Experimental (—) and theoretical (○) cyclic voltammograms for the reduction of BQ to $BQ^{\bullet-}$ in [C_2mim][NTf_2] on a Au microdisk (10 μm diameter) at scan rates of (a) 10, (b) 100 and (c) 1000 mV s^{-1}, in the potential range 0.00 to -0.65 V, using values of D_{BQ}, $D_{BQ^{\bullet-}}$ and c_{BQ} close to those obtained from chronoamperometry. The parameters determined from simulation are given in Table 5.2.

Table 5.2: Parameters for the $BQ|BQ^{\bullet-}$ redox couple in [C_2mim][NTf_2] on 10 μm diameter Au and Pt microdisks from the cyclic voltammetric simulation fits shown in Figure 5.3. Note that the formal potentials may not be unique as a quasi-reference was employed.

Parameter	Au	Pt
c_{BQ} /mM	5.17 ($\pm$ 0.08)	5.00 ($\pm$ 0.01)
D_{BQ} /m^2 s^{-1}	4.75 ($\pm$ 0.10) $\times$ 10^{-11}	4.63 ($\pm$ 0.07) $\times$ 10^{-11}
$D_{BQ^{\bullet-}}$ /m^2 s^{-1}	1.67 ($\pm$ 0.10) $\times$ 10^{-11}	1.77 ($\pm$ 0.27) $\times$ 10^{-11}
$k^0{}_{BQ\|BQ^{\bullet-}}$ /m s^{-1}	$\geq$ 3 $\times$ 10^{-4}	$\geq$ 3 $\times$ 10^{-4}
$E^{0'}_{BQ\|BQ^{\bullet-}}$ /V	-0.429 ($\pm$ 0.003)	-0.441 ($\pm$ 0.006)

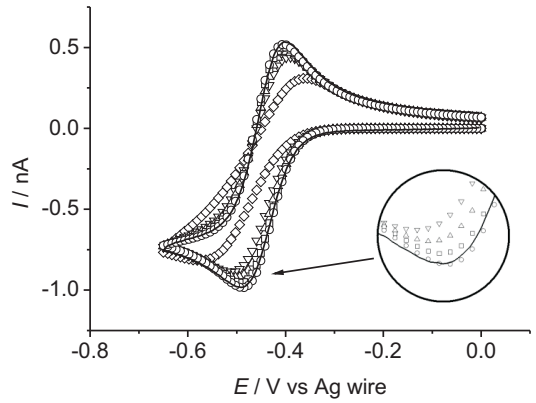


Figure 5.4: Experimental voltammetric (—) and theoretical fits for the reduction of BQ to $BQ^{\bullet-}$ in [C_2mim][NTf_2] on a 10 μm diameter Au microelectrode at 1000 mV s^{-1}, simulated using the parameters reported in Table 5.2 and various values of $k^0{}_{BQ|BQ^{\bullet-}}$: 1 $\times$ 10^{-5} ($\diamond$), 5 $\times$ 10^{-5} ($\triangledown$), 1 $\times$ 10^{-4} ($\triangle$), 3 $\times$ 10^{-4} ($\square$) and 0.007 ($\circ$) m s^{-1}.

It is important to note that the reduction of BQ to $BQ^{\bullet-}$ is a single electron process. The potentials applied over the course of the experiment are not sufficient enough to bring about the transfer of a second electron ($BQ^{\bullet-} + e^- \rightleftharpoons BQ^{2-}$), therefore, only BQ and $BQ^{\bullet-}$ are present in solution, comproportionation does not occur and the CV is independent of k_{comp} (the rate constant for a comproportionation reaction).

5.4.2 Reduction of BQ to $BQ^{\bullet-}$ and BQ^{2-}

Cyclic Voltammetry

The next step in this study was to look at the two-step electrochemical reduction of BQ in [C_2mim][NTf_2] on a Au microelectrode (10 μm diameter). The potential was scanned from 0.00 V to -0.95 V (*vs* Ag) and then scanned back to 0.00 V, and the CV obtained is shown in Figure 5.5 at scan rates of 10, 20, 40, 70, 100, 200, 400, 700 and 1000 mV s^{-1}. Two well-defined, chemically reversible redox couples were observed at half-wave potentials, $E_{\frac{1}{2}}$, of -0.45 V and -0.83 V *vs* Ag, corresponding, respectively, to the reduction of neutral BQ to the radical anion, $BQ^{\bullet-}$ (first step, see Equation 5.1), and at more negative potentials to the reduction of $BQ^{\bullet-}$ to the dianion, BQ^{2-} (second step, see Equation 5.2), with the process being described as an EE mechanism.

As in Section 5.4.1, the CV behaviour changes from almost steady-state at slower scan rates, to more transient at faster scan rates, with the back peak becoming more prominent as the scan rate increases. In this system, the redox couples are separated by *ca.* 380 mV, and it is the case where the second electron transfer takes place with greater thermodynamic difficulty than the first, comproportionation reactions are favoured to occur, where the electrogenerated BQ^{2-} dianion reacts with the initial BQ species to form two molecules of the intermediate $BQ^{\bullet-}$ radical anion, as in Equation (5.14).

$$BQ^{2-} + BQ \rightleftharpoons 2BQ^{\bullet-} \tag{5.14}$$

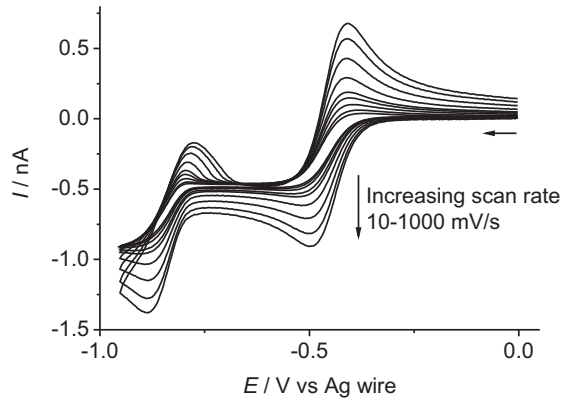


Figure 5.5: Cyclic voltammetry for the reduction of 5 mM BQ (to $BQ^{\bullet-}$ and BQ^{2-}) on a 10 μm diameter Au microelectrode in [C_2mim][NTf_2] (at room temperature) at scan rates of 10, 20, 40, 70, 100, 200, 400, 700 and 1000 mV s^{-1} in the potential range 0.00 to -0.95 V.

We determined earlier that the IL system used promotes a difference in the diffusion coefficient values for the different species in the redox reaction, with charged species diffusing more slowly than uncharged species. It is expected that the diffusion coefficient of the dianion will be slower than the radical anion due to the increased level of charge on BQ^{2-}. Accordingly, analysis of the voltammetry relating to the two separate redox processes by simulation techniques may give information relating to the comproportionation reaction. First, the technique of quadruple potential step chronoamperometry was undertaken to determine diffusion coefficients for all three reaction species.

Quadruple Potential Step Chronoamperometry

Potential step chronoamperometry was undertaken on the BQ→$BQ^{\bullet-}$→BQ^{2-} system to determine the diffusion coefficients of BQ, $BQ^{\bullet-}$ and BQ^{2-}, D_{BQ}, $D_{BQ^{\bullet-}}$ and $D_{BQ^{2-}}$. The potential was stepped from 0.0 V to -0.65 V, then to -0.95 V, and back to -0.60 V and finally 0.00 V and the resulting experimental (—) and best-fit theoretical (∘) transient is shown in Figure 5.6. The pre-determined values of c_{BQ} and D_{BQ}, from analysis using the Shoup and Szabo expression (Equations 2.4-2.6), and $D_{BQ^{\bullet-}}$, from the simulation technique described in Section 2.2, were input into the simulation program for analysing quadruple potential steps, described in Section 5.3.1, and values of $D_{BQ^{2-}}$ varied until the best fit was achieved. The parameters are given in Table 5.3. As predicted, the diffusion coefficient for the dianion is smaller than that of both the radical anion and neutral species, due to the increased

charge. The diffusion coefficient ratio, $D_{BQ^{2-}}/D_{BQ}$ is calculated to be 0.34.

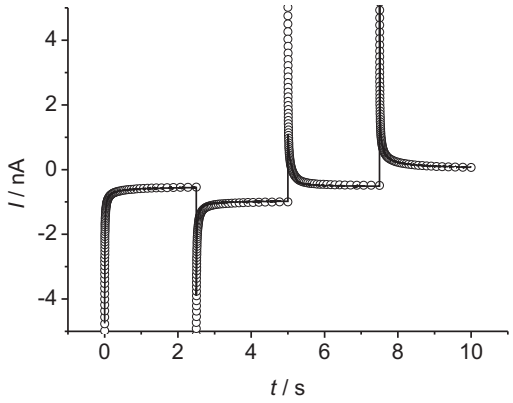


Figure 5.6: Best-fit theoretical (∘) transients to the experimental (—) quadruple potential step chronoamperometric data recorded for the $BQ|BQ^{2-}$ redox system in [C_2mim][NTf_2] on a 10 μm diameter Au microdisk at room temperature. The potential was stepped from 0.00 to -0.65 V then to -0.95 V, reversed and stepped back to -0.60 V and then to 0.00 V.

Table 5.3: Parameters for the two step reduction of BQ to $BQ^{\bullet-}$ and BQ^{2-} in [C_2mim][NTf_2] on a 10 μm diameter Au microelectrode from the best-fit cyclic voltammetric simulation fits shown in Figure 5.7. Note that the formal potentials may not be unique as a quasi-reference was employed.

Parameter	Measured value
c_{BQ} /mM	4.90 (± 0.32)
D_{BQ} /m^2 s^{-1}	4.62 (± 0.19) × 10^{-11}
$D_{BQ^{\bullet-}}$ /m^2 s^{-1}	1.82 (± 0.15) × 10^{-11}
$D_{BQ^{2-}}$ /m^2 s^{-1}	1.55 (± 0.15) × 10^{-11}
$k^0{}_{BQ\|BQ^{\bullet-}}$ /m s^{-1}	≥ 3 × 10^{-4}
$k^0{}_{BQ^{\bullet-}\|BQ^{2-}}$ /m s^{-1}	3 (± 0.5) × 10^{-5}
k_{comp} /m^3 mol^{-1} s^{-1}	10 (± 5)
$E^{0'}_{BQ\|BQ^{\bullet-}}$ /V	-0.438 (± 0.009)
$E^{0'}_{BQ^{\bullet-}\|BQ^{2-}}$ /V	-0.835 (± 0.015)

Simulation of the Two Step BQ Reduction CV

It has been suggested that simulation of the voltammograms for the $BQ|BQ^{\bullet-}$ and $BQ^{\bullet-}|BQ^{2-}$ reductions can be used to explore quantitatively the effect, if any, of comproportionation on the

voltammetry. The pre-determined values of D_{BQ}, $D_{\mathrm{BQ}^{\bullet-}}$, $D_{\mathrm{BQ}^{2-}}$, c_{BQ}, ${k^0}_{\mathrm{BQ|BQ}^{\bullet-}}$, $E^{0'}_{\mathrm{BQ|BQ}^{\bullet-}}$ and $\alpha_{\mathrm{BQ|BQ}^{\bullet-}}$ were input into the simulation program, written and developed by Belding *et al.* [24, 25]. Values of ${k^0}_{\mathrm{BQ}^{\bullet-}|\mathrm{BQ}^{2-}}$, $E^{0'}_{\mathrm{BQ}^{\bullet-}|\mathrm{BQ}^{2-}}$ and k_{comp} (rate constant for the comproportionation reaction, Equation (5.14)) were varied until the best fit between experimental and theoretical CVs were achieved, and these are shown in Figure 5.7 at (a) 10, (b) 100 and (c) 1000 mV s^{-1}. The parameters, shown in Table 5.3, were found to provide a very good fit over a wide range of scan rates (10–1000 mV s^{-1}). As before, parameters determined from cyclic voltammetric simulation match well with those determined from chronoamperometry. A ${k^0}_{\mathrm{BQ}^{\bullet-}|\mathrm{BQ}^{2-}}$ value of 3×10^{-5} m^2 s^{-1} suggests that, compared to the first reduction step, the second reduction process is more quasi-reversible on the voltammetric timescale. For this case of consecutive reductions, the electrode kinetics are fast relative to mass transport, which implies $E^{0'}_{\mathrm{BQ|BQ}^{\bullet-}} > E^{0'}_{\mathrm{BQ}^{\bullet-}|\mathrm{BQ}^{2-}}$, and the values obtained for the formal electrode potentials can be used to gain information about the kinetics and thermodynamics of the comproportionation reaction (denoted below),

$$\mathrm{BQ}^{2-} + \mathrm{BQ} \underset{k_{\mathrm{disp}}}{\overset{k_{\mathrm{comp}}}{\rightleftharpoons}} 2\mathrm{BQ}^{\bullet-} \tag{5.15}$$

including K_{eqm}, the equilibrium constant,

$$K_{\mathrm{eqm}} = \frac{[\mathrm{BQ}^{\bullet-}]^2}{[\mathrm{BQ}][\mathrm{BQ}^{2-}]} = \frac{k_{\mathrm{comp}}}{k_{\mathrm{disp}}} \tag{5.16}$$

and the Gibbs energy, $\Delta G^{\circ}_{\mathrm{comp}}$ of reaction (5.15),

$$\Delta G^{\circ}_{\mathrm{comp}} = -RT\ln(K_{\mathrm{eqm}}) = -F(E^{0'}_{\mathrm{BQ|BQ}^{\bullet-}} - E^{0'}_{\mathrm{BQ}^{\bullet-}|\mathrm{BQ}^{2-}}) \tag{5.17}$$

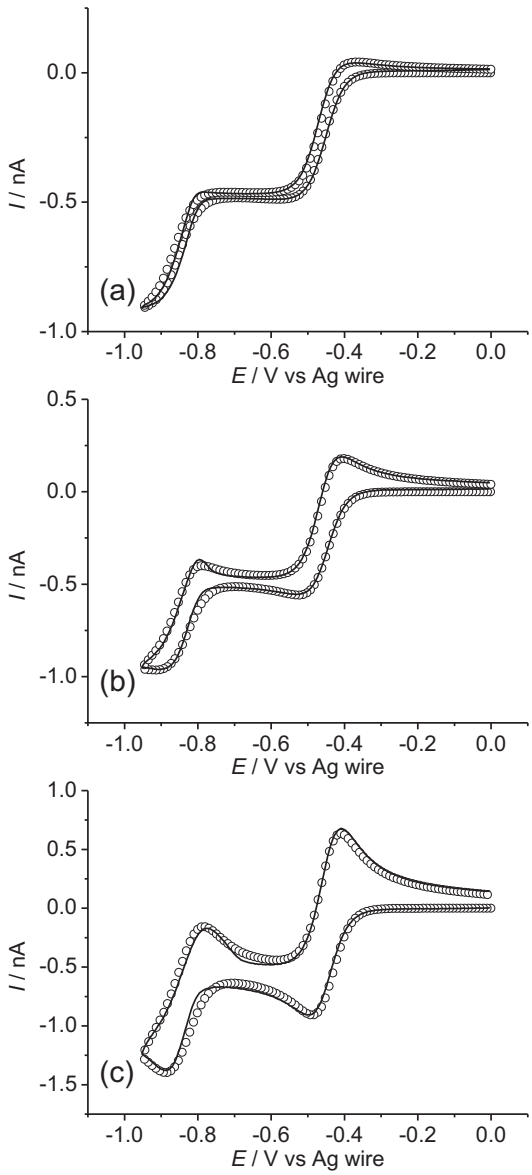


Figure 5.7: Experimental (—) and theoretical (○) voltammograms for the reduction of BQ to $BQ^{\bullet-}$ and BQ^{2-} in [C_2mim][NTf_2] on a 10 μm diameter Au microdisk electrode at scan rates of (a) 10, (b) 100 and (c) 1000 mV s^{-1} in the potential range 0.00 to -0.95 V. Values of D_{BQ}, $D_{BQ^{\bullet-}}$, $D_{BQ^{2-}}$ and c_{BQ} close to those obtained from chronoamperometry were used and best-fit simulation parameters are given in Table 5.3.

Using these equations, a ΔG°_{comp} value, calculated using the parameters in Table 5.3, of -38.3 kJ mol^{-1} suggests that the comproportionation of BQ^{2-} and BQ, to form $BQ^{\bullet-}$ is thermodynamically downhill. This value is comparable to ΔG°_{comp} of -33 kJ mol^{-1} reported for BQ in [C_2mim][BF_4] [37]. Values of -45, -61 and -77 kJ mol^{-1} were reported for BQ in PC [16], MeCN [44] and DMSO [37], respectively, suggesting that the BQ^{2-} species is more stable in IL media, and is somewhat less likely, thermodynamically, to undergo comproportionation with BQ, than more conventional solvents.

Recent papers [24, 25] suggest that, in the limit of electrochemical reversibility, the presence of

diffusion-controlled comproportionation can only be discerned from voltammetry when the scan rate is sufficiently fast or when the diffusion coefficients of the reaction species are significantly different, such that $D_{BQ^{\bullet-}}$ and $D_{BQ} > 1.5$ or $D_{BQ^{2-}}$ and $D_{BQ^{\bullet-}} < 0.75$. Figure 5.8 shows the experimental (—) data for the reduction of BQ in [C_2mim][NTf_2] and the theoretical CVs, at 1000 mV s^{-1}, simulated using the best-fit values in Table 5.3, with k_{comp} = 1 (△), 10 (□) and 100 (○) m^3 mol^{-1} s^{-1}. When comproportionation is set to 1 m^3 mol^{-1} s^{-1}, the simulation fit to the reduction and oxidation peaks, corresponding to the second redox process, is unsatisfactory. From the plots it is obvious that k_{comp} ≈ 10 m^3 mol^{-1} s^{-1} gives the best-fit between experimental and theoretical CVs, suggesting that the effect of comproportionation can be identified voltammetrically.

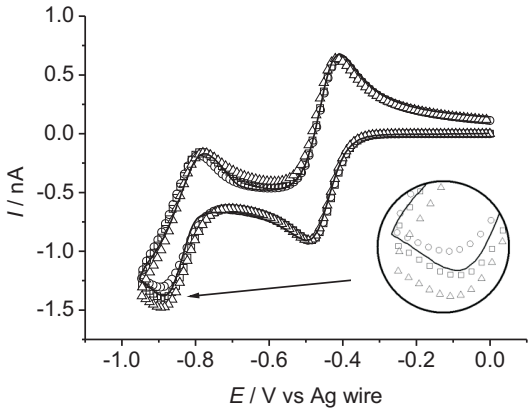


Figure 5.8: Experimental voltammetric (—) and theoretical fits for the two step reduction of BQ in [C_2mim][NTf_2] on a 10 μm diameter Au microelectrode at 1000 mV s^{-1}, simulated using the parameters reported in Table 5.3 and various values of k_{comp}: 100 (○), 10 (□) and 1 (△) m^3 mol^{-1} s^{-1}.

5.5 Conclusions

The stepwise two electron reduction of 1,4-benzoquinone (BQ) was investigated in the ionic liquid [C_2mim][NTf_2] at a gold microdisk electrode. Potential step chronoamperometric and cyclic voltammetric simulation techniques were used to permit the inference of thermodynamic and kinetic parameters for the reduction of BQ to $BQ^{\bullet-}$ and BQ^{2-}, including the standard heterogeneous rate constant and the formal electrode potentials for both redox couples, as well as the rate constant and Gibbs energy for the comproportionation reaction between BQ^{2-} and BQ to form $BQ^{\bullet-}$.

The first reduction steps from BQ to $BQ^{\bullet-}$ and BQ^{2-} was confirmed as reversible electron transfer

process from the fitting of simulating and experimental cyclic voltammograms which suggested a ${k^0}_{BQ|BQ^{\bullet-}}$ value higher than 3×10^{-4} /m s^{-1}. The same method was adopted to indicate the second reduction step was a quasi-reversible one with a best-fit ${k^0}_{BQ^{\bullet-}|BQ^{2-}}$ value of 3 ($\pm$ 0.5) $\times 10^{-5}$ /m s^{-1}. The In a [C_2mim][NTf_2] solution, the diffusion coefficients of BQ, $BQ^{\bullet-}$ and BQ^{2-} were found, by chronoamperometric simulation, decreasing as the charge increased. The reasons were suggested as the attraction between electro-generated species and solvent counter ions. This feature enables the observation and quantitative analysis of comproportionation reaction. The k_{comp} value was found at 10 ($\pm$ 5) /m^3 mol^{-1} s^{-1}.

References

[1] Y.B. Shim, S.M. Park, J. Electroanal. Chem. 425 (1997) 201–207.

[2] Y. Tang, Y. Wu, Z. Wang, J. Electrochem. Soc. 148 (2001) E133–E138.

[3] K.J. Vetter, Z. Elektrochem. 56 (1952) 797–806.

[4] J.M. Hale, R. Parsons, Trans. Faraday Soc. 59 (1963) 1429–1437.

[5] V.D. Parker, Electrochim. Acta 18 (1973) 519–524.

[6] E. Laviron, J. Electroanal. Chem. 164 (1984) 213–227.

[7] J.H. White, M.P. Soriaga, A.T. Hubbard, J. Electroanal. Chem. 85 (1985) 331–338.

[8] R.T. Robertson, B.D. Pendley, J. Electroanal. Chem. 374 (1994) 173–177.

[9] S.I. Bailey, I.M. Ritchie, Electrochim. Acta 30 (1985) 3–12.

[10] S. Wawzonek, R. Berkey, E.W. Blaha, M.E. Runner, J. Electrochem. Soc. 103 (1956) 456–459.

[11] I.M. Kolthoff, T.B. Reddy, J. Electrochem. Soc. 108 (1961) 980–985.

[12] W.R. Turner, P.J. Elving, J. Electrochem. Soc. 112 (1965) 1215–1217.

[13] V.J. Koshy, V. Swayambunathan, N. Periasamy, J. Electrochem. Soc. 127 (1980) 2761–2763.

[14] C. Rüssel, W. Jaenicke, J. Electroanal. Chem. 199 (1986) 139–151.

[15] R.D. Egeland, F. Marken, E.M. Southern, Anal. Chem. 74 (2002) 1590–1596.

[16] X.B. Ji, C.E. Banks, D.S. Silvester, A.J. Wain, R.G. Compton, J. Phys. Chem. C 111 (2007) 1496–1504.

[17] K. Aoki, J. Chen, Z. Hua, J. Electroanal. Chem. 610 (2007) 211–217.

[18] N. Gupta, H. Linschitz, J. Am. Chem. Soc. 119 (1997) 6384–6391.

[19] D. Pletcher, H. Thompson, J. Chem. Soc. Faraday Trans. 94 (1998) 3445–3450.

[20] Y.O. Kim, Y.M. Jung, S.B. Kim, S.M. Park, Anal. Chem. 76 (2004) 5236–5240.

[21] N.V. Rees, A.D. Clegg, O.V. Klymenko, B.A. Coles, R.G. Compton, J. Phys. Chem. B 108 (2004) 13047–13051.

[22] M.W. Lehmann, D.H. Evans, Anal. Chem. 71 (1999) 1947–1950.

[23] C.P. Andrieux, J.M. Savéant, J. Electroanal. Chem. 28 (1970) 339–348.

[24] E.O. Barnes, A.M. O'Mahony, S.R. Belding, R.G. Compton, J. Chem. Eng. Data ASAP article.

[25] S.R. Belding, R. Baron, E.J.F. Dickinson, R.G. Compton, J. Phys. Chem. C 113 (2009) 16042–16050.

[26] R.G. Evans, O.V. Klymenko, P.D. Price, S.G. Davies, C. Hardacre, R.G. Compton, ChemPhysChem 6 (2005) 526–533.

[27] D.H. Evans, Chem. Rev. 108 (2008) 2113–2144.

[28] R.G. Evans, O.V. Klymenko, S.A. Saddoughi, C. Hardacre, R.G. Compton, J. Phys. Chem. B 108 (2004) 7878–7886.

[29] D.S. Silvester, R.G. Compton, Z. Phys. Chem. 220 (2006) 1247–1274.

[30] D. Zigah, J. Ghilane, C. Lagrost, P. Hapiot, J. Phys. Chem. B 112 (2008) 14952–14958.

[31] D. Zigah, A. Wang, C. Lagrost, P. Hapiot, J. Phys. Chem. B 113 (2009) 2019–2023.

[32] P. Hapiot, C. Lagrost, Chem. Rev. 108 (2008) 2238–2264.

[33] E.I. Rogers, D.S. Silvester, D.L. Poole, L. Aldous, C. Hardacre, R.G. Compton, J. Phys. Chem. C 112 (2008) 2729–2735.

[34] R.G. Evans, O.V. Klymenko, C. Hardacre, K.R. Seddon, R.G. Compton, J. Electroanal. Chem. 556 (2003) 179–188.

[35] J. Ghilane, C. Lagrost, P. Hapiot, Anal. Chem. 79 (2007) 7383–7391.

[36] M.C. Buzzeo, O.V. Klymenko, J.D. Wadhawan, C. Hardacre, K.R. Seddon, R.G. Compton, J. Phys. Chem. A 107 (2003) 8872–8878.

[37] M.M. Islam, T. Ohsaka, J. Phys. Chem. C 112 (2008) 1269–1275.

[38] P. Bonhôte, A.P. Dias, N. Papageorgiou, K. Kalyanasundaram, M. Grätzel, Inorg. Chem. 35 (1996) 1168–1178.

[39] U. chröder, J.D. Wadhawan, R.G. Compton, F. Marken, P.A.Z. Suarez, C.S. Consorti, R.F. de Souza, J. Dupont, J. New J. Chem. 24 (2000) 1009–1015.

[40] T.W. Rosanske, D.H. Evans, J. Electroanal. Chem. 72 (1976) 277–285.

[41] R.D. Martin, P.R. Unwin, Anal. Chem. 70 (1998) 276–284.

[42] D.R. Lide, (Ed.), Handbook of Chemistry and Physics., 76th edn., CRC Press, Boca Raton, FL., 1996.

[43] M.C. Lagunas, W.R. Pitner, J.A. van den Berg, K.R. Seddon, ACS Symp. Ser. 856 (2003) 421–438.

[44] C. Russell, W. Janicke, J. Electroanal. Chem. 199 (1986) 139–151.

Chapter 6 A Kinetic and Mechanistic Study of the Electrochemical Oxidation of Hydroquinone in 1-Ethyl-3-methylimidazolium bis(trifluoromethanesulfonyl)imide, $[C_2mim][NTf_2]$

The work presented in this chapter was carried out in collaboration with

- **S.R. Belding** (for the theory and modelling parts)

and has been published in:

Y. Wang, S.R. Belding, E.I. Rogers, R.G. Compton, J. Electroanal. Chem. 650 (2011) 196–204

This chapter serves a further introduction of the application of RTILs in electrochemical analysis. Unlike the previous chapter mainly studying one-electron transfer processes, the topic of this chapter is investigating a two-electron transfer process followed by a separate chemical reaction. This chapter serves as a new insight into the application of RTILs in electrochemical analysis for more complex cases in the future.

The kinetics and mechanism of the oxidation of hydroquinone is studied in the room temperature ionic liquid 1-ethyl-3-methylimidazolium bis(trifluoromethanesulfonyl)imide, $[C_2mim][NTf_2]$. The two-electron transfer oxidation is shown to lead to the rapid release of two protons and the formation of benzoquinone which can be reduced itself at sufficient negative potentials. Tafel analysis and simulation show that the second electron transfer is rate determining. The protons lost are shown to associate with the anion of the RTIL leading to the reduction of bistrifluoromethanesulfonimide, $HNTf_2$ acid. This species can also undergo reduction on the reverse voltage sweep.

6.1 Introduction

The hydroquinone|benzoquinone system is of considerable importance as a model redox system not least as a basis for understanding several biological quinonoid systems and because the uptake|loss of electrons is coupled to protonation and deprotonation events.

6.1.1 Electro-oxidation of Hydroquinone in Aqueous Solutions

The electro-oxidation of hydroquinone (QH_2) in aqueous solution has been extensively researched [1–12]. The reaction mechanism was suggested as a heterogeneous two-electron oxidation (structures shown in Figure 6.1) [1]:

$$QH_2 - e^- \rightarrow QH_2^{+\bullet} \tag{6.1}$$

$$QH_2^{+\bullet} - e^- \rightarrow QH_2^{2+} \tag{6.2}$$

$$QH_2^{2+} \rightarrow Q + 2H^+ \tag{6.3}$$

This scheme is widely accepted, however, the detailed processes and kinetics can be influenced by different electrode materials as well as the modification of electrode.

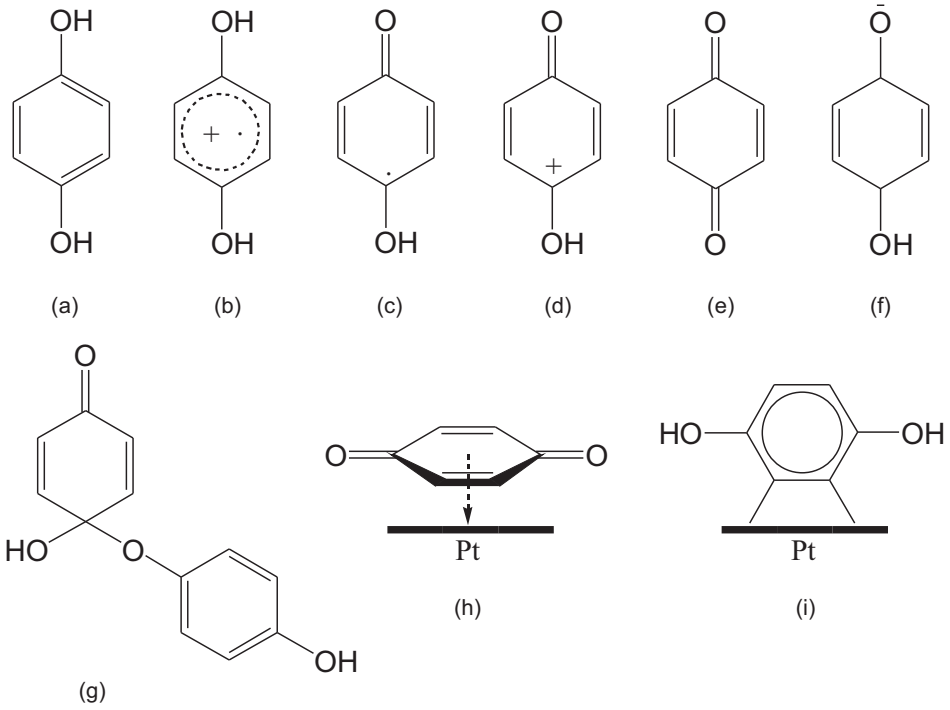


Figure 6.1: Structures of hydroquinone and its intermediates: (a) QH_2, (b) $QH_2^{+\bullet}$, (c) $QH^{\bullet}$, (d) QH^+, (e) Q, (f) QH^-, (g) $(QH)_2$, (h) Q adsorbed on Pt via a π bond, and (i) hydroquinone adsorbed on Pt via two σ bonds having lost two H atoms from C [13].

Platinum (Pt) electrodes were often chosen as the working electrode for electrochemistry of QH_2. However, many studies showed that the oriented adsorption of QH_2 on Pt could result in large differences of electrode kinetics and mechanisms [2, 3]. In addition, different ways of adsorption under various conditions made the situation more complicated. Soriaga *et al.* [2] reported that at low concentrations, QH_2 was adsorbed in a flat orientation (η^6, π-bonded attachment) releasing two $H^{\bullet}$ from O-H bonds to form quinone (Q), while when the concentration was increased, vertical edgewise-adsorption (η^2, di-σ attachment) by two H-Pt σ bonds became favorable, after which two $H^{\bullet}$ were released by breaking two C-H bonds to form Pt-C bonds. The suggested adsorption mechanisms at different concentrations were [3]:

$$(QH_2)_{aq} \xrightarrow{c \leq 0.1mM} (QH_2)_{ads} \tag{6.4}$$

$$(QH_2)_{ads} \rightarrow Q - Pt + 2H^{\bullet} \tag{6.5}$$

$$2H^{\bullet} \rightleftharpoons H_2 \tag{6.6}$$

at low concentration and for higher concentrations:

$$(QH_2)_{aq} \xrightarrow{c \geq 1mM} (QH_2)_{ads} \tag{6.7}$$

$$(QH_2)_{ads} \rightarrow QH_2 - Pt + 2H^{\bullet} \tag{6.8}$$

$$2H^{\bullet} \rightarrow H_2 \tag{6.9}$$

Gold (Au) electrodes have also been employed. QH_2 is known to absorb on Au surface as well [4, 14]. Baltruschat *et al*. examined this adsorption by spectroscopic techniques and suggested that QH_2 was adsorbed on Au via π electrons, they also found that there was no adsorbate as an intermediate (which can be found on Pt electrodes) during oxidation [14]. Almeida *et al*. pointed out these adsorptions were very slow processes replacing solvent molecules adsorbed on gold [4].

Plieth *et al*. examined the redox behaviour in a hydroquinone solution at mercury (Hg) electrodes, and suggested that the oxidation reaction can also be inhibited by adsorption. They carried out experiments based on those of platinum electrodes, and the suggested oxidation mechanism was as following [5]:

$$QH_2 \rightleftharpoons (QH_2)_{ads} \tag{6.10}$$

$$(QH_2)_{ads} \rightleftharpoons (QH)_{ads} + H^+ + e^- \tag{6.11}$$

$$(QH)_{ads} \rightleftharpoons (Q)_{ads} + H^+ + e^- \tag{6.12}$$

$$(Q)_{ads} \rightleftharpoons Q \tag{6.13}$$

although the detailed processes were not mentioned.

Karunina *et al*. used a nickel electrode to carry out similar studies on electro-oxidation of QH_2,

and found that different nickel oxides (Ni_2O_3, Ni_3O_4, etc.) can be formed on the electrode surface, which may change the shape and the position of the observed voltammetric peaks [6].

Electrodes made of other materials, for example, glassy carbon electrodes [7], diamond electrodes [8], polypyrrole and poly-*N*-methylpyrrole electrodes [11], and their modified electrodes [8–10] were also studied and different kinetics as well as mechanisms were found. In addition, experimental conditions such as, electrode aging [11], pH values [6] and micellar effects [12] were also found to influence the electrochemical behaviour of QH_2.

6.1.2 Electro-oxidation of Hydroquinone in Acetonitrile

The electrochemical behaviour of hydroquinone in aprotic solvents such as acetonitrile (MeCN) is complicated and not yet fully studied. Current understanding mainly comes from the early research by Eggins [15, 16]. Since the oxidation of hydroquinone as well as the corresponding reduction reactions are usually associated with the loss of protons, the mechanisms can differ according to different conditions at the presence or absence of basic molecules

The oxidation of hydroquinone in acetonitrile could be understood as an irreversible two-electron step which produces the protonated quinone (QH^+, structure shown in Figure 6.1) as following [15]:

$$QH_2 \rightarrow QH^+ + H^+ + 2e^- \tag{6.14}$$

This mechanism was examined by low scan rate cyclic voltammetry [15]. However, Eggins found that when the scan rate was increased, there was a decrease of the oxidation peak height (which did not agree with the assumption of two-electron oxidation), and also, the reduction peak of QH^+ was replaced by a more cathodic-shifted peak. He explained this phenomenon by the following one-electron mechanism (structures shown in Figure 6.1) [17]:

$$QH_2 \rightleftharpoons QH_2^{+\bullet} + e^- \tag{6.15}$$

$$QH_2^{+\bullet} \rightarrow QH^{\bullet} + H^+ \tag{6.16}$$

$$2QH^{\bullet} \overset{\text{fast}}{\rightarrow} (QH)_2 \tag{6.17}$$

$$(QH)_2 \overset{\text{slow}}{\rightarrow} Q + QH_2 \tag{6.18}$$

$$Q + H^+ \rightleftharpoons QH^+ \tag{6.19}$$

In this case, when the scan rate is fast enough, since the slow formation of Q and QH_2, the reduction of QH_2 could be inhibited which explained the disappearance of the corresponding reduction peak [18]. As for the assignment of the new peak, there was no conclusion, but possible processes suggested were the reduction of Q or $(QH)_2$.

Furthermore, Astudillo and his co-workers confirmed the two-electron nature by coulometry, and they suggested another possible mechanistic route based on the former study [19]:

$$QH_2 \rightleftharpoons QH_2^{+\bullet} + e^- \tag{6.20}$$

$$QH_2^{+\bullet} \overset{CH_3CN}{\rightleftharpoons} QH^{\bullet} + CH_3CN(H^+) \tag{6.21}$$

$$QH^{\bullet} \rightleftharpoons QH^+ + e^- \tag{6.22}$$

$$QH^+ \rightleftharpoons Q(H^+) \tag{6.23}$$

As Equation 6.21 indicated, the reactivity of $QH_2^{+\bullet}$ could be largely influenced by protons. In order to study this influence, they also measured the voltammetry in the presence of 160 mM triflic acid (CF_3SO_3H). The result showed the reversibility was greatly increased, which could be explained by the following step replacing Equation 6.22 [20]:

$$QH^{\bullet} + QH_2^{+\bullet} \rightleftharpoons QH^+ + QH_2 \tag{6.24}$$

In this case, $QH_2^{+\bullet}$ could be stabilised in solution in the presence of excess $CH_3CN(H^+)$ (see Equation 6.21) and undergo a reaction with $QH^{\bullet}$ to form QH_2.

The activity of protons could also have influence on the reduction peaks. Eggins studied the different voltammograms of a 2 : 1 and a 1 : 1 mixture of perchloric acid to quinone, and suggested that in the presence of excess protons, the reduction underwent as following (structures shown in Figure 6.1) [17]:

$$Q + H^+ + e^- \rightarrow QH^\bullet \overset{e^-}{\rightarrow} QH^- \overset{H^+}{\rightarrow} QH_2 \tag{6.25}$$

When there was not enough acid, another peak was found in a more negative position, which could be suggested as the reduction of Q as the following scheme:

$$Q + e^- \rightleftharpoons Q^{-\bullet} \tag{6.26}$$

This mechanism was further confirmed by Parker who studied the voltammetry in presence of a base, 2, 6-lutidine, and found that only Q could be detected under either rapid or slow conditions [13].

In short, the reaction paths are highly related with the gain and loss of protons and donor and acceptor molecules in solution. In most electrochemical cases, electrolytes (which are necessary in acetonitrile and other aprotic solvents) may act as either donors or acceptors, which make the electrochemical reactions complicated and various under different conditions.

6.1.3 Electro-oxidation of Hydroquinone in Other Solutions

Ji and his co-workers investigated the kinetics of electro-oxidation of QH_2 in a propylene carbonate (PC) solution, and suggested the following mechanism:

$$QH_2 \overset{-2e^-}{\rightleftharpoons} QH_2^{2+} \tag{6.27}$$

They also suggested a framework of kinetic parameters (reaction rate: $k_s = 2.8 \times 10^{-7}$ cm s^{-1}, electron transfer rate: $\alpha = 0.5$, diffusion coefficient for QH_2: $D = 3.0 \times 10^{-10}$ m^2 s^{-1}) by simulation of the voltammetry. Voltammetric experiments were also carried out in dimethylformamide (DMF) and

room temperature ionic liquid (RTIL), 1-ethyl-3-methylimidazolium bis(trifluoromethylsulfonyl)imide ([C_2mim][NTf_2]) to explore the possibility of detecting ammonia [21], however, specific studies on kinetics and mechanisms in those or related solutions were not attempted.

It was widely reported that many species, for example, Cl_2 [22], NO_3^-, PCl_3 and $POCl_3$ [23], display remarkably different mechanisms in RTILs to conventional solvents. It is also possible that QH_2 may show different behaviours in RTILs. However, currently there is no report about electrochemical processes of the QH_2|Q redox couple in RTILs. Therefore, it is interesting to explore the electrochemistry of this redox in RTILs. In this chapter we attempt a quantitative mechanistic and kinetic study of QH_2 oxidation in the RTIL 1-ethyl-3-methylimidazolium bis(trifluoromethanesulfonyl)imide, [C_2mim][NTf_2].

6.2 Experimental

6.2.1 Chemical Reagents

Hydroquinone (QH_2, Sigma-Aldrich, 99 %), ferrocene ($Fe(C_5H_5)_2$, Aldrich, 98 %), tetra-*n*-butylammonium perchlorate (TBAP, Fluka, > 99 %), bistrifluoromethanesulfonimide ($HNTf_2$, Fluka, ≥ 95 %) and acetonitrile (MeCN, Fischer scientific, dried and distilled, > 99 %) were used directly, without further purification. 1-Ethyl-3-methylimidazolium bis(trifluoromethane -sulfonyl)imide ([C_2mim][NTf_2]) was prepared by the standard literature processes [24].

6.2.2 Instrumental

Hydroquinone solutions were prepared to a known concentration (*ca.* 20 mM) by dissolving solid directly into the RTIL, and stirred for *ca.* 2 hours before experiments in a sealed vial. A two-electrode set-up was applied in a T-cell. A small section of disposable pipette tip was modified on each electrode, into which 20 μL of solution was added. The working electrodes were inserted into the bottom of the T-cell, while a 0.5 mm diameter silver (Ag) wire was introduced from the top as a quasi-reference electrode. The T-cell was placed under vacuum for at least 90 minutes to remove atmospheric oxygen

and water impurities. All the experiments were performed within a Faraday cage thermostatted at 298 K.

6.3 Theory

6.3.1 Suggested Mechanism

A two-electron irreversible electro-oxidation with an following homogeneous chemical reaction was considered as the reaction mechanism at a microdisk electrode:

$$QH_2 - 2e^- \rightleftharpoons QH_2^{2+} \quad k^0{}_{QH_2|QH_2^{2+}},\ E^{0'}_{QH_2|QH_2^{2+}} \tag{6.28}$$

$$QH_2^{2+} + 2NTf^- \rightarrow 2HNTf_2 + Q \quad k_{QH_2^{2+}|HNTf_2} \tag{6.29}$$

$$HNTf_2 + e^- \rightleftharpoons H^\bullet + NTf^- \quad k^0{}_{HNTf_2|H^\bullet},\ E^{0'}_{HNTf_2|H^\bullet} \tag{6.30}$$

$$2H^\bullet \overset{\text{fast}}{\rightarrow} H_2 \quad k_{H^\bullet|H_2} \tag{6.31}$$

where $k^0{}_{QH_2|QH_2^{2+}}$ and $k^0{}_{HNTf_2|H^\bullet}$ are the heterogeneous rate constants for Equation 6.28 and 6.30, $E^{0'}_{QH_2|QH_2^{2+}}$ and $E^{0'}_{HNTf_2|H^\bullet}$ are the formal potentials for the corresponding steps, and $k_{QH_2^{2+}|HNTf_2}$ and $k_{H^\bullet|H_2}$ are the homogeneous rate constants for Equation 6.29 and 6.31.

6.3.2 Cyclic Voltammetric Simulation Techniques

We consider the mechanism denoted in Equation (6.28)–(6.31). A simulation program was written based on the theory in Appendix III. This program allowed input of a series of fixed or measured parameters, including the scan rate (v), start, vertex and end potentials (E_{start}, E_{vertex} and E_{end}), diffusion coefficients of species QH_2 and $HNTf_2$ (D_{QH_2} and D_{HNTf_2}), concentration of QH_2 (c_{QH_2}), electron transfer rates ($\alpha_{QH_2|QH_2^{2+}}$ and $\alpha_{HNTf_2|H^\bullet}$), and the electrode radius (r_d). The fit between experimental and theoretical voltammograms were achieved manually by varying other relevant kinetic and thermodynamic parameters including the diffusion coefficient of QH_2^{2+} ($D_{QH_2^{2+}}$), standard rate

constants ($k^0_{QH_2|QH_2^{2+}}$ and $k^0_{HNTf_2|H\bullet}$), formal potentials ($E^{0\prime}_{QH_2|QH_2^{2+}}$ and $E^{0\prime}_{HNTf_2|H\bullet}$), and the homogeneous rate constant of deprotonation ($k_{QH_2^{2+}|HNTf_2}$). These parameters were optimised until the best fit was gained over a range of scan rates.

6.4 Results and Discussion

6.4.1 Cyclic Voltammetry

A typical cyclic voltammogram for the electro-oxidation of 20 mM hydroquinone in [C_2mim][NTf_2] on a 10 μm diameter Au microdisk electrode at scan rates from 10 to 1000 mV s^{-1} is shown in Figure 6.2. The potential was scanned from -0.50 to 1.75 V *vs* a 0.5 mm diameter Ag wire quasi-reference electrode. A sharp large oxidation peak is seen with a peak potential, E_p of *ca.* + 1.40 V *vs* Ag, whilst a small, broad reduction wave is seen on the reverse, reductive scan.

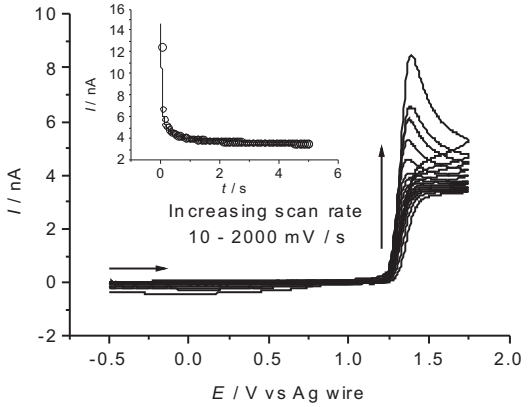


Figure 6.2: Cyclic voltammetry for the oxidation of QH_2 in [C_2mim][NTf_2] on a Au microdisk (10 μm diameter) at varying scan rates (10, 20, 40, 70, 100, 200, 400, 700, 1000 and 2000 mV s^{-1}) in the potential range -0.50 to -1.75 V. Inset is the experimental (—) and best-fit theoretical (○) chronoamperometric transient for the $QH_2|QH_2^{2+}$ redox couple in the same potential range.

It can be inferred from the shape of the peaks that the oxidation process exhibits a relatively fast electrode kinetics, and the reduction process possesses a much slower reaction rate. The absence of a corresponding reduction peak to the oxidation peak indicates a chemically irreversible oxidation. The cyclic voltammetry of a 5 mM $HNTf_2$ RTIL solution at the scan rate of 2000 mV s^{-1} compared to that of a 20 mM QH_2 solution is shown in Figure 6.3. It can be inferred, by comparing Figures 6.2 and 6.3, from the similar shape and position (-0.12 V for $HNTf_2$, and -0.16 V for QH_2) of the reduction

peak that the reduction in the solution was probably that from $HNTf_2$ to H_2. The similarity of the waves and the peak potentials of the $HNTf_2$ peak, and the peaks wave seen in Figure 6.2 suggest that the product of the QH_2 oxidation is $HNTf_2$:

$$2NTf_2^- + QH_2 - 2e^- \rightarrow Q + 2HNTf_2 \tag{6.32}$$

A Tafel plot of the reduction peak in the $HNTf_2$ solution is shown in Figure 6.4 compared with that obtained for the corresponding wave in Figure 6.2. Both plots suggest an irreversible electron transfer coefficient, $\alpha_{HNTf_2|H\bullet}$, of *ca.* 0.08, where

$$\text{flux} = k^0_{HNTf_2|H\bullet}\ [HNTf_2]_0\ \exp\left(-\frac{\alpha_{HNTf_2|H\bullet}F}{RT}(E - E^{0\prime}_{HNTf_2|H\bullet})\right) \tag{6.33}$$

where $[HNTf_2]_0$ denotes concentration at the electrode surface. Again the similarity of the data provides further evidence for the reaction proposed in Equation 6.32. Note that adsorbed quinone species are typically oxidised at lower potentials than solution phase species. In this study there was no evidence of adsorbed hydroquinone, implying such species are not formed, or their contribution is negligible.

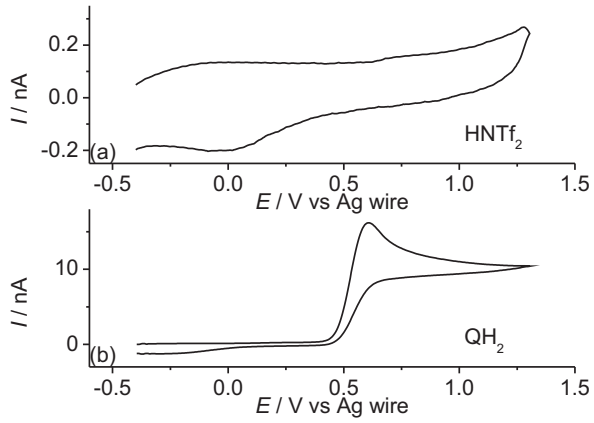


Figure 6.3: Cyclic voltammograms in [C_2mim][NTf_2] on a Au microdisk (10 μm diameter) at scan rate of 2000 mV s^{-1} for (a) 5 mM $HNTf_2$ and (b) 20 mM QH_2.

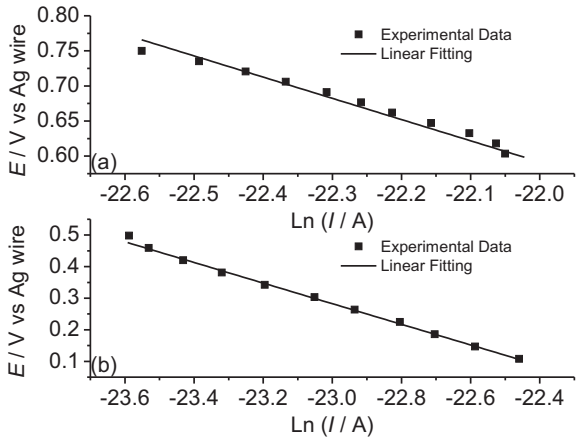


Figure 6.4: Tafel plot for reduction of (a) oxidised 20 mM QH_2 (measured on the cathodic scan of a CV such as shown in Figure 6.2) and (b) 5 mM $HNTf_2$ in [C_2mim][NTf_2] on a Au microdisk electrode(10 μm diameter).

6.4.2 Chronoamperometry

Next, chronoamperometry was performed to measure the diffusion coefficients for QH_2 (D_{QH_2}). First, the potential was held at 0.00 V for 20 seconds, and stepped to 1.50 V. The chronoamperometric transient (—) is given as an inset to Figure 6.2 with the best theoretical fit (○) by the Shoup and Szabo method (see Equations 2.4-2.6). The obtained D_{QH_2} value is 4.27 ± 0.03 × 10^{-11} m^2 s^{-1}, which is two orders of magnitude smaller than those obtained in water (2.26 × 10^{-9} m^2 s^{-1} [12]) and acetonitrile (3.16 ± 0.15 × 10^{-9} m^2 s^{-1} [17]), and about one order of magnitude smaller than in propylene carbonate (2.7 × 10^{-10} m^2 s^{-1} [25]). The slower diffusion in RTIL is reasonable regarding the high viscosity of [C_2mim][NTf_2] (34 cP at 298 K) [26] compared to water (0.89 cP) [27], acetonitrile (0.34 cP) [28], and PC (2.5 cP) [25] at 298 K.

The diffusion coefficient of $HNTf_2$ (D_{HNTf_2}) was also measured at 298 K in a [C_2mim][NTf_2] solution stepped from 1.50 V to -1.00 V (shown in Figure 6.5), and the obtained value was 3.75 ± 0.08 × 10^{-11} m^2 s^{-1}.

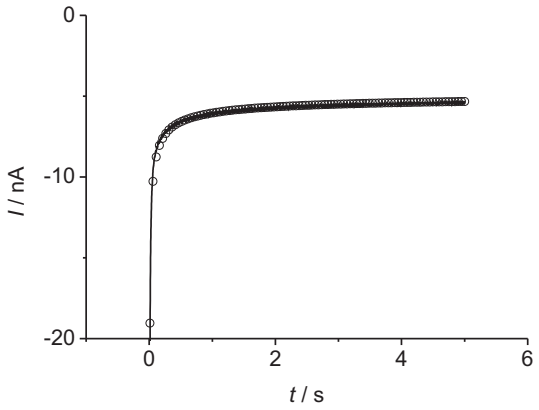


Figure 6.5: The experimental (—) and best-fit theoretical (∘) chronoamperometric transient for the reduction of $HNTf_2$ stepped to -1.00 V.

6.4.3 Interpreting and Simulating the Cyclic Voltammetry

Cyclic voltammetric simulation techniques were used to elucidate the kinetic and thermodynamic parameters for the entire electrode process using the known or pre-determined values for D_{QH_2}, D_{HNTf_2}, c_{QH_2} and $\alpha_{HNTf_2|H^\bullet}$.

For the reduction process:

$$HNTf_2 - e^- \rightarrow H^\bullet + {NTf_2}^- \tag{6.34}$$

corresponding to the cathodic scan in Figure 6.2 and 6.3, the voltammetry in Figure 6.3(a) as well as Figure 6.2 and Figure 6.3(b) were analysed to give a value of the component parameter,

$$k^0 \exp\left(+\frac{\alpha F}{RT}\ E^{0'}_{HNTf_2|H^\bullet}\right) \tag{6.35}$$

Note that this feature is entirely electrochemically irreversible the separate determination of k^0 and $E^{0'}_{HNTf_2|H^\bullet}$ is not possible.

Turning to the oxidation wave of QH_2, Figure 6.2 shows first that the peak potential, in the limit of planar diffusion (fast scan rates), is independent of scan rate, hinting at electrochemically reversible

behaviour. Second, the Tafel analysis in Figure 6.6 suggests a value of $\beta_{QH_2|QH_2{}^{2+}}$ of 1.53, where

$$\text{flux} = k^0_{QH_2|QH_2{}^{2+}} \left[[QH_2]_0 \exp\left(\frac{\beta F}{RT}(E - E^{0'}_{QH_2|QH_2{}^{2+}})\right) - [QH_2{}^{2+}]_0 \exp\left(\frac{-\alpha F}{RT}(E - E^{0'}_{QH_2|QH_2{}^{2+}})\right)\right] \tag{6.36}$$

and this suggests that the second electron transfer is rate determining:

$$QH_2 - e^- \overset{\text{fast}}{\rightleftarrows} QH_2{}^+ \underset{-e^-}{\overset{\text{slow}}{\rightarrow}} QH_2{}^{2+} \tag{6.37}$$

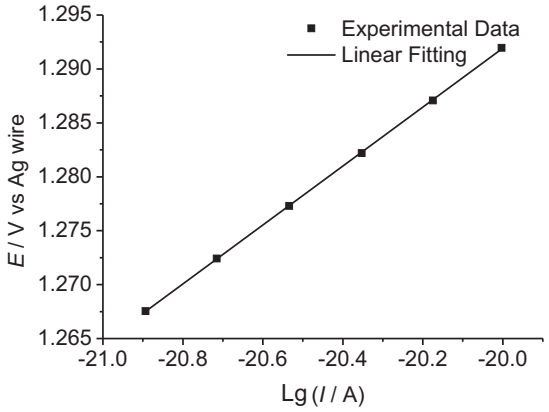


Figure 6.6: Tafel plot for oxidation of 20 mM QH_2 in [C_2mim][NTf_2] on a Au microdisk electrode(10 μm diameter).

Third, the slope of the voltammetry for the oxidation of QH_2 in Figure 6.2 is strongly indicative of fast ('reversible') electrode kinetics. The apparent contradiction between these three statements can be resolved [29] by the recognition that a fast follow up homogeneous chemical reaction subsequent to electron transfer can make a fast ('reversible') electron transfer appear irreversible in terms of its Tafel gradients; this can be understood because of the loss of [$QH_2{}^{2+}$] so that the second term in the kinetic equation above does not operate as [$QH_2{}^{2+}$] $\rightarrow 0$. This observation then reconciles the three observations above and also explains the absence of a back peak in the voltammetry of QH_2 corresponding to the oxidation peak. We thus propose the following kinetic scheme:

$$QH_2 - e^- \overset{\text{very fast}}{\rightleftharpoons} QH_2{}^+ \tag{6.38}$$

$$QH_2^+ - e^- \overset{\text{fast}}{\rightarrow} QH_2^{2+} \tag{6.39}$$

$$QH_2^{2+} + 2NTf_2^- \overset{\text{very fast}}{\rightarrow} Q + 2HNTf_2 \tag{6.40}$$

The formation of $HNTf_2$ is confirmed voltammetrically as discussed above. The formation of Q was demonstrated by cyclic voltammetry running to more negative potentials, on the reverse scan, than shown in Figure 6.2. Figure 6.7 shows a reduction peak at -0.40 V *vs* Ag correlating to the process

$$Q + e^- \rightleftharpoons Q^- \tag{6.41}$$

as confirmed by a separate experiment on the reduction of Q in the ionic liquid (a large 32 μm radius Au electrode was employed to gain larger signals and observe more clear reduction peaks).

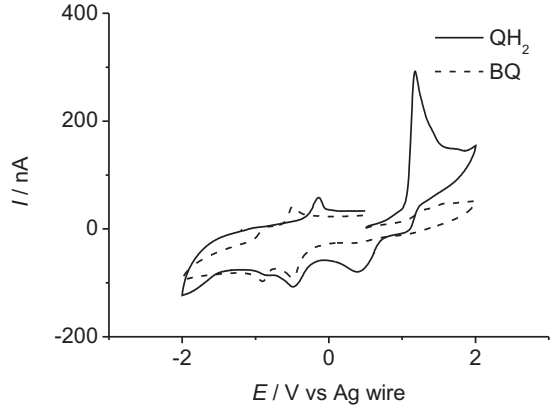


Figure 6.7: The cyclic voltammograms for the reduction of 40 mM oxidised QH_2 (solid) and BQ (dash) in [C_2mim][NTf_2] on a Au microdisk (32 μm diameter) at scan rate of 2000 mV s^{-1}.

Last, the cyclic voltammograms measured for the oxidation of QH_2 as a function of scan rate (10–2000 mV s^{-1}) were simulated using the above chemical model and the parameters in Table 6.1. Note that because of the fast following chemical reaction the determination of such parameters is necessarily approximate and these are marked as such in the table. In particular, unique fits cannot be guaranteed because of the large number of parameters to be fitted, but the level of agreement between simulation and experiment in Figure 6.8 is excellent, giving confidence in the reaction scheme proposed. Figures 6.9 and 6.10 show the effect of varying the electrochemical and homogeneous rate constant indicating

that despite the follow up kinetics there is a vestigial sensitivity to these parameters. However, the values should nevertheless be treated as highly approximate estimates.

Table 6.1: Parameters for electro-oxidation of QH_2 in [C_2mim][NTf_2] on a 10 μm diameter Au microelectrode from the best-fit cyclic voltammetric simulation fits shown in Figure 6.8, error bars were calculated from the standard deviation of the best theoretical fits of voltammograms at different scan rates. * denotes approximate values, probably not unique fits.

Parameter	Theoretical value
D_{QH_2} /m^2 s^{-1}	4.3 ($\pm$ 0.1) $\times$ 10^{-11}
$D_{QH_2{}^{2+}}$ /m^2 s^{-1}	$\sim$ 3.2 ($\pm$ 0.1) $\times$ 10^{-11*}
D_{HNTf_2} /m^2 s^{-1}	3.7 ($\pm$ 0.1) $\times$ 10^{-11}
$k^0_{QH_2\|QH_2^{2+}}$ /m s^{-1}	$\sim$ 3.3 ($\pm$ 0.1) $\times$ 10^{-4*}
$E^{0'}_{QH_2\|QH_2^{2+}}$ /V	$\sim$ 1.40 ($\pm$ 0.01)*
$\alpha_{QH_2\|QH_2^{2+}}$	0.50 ($\pm$ 0.01)
$\alpha_{HNTf_2\|H\bullet}$	0.08 ($\pm$ 0.01)
$k_{homo,QH_2^{2+}\|H^+}$ /s^{-1}	25000 ($\pm$ 5000)
$k^0 \exp\left(+\frac{\alpha F}{RT}\ E^{0'}_{HNTf_2\|H\bullet}\right)$ /m s^{-1}	3.3 $\times$ 10^{-5}

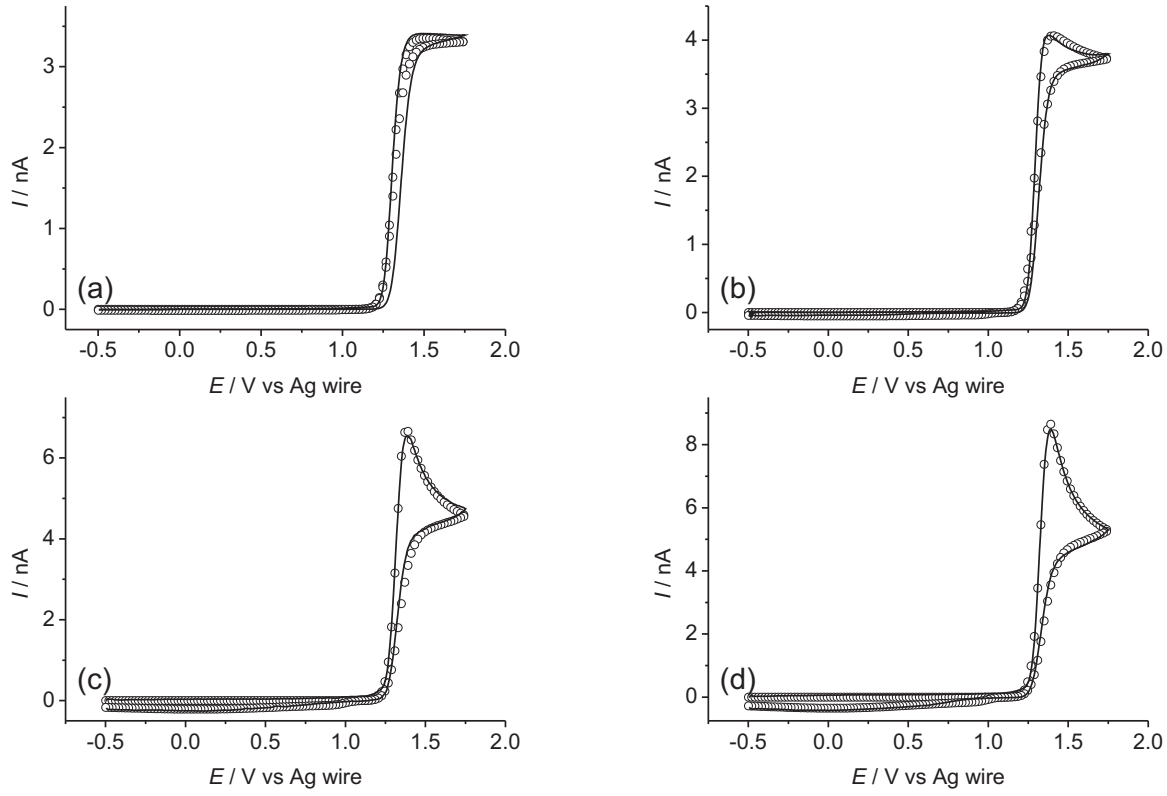


Figure 6.8: The experimental (—) and best-fit theoretical (○) cyclic voltammograms for the oxidation of QH_2 in [C_2mim][NTf_2] on a Au microdisk (10 μm diameter) at scan rate of (a) 10, (b) 100, (c) 1000, and (d) 2000 mV s^{-1}.

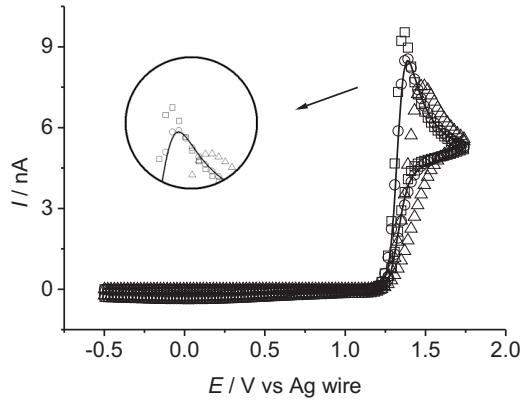


Figure 6.9: The experimental (—) and theoretical cyclic voltammograms for the oxidation of QH_2 in [C_2mim][NTf_2] on a Au microdisk (10 μm diameter) at scan rate of 2000 mV s^{-1} using the best-fit values in Table 6.1, with $k^0_{QH_2|QH_2^{2+}}$ = 3.30 × 10^{-3} (□), 3.30 × 10^{-4} (○) and 3.30 × 10^{-5} (△) m s^{-1}.

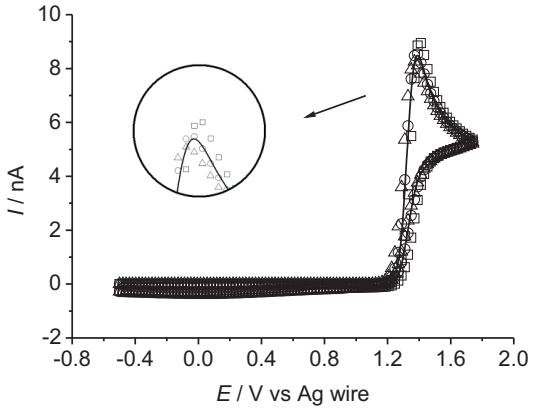


Figure 6.10: Examples of the fitting of experimental (—) and theoretical cyclic voltammograms for the oxidation of QH_2 in [C_2mim][NTf_2] on a Au microdisk (10 μm diameter) at scan rate of 2000 mV s^{-1} using the best-fit values in Table 6.1, with $k_{QH_2^{2+}|HNTf_2}$ = 2.50 × 10^3 (□), 2.50 × 10^4 (○) and 2.50 × 10^5 (△) s^{-1}.

6.5 Conclusions

The RTIL, [C_2mim][NTf_2], was demonstrated as a solvent to investigate mechanistic and kinetic properties of the electro-oxidation of hydroquinone. Chronoampreometric techniques were carried out to gain the diffusion coefficient of hydroquinone, which was found at 4.3 (± 0.07) × 10^{-11} m^2 s^{-1}. Cyclic voltammograms then were employed to suggest an EC mechanism.

The oxidation of the hydroquinone in [C_2mim][NTf_2] has been shown to be chemically irreversible with the formation of $HNTf_2$ and neutral p-benzoquinone. The electrode process shows relatively fast electrode kinetics with the second electron transfer rate limiting. The fast follow up deprotonation

reaction allows the transfer coefficient for the oxidation, of $\beta \cong 1.53$, to be inferred through simulation.

References

[1] Y.B. Vasil'ev, V.S. Bagotskii, Elektrokhimiya 1 (1965) 170.

[2] M.P. Soriaga, A.T. Hubbard, J. Am. Chem. 104 (1982) 3937–3945.

[3] V.K.F. Chia, M.P. Soriaga, A.T. Hubbard, J. Phys. Chem. 91 (1987) 78–82.

[4] N.V. Almeida, S.M. Esquenoni, A.E. Von Mengershausen, M.G. Sustersic, Informacion Tecnologica 11 (2000) 71–77.

[5] W.J. Plieth, I. Stellmecher, B. Quast, Electrochim. Acta 20 (1975) 335–340.

[6] O.V. Karunina, L.I. Skvortsova, V.N. Kiryushov, J. Anal. Chem. 64 (2007) 57–62.

[7] A.J.S. Ahammad, S. Sarker, M.A. Rahman, J.J. Lee, Electroanalysis 22 (2010) 694–700.

[8] R. Ramesham, M.F. Rose, J. Mater. Sci. Lett. 16 (1997) 1693–1699.

[9] M. Mercado, M. Rodríguez-López, O. López, G. Rodríguez, E.R. Fachini, P.T. Blanco, A. Carrasquillo Jr. 604 (2007) 26–32.

[10] S.A. Trammell, D.A. Lowy, D.S. Seferos, M. Moore, G.C. Bazan, N. Lebedev, J. Electroanal. Chem. 607 (2007) 33–38.

[11] R.C.M. Jakobs, L.J.J. Janssen, E. Barendrecht, Electrochim. Acta 30 (1985) 1313–1321.

[12] J. Peng, Z.N. Gao, Anal. Bioanal. Chem. 384 (2006) 1525–1532.

[13] V.D. Parker, Electrochim. Acta 18 (1973) 519–524.

[14] H. Baltruschat, N. Staud, J. Heitbaum, J. Electroanal. Chem. 239 (1987) 361–374.

[15] B.R. Eggins, J.Q. Chambers, Chem. Comm. 5 (1969) 232–233.

[16] B.R. Eggins, Chem. Comm. 21 (1969) 1267–1268.

[17] B.R. Eggins, J.Q. Chambers, J. Electrochem. Soc. 117 (1970) 186–192.

[18] R.E. Moser, D.G. Cassidy, J. Am. Chem. Soc. 87 (1965) 3463–3467.

[19] C.P. Andrieux, J.M. Savéant, J. Electroanal. Chem. 28 (1970) 339–348.

[20] C. Amatore, J.M. Savéant, J. Electroanal. Chem. 85 (1977) 27.

[21] D. Giovanelli, M.C. Buzzeo, N.S. Lawrence, C. Hardacre, K.R. Seddon, R.G. Compton, Talanta 62 (2004) 904–911.

[22] X.J. Huang, D.S. Silvester, I. Streeter, L. Aldous, C. Hardacre, R.G. Compton, J. Phys. Chem. C 112 (2008) 19477–19483.

[23] D.S. Silvester, E.I. Rogers, L.E. Barrosse-Antle, T.L. Border, R. Compton, J. Braz. Chem. Soc. 19 (2008) 611–620.

[24] P. Bonhôte, A.P. Dias, N. Papageorgiou, K. Kalyanasundaram, M. Grätzel, Inorg. Chem. 35 (1996) 1168–1178.

[25] X.B. Ji, C.E. Banks, D.S. Silvester, A.J. Wain, R.G. Compton, J. Phys. Chem. C 111 (2007) 1496–1504.

[26] R.G. Evans, O.V. Klymenko, C. Hardacre, K.R. Seddon, R.G. Compton, J. Electroanal. Chem. 556 (2003) 179–188.

[27] D.R. Lide, (Ed.), Handbook of Chemistry and Physics., 76th edn., CRC Press, Boca Raton, FL., 1996.

[28] H.G. Fernandez, M.A. Zon, J. Electroanal. Chem. 332 (1992) 237–255.

[29] I. Streeter, S.F. Jenkinson, G.W.J. Fleet, R.G. Compton, J. Electroanal. Chem. 600 (2007) 285–293.

Part IV Study of Weakly-supported Electrochemistry

Simple quantitative analysis of electrochemistry in conventional solvents considers mainly the diffusional behaviour of electroactive species and electron transfer processes, so that an excess amount supporting electrolyte should be added in order to reduce the Ohmic drop and diminish the contribution from the migration effect. However, recent studies show that the analysis of weakly supported systems can give several key insights into the kinetics and mechanisms that are unable to be revealed in fully supported solutions. Therefore, a strategy for quantitative analysis of weakly supported electrochemistry is developed and presented in this part of thesis.

Chapter 7 Voltammetry in the Absence of Excess Supporting Electrolyte - ECE-DISP1 Reactions: the Electrochemical Reduction of 2-Nitrobromobenzene in Acetonitrile Solvent

The work presented in this chapter was carried out in collaboration with

- **E.O. Barnes** (for the theory and modelling parts)

and has been published in:

E.O. Barnes, Y. Wang, J.G. Limon-Petersen, S.R. Belding, R.G. Compton, J. Electroanal. Chem. 659 (2011) 25–35

The reduction of 2-nitrobromobenzene in acetonitrile has been studied in the presence and near absence of supporting electrolyte at a mercury hemispherical microlectrode. In the presence of a high concentration of tetra-n-butylammonium perchlorate, voltammetric studies over a wide range of voltage scan rates spanning the transition from convergent to linear diffusion confirms the reduction mechanism as DISP1 (an EC process followed by a disproportionation reaction), rather than ECE, as previously thought by the majority of earlier studies. A rate constant of approximately 23 s^{-1} at 298K was inferred for the loss of bromide ion from the 2-nitrobromobenzene radical anion. In the presence of weak support, with concentration ratios of electrolyte to reactant of 5 and 0.5, the Nernst-Planck-Poisson system of equations were used to model the coupled diffusion-migration-reaction. It was found the both the mechanism of reaction and the derived homogeneous kinetics were unchanged in the near absence of supporting electrolyte.

7.1 Introduction

The reduction of aryl halides such as 2-nitrobromobenzene in acetonitrile has been widely studied and the difficulty in distinguishing between ECE and DISP1 processes, both generally and in this specific case, noted [1–4]. In particular a large variety of voltammetric techniques have been applied to this topic with many authors resorting to spectro-electrochemical methods to support their claims. In this chapter we address the problem in two separate and distinct approaches. First we study the reaction of 2-bromonitrobenzene at a mercury microhemisphere electrode over a very wide range of voltage scan rates encompassing the transition from convergent to linear diffusion and show that, if very precise experimental data is available, then an ECE/DISP1 disctinction *may* be visible on close examination of the reverse voltage scan, provided a wide scan rate range is available. Second, we consider the voltammetry under weakly supported conditions so that the effects of migration are added to the mass transport. All conclusions point to a DISP1 mechanism in the case of 2-nitrobromobenzene.

7.1.1 The ECE/DISP1 problem

The following mechanism is often encountered, especially when species 'A' is an aryl halide [3]

$$\mathrm{A} + \mathrm{e}^- \rightleftharpoons \mathrm{B} \qquad E^{0'}_{\mathrm{A/B}} \tag{7.1}$$

$$\mathrm{B} \rightleftharpoons \mathrm{C} + \mathrm{F} \tag{7.2}$$

$$\mathrm{C} + \mathrm{HS} \rightleftharpoons \mathrm{HC} + \mathrm{S} \tag{7.3}$$

$$\mathrm{HC} + \mathrm{e}^- \rightleftharpoons \mathrm{D} \qquad E^{0'}_{\mathrm{C/D}} \tag{7.4}$$

$$\mathrm{B} + \mathrm{HC} \rightleftharpoons \mathrm{A} + \mathrm{D} \tag{7.5}$$

$$\mathrm{S} + \mathrm{e} \rightleftharpoons \mathrm{G} \tag{7.6}$$

where species 'HS' corresponds to a solvent molecule. When $E^{0'}_{\mathrm{C/D}} > E^{0'}_{\mathrm{A/B}}$, all steps in this mechanism are thermodynamically, but not necessarily kinetically, viable. When steps 7.5 and 7.6 do not occur, the mechanism is denoted ECE. When step 7.4 and 7.6 do not occur, the mechanism is denoted DISP1 or

DISP2 depending on whether the rate determining step is step 7.2 or step 7.5 respectively. When step 7.5 does not occur but step 7.6 does, the mechanism is denoted ECEE [5]. Using classical voltammetric techniques, the DISP2 mechanism can be readily assigned [6]; however, the voltammetric discrepancy between ECE, DISP1 and ECEE is negligible when studied using cyclic voltammetry under linear diffusion conditions, and the unambiguous resolution of these mechanisms has been a long standing problem [1–4] in electrochemistry, leading researchers to often turn to non-voltammetric techniques, such as ESR [3], to complement the voltammetry.

In particular, the resolution of ECE and DISP1 mechanisms is most difficult [4, 7–10]. A range of voltammetric strategies have been used to make this distinction. The most common involve double potential step chronoamperometry [11] or the setting up of a competing homogeneous [11] or heterogeneous process [12]. Each technique capitalises on the fact that, although the starting materials and final products form the ECE and DISP1 processes are identical, the intermediates are not.

7.1.2 Weakly Supported Voltammetry

In a quiescent voltammetric experiment, there are two modes of mass transport: diffusion and migration. Diffusion is an entropically driven process and is undergone by any species in a liquid above absolute zero. In contrast, migration is exclusive to ions and can be suppressed by the addition of excess inert electrolyte ('supporting electrolyte'). These 'diffusion-only' systems are conventionally used by experimental electrochemists because the modeling is greatly simplified and the results are relatively easy to rationalise through the use of suitable equations and/or simulations [13–16]. However, it has been shown [17–22] that new mechanistic and chemical insights can be attained by studying such systems under a more complicated mass transport regime in which diffusion and migration occur concurrently. In this chapter we consider ECE and DISP1 processes in this light.

When the concentration of supporting electrolyte is high, the potential gradient is confined to within a region *ca.* 1 nm from the electrode surface and electrons can tunnel directly between the electrode and bulk solution. Therefore, at no point in the system does mass transport take place in the presence of a significant potential gradient: migration has been eliminated. Traditionally,

transient voltammetry is considered purely diffusional if the supporting electrolyte is present in a concentration greater than approximately 30 times that of the electroactive species [23]. However, recently Dickinson *et al.* [24] have shown that, in many cases, a factor of more than 100 is necessary for transient voltammetry; steady state voltammetry is more forgiving [23].

In this chapter we investigate the electro-reduction of 2-nitrobromobenzene under both full support and weak support, in each case over a wide range of scan rates, and see that a distinction *may* be made between an ECE and DISP1 mechanisms under certain conditions.

7.2 Experimental

7.2.1 Chemical Reagents

1-Bromo-2-nitrobenzene (*o*-BrNB, Aldrich, ≥99%), nitrobenzene (NB, Aldrich, 99%), tetra-*n*-butylammonium perchlorate (TBAP, Fluka, >99%), mercury(I) nitrate dihydrate ($Hg_2(NO_3)_2 \cdot 2H_2O$, Aldrich, ≥97%), nitric acid (HNO_3, Fischer scientific, 70%), ferrocene ($Fe(C_5H_5)_2$, Aldrich, 98%), acetonitrile (MeCN, Fischer scientific, dried and distilled, >99 %) and nitrogen (N_2, BOC Gases) were used as received, without further purification.

7.3 Results and Discussion

7.3.1 Experiments under full support

Experiments were carried out using a fully supported solution of nitrobenzene in acetonitrile containing 2 mM nitrobenzene and 100 mM TBAP as supporting electrolyte, where the concentration ratio of the supporting electrolyte to the electrochemical species (c_{sup}) was 50.

Cyclic voltammograms were first recorded to study the dynamics and confirm the mechanisms of reduction of nitrobenzene, which is widely accepted as a one electron reversible process in aprotic solvents [27–29]. To determine the diffusion coefficients for nitrobenzene and the nitrobenzene radical anion, D_{NB} and $D_{NB^{\bullet -}}$, double potential step chronoamperometric transients were measured for 5 s by stepping the potential from -0.5 V vs. Ag wire (where there was no faradaic current) to -1.2 V vs.

Ag wire, assuring the reduction was diffusion controlled. Then the potential was stepped back to -0.5 V vs. Ag wire for another 5 s. The first step current-time transient was analysed by the Shoup and Szabo method [30]. The diffusion coefficient for nitrobenzene, D_{NB}, was obtained by the best fit of the theoretical and the experimental transients.

The second step was fitted by a computer simulation program described by Klymenko *et al.*) [31]. The value of the diffusion coefficient for nitrobenzene, D_{NB}, was used as given by the first step fitting to get the diffusion coefficient for the nitrobenzene radical anion, $D_{\mathrm{NB}^{\bullet-}}$, by the best fit.

Figure 7.1 shows the fitting of the experimental (–) and the theoretical (○) transients, giving a D_{NB} value of 3.30 ± 0.05 × 10^{-9} m^2 s^{-1} which is similar compared to the literature value of 3.5 × 10^{-9} m^2 s^{-1} [32]. The obtained value for $D_{\mathrm{NB}^{\bullet-}}$ was 2.80 ± 0.05 × 10^{-9} m^2 s^{-1}. To the author's knowledge, there is no previous report about the diffusion coefficient for the nitrobenzene radical anion in acteonitrile solvent.

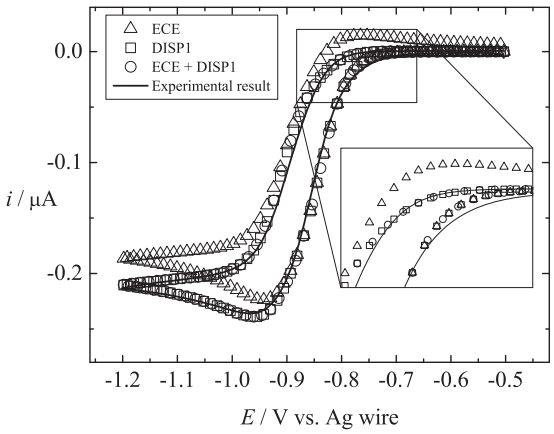


Figure 7.1: The experimental and theoretical cyclic voltammograms for the reduction of 2-nitrobromobenzene in acetonitrile on a Hg hemisphere electrode (25 μm radius) at the scan rate of 500 mV s^{-1} using the best-fit values in Table 7.2.

The commercial voltammetric simulation package DigiSim (version 3.0, BAS Technicol, USA, developed by Rudolph [33–37]) was employed to model the theoretical cyclic voltammograms by using the diffusion coefficients obtained by chronoamperometric fittings. The electrochemical kinetics were assumed to be infinitely fast (where $k^0_{\mathrm{NB/NB}^{\bullet-}}$ was fixed as 100 m s^{-1} which is artificially high to ensure full electrochemical reversibility, and the electron transfer coefficients, α and β, were both set as 0.5) because this reaction is considered as a highly electrochemically reversible process [27–29].

Figure 7.2 shows the the experimental (–) and the theoretical (∘) 1 electron reduction voltammograms of nitrobenzene over a range of different scan rates (50, 200 and 1000 mV s^{-1}). Good fits were obtained using the parameters listed in Table 7.1.

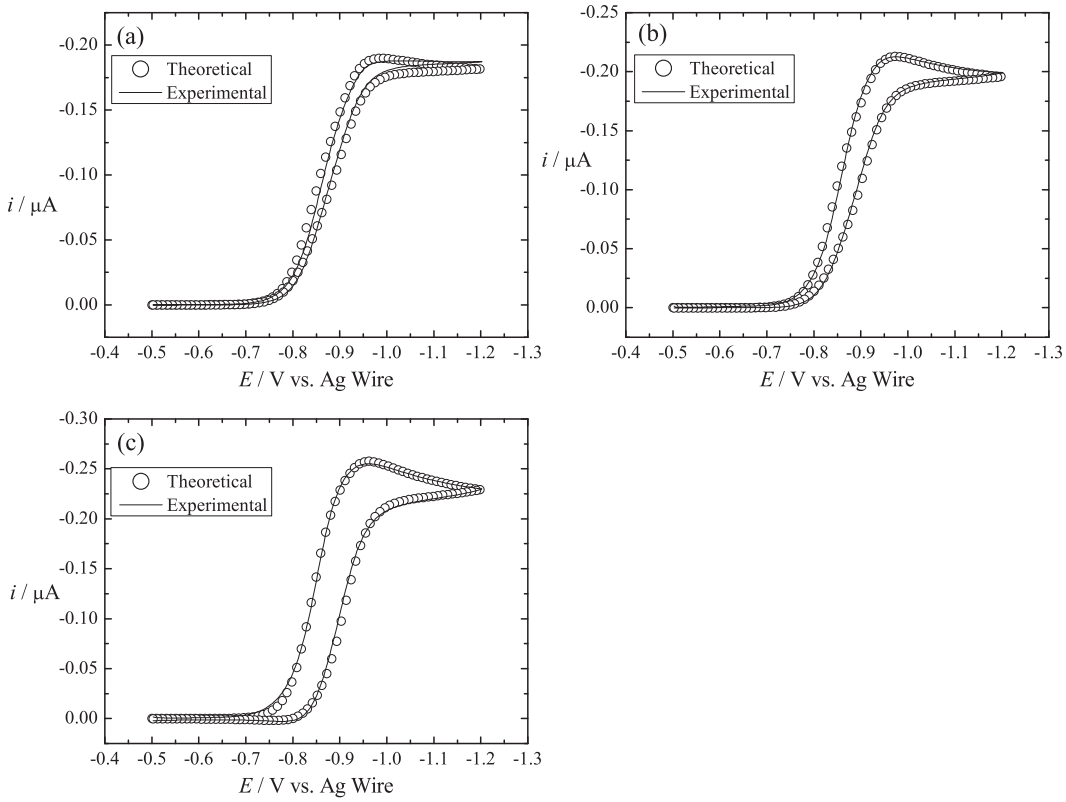


Figure 7.2: Experimental and theoretical cyclic voltammograms for a 2 mM 2-nitrobromobenzene solution in MeCN with 100 mM TBAP as supporting electrolyte using the parameters from Table 7.2. The potential was scanned from -0.5 to -1.2 and back to -0.5 V vs. Ag wire at the scan rates of: (a) 50 mV s^{-1}, (b) 200 mV s^{-1} and (c) 1000 mV s^{-1}.

Table 7.1: Parameters[a,b] for 2 mM nitrobenzene solutions in acetonitrile with with 100 mM, 10 mM and 1 mM TBAP as supporting electrolyte on a *ca.* 25 μm radius Hg hemisphere electrode from the best-fit cyclic voltammetric simulation fits shown in Figures 7.2, 7.3 and 7.4.

Parameter	Measured value		
	$c_{sup} = 50$	$c_{sup} = 5$	$c_{sup} = 0.5$
D_{NB} /m^2 s^{-1}	3.30 (± 0.04) × 10^{-9}	3.30 (± 0.03) × 10^{-9}	3.30 (± 0.04) × 10^{-9}
$D_{NB^{\bullet-}}$ /m^2 s^{-1}	2.77 (± 0.27) × 10^{-9}	2.87 (± 0.13) × 10^{-9}	3.20 (± 0.01) × 10^{-9}
$k^0_{NB\|NB^{\bullet-}}$ / m s^{-1}		∼100[c]	

[a] NB = nitrobenzene, $NB^{\bullet-}$ = nitrobenzene radical anion.
[b] Error bars were calculated from the standard deviation of the best theoretical fits from cyclic voltammograms at different scan rates.
[c] Set high to ensure the complete reversibility, probably not unique fit.

Over the years, there has been a literature controversy about the mechanism of the reduction of 2-nitrobromobenzene in acetonitrile [13, 28, 38–42]. Several different schemes including ECE, DISP1,

DISP2, and even [28] ECEE have been suggested, with ECE [38, 39] and DISP1 [40] being the most widely cited. These two mechanisms are summarised by reactions 7.1 to 7.5 above. Reactions 7.2 and 3 can be considered as a single pseudo first order reaction, since the solvent is present in large excess.

Cyclic voltammograms on the Hg hemisphere electrode were recorded to investigate the mechanism of the electrochemical reduction of 2-nitrobromobenzene in a fully supported acetonitrile solution (2 mM 2-nitrobromobenzene and 100 mM TBAP, $c_{\text{sup}} = 50$). Figure Appx III.5 in Appendix III shows the comparison of the voltammograms corresponding to a 2 mM 2-nitrobromobenzene solution, a 2 mM nitrobenzene solution and a mixed solution of 2 mM 2-nitrobromobenzene and 2 mM nitrobenzene (all supported by 100 mM TBAP) at the scan rate of 500 mV s^{-1}. The peak current of the 2-nitrobromobenzene reduction is approximately twice large as the one for the nitrobenzene reduction, which implies that it seems possible that the reduction process for 2-nitrobromobenzene involves two electron transfer processes and may include a nitrobenzene reduction step. However, the smaller back peak of the mixed solution compared to the nitrobenzene solution indicates that the presence of the parent 2-nitrobromobenzene does have an influence on the concentrations of the electroactive species, which gives indirect evidence of disproportionation. In addition, disproportionation can also increase the peak reduction current by making the concentration profile of nitrobenzene near the electrode surface steeper.

To study the mechanism, DigiSim was used to simulate the voltammograms assuming that both the nitrobenzene reduction step and the comproportionation step exist (ECE + DISP1). The best fit of the experimental and theoretical voltammograms of a solution of 2 mM 2-nitrobromobenzene supported by 100 mM TBAP in acetonitrile over a range of scan rates (50 to 1000 mV s^{-1}) was obtained, giving a framework of kinetic and dynamic parameters (given in Table 7.2). Then the ECE and DISP1 mechanisms were examined separately using the same parameters with the ECE + DISP1 best-fit ones (generated by the cyclic voltammetric fitting function available in DigiSim). A comparison of these three mechanisms is shown in Figure 7.1. There is no significant difference between the voltammograms of the ECE + DISP1 ($\circ$) and the DISP1 ($\square$) mechanism, while the

ECE (△) mechanism leads to a lower forward peak and a larger backward peak compared to the experimental data (–). Therefore, it is reasonable to suggest that 2-nitrobromobenzene probably undergoes a DISP1 mechanism in acetonitrile.

Table 7.2: Parameters[a] for 2 mM 2-nitrobromobenzene solutions in acetonitrile with 100 mM, 10 mM and 1 mM TBAP as supporting electrolyte on a *ca.* 25 μm radius Hg hemisphere electrode from the best-fit cyclic voltammetric simulation fits shown in Figures 7.2, 7.3 and 7.4 [b].

Parameter	Measured value		
	$c_{\text{sup}} = 50$	$c_{\text{sup}} = 5$	$c_{\text{sup}} = 0.5$
$D_{o-\text{BrNB}}$ /m^2 s^{-1}	3.10 (± 0.05) × 10^{-9}	3.10 (± 0.05) × 10^{-9}	3.10 (± 0.03) × 10^{-9}
$D_{o-\text{BrNB}^{\bullet-}}$ /m^2 s^{-1}	3.00 (± 0.05) × 10^{-9}	3.00 (± 0.05) × 10^{-9}	3.00 (± 0.04) × 10^{-9}
D_{NB} /m^2 s^{-1}	3.30 (± 0.04) × 10^{-9}	3.30 (± 0.03) × 10^{-9}	3.30 (± 0.04) × 10^{-9}
$D_{\text{NB}^{\bullet-}}$ /m^2 s^{-1}	2.80 (± 0.05) × 10^{-9}	2.87 (± 0.27) × 10^{-9}	3.13 (± 0.13) × 10^{-9}
k_{f} / s^{-1}		∼23[c]	

[a] *o*-BrNB = 2-nitrobromobenzene, *o*-BrNB$^{\bullet-}$ = 2-nitrobromobenzene radical anion, NB = nitrobenzene, NB$^{\bullet-}$ = nitrobenzene radical anion.
[b] Error bars were calculated from the standard deviation of the best theoretical fits from cyclic voltammograms at different scan rates.
[c] Approximate values, probably not unique fits.

The rate constant for the DISP step (k_{DISP}) was artificially set as 1 × 10^9 dm^3 mol^{-1} s^{-1} which is high enough to ensure fast disproportionation. The fitting of the experimental (–) and the theoretical voltammograms assuming DISP1 mechanism at different scan rates (50, 200 and 1000 mV s^{-1}) is shown in Figure 7.2, and the best-fit kinetic and dynamic parameters are summarised in Table 7.2. The homogeneous rate constant of the cleavage of the C-Br bond from the 2-nitrobromobenzene radical anion, k_{f} was determined as 23 (± 5) s^{-1}, which has an excellent agreement with the literature values around 20 s^{-1} [39, 42]. The obtained diffusion coefficient for 2-nitrobromobenzene, $D_{o-\text{BrNB}}$, of 3.10 (± 0.05) × 10^{-9} m^2 s^{-1} is close to the literature value of 2.80 (± 0.20) × 10^{-9} m^2 s^{-1} suggested by Svir *et al* [39].

7.3.2 Experiments under weak support

To study the weakly supported systems, solutions containing 2 mM nitrobenzene supported by 10 mM and 1 mM TBAP (concentration ratios of supporting electrolyte to electroactive species of $c_{sup} = 5$ and 0.5 respectively) in acetonitrile were made. Cyclic voltammograms were measured by scanning from -1.0 to -1.7 then back to -1.0 V vs. Ag wire for the solution with a c_{sup} value of 5, and from

-0.9 to -1.4 then back to -0.9 V vs. Ag wire for the one where c_{sup} value was 0.5 over a range of scan rates (50 to 1000 mV s^{-1}). The voltammograms are shown in Figures 7.3 and 7.4. It is observed that the peak to peak separation increases as c_{sup} decreases. For instance, at the scan rate of 1000 mV s^{-1}, the peak to peak separation is equal to 0.09 V when c_{sup} is 50, and it rises to 0.12 V and 0.22 V when the c_{sup} value goes down to 5 and 0.5 respectively. Also, the peak current of the reduction peak diminishes from -0.19 μA to -0.16 μA as the decrease c_{sup}. Both of the phenomena can be considered as the evidence of Ohmic drop and migration [24].

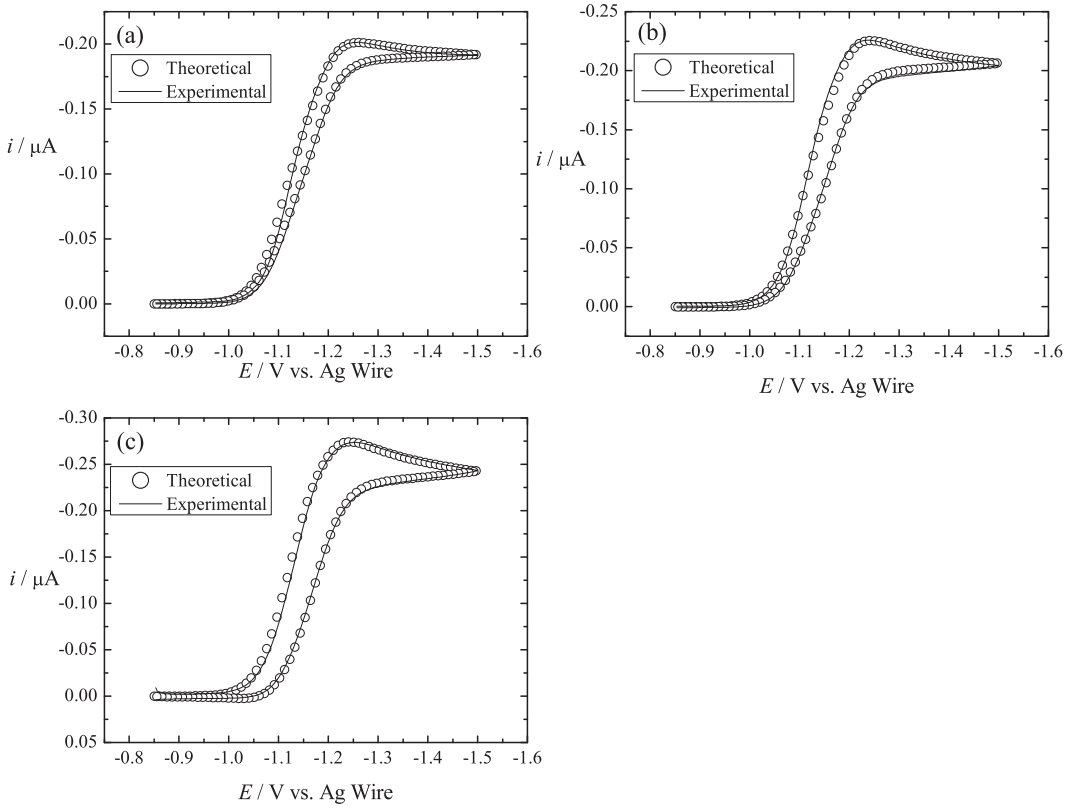


Figure 7.3: Experimental and theoretical cyclic voltammograms for a 2 mM 2-nitrobromobenzene solution in MeCN with 10 mM TBAP as supporting electrolyte using the parameters from Table 7.2. The potential was scanned from -0.9 to -1.5 and back to -0.9 V vs. Ag wire, at the scan rates of: (a) 50 mV s^{-1}, (b) 200 mV s^{-1} and (c) 1000 mV s^{-1}.

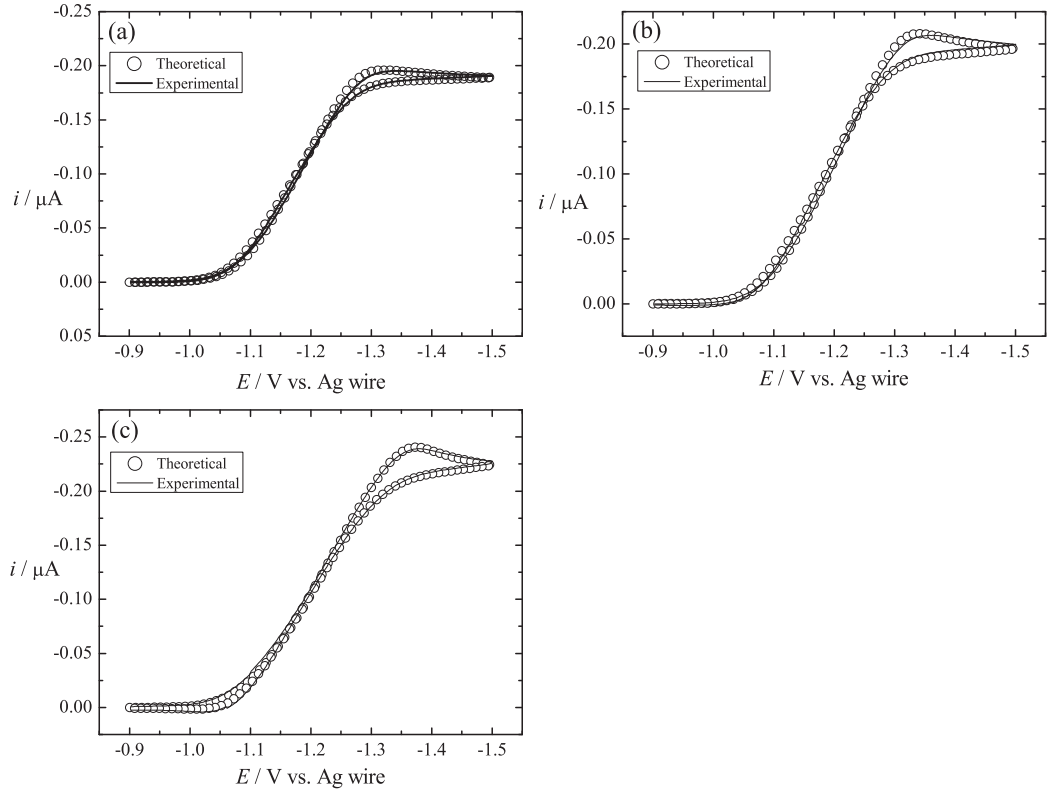


Figure 7.4: Experimental and theoretical cyclic voltammograms for a 2 mM 2-nitrobromobenzene solution in MeCN with 1 mM TBAP as supporting electrolyte using the parameters from Table 7.2. The potential was scanned from -0.9 to -1.5 and back to -0.9 V vs. Ag wire, at the scan rates of: (a) 50 mV s^{-1}, (b) 200 mV s^{-1} and (c) 1000 mV s^{-1}.

The theoretical voltammograms were modeled by a computer program based the theory described in Appendix IV. Literature values of the diffusion coefficients for the TBAP ions, $D_{\mathrm{TBA^+}}$ of 0.68 $\times$ 10^{-9} m^2 s^{-1}, and $D_{\mathrm{ClO_4^-}}$ of 2.35 $\times$ 10^{-9} m^2 s^{-1} [43] were used in the modeling. A literature value for the relative permittivity of the solvent (ϵ_r) of 37.5 [44] was also used, and all the other parameters were consistent with those obtained in the fully supported system as shown in Table 7.1.

Furthermore, cyclic voltammograms were obtained to study the 2-nitrobromobenzene system under weak support. Solutions with 2 mM 2-nitrobromobenzene in acetonitrile supported by 10 mM and 1 mM TBAP ($c_{\mathrm{sup}} = 5$ and 0.5) were made and measured by scanning from -0.9 to -1.4 and back to -0.9 V vs. Ag wire. A modeling program based on the theory explained in Appendix IV was employed to obtain the theoretical voltammograms with the parameters summarised in Table 7.2, which agree well with the fully supported system and the weakly supported nitrobenzene system, including the homogeneous rate constant of 23 ($\pm$ 5) s^{-1}. The fitting of the experimental (–) and the theoretical

(○) voltammograms over a range of different scan rates (50, 200 and 1000 mV s^{-1}) is shown in Figures 7.3 and 7.4.

7.4 Conclusions

The electro-reduction of 2-nitrobromobenzene in acetonitrile solutions was studied at a mercury hemispherical microelectrode. To clarify its ambiguous mechanism, either an ECE or a DISP1 process, simulated voltammetric responses of these two mechanisms were compared at high support. By comparing the responses at a variety of scan rates, it is found that under some kinetic conditions, where the fragmentation step occurs on a similar timescale to the experiment, a distinction can be made between the mechanistic limits by careful examination of the reverse voltammetric wave. The process was repeated under conditions of low support, and no new distinctions were apparent, due to identical charges of both electro-active species in the ECE limit: migration effects are the same for each mechanism.

The electrochemical reduction of 2-nitrobromobenzene was carried out at various support ratios, and theoretical results were fitted to the experimental data. A DISP1 mechanisms was inferred, with a rate constant for the fragmentation step of approximately $23 \pm 5\ s^{-1}$, in good agreement with existing literature. Both the mechanism of the reaction and the homogeneous kinetics were found to be consistent over the range of support ratios and scan rates investigated.

References

[1] J.D. Wadhawan, P.J. Welford, E. Maisonhaute, V. Climent, N.S. Lawrence, R.G. Compton, H.B. McPeak, C.E.W. Hahn, J. Phys. Chem. B 105 (2001) 10659–10668.

[2] M.C. Buzzeo, O.V. Klymenko, J.D. Wadhawan, C. Hardacre, K.R. Seddon, R.G. Compton, J. Phys. Chem. B 108 (2004) 3947–3954.

[3] R.G. Compton, R.A.W. Dryfe, J. Electroanal. Chem. 375 (1994) 247 – 255.

[4] R.G. Compton, R.G. Harland, P.R. Unwin, A.M. Waller, J. Chem. Soc., Faraday Trans. 1 83 (1987) 1261–1268.

[5] A.C. Testa, W.H. Reinmuth, Anal. Chem. 33 (1961) 1320–1324.

[6] R. Mueller, L. Lamberts, M. Evers, J. Electroanal. Chem. 417 (1996) 35 – 43.

[7] C. Amatore, J. Savéant, J. Electroanal. Chem. 86 (1978) 227 – 232.

[8] R.G. Compton, P.J. Daly, P.R. Unwin, A.M. Waller, J. Electroanal. Chem. 191 (1985) 15 – 29.

[9] M. Fleischmann, F. Lasserre, J. Robinson, J. Electroanal. Chem. 177 (1984) 115 – 127.

[10] L.S. Marcoux, R.N. Adams, S.W. Feldberg, J. Phys. Chem. 73 (1969) 2611–2614.

[11] L. Nadjo, J.M. Savéant, J. Electroanal. Chem. 33 (1971) 419 – 451.

[12] P.R. Unwin, J. Electroanal. Chem. 297 (1991) 103 – 124.

[13] R.G. Compton, C.E. Banks, Understanding Voltammetry, 2nd edn., Imperial College Press, 2010.

[14] A.C. Fisher, Electrode Dynamics, Oxford University Press, New York, 1996.

[15] A.J. Bard, L.R. Faulkner, Electrochemical Methods, Fundamentals and Applications, 2nd edn., John Wiley & Sons Inc., Hoboken, NJ, 2001.

[16] J. Wang, Analytical Electrochemistry, 2nd edn., John Wiley & Sons, New Jersey, 1994.

[17] S.R. Belding, J.G. Limon-Petersen, E.J.F. Dickinson, R.G. Compton, Angew. Chemie Int. Ed. 49 (2010) 9242–9245.

[18] O.V. Klymenko, C. Amatore, I. Svir, Anal. Chem. 79 (2007) 6341–6347.

[19] C. Amatore, M.R. Deakin, R. Wightman, J. Electroanal. Chem. 225 (1987) 49 – 63.

[20] C. Amatore, B. Fosset, J. Bartelt, M. Deakin, R. Wightman, J. Electroanal. Chem. 256 (1988) 255–268.

[21] A.M. Bond, D.C. Coomber, S.W. Feldberg, K.B. Oldham, T. Vu, Anal. Chem. 73 (2001) 352–359.

[22] J.B. Cooper, A.M. Bond, K.B. Oldham, J. Electroanal. Chem. 331 (1992) 877–895.

[23] K.B. Oldham, C.G. Zoski, C.H. Bamford, R.G. Compton (Eds.) Comprehensive Chemical Kinetics, vol. 26, 122, Elsevier, Amsterdam, The Netherlands (1986) .

[24] E.J.F. Dickinson, J.G. Limon-Petersen, N.V. Rees, R.G. Compton, J. Phys. Chem. C 113 (2009) 11157–11171.

[25] M. Sharp, Electrochim. Acta 28 (1983) 301–308.

[26] J. Mauzeroll, E.A. Hueske, A.J. Bard, Anal. Chem. 75 (2003) 3880–3889.

[27] P. Morkovska, M. Hromadova, L. Pospisil, S. Giannarelli, Langmuir 22 (2006) 1896–1902.

[28] M. Bento, M. Medeiros, M. Montenegro, C. Beriot, D. Pletcher, J. Electroanal. Chem. 345 (1993) 273 – 286.

[29] J.G. Lawless, M. Hawley, J. Electroanal. Chem. 21 (1969) 365 – 375.

[30] D. Shoup, A. Szabo, J. Electroanal. Chem. 140 (1982) 237–245.

[31] O.V. Klymenko, R.G. Evans, C. Hardacre, I.B. Svir, R.G. Compton, J. Electroanal. Chem. 571 (2004) 211–221.

[32] S.R. Ragsdale, H.S. White, J. Electroanal. Chem. 432 (1997) 199 – 203.

[33] M. Rudolph, J. Electroanal. Chem. 314 (1991) 13–22.

[34] M. Rudolph, J. Electroanal. Chem. 338 (1992) 85–98.

[35] M. Rudolph, D.P. Reddy, S.W. Feldberg, Analytical Chemistry 66 (1994) 589A–600A.

[36] W. Luo, S.W. Feldberg, M. Rudolph, J. Electroanal. Chem. 368 (1994) 109–113.

[37] M. Rudolph, J. Electroanal. Chem. 375 (1994) 89–99.

[38] A.J. Wain, R.G. Compton, J. Electroanal. Chem. 587 (2006) 203 – 212.

[39] I. Svir, A. Oleinick, K. Yunus, A.C. Fisher, J.D. Wadhawan, T.J. Davies, R.G. Compton, J. Electroanal. Chem. 578 (2005) 289 – 299.

[40] W.M. Leslie, J.A. Alden, R.G. Compton, T. Silk, J. Phys. Chem. 100 (1996) 14130–14136.

[41] R.G. Compton, R. Wellington, P.J. Dobson, P.A. Leigh, J. Electroanal. Chem. 370 (1994) 129 – 133.

[42] R.F. Nelson, A.K. Carpenter, E.T. Seo, J. Electrochem. Soc. 120 (1973) 206–210.

[43] J. Szymanska, M.J. Palys, B. van den Bossche, Anal. Chem. 76 (2004) 5937–5944.

[44] G. Ritzoulis, N. Papadopoulos, D. Jannakoudakis, J. Chem. Eng. Data 31 (1986) 146–148.

Chapter 8 New Chemical Insights Using Weakly Supported Voltammetry: Ion Pairing in the EC_2 Reduction of 2,6-Diphenylpyrylium in Acetonitrile

The work presented in this chapter was carried out in collaboration with

- **E.O. Barnes and S.R. Belding** (for the theory and modelling parts)

and has been published in:

E.O. Barnes, Y. Wang, S.R. Belding, R.G. Compton, ChemPhysChem 13 (2012) 92–95

After we confirmed the theory and application of using low-support system to investigate the complex mechanism, DISP1, the chapter mainly focuses on a new chemical insight, the examination of ion-pairing effect for an electrochemical process. Unlike the previous chapter, low-support studies provides an unique tool to investigate this effect, which can hardly achieved by traditional full-support electrochemical studies. This may expand the application of electroanalytical techniques with weak support.

Varying the concentration of support electrolyte in the electrochemical EC_2 reduction of 2,6-diphenylpyrylium reveals the presence of ion pairing between the electroactive species and BF_4^-. Experiment and theory are shown to be in good agreement only if ion pairing is included in the simulations. This previously unanticipated effect is only observable if voltammetry is performed under conditions of weak support.

8.1 Introduction

Voltammetry is usually carried out in the presence of a large excess of added supporting electrolyte. This serves to compress the generated electric field to a region very close to the electrode surface so

that electron transfer can take place via quantum mechanical tunneling through this field. This eliminates migration effects and 'diffusion-only' voltammetry is observed. However, it has very recently been suggested [1] that performing cyclic voltammetry in the presence of varying concentrations of supporting electrolyte, from a large excess to very little, can reveal quantitative mechanistic information not observable in diffusion-only conditions. This chapter builds on early empirical and/or qualitative work by others [2–5] and reports new insights arising from such experiments.

8.2 Experimental

8.2.1 Chemical Reagents

Tetra-*n*-butylammonium tetrafluoroborate ($NBu_4^+BF_4^-$, Fluka, >98%), mercury(I) nitrate dihydrate ($Hg_2(NO_3)_2 \cdot 2H_2O$, Aldrich, ≥97%), nitric acid (HNO_3, Fischer scientific, 70%), ferrocene ($Fe(C_5H_5)_2$, Aldrich, 98%), acetonitrile (MeCN, Fischer scientific, dried and distilled, >99 %) and nitrogen (N_2, BOC Gases) were used as received, without further purification. 2,6-Diphenlypyrylium tetrafluoroborate ($DDP^+BF_4^-$) was synthesised using a previously described method [7], by crystallising the product from a heated solution of 5.9 mM 1,3-dibenzoylpropane, 5.9 mM *trans*-chalcone and 4.3 mL boron trifluoride diethyletherate.

8.2.2 Instrumental

A two electrode cell was used, with a silver wire used as a quasi counter/reference electrode. A 25 μm mercury hemisphere working electrode was prepared according to the literature procedure [8, 9]. All solutions were thoroughly degassed before each experiment by bubbling N_2 through the solution. All solutions contained 2.0 mM 2,6-diphenylpyrylium tetrafluoroborate and various concentrations of tetra-*n*-butylammonium tetrafluoroborate as supporting electrolyte. Data was collected at scan rates of 20, 50, 100, 200, 500, 1000 and 2000 mV s^{-1}. UV/Visible spectrometry was carried out using a UV/Visible spectrometer (Evolution 60, Thermo Scientific).

8.3 Results and discussion

We report the EC_2 reduction of 2,6-diphenylpyrylium (DPP) cations in acetonitrile:

$$\mathrm{DPP^+ + e^-} \rightleftharpoons \mathrm{DPP^\bullet} \quad E^{0\prime}_{\mathrm{DPP^+/DPP^\bullet}} \tag{8.1}$$

$$\mathrm{2DPP^\bullet} \rightarrow \mathrm{DPP_2} \quad k_{\mathrm{dim}} \tag{8.2}$$

where k_{dim} is the rate constant for dimerisation. Previous studies of this mechanism have reported surprisingly different values of k_{dim}, from [7] 2.5×10^7 $\mathrm{M^{-1}\ s^{-1}}$ to [6, 10] 2.5×10^9 $\mathrm{M^{-1}\ s^{-1}}$. In this investigation, we use weakly supported voltammetry to show that an ion pairing equilibrium exists between $\mathrm{DPP^+}$ and anions present in solution, as the counter ion to $\mathrm{DPP^+}$ or the anion of the supporting electrolyte. This is modelled as a simple equilibrium between $\mathrm{DPP^+}$ and some anion, $\mathrm{X^-}$:

$$\mathrm{DPP^+ + X^-} \rightleftharpoons \mathrm{DPP^+ \cdot X^-} \quad K_{\mathrm{eqm}} = \frac{k_{\mathrm{f}}}{k_{\mathrm{r}}} \tag{8.3}$$

where K_{eqm} is the equilibrium constant for the ion pairing, defined as the ratio of forward to reverse rate constants. We perform cyclic voltammetry over a wide range of supporting electrolyte concentrations, and the ion pairing effect is seen to become more significant as the concentration of anions in solution increases, resulting in a decreased concentration of uncomplexed electroactive species and a diminished peak current height in the voltammogram. Previous studies [6, 7] have previously only carried out voltammetry at full support, and the concentration of supporting electrolyte is not varied, meaning the possible presence of ion pairing is not observable.

We have previously developed a theoretical model to simulate voltammetry at arbitrary levels of support which can be generalised to any mechanism [1, 11, 12]. The model makes use of the Nernst-Planck-Poisson (NPP) system of equations. The Nernst-Planck equation describes the mass transport of the species due to diffusion and migration, the latter of which arises when supporting electrolyte is not present in large excess. The Poisson equation describes the potential profile in solution. The

iterative Newton-Raphson method is used for the simultaneous solution of these coupled, non-linear equations, subject to the zero-field approximation [13], and appropriate boundary conditions describing a cyclic voltammetry experiment. A full account of the mathematical model is given in the Appendix V.

Cyclic voltammetry of a 2 mM solution of $DPP^+BF_4^-$ in acetonitrile in the presence of varying concentrations of supporting electrolyte, $NBu_4^+BF_4^-$, was studied at a wide range of scan rates at a hemispherical mercury electrode (radius 25 μm). As expected, a single reduction wave was observed, at potentials relative to the silver wire reference electrode ranging from approximately -0.15 V at the highest support ratio to -0.4 V at the lowest. No back peak was observed due to the fast dimerisation of $DPP^\bullet$. The peak current height became larger as the support ratio was reduced, since the positive electroactive species will be attracted to the electrode surface as unscreened negative charge builds up there. Figure 8.1 shows the variation of experimental peak current height (I_p) with c_{sup}, the ratio of supporting electrolyte concentration to the concentration of DPP^+. Concentrations of BF_4^- ions higher than those shown promoted oxidation of the mercury hemisphere, so data could not be collected. Also shown are the theoretical results assuming no ion pairing is present ($k_f = 0$). These simulated results use the best fit parameters shown in Table 8.3. It is seen that the experimental and theoretical results are not in good agreement with each other, particularly at higher concentrations of supporting electrolyte where theoretical results suggest the peak current height should approach a constant value (the fully supported limit), but experimental peak current heights continue to diminish. This suggests ion pairing occurs between the electroactive DPP^+ and the anion BF_4^-.

Table 8.1: Parameters used for simulations

Parameter	Value
α	0.5
D_{DPP^+} / 10^{-9} m^2 s^{-1}	1.35
$D_{DPP^\bullet}$ / 10^{-9} m^2 s^{-1}	1.35
D_{DPP_2} / 10^{-9} m^2 s^{-1}	0.5
$D_{DPP^+\cdot X^-}$ / 10^{-9} m^2 s^{-1}	1.1
$D_{NBu_4^+}$ / 10^{-9} m^2 s^{-1}	0.68 [14]
$D_{BF_4^-}$ / 10^{-9} m^2 s^{-1}	2.57[a]
ϵ_s	37.5 [15]
$E^{0'}$ / V vs Ag wire	-0.43[b]
K_{eqm} / m^3 mol^{-1}	0.035
$k^0_{DPP^+/DPP^\bullet}$ / m s^{-1}	4×10^{-3}
k_f / m^3 mol^{-1} s^{-1}	$> 10^6$
k_{dim} / m^3 mol^{-1} s^{-1}	5×10^5

[a] Estimated from molar conductivity [16], see Appendix IV.

[b] Measured in a 2mM $DPP^+BF_4^-$ solution without added supporting electrolyte.

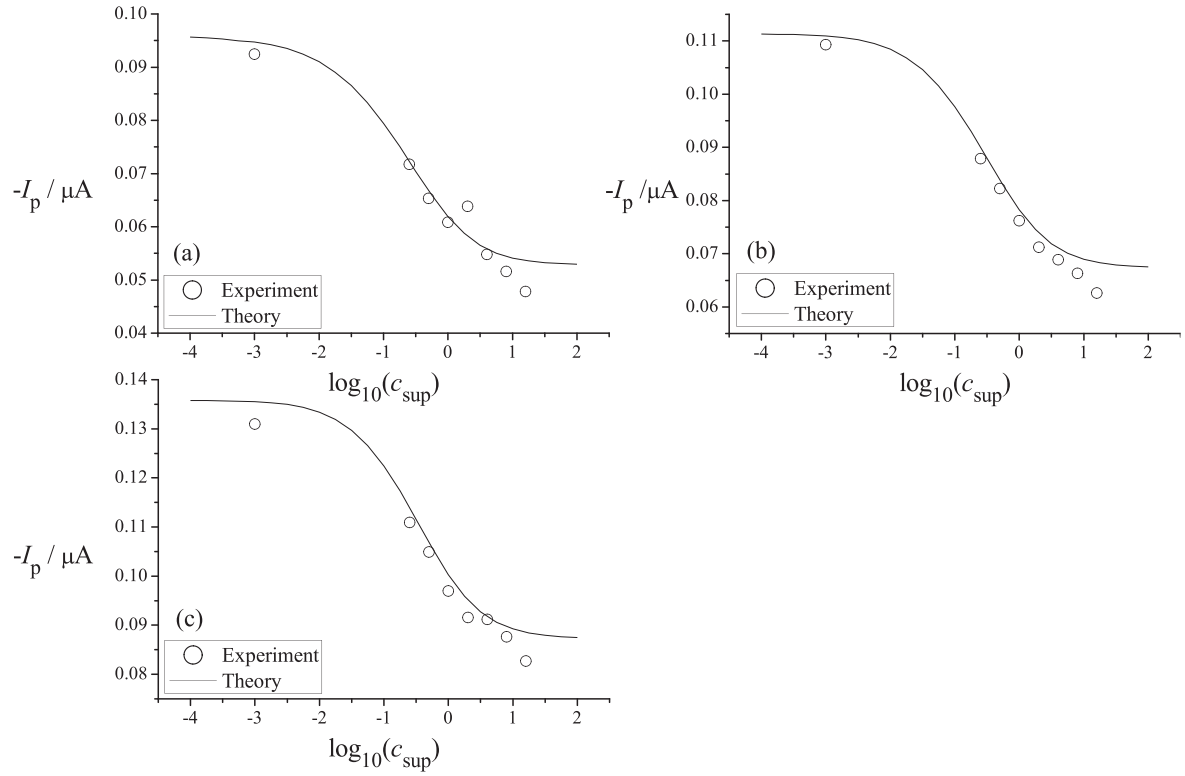


Figure 8.1: Experimental and simulated peak current heights for the reduction of 2 mM $DPP^+BF_4^-$ in acetonitrile, at various support ratios, at a 25 μm radius hemispherical mercury electrode, with no ion pairing equilibrium included. (a): $v = 50$ mV s^{-1}, (b): $v = 200$ mV s^{-1}, (c): $v = 500$ mV s^{-1}. c_{sup} is the concentration of supporting electrolyte normalized to the bulk DPP^+ concentration (2 mM).

To confirm this, the simulations were repeated, with the ion pairing equilibrium included. k_f

was set equal to 10^6 m^3 mol^{-1} s^{-1}, establishing an rapid ion pairing equilibrium. The comparison of experimental and theoretical peak heights with this equilibrium included is shown in Figure 8.2. Much better agreement between experiment and theory is now seen, especially at the higher support ratios investigated. When the concentration of BF_4^- is high, the position of equilibrium is displaced to favour formation of the ion pair. This diminishes the concentration of DPP^+ cations in solution, resulting in a lower flux of electroactive species at the electrode surface and a lower recorded current.

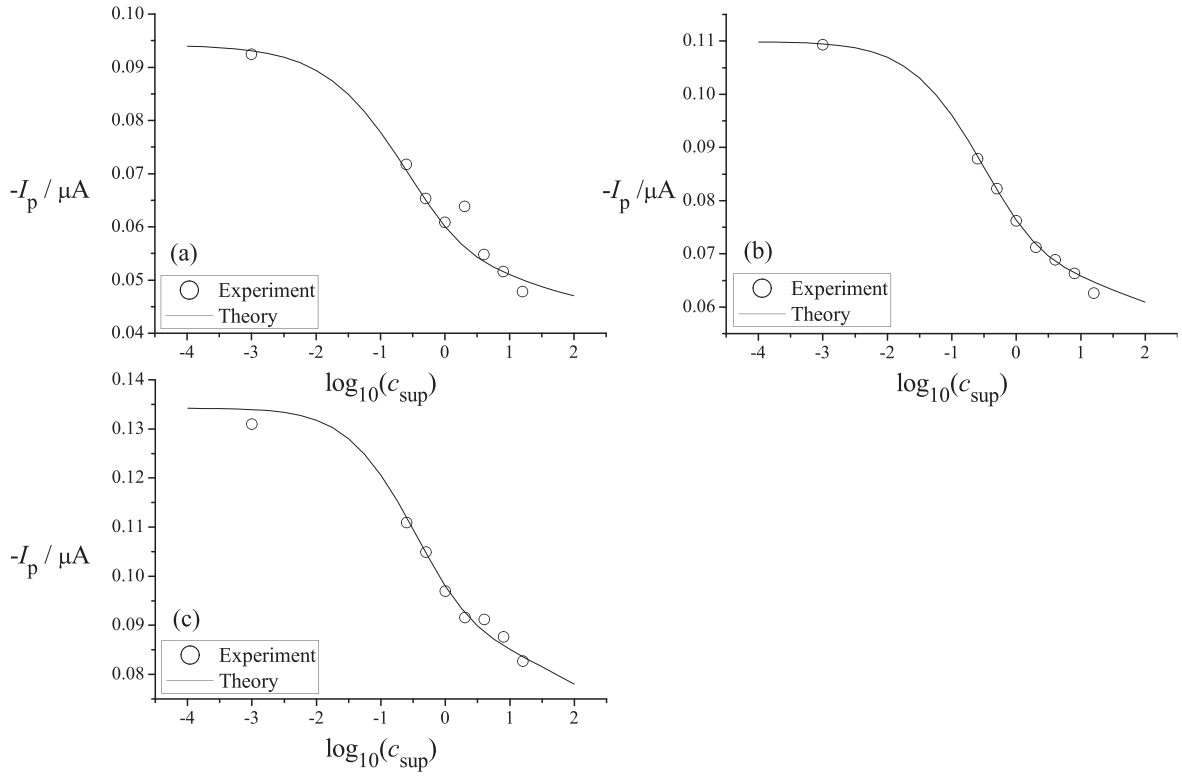


Figure 8.2: Experimental and simulated peak current heights for the reduction of 2 mM $DPP^+BF_4^-$ in acetonitrile, at various support ratios, at a 25 μm radius hemispherical mercury electrode, where an ion pairing equilibrium is included in the simulations. (a): v = 50 mV s^{-1}, (b): v = 200 mV s^{-1}, (c): v = 500 mV s^{-1}. c_{sup} is the concentration of supporting electrolyte normalized to the bulk DPP^+ concentration (2 mM).

Figures 8.3 and 8.4 show comparisons of the experimental and theoretical voltammograms in the presence of 0 and 16 mM $NBu_4^+BF_4^-$ respectively. Good agreement is seen, lending further support to the conclusion that ion pairing is significant. Independent verification of the existence of ion-pairing and of the value for K_{eqm} was obtained using UV/Visible spectrometry as detailed in the Appendix IV.

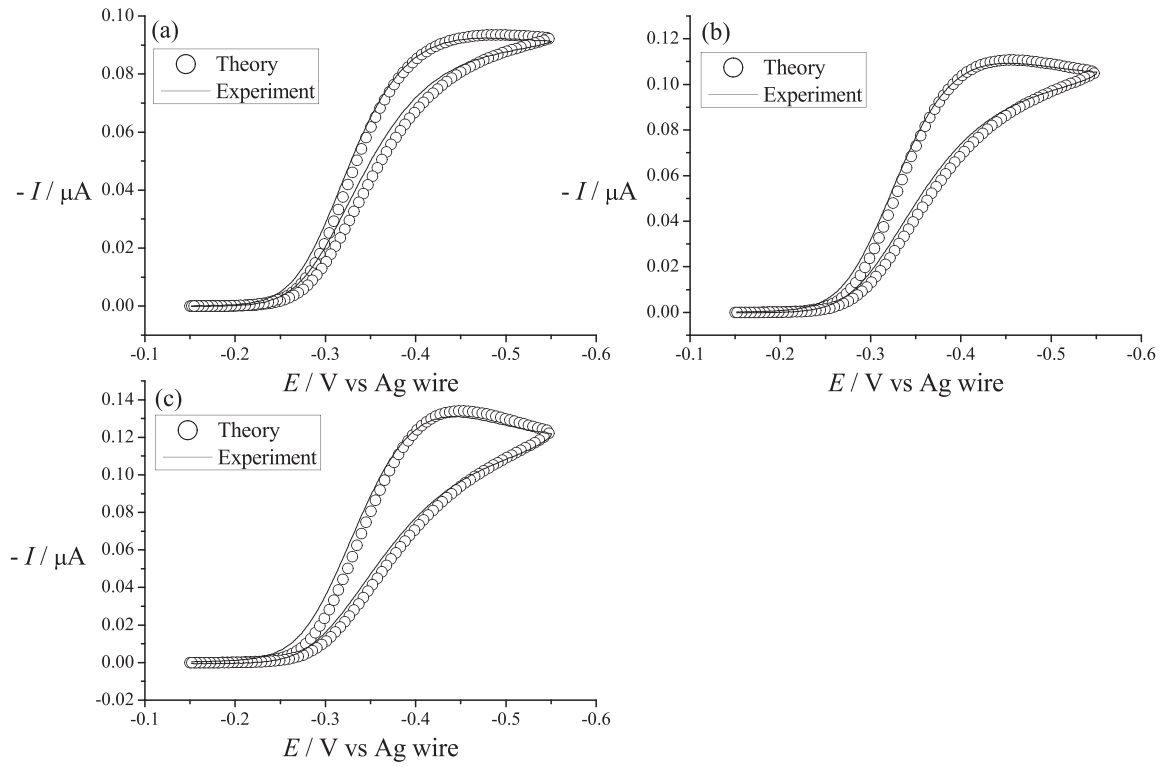


Figure 8.3: Experimental and simulated voltammograms for the reduction of 2 mM $DPP^+BF_4^-$ in acetonitrile, with no added supporting electrolyte, at a 25 μm radius hemispherical mercury electrode, where an ion pairing equilibrium is included in the simulations. (a): $v = 50$ mV s^{-1}, (b): $v = 200$ mV s^{-1}, (c): $v = 500$ mV s^{-1}.

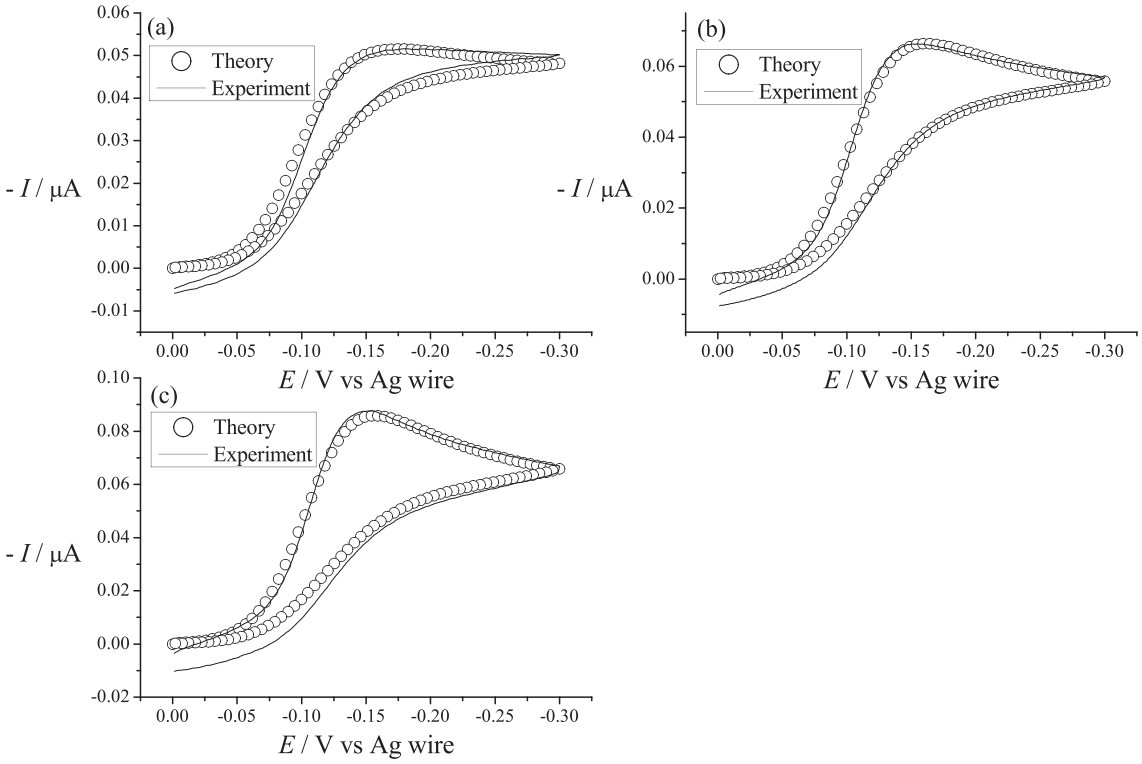


Figure 8.4: Experimental and simulated voltammograms for the reduction of 2 mM $DPP^+BF_4^-$ in acetonitrile, in the presence of 16 mM $NBu_4^+BF_4^-$, at a 25 μm radius hemispherical mercury electrode, where an ion pairing equilibrium is included in the simulations. (a): $v = 50$ mV s^{-1}, (b): $v = 200$ mV s^{-1}, (c): $v = 500$ mV s^{-1}.

Previous studies of this reduction did not use the same systems. Streeter *et. al.* used the tetrafluoroborate salt of DPP^+ with tetra-*n*-butylammonium perchlorate as supporting electrolyte [7], while Amatore *et. al.* used the perchlorate salt of DPP^+ with tetra-*n*-butylammonium tetrafluoroborate as supporting electrolyte [6]. The different coordination properties of the supporting electrolytic anions used lead the investigators to very different values of the homogeneous rate constant, as discussed above. This work resolves the controversy by including an ion pairing equilibrium in the mechanism, and a dimerisation rate constant of approximately 5×10^5 mol^{-1} s^{-1} is found. A heterogenous rate constant for the $DPP^+/DPP^\bullet$ redox couple at a mercury electrode $k^0_{DPP^+/DPP^\bullet} = 4 \times 10^{-3}$ m s^{-1} is also found, which to the authors' knowledge has not been previously reported.

8.4 Conclusion

The chapter studied the electro-reduction of 2,6-diphenylpyrylium supported by tetra-*n*-butylammonium tetrafluoroborate at a range of various concentrations. Weak-support votalmmetric analytical techniques were employed, because in this case undertaking experiments with full support required a relatively positive potential which may damage the mercury electrode. The simulated voltammetric response assuming a typical EC_2 did not have a good agreement with the experimental results. Therefore, a separate step representing ion-pairing was added into the theoretical model, which gave a better fitting with the experiments.

This chapter emphasised the utility of performing cyclic voltammetry over a range of supporting electrolyte concentrations, which can reveal mechanistic details not observable to fully supported voltammetry alone. This powerful new approach expands the scope of voltammetry as a mechanistic probe, its importance to the experimental electrochemist is quickly becoming evident.

References

[1] S.R. Belding, J.G. Limon-Petersen, E.J.F. Dickinson, R.G. Compton, Angew. Chemie Int. Ed. 49 (2010) 9242–9245.

[2] A. Bond, M. Fleischmann, J. Robinson, J. Electroanal. Chem. 168 (1984) 299–312.

[3] A. Jaworski, M. Donten, Z. Stojek, J. Osteryoung, Anal. Chem. 71 (1999) 167–173.

[4] S. Daniele, C. Bragato, M. Baldo, J. Electroanal. Chem. 456 (1998) 105 – 112.

[5] A. Jaworski, Z. Stojek, J.G. Osteryoung, J. Electroanal. Chem. 558 (2003) 141 – 153.

[6] C. Amatore, A. Jutand, F. Pflüger, J. Electroanal. Chem. 218 (1987) 361–365.

[7] I. Streeter, S.F. Jenkinson, G.W.J. Fleet, R.G. Compton, J. Electroanal. Chem. 600 (2007) 285–293.

[8] J. Mauzeroll, E.A. Hueske, A.J. Bard, Anal. Chem. 75 (2003) 3880–3889.

[9] J.G. Limon-Petersen, N.V. Rees, I. Streeter, A. Molina, R.G. Compton, J. Electroanal. Chem. 623 (2008) 165–169.

[10] C. Amatore, C. Lefrou, Portugaliae Electrochimica 9 (1991) 311.

[11] E.J.F. Dickinson, J.G. Limon-Petersen, N.V. Rees, R.G. Compton, J. Phys. Chem. C 113 (2009) 11157–11171.

[12] J.G. Limon-Petersen, J.T. Han, N.V. Rees, E.J.F. Dickinson, I. Streeter, R.G. Compton, J. Phys. Chem. C 114 (2010) 2227–2236.

[13] I. Streeter, R.G. Compton, J. Phys. Chem. C 112 (2008) 13716–13728.

[14] J. Szymanska, M.J. Palys, B. Van den Bossche, Anal. Chem. 76 (2004) 5937–5944.

[15] G. Ritzoulis, N. Papadopoulos, D. Jannakoudakis, J. Chem. Eng. Data 31 (1986) 146–148.

[16] H. Wang, J. Wang, S. Zhang, Y. Pei, K. Zhuo, Chem. Phys. Chem. 10 (2009) 2516–2523.

Chapter 9 Differential Pulse Techniques in Weakly Supported Media. Changes in the Kinetics and Thermodynamics of Electrode Processes Resulting from the Supporting Electrolyte Concentration

The work presented in this chapter was carried out in collaboration with

- **E.O. Barnes, E. Laborda** and **A. Molina** (for the theory and modelling parts)

and has been published in:

Y. Wang, E.O. Barnes, E. Laborda, A. Molina, R.G. Compton, J. Electroanal. Chem. 673 (2012) 13–23

Square wave voltammetry (SWV) and differential multipulse voltammetry (DMPV) in weakly supported media are investigated. The numerical simulation procedures reported in literature [1, 2] for electrochemical experiments in low conductivity solutions is applied with success. From this theory, the influence of the concentration of supporting electrolyte on the voltammograms is discussed for different redox couples and at electrodes of different size. The variation of the peak current and peak potential due to migration and Ohmic drop effects are reported.

The theory is applied to the study of the one-electron reduction processes of cobaltocenium and cobalt(III)sepulchrate at mercury hemispherical electrodes of 25 μm radius. The kinetic parameters and formal potential are obtained in a wide range of support ratio from the SWV and DMPV voltammograms. Possible changes of the kinetic and thermodynamic properties of the electrode reactions are analyzed as a function of the level of support.

9.1 Introduction

The use of highly supported media for carrying out electrochemical experiments is widespread since it enables one to avoid effects associated to the electric field in solution which are complex to model [1–7]. However, there are important circumstances where it is not possible (such as nonpolar solvents) [8] or not recommended to add large quantities of salts (such as colloidal, nanoparticle or biological reactions). Moreover, some redox systems can be affected by the ionic strength or show behaviours reflecting interactions or chemical reactions with the coexisting ions [5, 9, 10]. Further, weakly supported conditions can be more informative about the mechanism and kinetics of the experimental system, such as revealing the presence of comproportionation [11] or resolving mechanistic ambiguities [4, 5]. Its understanding is also essential for the development of nanoelectrochemistry [12].

Under weakly supported conditions migration transport and Ohmic potential drop effects operate, causing distortions from diffusion only voltammograms. Further, the kinetic and thermodynamic properties of the system may be also affected by the nature and concentration of ions in solution.

Accordingly, the development of theoretical approaches to model electrochemical experiments in weakly supported media is essential for a rigorous analysis of these media and has been tackled by many researchers [13–28]. In previous papers, Compton *et al*. have developed an adequate numerical strategy that involves the resolution of the so-called Nernst-Planck-Poisson equation system [29] without the constraint of electroneutrality. This has been applied with success to describe cyclic voltammetry, stripping voltammetry and chronoamperometry of several redox systems at macroelectrodes and hemispherical microelectrodes in resistive media [1–7].

In this chapter, this computational approach is applied to the most common pulse techniques in electrochemistry [30]: square wave voltammetry (SWV) and differential multipulse voltammetry (DMPV). The interest of these techniques in electroanalysis is well established, and they are also valuable for kinetic and mechanistic studies [31–39]. Moreover, differential pulse techniques are particularly insightful when electrodes of micrometric size are employed, since a peak-shaped response is obtained even under steady state conditions. Given the high resistivity media considered in this

chapter, the use of electrodes of micrometric size is recommended in order to minimize the potential drop in solution.

From the theoretical results, the effects of the concentration of supporting electrolyte on differential pulse voltammograms are analyzed. The analysis enables us to identify distortions due to additional influences of the supporting electrolyte on the kinetics or thermodynamics of the redox system.

The results are applied to the experimental study of the one-electron reduction processes of cobaltocenium ($CoCp_2^+$) in acetonitrile and cobalt(III)sepulchrate ($CoSep^{3+}$) in water with mercury microhemispheres as working electrodes:

$$CoCp_2^+ + e^- \rightleftarrows CoCp_2 \tag{9.1}$$

$$CoSep^{3+} + e^- \rightleftarrows CoSep^{2+} \tag{9.2}$$

Under fully supported conditions, both redox processes are reversible electron transfers at macroelectrodes with no complications due to adsorption or coupled chemical reactions [40, 41].

From the experiments carried out, the theory is corroborated and the influence of coexisting ions on the properties of these redox couples are investigated. Thus, the fitting of theoretical and experimental results enables the determination of the kinetic and thermodynamic parameters for different levels of concentration of the supporting electrolyte.

9.2 Experimental

9.2.1 Chemical Reagents

Bis(cyclopentadienyl)cobalt(III) hexafluorophosphate ($CoCp_2PF_6$, Aldrich, 95%), cobalt(III)se -pulchrate trichloride ($CoSepCl_3$, Aldrich, 98%), potassium chloride (KCl, Aldrich, >99%), tetra-*n*-butylammonium perchlorate (TBAP, Fluka, >99%), mercury(I) nitrate dihydrate ($Hg_2(NO_3)_2 \cdot 2H_2O$, Aldrich, ≥97%), nitric acid (HNO_3, Fischer scientific, 70%), ferrocene ($Fe(C_5H_5)_2$, Aldrich, 98%) and acetonitrile (MeCN, Fischer scientific, dried and distilled, >99 %) were all used as received, without further purification.

9.2.2 Instrumental and Solutions

A 25 μm radius platinum (Pt) microdisc electrode made of 99.99% pure platinum wire (Goodfellow Cambridge Ltd, Cambridge) was used for deposition of the mercury hemisphere. Gold foil was used as counter electrode in all the experiments. A SCE electrode was employed as reference electrode in water solutions, whereas a silver/silver ion electrode was used in acetonitrile solutions. This consists of a silver wire immersed in an acetonitrile solution of 10 mM silver nitrate and 0.1 M TBAP.

All experiments were performed in a thermostated Faraday Cage at 298 K. Solutions were degassed with N_2 for 30 minutes before experiments, and N_2 pressure was kept during measurements.

Bulk solutions containing 2 mM $CoCp_2BF_6$ in acetonitrile and 2 mM $CoSepCl_3$ in water were made up. TBAP was used as supporting electrolyte in $CoCp_2BF_6$ solutions and KCl for $CoSepCl_3$. Solutions with 4 mM, 40 mM and 400 mM supporting electrolytes were prepared in order to study the variations between low and high support ratios.

9.2.3 Determination of diffusion coefficients

The diffusion coefficients of the electroactive species were determined by double potential step chronoamperometry as described previously [42]. The diffusion coefficients for $CoCp_2^+$ ($D_{CoCp_2^+}$), $CoCp_2$ (D_{CoCp_2}) in acetonitrile, and $CoSep^{3+}$ ($D_{CoSep^{3+}}$), $CoSep^{2+}$ ($D_{CoSep^{2+}}$) in water were determined to be (1.9 $\pm$ 0.1) $\times$ 10^{-9} m^2 s^{-1}, (3.1 $\pm$ 0.1) $\times$ 10^{-9} m^2 s^{-1}, (6.0 $\pm$ 0.2) $\times$ 10^{-10} m^2 s^{-1}, and (8.9 $\pm$ 0.2) $\times$ 10^{-10} m^2 s^{-1}, respectively. Good agreement with literature values was found [2, 41, 43–47]. No significant differences were encountered in the values of the diffusion coefficients when varying the concentration of supporting electrolyte from 4 to 400 mM.

9.2.4 Voltammetric studies

The effects of the support ratio was studied by means of differential multipulse voltammetry (DMPV) and square wave voltammetry (SWV) (see Figures 9.1 and 9.2).

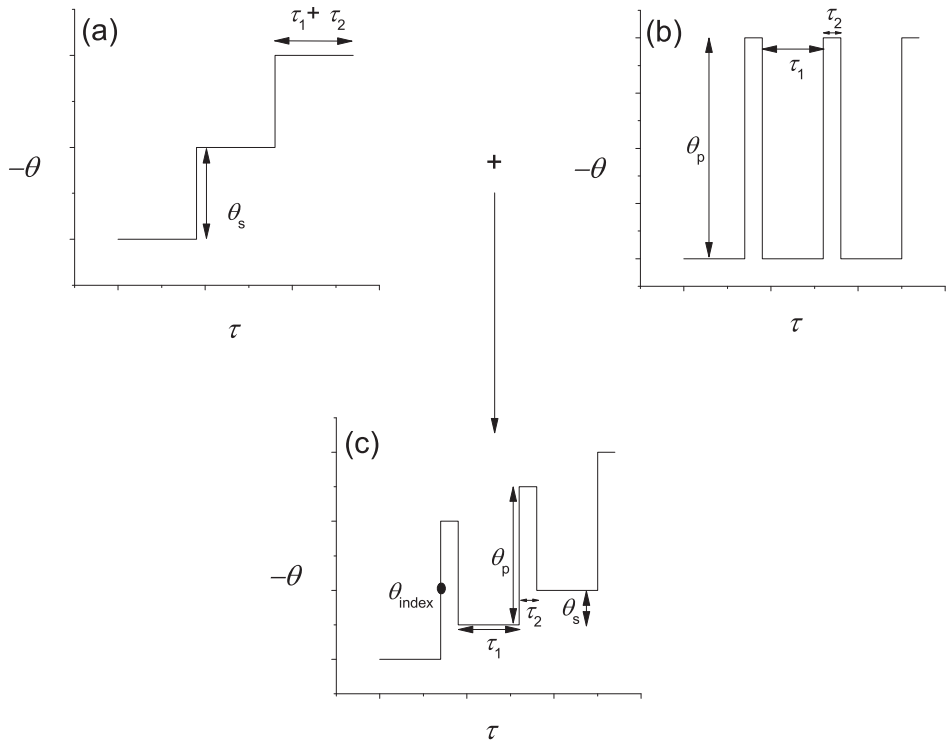


Figure 9.1: Staircase (a) and pulse (b) profiles for DMPV, and their sum giving the overall waveform (c). θ_s is the step potential, θ_p is the pulse amplitude, τ_2 is the sample period, and $\tau_1 + \tau_2$ is the pulse period.

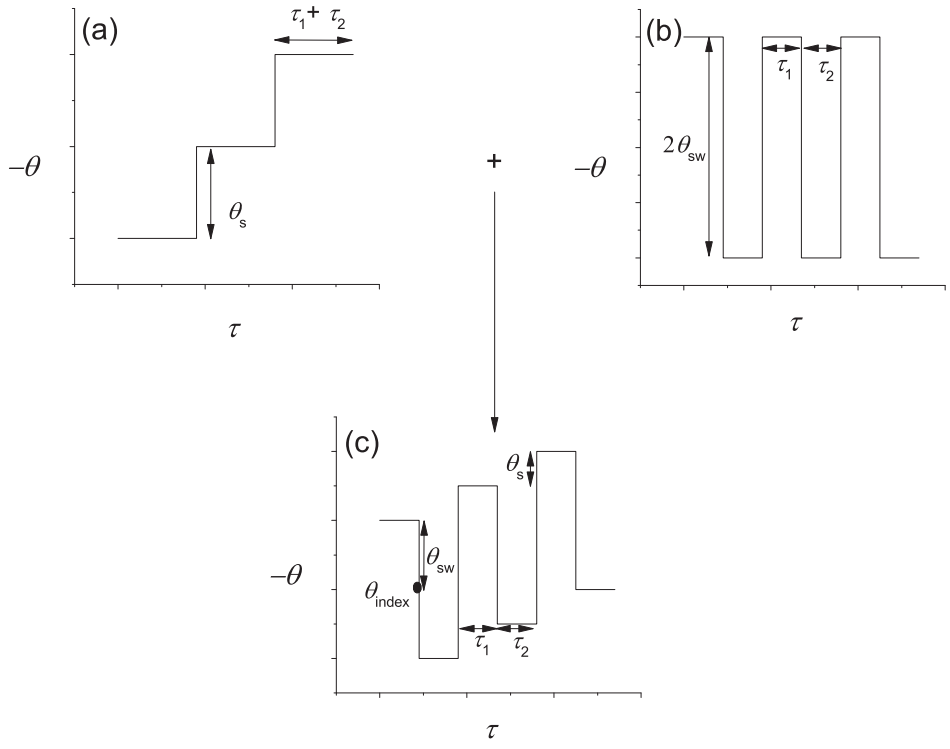


Figure 9.2: Staircase (a) and pulse (b) profiles for SWV, and their sum giving the overall waveform (c). θ_{sw} is the step potential, τ_2 is the sample period, θ_s is the pulse amplitude, and $\tau_1 + \tau_2$ is the pulse period.

For DMPV studies, different modulation times (t_2) from 2 to 32 ms were used with a unique interval time ($t_1 + t_2$) of 100 ms. The pulse amplitude, E_p was 25 mV, and the step potential, $E_\mathrm{s} = 10$ mV. Regarding SWV, the frequency ($f = (2t_1)^{-1} = (2t_2)^{-1}$) ranged from 10 Hz to 200 Hz, the pulse amplitude $E_\mathrm{SW} = 25$ mV and the step potential $E_\mathrm{s} = 10$ mV. Both forward and backward scans were recorded.

Experimental voltammetries of different support ratios were all fitted using a homemade program described in the Theory section, which follows.

9.3 Theory

A variety of electrochemical experiments, including chronoamperometry [1, 2], cyclic voltammetry [3–5] and stripping voltammetry [6, 7] have been successfully simulated under conditions of weak support using the Nernst-Plank-Poisson (NPP) system of equations to model coupled diffusion and migration. This chapter seeks to apply the model to simulate two different, but related, kinds of voltammetry, differential multi pulse voltammetry (DMPV) and square wave voltammetry (SWV), at several supporting electrolyte concentrations.

The one electron reduction of a variety of species, bearing arbitrary charge z, is simulated:

$$\mathrm{A}^\mathrm{z} + \mathrm{e}^- \rightleftharpoons \mathrm{B}^{\mathrm{z}-1} \tag{9.3}$$

Also present in solution is a fully dissociated monovalent salt, $\mathrm{M}^+\mathrm{X}^-$, present at an arbitrary concentration C_sup, and a monovalent counter ion for species A if necessary.

The mass transport of species in solution in the presence of an electric field is described by the Nernst-Planck equation, given in hemispherical space by:

$$\frac{\partial C_\mathrm{i}}{\partial t} = D_\mathrm{i}\left[\frac{\partial^2 C_\mathrm{i}}{\partial r^2} + \frac{2}{r}\frac{\partial C_\mathrm{i}}{\partial r} + \frac{z_\mathrm{i}F}{RT}\left(\frac{\partial C_\mathrm{i}}{\partial r}\frac{\partial \phi}{\partial r} + C_\mathrm{i}\frac{\partial^2 \phi}{\partial r^2} + C_\mathrm{i}\frac{2}{r}\frac{\partial \phi}{\partial r}\right)\right] \tag{9.4}$$

where C_i is the concentration of any of the four species A, B, M or X (mol dm^{-3}), t is time (s), D_i

is the diffusion coefficient of any of the species A, B, M or X ($m^2\ s^{-1}$), r is the radial distance from the electrode surface (m), and ϕ is the potential in solution at point r (V). All symbols are defined in Table 9.1.

Table 9.1: List of symbols used in this chapter and their definitions.

Parameter	Description	Units
$\alpha_{i/j}$	Transfer coefficient of the i/j redox couple	Unitless
D_i	Diffusion coefficient of species i	$m^2\ s^{-1}$
C_i	Concentration of species i	mol
C_i^*	Bulk solution concentration of species i	mol
C_i^0	Concentration of species i at the electrode surface	mol
C_{sup}	Concentration of supporting electrolyte	mol
E	Applied potential	V
$E_{i/j}^{0'}$	Formal potential of i/j couple	V
E_s	Step potential in staircase profiles	V
E_p	Pulse height in DMPV pulse profile	V
E_{sw}	Half pulse height in SWV pulse profile	V
ϵ_s	Dielectric constant (relative permittivity) of solvent	Unitless
ϵ_0	Permittivity of free space ($=8.854 \times 10^{-12}$)	$F\ m^{-1}$
F	Faraday constant (=96485)	$C\ mol^{-1}$
i	Current measured at working electrode	A
$k_{i/j}^0$	Electrochemical rate constant of i/j redox couple	$m\ s^{-1}$
R	Gas constant (=8.314)	$J\ K^{-1}\ mol^{-1}$
ϕ	Solution potential	V
ϕ_0	Solution potential at electrode surface	V
r	Distance	m
r_e	Electrode radius	m
t	Time	s
t_1	Time between pulses	s
t_2	Duration of pulses	s
z_i	Charge on species i	Unitless

A second equation, the Poisson equation, is used to define the potential in solution:

$$\frac{\partial^2 \phi}{\partial r^2} + \frac{2}{r}\frac{\partial \phi}{\partial r} = -\frac{F}{\epsilon_s \epsilon_0}\sum_i z_i C_i \tag{9.5}$$

where ϵ_s is the relative permittivity of the solvent, and ϵ_0 is the permittivity of free space. These two equations together make up the NPP system of equations.

9.3.1 Normalised Parameters

In order to remove scaling factors from simulations, and to reduce the number of independent parameters, a number of variables are normalised. For example, all concentrations and diffusion coefficients are taken relative to those of species A, and all distances are taken relative to the radius of the electrode. A full list of normalised parameters, and their definitions, is given in Table 9.2.

Table 9.2: List of normalised parameters and their relation to true, dimensional parameters

Normalised Parameter	Dimensional counterpart	Definition
c_i	Concentration of species i	$\frac{C_\mathrm{i}}{C^*_\mathrm{A}}$
c_sup	Concentration of supporting electrolyte	$\frac{C_\mathrm{sup}}{C^*_\mathrm{A}}$
D'_i	Diffusion coefficient of species i	$\frac{D_\mathrm{i}}{D_\mathrm{A}}$
j	Current measure at working electrode	$\frac{i}{2\pi r_e F D_\mathrm{A} C_\mathrm{A}}$
$K^0_\mathrm{i/j}$	Electrochemical rate constant of i/j redox couple	$\frac{r_e}{D_\mathrm{A}} k^0_\mathrm{i/j}$
θ_app	Applied potential	$\frac{F}{RT} E_\mathrm{app}$
$\theta_\mathrm{f,i/j}$	Formal potential of the i/j redox couple	$\frac{F}{RT} E^{0'}_\mathrm{A/B}$
θ_s	Step potential in staircase profiles	$\frac{F}{RT} E_\mathrm{s}$
θ_p	Pulse height in DMPV pulse profile	$\frac{F}{RT} E_\mathrm{p}$
θ_sw	Half pulse height in SWV pulse profile	$\frac{F}{RT} E_\mathrm{sw}$
θ	Solution potential	$\frac{F}{RT} \phi$
θ_0	Solution potential at electrode surface	$\frac{F}{RT} \phi_0$
R	Distance	$\frac{r}{r_\mathrm{e}}$
R_e	Electrode radius (relative to the Debye length) [3]	$r_\mathrm{e}\sqrt{\frac{F^2 C^*_\mathrm{A}}{RT\epsilon_\mathrm{s}\epsilon_0}}$
τ	Time	$\frac{D_\mathrm{A}}{r_\mathrm{e}^2} t$
τ_1	Time between pulses	$\frac{D_\mathrm{A}}{r_\mathrm{e}^2} t_1$
τ_2	Duration of pulses	$\frac{D_\mathrm{A}}{r_\mathrm{e}^2} t_2$

When these normalised parameters are introduced into the NPP equations, they become:

$$\frac{\partial c_\mathrm{i}}{\partial \tau} = D'_\mathrm{i}\left[\frac{\partial^2 c_\mathrm{i}}{\partial R^2} + \frac{2}{R}\frac{\partial c_\mathrm{i}}{\partial R} + z_\mathrm{i}\left(\frac{\partial c_\mathrm{i}}{\partial R}\frac{\partial \theta}{\partial R} + c_\mathrm{i}\frac{\partial^2 \theta}{\partial R^2} + c_\mathrm{i}\frac{2}{R}\frac{\partial \theta}{\partial R}\right)\right] \tag{9.6}$$

and

$$\frac{\partial^2 \theta}{\partial R^2} + \frac{2}{R}\frac{\partial \theta}{\partial R} = -R_\mathrm{e}^2 \sum_\mathrm{i} z_\mathrm{i} c_\mathrm{i} \tag{9.7}$$

9.3.2 Boundary Conditions

The NPP equations must be solved subject to a series of boundary conditions defining the experiment to be simulated. There will be 10 ($(4+1)\times 2$) boundary conditions: at the electrode surface boundary ($R = 1$) and the semi infinite bulk solution boundary ($R = R_{\max}$) for each species plus the solution potential.

Electrode Surface

The electrode surface boundary condition for an electroactive species uses the Butler-Volmer equation:

$$\begin{aligned} D'_{\mathrm{A}}\left(\frac{\partial c_{\mathrm{A}}}{\partial R}\right)_{R=1} &= K^0_{\mathrm{A/B}} c^0_{\mathrm{A}} \exp\left[-\alpha_{\mathrm{A/B}}\left(\theta_{\mathrm{app}} - \theta_0 - \theta_{\mathrm{f,A/B}}\right)\right] \\ &\quad - K^0_{\mathrm{A/B}} c^0_{\mathrm{B}} \exp\left[\left(1-\alpha_{\mathrm{A/B}}\right)\left(\theta_{\mathrm{app}} - \theta_0 - \theta_{\mathrm{f,A/B}}\right)\right] \end{aligned} \tag{9.8}$$

where θ_0 is the dimensionless solution potential at the electrode surface, the inclusion of which represents Ohmic drop.

By conservation of mass:

$$D'_{\mathrm{B}}\left(\frac{\partial c_{\mathrm{B}}}{\partial R}\right)_{\mathrm{R=1}} = -D'_{\mathrm{A}}\left(\frac{\partial c_{\mathrm{A}}}{\partial R}\right)_{\mathrm{R=1}} \tag{9.9}$$

For non electroactive species, a zero flux boundary condition is imposed at the electrode surface (assuming the electrode to be inert and impermeable):

$$D'_{\mathrm{i}}\left(\frac{\partial c_{\mathrm{i}}}{\partial R}\right)_{R=1} = 0 \tag{9.10}$$

The variation of θ_{app} with time is defined in different ways for DMPV and SWV. In each case, the overall waveform is the sum of two separate waveforms, one "staircase" wave and one "pulse" wave. The staircase wave is the same in each case. A constant potential is applied for duration $\tau_1 + \tau_2$, which then steps by a value θ_{s}, and so on. This is shown schematically in Figures 9.1 (a) and 9.2 (a).

The pulse waveform in DMPV consists of a series of pulses of magnitude θ_p and duration τ_2, separated by duration τ_1, as shown in Figure 9.1 (b). When added to the staircase profile, the final waveform is generated, as shown in Figure 9.1 (c).

In SWV, it is the convention that the height of the pulse in the pulse profile is equal to $2\theta_{sw}$ (Figure 9.2). The sign of θ_{sw} is opposite to that of θ_s, *i.e.* for a reduction, θ_s is negative and θ_{sw} is positive (on the forward scan). Also in SWV, τ_1 is equal to τ_2, *i.e.* the duration of the pulses is equal to the time between them. This results in the waveform shown in Figure 9.2 (b), which when added to the staircase profile generates the overall potential profile shown in Figure 9.2 (c).

The obtain a boundary condition for the solution potential at the electrode surface, we make the zero field approximation. [48] This approximation, shown to be valid for electrodes larger than the nano-scale, [1] assumes that the electrical double layer at the electrode surface is negligibly small when compared to the diffusion layer. In this vanishingly small layer, the charge in solution exactly balances the charge on the electrode surface, resulting in zero electric field. If there is no electric field, there is no potential gradient, hence:

$$\left(\frac{\partial\theta}{\partial R}\right)_{R=1} = 0 \tag{9.11}$$

Bulk Solution

The bulk solution boundary is set at:

$$R_{max} = 1 + 6\sqrt{D'_{max}\tau_{max}} \tag{9.12}$$

where D'_{max} is the highest normalised diffusion coefficient in the system, and τ_{max} is the normalised time taken to complete the experiment. This semi-infinite boundary has been shown to be well outside the depletion layer around the electrode. [49–52] At this boundary, a zero flux condition is imposed on all species in solution:

$$D'_i\left(\frac{\partial c_i}{\partial R}\right)_{R=R_{max}} = 0 \tag{9.13}$$

To define the solution potential boundary condition at this limit, we assume the solution to be electroneutral outside the depletion layer. The Poisson equation for an electroneutral solution is:

$$\frac{\partial^2\theta}{\partial R^2} = 0 \tag{9.14}$$

which, when solved under the condition that $\theta \to 0$ as R $\to \infty$, gives the boundary condition:

$$\theta_{R=R_{\max}} + R_{\max}\left(\frac{\partial\theta}{\partial R}\right)_{R=R_{\max}} = 0 \tag{9.15}$$

9.3.3 Numerical Methods

The NPP equations and boundary conditions are discretised using the Crank-Nicolson finite difference method [53, 54], and solved using the iterative Newton-Raphson method. This discretisation process requires appropriate spatial and temporal grids to be formulated. The spatial grid used in this investigation has previously been established, and demonstrated to be appropriate [2–5, 7, 55]. This grid is non regular, with a very dense, regularly spaced region near the electrode surface, which then begins to expand past a switching point, R_{s}, as defined below:

$$R_{\mathrm{j}} = R_{\mathrm{j}-1} + \gamma_{\mathrm{R}}(R_{\mathrm{s}} - 1) \qquad R < R_{\mathrm{s}} \tag{9.16}$$

$$R_j = R_{\mathrm{j}-1} + \gamma_{\mathrm{R}}(R_{\mathrm{j}-1} - 1) \qquad R \geq R_{\mathrm{s}} \tag{9.17}$$

R_0 is the point at the electrode surface, and is equal to 1 (*i.e.* one electrode radius).

To construct the temporal grid, the τ_1 and τ_2 portions of each "cycle" in the wave forms are divided into n_1 and n_2 equal points respectively.

Convergence testing showed that the following parameters gave results within 0.5% of a fully converged value: $\gamma_{\mathrm{R}} = 1 \times 10^{-2}$ and $R_{\mathrm{s}} = R_0 + \left(2 \times 10^{-3}\right)$. For DMPV, $n_1 = 10$ and $n_2 = 50$, for SWV $n_1 = n_2 = 50$. All simulations were programmed in C++ and run on a desktop computer, (Intel Core2 Quad, 2.4 GHz, 2 GB RAM), with a typical running time of a few minutes per simulation.

9.4 Results and Discussion

9.4.1 Theoretical results

In Figures 9.3 and 9.4, the effects predicted on the SWV response of fast electron transfer processes ($k_0 = 1$ cm s^{-1}, $\alpha = 0.5$, see Table 9.3 for more details) at a hemispherical microelectrode with $r_0 = 25$ μm are shown. The variation of the peak current and peak potential with the support ratio $c^*_{\mathrm{sup}}/c^*_{\mathrm{A}}$ are plotted for the one-electron reduction of differently charged electroactive species. These results can be explained by the simultaneous appearance of migration transport and Ohmic potential drop, which are more apparent as the concentration of the supporting electrolyte is diminished. As a consequence, the potential at the site of the electron transfer is different from its value in bulk solution. This affects the mass transport of the electroactive species (through migration) and the rate of the electron transfer (through the real driving force experienced by the reactant).

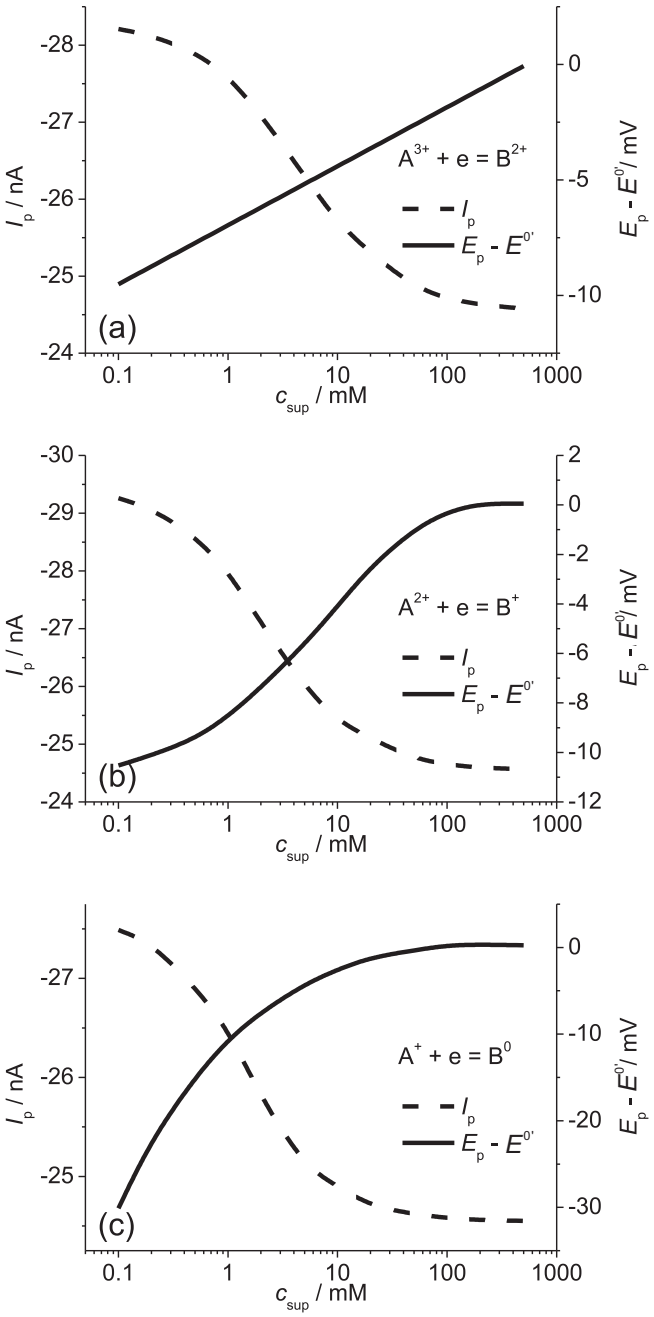


Figure 9.3: Variation of the peak current (I_p) and peak potential (E_p) in SWV with the concentration of the supporting electrolyte at a 25 μm radius hemispherical microelectrode for one-electron reductions of positively charged species. Frequency = 10 Hz, step potential = 10 mV, amplitude potential = 25 mV.

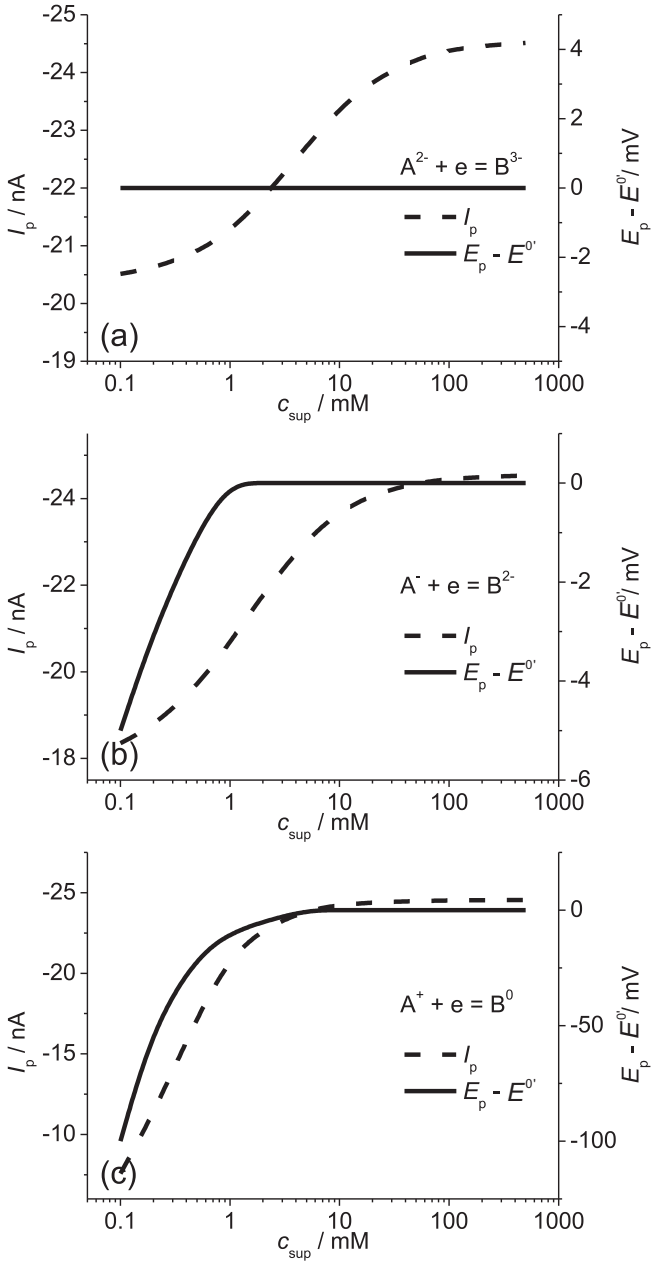


Figure 9.4: Variation of the peak current (I_p) and peak potential (E_p) in SWV with the concentration of the supporting electrolyte at a 25 μm radius hemispherical microelectrode for one-electron reductions of neutral and anionic species. Frequency = 10 Hz, step potential = 10 mV, amplitude potential = 25 mV.

Table 9.3: Parameters employed in simulations shown in Theory1 9.3- 9.7. Other conditions indicated in figure captions.

Parameter	Value
k_0	1 cm s^{-1}
α	0.5
$E^{0'}_{A/B}$	0 V
D_i	10^{-9} m^2 s^{-1}
c^*_A	1 mM
c^*_B	0 mM

With respect to the migration effects, obviously these depend on the change of charge caused by the electron transfer. For the reduction of cations, migration will increase reactant flux towards the electrode due to the negative charge generated around the electrode surface. The reduction of anions shows the opposite behaviour. Regarding the Ohmic potential drop, this leads to the shift of the voltammograms towards greater overpotentials along with the decrease of the electrochemical response due to the decrease of the real applied potential.

The magnitude of the distortion with respect to fully-supported conditions relates to the ability of the system to compensate the charge created by the electrode process through the transport of ions. Thus, when the redox couple involves highly charged ions, the electroactive species or its counterions can mitigate the electric field and its effects: self-support conditions. The lower the charge of the electroactive species, the smaller the ability to compensate the charge generated. In the case of neutral species, self-support conditions are not possible and therefore the distortion of the peak current and potential in the absence of supporting electrolyte is maximum.

This behaviour can be observed in the variation of the peak potential predicted in Figures 9.3 and 9.4 for SWV (see Table 9.3 for simulation details). The shift with respect to full support is maximum in the case of the reduction of neutral species (reaching 100 mV for $c^*_{sup}/c^*_A = 0.1$) and it decreases as the charge of the electroactive species increases and the self-support is more efficient.

On the other hand, analysis of the peak current does not at first sight reflect the behaviour expected for the reduction of cations. Thus, the increase of the peak current predicted for the couples A^{2+}/B^{1+} and A^{3+}/B^{2+} is greater than for A^{1+}/B^{0}. This contrasts with the behaviour of the peak potential and with that predicted for the peak current in cyclic voltammetry [2]. It is the result of the forward-backward potential-time profile employed in SWV together with the subtractive nature of the net current: $I_{SWV} = I_{\text{forward}} - I_{\text{backward}}$ (see Figure 9.2). Consequently, sometimes the analysis of the net current is not intuitive as in direct techniques such as cyclic voltammetry, and it must be carried out cautiously. In these circumstances, the study of the forward current is more conclusive as can be seen in Figure 9.5 (see Table 9.3 for simulation details). Thus, the peak current in I_{forward} under weakly supported conditions follows the tendency expected according to the above discussion: $A^{1+}/B^{0} > A^{2+}/B^{1+} > A^{3+}/B^{2+} >$ full support.

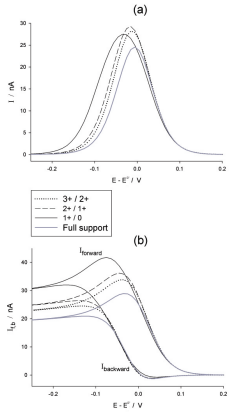


Figure 9.5: (a) Net current and (b) forward and backward components of square wave voltammograms under weakly supported conditions, $c^*_{\text{sup}}/c^*_{\text{A}} = 0.1$, for different one-electron reduction processes of cations on a 25 μm radius hemispherical microelectrode. Frequency = 10 Hz, step potential = 10 mV, amplitude potential = 25 mV.

The magnitude of the distortion is also dependent on the electrode size. This is studied in Figure 9.6 where the changes in the peak current and the peak potential between fully-supported ($c^*_{\text{sup}}/c^*_{\text{A}} = 500$) and nearly self-supported ($c^*_{\text{sup}}/c^*_{\text{A}} = 0.1$) conditions are plotted versus the radius of the hemispherical electrode (see Table 9.3 for simulation details).

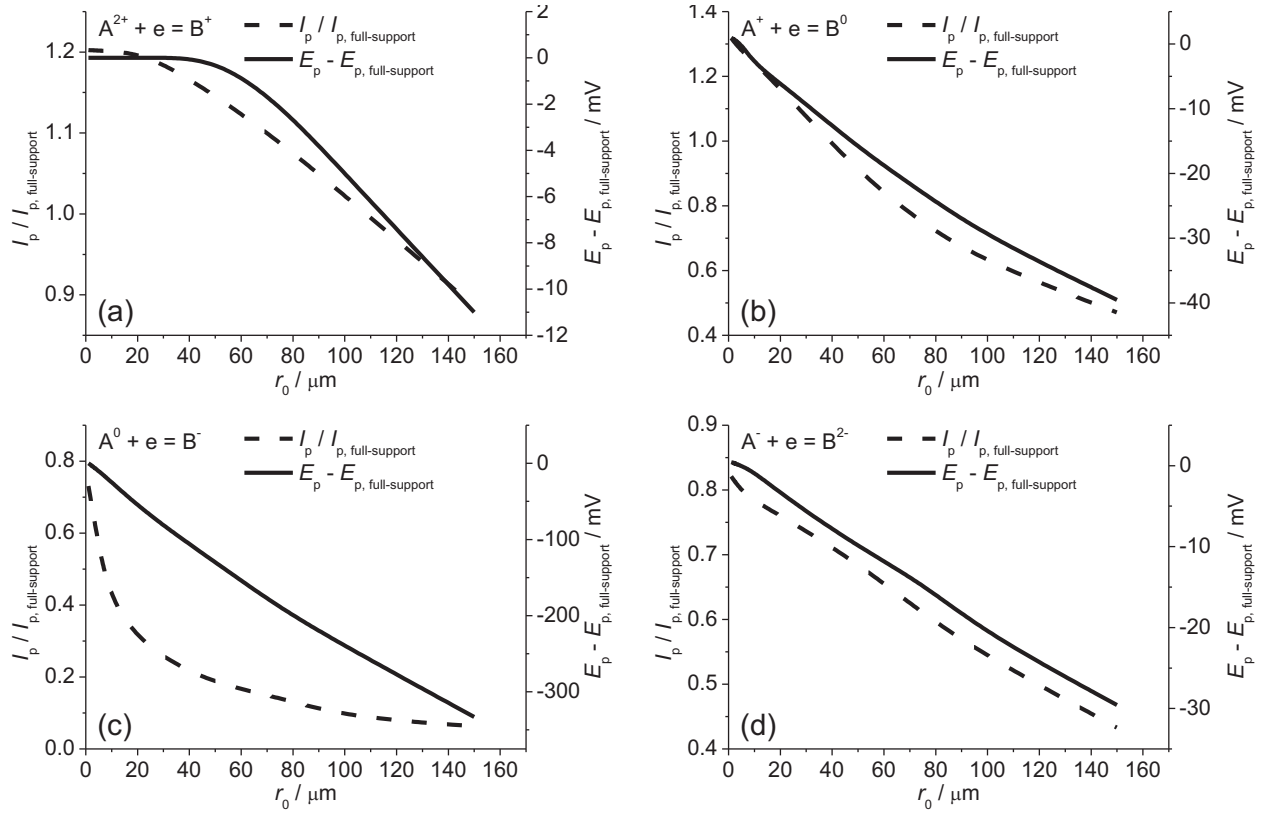


Figure 9.6: Variation of the peak current (I_{p}) and peak potential (E_{p}) at $c^*_{\text{sup}}/c^*_{\text{A}} = 0.1$ relative to those at full support with the electrode radius in SWV at hemispherical electrodes. Frequency = 10 Hz, step potential = 10 mV, amplitude potential = 25 mV.

The decrease of the size in the electrode makes the dispersion of the charge generated by the electrode reaction more efficient. Accordingly, in all cases, the shift of the peak potential towards more negative values is more significant as the electrode size is increased. Again, the nature of the signal in SWV gives rise to apparently contradictory effects on the peak current corresponding to the reduction of cations. Thus, when the electrode radius is increased ($r_0 > 110$ μm for the conditions of Figure 9.6.a), the peak current under weakly supported conditions goes from being larger than it is at full support to smaller. In the case of the reduction of an neutral or anionic species, the ratio $I_{\text{p}}/I_{\text{p,full-support}}$ is always smaller than unity and it decreases as the electrode employed becomes larger and the transport of species is less efficient (see Figures 9.6.b and 9.6.c).

Finally, the effect of the pulse time (i.e., scan frequency) is considered in Figure 9.7. In all cases, the distortion of the voltammograms due to electric field effects increases with frequency, that is, as the pulse time becomes shorter. The current driven after the application of a potential step is higher at short times, generating greater uncompensated charge and potential drop in solution.

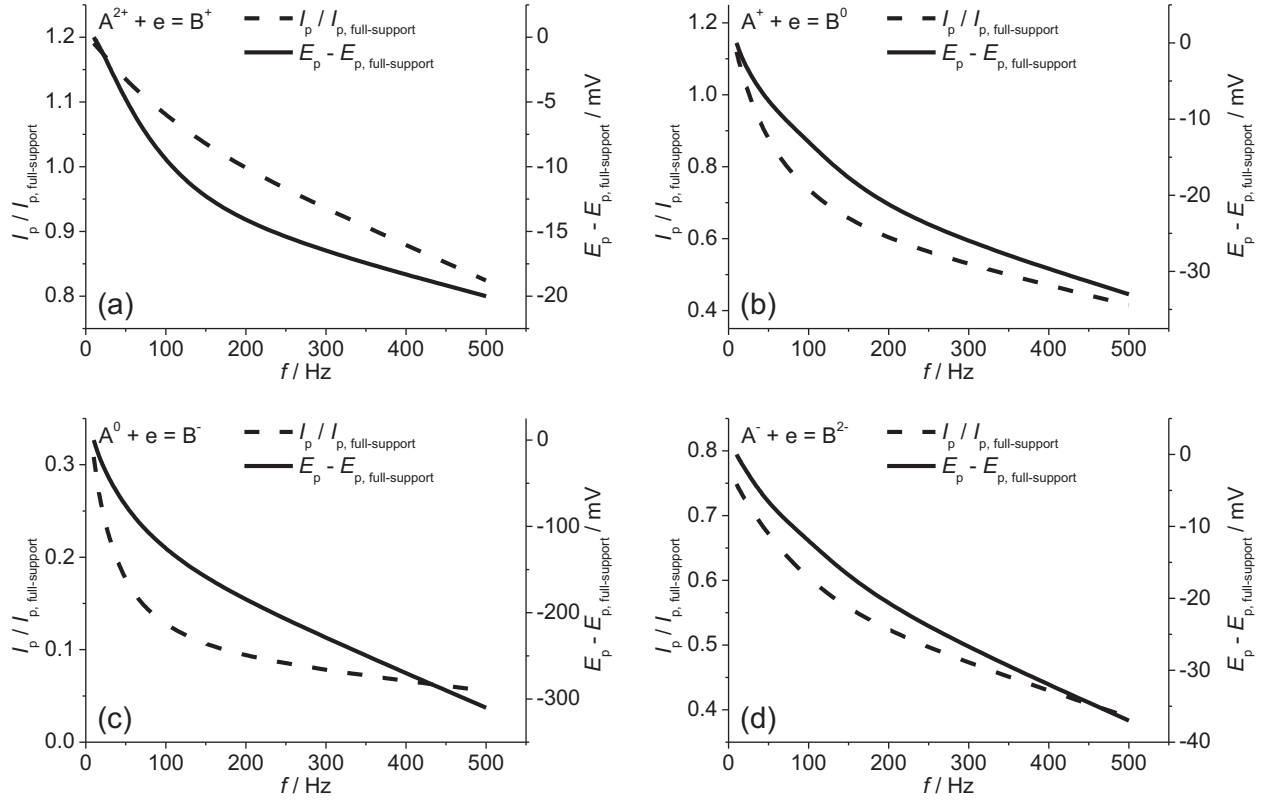


Figure 9.7: Variation of the peak current (I_p) and peak potential (E_p) at $c^*_\mathrm{sup}/c^*_\mathrm{A} = 0.1$ relative to those at full support with the frequency in SWV at hemispherical electrodes. $r_0 = 25$ μm, step potential = 10 mV, amplitude potential = 25 mV.

9.4.2 Experimental results

The above theory was applied to the analysis of experimental DMPV and SWV voltammograms with varying amounts of supporting electrolyte for the electro-reduction of $CoCp_2^+$ in acetonitrile and $CoSep^{3+}$ in water on mercury hemispherical electrodes. Having at our disposal the corresponding theory has enabled rigorous study of the effects of the concentration of supporting electrolyte on the kinetics and thermodynamics of these redox systems.

As can be seen in Figures 9.8-9.11, the experimental results were fitted very satisfactorily with the parameters given in Tables 9.4 and 9.5 in both techniques and in the whole range of support

ratio 2-200. In all conditions, the electrode reaction was found to be "reversible" and no effect of the concentration of supporting electrolyte is observed on the electrode kinetics.

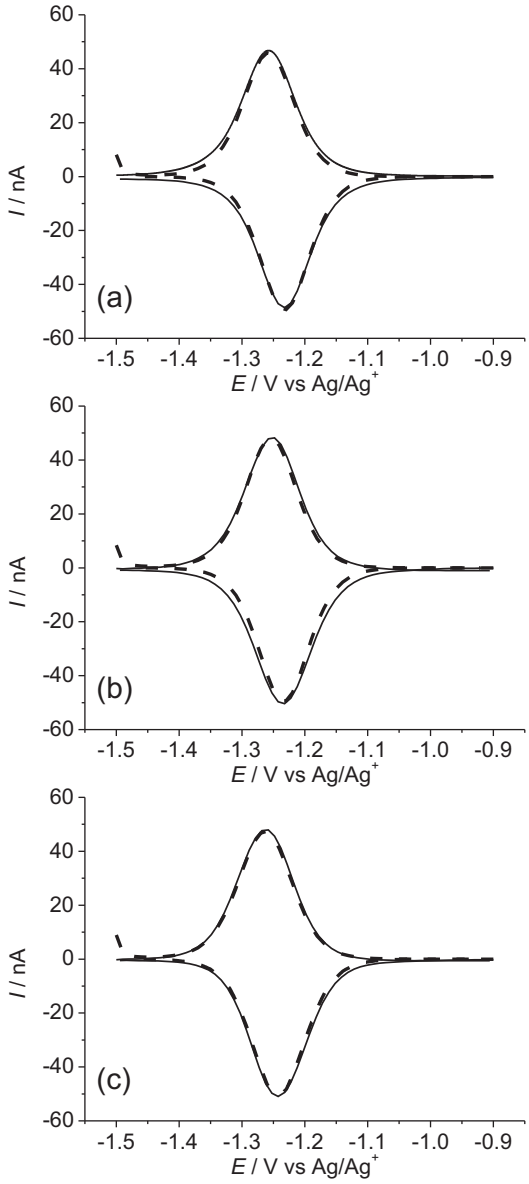


Figure 9.8: Experimental (–), best-fit theoretical (**- -**) differential multipulse voltammograms with different concentrations of TBAP (a. 400 mM, b. 40 mM and c. 4 mM) for 2 mM $CoCp_2PF_6$ acetonitrile solutions. Both forward and backward scans are presented. Modulation time = 16 ms, interval time = 100 ms, step potential = 10 mV, amplitude potential = 25 mV.

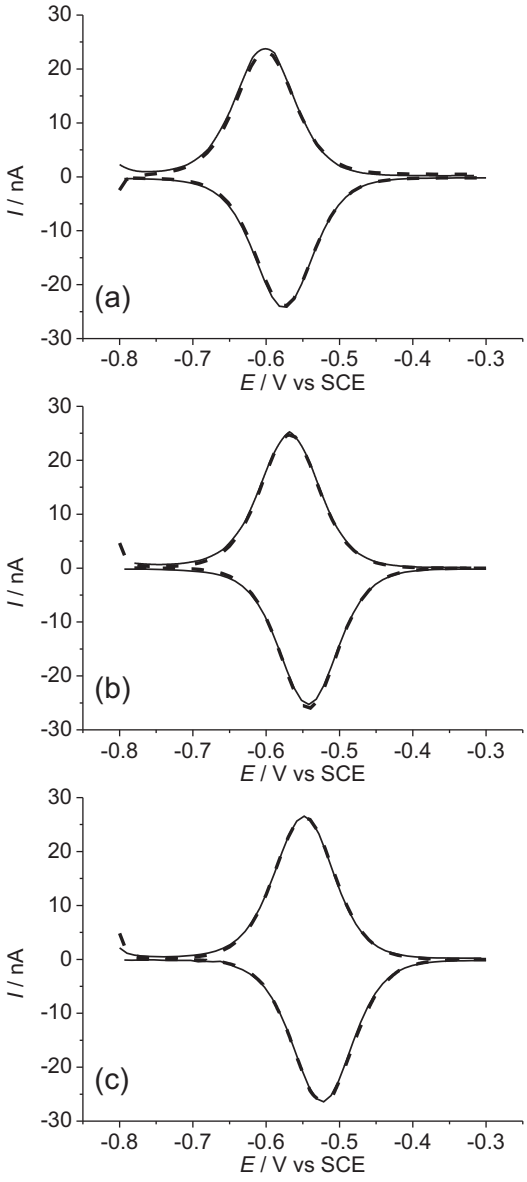


Figure 9.9: Experimental (–), best-fit theoretical (**- -**) differential multipulse voltammograms with different concentrations of KCl (a. 400 mM, b. 40 mM and c. 4 mM) for 2 mM $CoSepCl_3$ aqueous solutions. Both forward and backward scans are presented. Modulation time = 16 ms, interval time = 100 ms, step potential = 10 mV, amplitude potential = 25 mV.

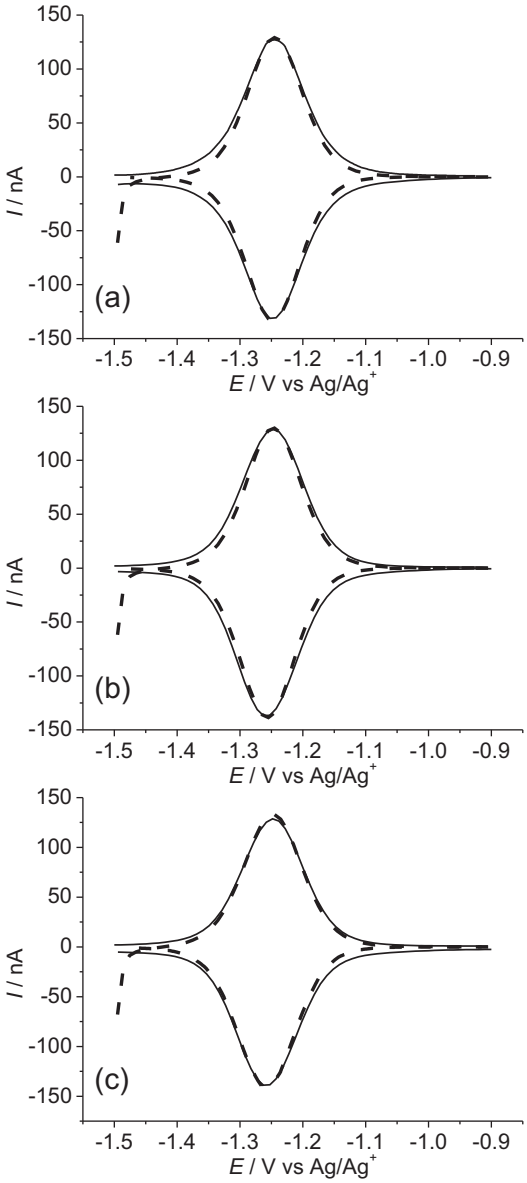


Figure 9.10: Experimental (–), best-fit theoretical (**- -**) square wave voltammograms with different concentrations of TBAP (a. 400 mM, b. 40 mM and c. 4 mM) for 2mM $CoCp_2PF_6$ acetonitrile solutions. Both forward and backward scans are presented. Frequency = 50 Hz, step potential = 10 mV, amplitude potential = 25 mV.

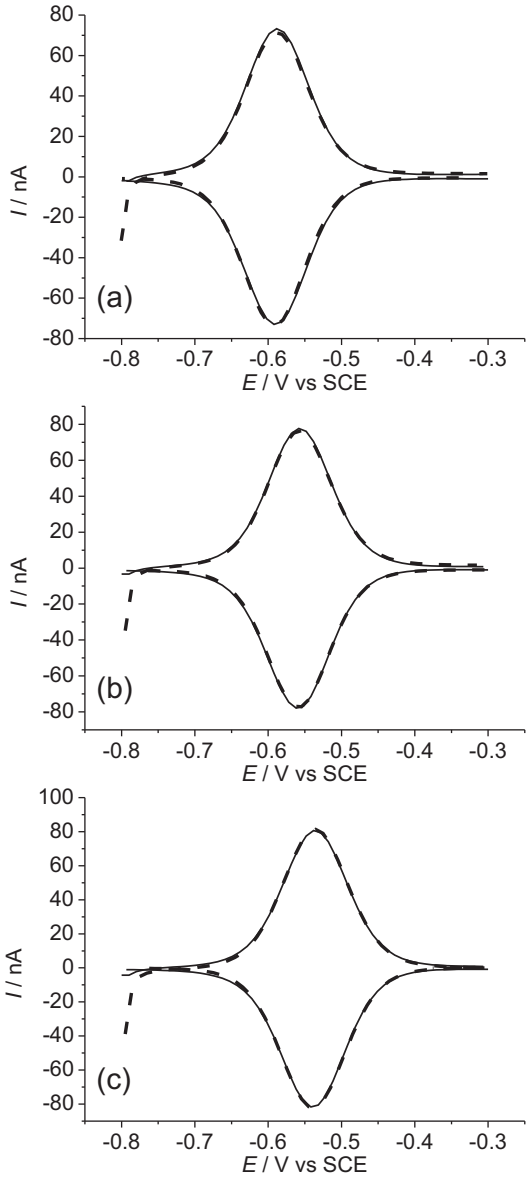


Figure 9.11: Experimental (–), best-fit theoretical (**- -**) square wave voltammograms with different concentrations of KCl (a. 400 mM, b. 40 mM and c. 4 mM) for 2 mM $CoSepCl_3$ aqueous solutions. Both forward and backward scans are presented. Frequency = 50 Hz, step potential = 10 mV, amplitude potential = 25 mV.

Table 9.4: Parameters for the electro-reduction of $CoCp_2^+$ in 2mM acetonitrile solutions and $CoSep^{3+}$ in 2mM aqueous solutions with 4mM, 40mM and 400mM supporting electrolytes on a *ca.* 25 μm radius Hg hemisphere electrode obtained from the best-fit differential multi pulse and square wave voltammograms.

	Parameter	Best-fit value	Reference
$CoCp_2^+$|$CoCp_2$	$D_{CoCp_2^+}$ / 10^{-9} m^2 s^{-1}	1.9 ($\pm$ 0.1)[a]	This work
	D_{CoCp_2} / 10^{-9} m^2 s^{-1}	3.1 ($\pm$ 0.1)[a]	This work
	D_{TBA^+} / 10^{-9} m^2 s^{-1}	2.1	[2]
	$D_{ClO_4^-}$ / 10^{-9} m^2 s^{-1}	3.0	[2]
	k_0 / cm s^{-1}	0.3 ($\pm$ 0.1)[b]	This work
	$\epsilon_{r,MeCN}$[c]	37.5	[11, 57]
$CoSep^{3+}$|$CoSep^{2+}$	$D_{CoSep^{3+}}$ / 10^{-10} m^2 s^{-1}	6.0 ($\pm$ 0.2)[a]	This work
	$D_{CoSep^{2+}}$ / 10^{-10} m^2 s^{-1}	8.9 ($\pm$ 0.2)[a]	This work
	D_{K^+} / 10^{-10} m^2 s^{-1}	1.9	[58]
	D_{Cl^-} / 10^{-10} m^2 s^{-1}	1.9	[58]
	k_0 / cm s^{-1}	>1	This work
	ϵ_{r,H_2O}[c]	78	[59]

[a] From the best-fit values of chronoamperometric curves; error bars were calculated from the standard deviation of several repeat chronoamperograms.

[b] Error bar was calculated from the standard deviation of the best theoretical fits from voltammograms with different modulation times (for DMPV) and frequencies (for SWV).

[c] Relative permittivity of solvent.

Table 9.5: Formal potentials[a] for the electro-reduction of $CoCp_2^+$ in 2mM acetonitrile solutions and $CoSep^{3+}$ in 2mM aqueous solutions with 4mM, 40mM and 400mM supporting electrolytes on a *ca.* 25 μm radius Hg hemisphere electrode from the best-fit differential multi pulse and square wave voltammograms.

	$c_{\text{supporting electrolyte}}$	Best-fit E_f
$CoCp_2^+$|$CoCp_2$	4mM	-1.257$\pm$ 0.001V vs Ag/Ag$^+$
	40mM	-1.256$\pm$ 0.003V vs Ag/Ag$^+$
	400mM	-1.254$\pm$ 0.001V vs Ag/Ag$^+$
$CoSep^{3+}$|$CoSep^{2+}$	4mM	-0.538$\pm$ 0.002V vs SCE
	40mM	-0.562$\pm$ 0.002V vs SCE
	400mM	-0.595$\pm$ 0.001V vs SCE

[a] Error bar was calculated from the standard deviation of the best theoretical fits from voltammograms with different modulation times (for DMPV) and frequencies (for SWV).

With respect to the effects on the voltammograms, as predicted from the theory for these conditions, the decrease of the supporting electrolyte concentration results in a systematic rise of the peak current(see Figures 9.12 and 9.13). The increase is slightly greater for the reduction of $CoSep^{3+}$ with an increase of *ca.* 10 % of the peak current when varying the KCl concentration from 400 mM to 4 mM.

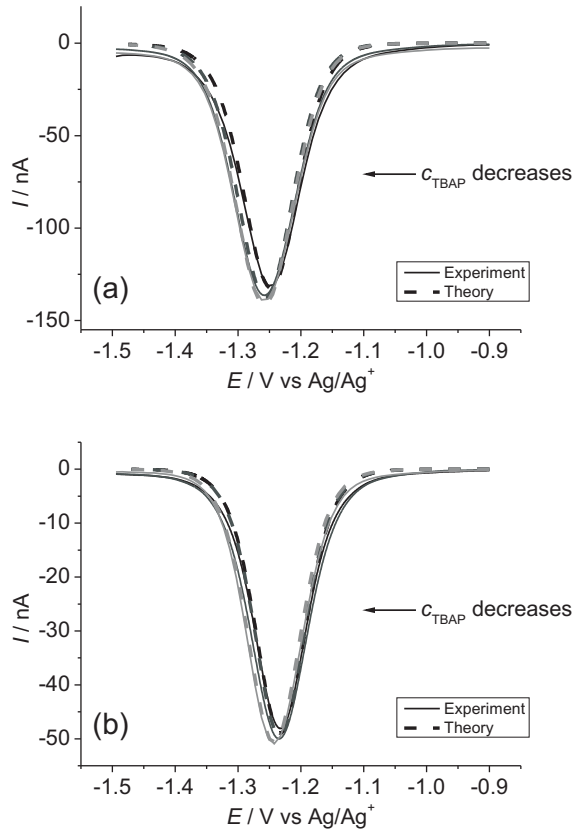


Figure 9.12: Experimental forward a. SWV and b. DMPV with different concentrations of TBAP (400 mM, 40 mM and 4 mM) for 2 mM $CoCp_2PF_6$ acetonitrile solutions. Frequency = 50 Hz (SWV), modulation time = 16 ms (DMPV), interval time = 100 ms (DMPV), step potential = 10 mV, amplitude potential = 25 mV.

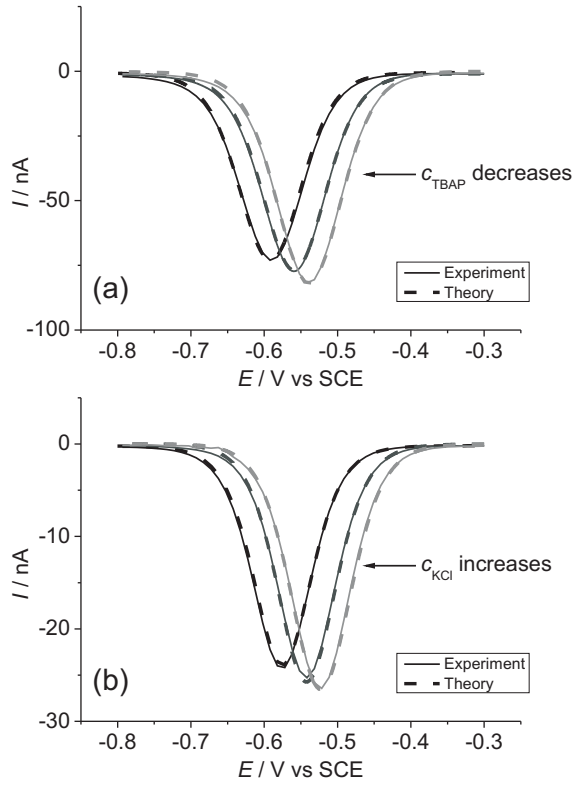


Figure 9.13: Experimental forward a. SWV and b. DMPV with different concentrations of KCl (400 mM, 40 mM and 4 mM) for 2 mM $CoSepCl_3$ aqueous solutions. Frequency = 50 Hz (SWV), modulation time = 16 ms (DMPV), interval time = 100 ms (DMPV), step potential = 10 mV, amplitude potential = 25 mV.

When analyzing the behaviour of the peak potential for the couple $CoSep^{3+}|CoSep^{2+}$ (Figures 9.9, 9.11 and 9.13) one finds that, in spite of the Ohmic drop effects, the peak shifts to more negative values (i.e., greater overpotentials) as the support ratio increases. This is a consequence of the change in the value of the formal potential (see Table 9.5), dependent on the activity coefficients of the electroactive species and therefore on the ionic strength. Thus, the more charged, oxidized species, $CoSep^{3+}$, is further stabilized by the counterions of the supporting electrolyte as reported for the redox couple $Ru(NH_3)_6{}^{3+}|Ru(NH_3)_6{}^{2+}$ in water [56]. Accordingly, when the reduced species is the most charged of a redox pair the formal potential is expected to shift to more positive values when the concentration of supporting electrolyte is increased. This phenomenon was found for the redox couples $IrCl_6{}^{2-}|IrCl_6{}^{3-}$ and $Fe(CN)_6^{3-}|Fe(CN)_6^{4-}$ in water [56].

In the case of the reduction of $CoCp_2^+|CoCp_2$, no significant effects of the supporting electrolyte concentration on the value of the formal potential are inferred from the experimental results.

The study of the variation of the formal potential with the concentration and nature of supporting electrolyte can assist the study of ion-ion interactions by means of electrochemical methods and the determination of standard potentials. Further, the use of low supported media can be beneficial when leading to smaller peak overpotentials.

9.5 Conclusions

Theory for weakly supported media at hemispherical microelectrodes has been applied to square wave voltammetry (SWV) and differential multipulse voltammetry (DMPV). The effects of the absence of supporting electrolyte on the peak current and potential due to the potential drop in solution have been described for different redox systems.

In all cases, the distortion of the voltammograms leads to the shift of the peak towards greater overpotentials as the concentration of supporting electrolyte is diminished. Regarding the peak current, it increases with the supporting electrolyte concentration in the case of the reduction of neutral and anionic species. The behaviour of the peak current for the reduction of cations is more complex due to the nature of the SWV response. Thus, when microelectrodes are employed, greater peak currents are expected for the electro-reduction of cations in weakly supported media, whereas smaller peaks are predicted when large- and medium-sized electrodes are employed. In these last circumstances, the analysis of the forward component of the voltammograms can be more conclusive.

The magnitude of the effects of highly resistive media on the peaks is greater at large electrodes and/or high frequencies due to the greater uncompensated charge in solution. These are also more apparent for neutral species where the compensation of charge by the electroactive species or its counterion (self-support) is not possible.

The experimental study of additional effects of the support ratio on the electrode kinetics and the thermodynamic stability of the electroactive species has also been carried out. Hence, we have applied the theoretical results to the study of the one-electron reductions of cobaltocenium in acetonitrile and cobalt(III)sepulchrate in water at 25 μm mercury microhemispheres. The experimental SWV

and DMPV voltammograms have been fitted satisfactorily extracting the kinetic parameters and the formal potential. The results show that the kinetics of both redox couples are not affected significantly when the support ratio is varied in the range 2-200. In all the conditions fast electron transfers are observed.

On the other hand, the formal potential of the redox couple $CoSep^{3+}|CoSep^{2+}$ is highly affected, with a shift of +57 mV from high to low KCl concentrations. This can be explained through the stabilization of the more charged species by the corresponding counterions of the supporting electrolyte.

This points out the importance of developing theoretical tools to perform electrochemical experiments under varying concentration of supporting electrolyte as a source of information of the interactions of the species in solution. Moreover, the shift of the formal potential to lower values can be beneficial.

References

[1] I. Streeter, R.G. Compton, J. Phys. Chem. C 112 (2008) 13716–13728.

[2] J.G. Limon-Petersen, J.T. Han, N.V. Rees, E.J.F. Dickinson, I. Streeter, R.G. Compton, J. Phys. Chem. C 114 (2010) 2227–2236.

[3] E.J.F. Dickinson, J.G. Limon-Petersen, N.V. Rees, R.G. Compton, J. Phys. Chem. C 113 (2009) 11157–11171.

[4] E.O. Barnes, S.R. Belding, R.G. Compton, J. Electroanal. Chem. 660 (2011) 185–194.

[5] E.O. Barnes, Y. Wang, J.G. Limon-Petersen, S.R. Belding, R.G. Compton, J. Electroanal. Chem. 659 (2011) 25–35.

[6] J.G. Limon-Petersen, E.J.F. Dickinson, T. Doneux, N.V. Rees, R.G. Compton, J. Phys. Chem. C 114 (2010) 7120–7127.

[7] J.G. Limon-Petersen, E.J.F. Dickinson, N.V. Rees, R.G. Compton, J. Phys. Chem. C 113 (2009) 15320–15325.

[8] M. Ciszkowska, Z. Stojek, J. Electroanal. Chem. 466 (1999) 129–143.

[9] M.J. Palys, Z. Stojek, M. Bos, W.E.L. van der, Anal. Chim. Acta 337 (1997) 5–28.

[10] J.J. Watkins, H.S. White, Langmuir 20 (2004) 5474–5483.

[11] S.R. Belding, J.G. Limon-Petersen, E.J.F. Dickinson, R.G. Compton, Angew. Chem. Int. Ed. 49 (2010) 9242–9245.

[12] R.G. Compton, C.E. Banks, Understanding Voltammetry, 2nd edn., Imperial College Press, London, 2011.

[13] R.P. Buck, J. Electroanal. Chem. Interfacial Electrochem 46 (1973) 1–23.

[14] C. Amatore, M.R. Deakin, R.M. Wightman, J. Electroanal. Chem. 220 (1987) 49–63.

[15] C. Amatore, B. Fosset, J. Bartelt, M.R. Deakin, R.M. Wightman, J. Electroanal. Chem. 256 (1988) 255–268.

[16] J.D. Norton, H.S. White, S.W. Feldberg, J. Phys. Chem. 94 (1990) 6772–6780.

[17] W.D. Murphy, J.A. Manzanares, S. Mafé, H. Reiss, J. Phys. Chem. 96 (1992) 9983–9991.

[18] C.P. Smith, H. White, Anal. Chem. 65 (1993) 3343–3353.

[19] A. Jaworski, M. Donten, Z. Stojek, Anal. Chim. Acta 305 (1995) 106–113.

[20] W. Hyk, M. Palys, Z. Stojek, J. Electroanal. Chem. 415 (1996) 13–22.

[21] W. Hyk, Z. Stojek, J. Electroanal. Chem. 439 (1997) 81–88.

[22] M. Ciszkowska, A. Jaworski, J. Osteryoung, J. Electroanal. Chem. 423 (1997) 95–101.

[23] K.B. Oldham, Anal. Chem. 69 (1997) 446–453.

[24] K.B. Oldham, A.M. Bond, J. Electroanal. Chem. 508 (2001) 28–40.

[25] A. Bonnefont, F. Argoul, M.Z. Bazant, J. Electroanal. Chem. 500 (2001) 52–61.

[26] R. He, S. Chen, F. Yang, B. Wu, J. Phys. Chem. B 110 (2006) 3262–3270.

[27] X. Yang, G. Zhang, Nanotechnology 18 (2007) 335201.

[28] O.V. Klymenko, C. Amatore, I. Svir, Anal. Chem. 79 (2007) 6341–6347.

[29] I. Streeter, R.M. Lynden-Bell, R.G. Compton, J. Phys. Chem. C 112 (2008) 14538–14544.

[30] A. Molina, E. Laborda, F. Martinez-Ortiz, D.F. Bradley, D.J. Schiffrin, R.G. Compton, J. Electroanal. Chem. 659 (2011) 12–24.

[31] V. Mirčeski, Š. Komorsky-Lovrić, M. Lovrić, Square-Wave Voltammetry: Theory and Application, Springer, 2007.

[32] R. Gulaboski, V. Mirčeski, M. Lovrić, I. Bogeski, Electrochem. Commun. 7 (2005) 515–522.

[33] V. Pavlova, V. Mirčeski, S. Komorsky-Lovrić, S. Petrovska-Jovanović, B. Mitrevski, Anal. Chim. Acta 512 (2004) 49–56.

[34] D. Jadreško, M. Zelić, M. Lovrić, J. Electroanal. Chem. 645 (2010) 103–108.

[35] F. Garay, M. Lovrić, J. Electroanal. Chem. 518 (2002) 91–102.

[36] F. Garay, M. Lovrić, J. Electroanal. Chem. 527 (2002) 85–92.

[37] A. Molina, C. Serna, F. Martinez-Ortiz, J. Electroanal. Chem. 486 (2000) 9–15.

[38] J.J. O'Dea, J. Osteryoung, R.A. Osteryoung, J. Phys. Chem. 87 (1983) 3911–3918.

[39] A. Molina, J. Gonzalez, E. Laborda, Y. Wang, R.G. Compton, Phys. Chem. Chem. Phys. 13 (2011) 16748–16755.

[40] J. Mauzeroll, E.A. Hueske, A.J. Bard, Anal. Chem. 75 (2003) 3880–3889.

[41] A. Molina, E. Laborda, E.I. Rogers, F. Martinez-Ortiz, C. Serna, J.G. Limon-Petersen, N.V. Rees, R.G. Compton, J. Electroanal. Chem. 634 (2009) 73–81.

[42] Y. Wang, E. Laborda, M.C. Henstridge, F. Martinez-Ortiz, A. Molina, R.G. Compton, J. Electroanal. Chem. 668 (2012) 7–12.

[43] N.G. Tsierkezos, J. Mol. Liq. 138 (2008) 1–8.

[44] J.G. Limon-Petersen, E.J. Dickinson, S.R. Belding, N.V. Rees, R.G. Compton, J. Electroanal. Chem. 650 (2010) 135–142.

[45] C.E. Banks, N.V. Rees, R.G. Compton, J. Electroanal. Chem. 535 (2002) 41–47.

[46] C.E. Banks, R.G. Compton, A.C. Fisher, I.E. Henley, Phys. Chem. Chem. Phys. 6 (2004) 3147–3152.

[47] T.J. Davies, B.A. Brookes, A.C. Fisher, K. Yunus, S.J. Wilkins, P.R. Greene, J.D. Wadhawan, R.G. Compton, J. Phys. Chem. B 107 (2003) 6431–6444.

[48] E.J. Dickinson, R.G. Compton, Chem. Phys. Lett. 497 (2010) 178 – 183.

[49] D.J. Gavaghan, J. Electroanal. Chem. 456 (1998) 1–12.

[50] D.J. Gavaghan, J. Electroanal. Chem. 456 (1998) 13–23.

[51] D.J. Gavaghan, J. Electroanal. Chem. 456 (1998) 25–35.

[52] I.B. Svir, A.I. Oleinick, R.G. Compton, Radiotekhnika 116 (2001) 114.

[53] J. Crank, E. Nicolson, Proc. Camb. Phil. Soc. 43 (1947) 50–67.

[54] M. Störzbach, J. Heinze, J. Electroanal. Chem. 346 (1993) 9242–9245.

[55] S.R. Belding, J.G. Limon-Petersen, E.J.F. Dickinson, R.G. Compton, Angew. Chem. Int. Ed. 49 (2010) 9242–9245.

[56] C. Beriet, D. Pletcher, J. Electroanal. Chem. 375 (1994) 213–218.

[57] G. Ritzoulis, N. Papadopoulos, D. Jannakoudakis, J. Chem. Eng. Data 31 (1986) 146–148.

[58] V.M.M. Lobo, A.C.F. Ribeiro, L.M.P. Verissimo, J. Mol. Liq. 78 (1998) 139–149.

[59] F. Hernández-Luis, R. Rodríguez-Raposo, D. Grandoso, J. Chem. Eng. Data 56 (2011) 3940–3948.

Part V Comparative Study of Butler-Volmer and Marcus-Hush Kinetics

The exploration of electrochemical kinetics is an important function of electroanalytical chemistry. There is an ongoing interest in investigating the merits and faults of the two main theories, the Butler-Volmer and Marcus-Hush formalisms. This part presents a comparison between these two theories and improvements of our understanding of electrochemical kinetics.

Chapter 10 An Experimental Comparison of the Marcus-Hush and Butler-Volmer Descriptions of Electrode Kinetics Applied to Cyclic Voltammetry. the One Electron Reductions of Europium (III) and 2-Methyl-2-Nitropropane Studied at A Mercury Microhemisphere Electrode

The work presented in this chapter was carried out in collaboration with

- **M.C. Henstridge, J.G. Limon-Petersen, and E. Laborda** (for the theory and modelling parts)

and has been published in:

M.C. Henstridge, Y. Wang, J.G. Limon-Petersen, E. Laborda, R.G. Compton, Chem. Phys. Lett. 517 (2011) 29–35

We present a comparative experimental evaluation of the Butler-Volmer and Marcus-Hush models using cyclic voltammetry at a microelectrode. Numerical simulations are used to fit experimental voltammetry of the one electron reductions of europium (III) and 2-methyl-2-nitropropane, in water and acetonitrile respectively, at a mercury microhemisphere electrode. For Eu(III) very accurate fits to experiment were obtained over a wide range of scan rates using Butler-Volmer kinetics, whereas the Marcus-Hush model was less accurate. The reduction of 2-methyl-2-nitropropane was well simulated by both models, however Marcus-Hush required a reorganisation energy lower than expected.

10.1 Introduction

The Butler-Volmer theory [1, 2] of electron transfer kinetics has proved very successful in the analysis of electron transfer for a wealth of systems and has become the standard kinetic model for electrochemical simulation. The model relates the rate of electron transfer to a standard heterogeneous rate constant,

k_0, and two transfer coefficients α (for reduction) and β (for oxidation), which obey $\alpha + \beta = 1$ for a one-electron process. This leads to the familiar classical interpretation of the transfer coefficients as indicating the "position" of the transition state on the reaction coordinate between reactants and products. [3]

Despite its widespread usage and numerous successes, Butler-Volmer theory does have its defects. Notably it predicts that the rate of electron transfer should continue following an exponential dependence on overpotential ad infinitum. A further drawback of the Butler-Volmer approach is that, due to its phenomenological nature, it offers limited physical insight into the process it describes.

By way of contrast, Marcus theory [4–9] has developed to cover a huge variety of electron transfer reactions, many aspects of which have been verified experimentally, not least the prediction of the existence of the so-called "inverted region" and the theoretical basis of curved Tafel plots. [10, 11] By relating the standard heterogeneous rate constant to a reorganisation energy, it has provided a more insightful physical model for understanding the rate of electron transfer as well as a means of its calculation. The total reorganisation energy may be divided into inner sphere and outer sphere contributions, the inner sphere reorganisation energy may then be calculated by consideration of changes in molecular geometry (e.g. using density functional theory) and the outer-sphere (solvent) reorganisation energy from the Born-Marcus solvation equation.

Following Chidsey's work, [11] which built upon earlier theoretical works [12] and is widely regarded as seminal, the Marcus-Hush approach has become increasingly widespread. This treatment considers Marcusian electron transfer between the redox species and the continuum of energy levels in the electrode. Its prediction of a finite limiting rate constant at high overpotential, which is in contrast to both the Butler-Volmer model and conventional Marcus theory, has been observed experimentally for many systems within the context of potential step chronoamperometry for surface bound species. [11, 13–16] Feldberg has recently published theoretical work concerning the limits in which Butler-Volmer and Marcus-Hush formalisms are indistinguishable for steady state voltammetry in solution [17] and Oldham has published work concerning an approximation to the Marcus-Hush integral, [18] but

comparative experimental studies have been limited for redox systems in the solution phase. [19]

We have previously compared the Marcus-Hush (MH) and Butler-Volmer (BV) formalisms using pulse voltammetry. [20] The one electron reduction of 2-methyl-2-nitropropane (MeNP) was studied using reverse scan square wave voltammetry. Using BV kinetics it was possible to fit the experimental data satisfactorily, however MH kinetics could not fit both peaks simultaneously for any value of reorganisation energy.

Given the clear distinction made between BV and MH kinetics under pulse voltammetry the question arises as to the extent to which similar contrasts might be revealed by using cyclic voltammetry which is by far the most popular voltammetric method employed by both electrochemists and non-specialists. In this chapter we undertake a similar comparison of the two kinetic formalisms using cyclic voltammetry. We again study the one electron reduction of MeNP in acetonitrile, as well as the one electron reduction of europium (III) chloride in aqueous solution, both at a mercury microhemisphere electrode. These systems were chosen due to their irreversible kinetics and literature α values which deviate from $\frac{1}{2}$, [21, 22] such systems are predicted to produce the most marked differences in the two kinetic models. [17] Experimental voltammetry was fitted using numerical simulations for both the BV and MH models. In particular we focus on fitting the entire cyclic voltammetric waveshape to identify significant differences between the two kinetic models. We do not seek curved Tafel plots [23] and no a priori assumptions are made, in contrast with earlier work [24] which extracts effective rate constants as a function of potential which are not inconsistent with Marcus theory.

The enhanced mass transport properties of microelectrodes (as opposed to macroelectrodes) make them ideal for use in kinetic investigations such as this. [3] The use of a mercury microhemisphere electrode made it possible to verify, *via* simulation using programs developed previously, [25] that all experimental solutions contained sufficient supporting electrolyte to be considered diffusion-only systems. Owing to its one-dimensional symmetry, cyclic voltammetry at a hemispherical electrode is also much faster, more accurate and more straightforward to simulate than voltammetry at the more conventional microdisc, allowing fitting of the entire voltammetric wave. In this way we show

that measurable differences between simple MH kinetics and BV kinetics are apparent even in cyclic voltammetry.

10.2 Experimental Methods

A three electrode cell was used. Hemispherical mercury ultramicroelectodes were used (radius 50 μm for Eu(III) and radius 25 μm for MeNP) as the working electrode. A platinum wire was used as a counter electrode and a silver wire was used as the pseudo-reference electrode in non-aqueous solutions, a saturated calomel electrode electrode (SCE, Radiometer, Copenhagen) was used instead in aqueous solutions. All electrochemical experiments were carried out at 298 K.

Europium (III) chloride (Aldrich, 99.99%), 2-methyl-2-nitropropane (Aldrich, 99%), potassium chloride (Aldrich, >99%), tetra-n-butylammonium perchlorate (TBAP, Aldrich, >99%) and acetonitrile (Fischer Scientific, HPLC grade) were all used as received with no further purification. Aqueous solutions were made up using water of resistivity not less than 18.2 MΩ cm^{-1} at 298 K (Millipore, UK).

All solutions were thoroughly deoxygenated, for at least 30 minutes, with nitrogen pre-saturated with the corresponding solvent.

10.3 Experimental Results

10.3.1 Quantifying quality of fit

In order to quantify agreement between simulation and experiment, a mean scaled absolute deviation (MSAD) was calculated for each voltammogram, [26] which is defined by:

$$\% \text{ MSAD} = \frac{1}{n} \sum_{n} \left| \frac{i_{\text{exp}} - i_{\text{sim}}}{i_{\text{exp}}} \right| \times 100 \tag{10.1}$$

where i_{exp} and i_{sim} are experimental and simulated current respectively and n is the number of data points. Since the points of the simulated voltammetry are not necessarily aligned at the same potential

values as those of the experimental voltammetry, spline interpolation was used to calculate i_{sim} at the potentials of the experimental points. Additionally a narrow strip of the experimental voltammetry near $i = 0$ was omitted from the MSAD calculations because dividing by a very small value of i_{exp} yields a very large value of MSAD even if $i_{\text{exp}} - i_{\text{sim}}$ is small.

10.3.2 The one electron reduction of Eu(III)

In order to study the system $\text{Eu}^{3+}_{\text{aq}} + \text{e} \rightleftharpoons \text{Eu}^{2+}_{\text{aq}}$, cyclic voltammetry (CV) was carried out over a wide range of voltage scan rates (10 mV s^{-1} to 1 V s^{-1}) on a 1 mM aqueous solution of europium (III) chloride containing 0.4 M potassium chloride as supporting electrolyte. Prior to attempting theoretical fitting of the experimental data the diffusion coefficients of Eu^{3+} and Eu^{2+} were determined via double potential step chronoamperometry at the Hg microhemisphere. The resulting transient was fitted for both diffusion coefficients and the concentration using a previously reported program [27] based on the Shoup & Szabo expression. [3] The diffusion coefficients for Eu^{3+} and Eu^{2+} were found to be 6.4×10^{-6} cm^2 s^{-1} and 9.0×10^{-6} cm^2 s^{-1} respectively at 298 K, in excellent agreement with literature values. [28–30]

Although the Shoup & Szabo expression assumes infinite electrode kinetics at high overpotentials, its use was justified as follows: the Shoup & Szabo value for the diffusion coefficient was used in fitting the experimental CV data. Once fitting was completed the best fit values for k_0 were substituted into a second potential step program, based upon finite electrode kinetics, [31] to fit the same chronoamperometric transient fitted previously. For both BV and MH cases the diffusion coefficient was found to be effectively equal to that originally obtained from Shoup & Szabo.

Supplementary CV simulations were carried out to check the validity of simulating the system as "diffusion-only". These simulations used a previously reported program which solves the Nernst-Planck-Poisson system of equations and thus does not neglect migration. There was no observable difference between the diffusion-only simulations and the diffusion-migration simulations for the support ratios used in the present experiments, thus we consider the system fully supported and the diffusion-only approximation assumed valid. [32]

Additional experiments were also carried out to discount possible double layer effects, so-called "Frumkin effects", [33] which could potentially have minor distorting effects on the voltammetry. Cyclic voltammetry was carried out for both 1 mM and 2 mM analyte in a range of supporting electrolyte concentrations (0.1 M – 1.0 M). When this voltammetry was fitted (using Butler-Volmer kinetics) negligible and non-systematic variation was seen for both k_0 and α. We therefore exclude possible Frumkin effects. This experimental justification is also supported by recent theoretical work [34] which considers electron transfer occurring at a range of distances from the electrode (rather than at a single distance as in Frumkin's original work [33]). This work indicates that the inclusion of this range of tunneling distances acts so as to substantially mitigate the predicted effects. Thus the experimental voltammetry was further analysed without consideration of Frumkin effects.

Experimental Eu(III) voltammetry is shown for two different scan rates in Figure 10.1, along with best fit simulations using both Butler-Volmer and Marcus-Hush kinetics.

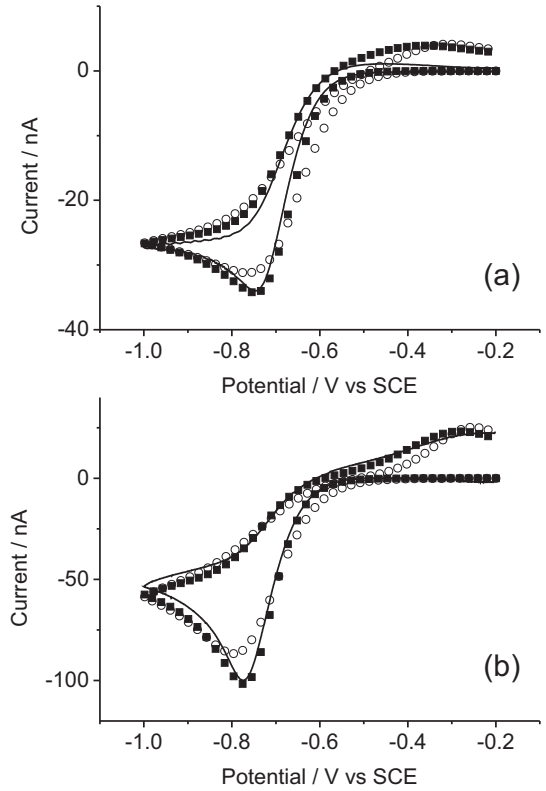


Figure 10.1: Comparison of experimental Eu(III) voltammetry (line) with best fit simulations using Butler-Volmer (■) and Marcus-Hush (○) kinetics. Parameters are given in Table 10.1. (a) 50 mV s^{-1} (b) 1000 mV s^{-1}.

For the BV model, the best fit kinetic parameters were $k_0 = 3.5 \times 10^{-4}$ cm s^{-1} and $\alpha = 0.65$,

which are in good agreement with values found in the literature. [29] Figure 10.1 clearly shows good agreement between simulation and experiment across a wide range of scan rates. At high scan rates a very close fit is achieved throughout the entirety of the voltammetric transient, with both the peak potential and peak current being accurately reproduced by simulations on the forward sweep, although at low scan rates the reverse peak current is overestimated by the simulations. Quantitative analysis of the fits yielded a small MSAD value of 9.4%.

The best fit achieved using MH kinetics used $k_0 = 2.0 \times 10^{-4}$ cm s^{-1} and $\lambda = 2.0$ eV. This value of λ is equal to a value calculated using the Arrhenius and Marcus relations from k_0 by Elzanowska et al. [21] Similar values for reorganisation energy, between 1.0 and 3.0 eV, have also been reported for numerous other metals. [35]

Figure 10.1 shows that for both high and low scan rates fits the experimental data is not fitted as accurately as was the case for BV kinetics. The forward peak current is too low and the peak too broad across the whole scan rate range. The simulated voltammetry fits the back peaks more closely than the forward, but the oxidative peak current is overestimated at all scan rates. Despite the large discrepancy between simulation and experiment, it was not possible to obtain a better fit. With both reactant and product diffusion coefficients fixed via double potential step experiments and k_0 fixed to a large degree by the peak separation, λ is the only remaining parameter able to effect a change in the voltammetric waveshape. The MSAD value calculated for the MH model was 20.3%, more than double the value obtained for the BV simulations.

This *relative* inability of MH kinetics to accurately fit the experimental voltammetry is, perhaps, not surprising. As discussed in the Theoretical Results section, there is no equivalence between MH kinetics (for any λ) and BV kinetics using a value of α which significantly deviates from $\frac{1}{2}$. Given that the experimental voltammetry was fitted well when using BV kinetics with $\alpha = 0.65$, it was unlikely that it would be possible to accurately fit the experimental data using MH kinetics.

Table 10.1: Simulation parameters for the reduction of Eu(III).

	Butler-Volmer	Marcus-Hush
k_0 / cm s^{-1}	3.5×10^{-4}	2.0×10^{-4}
α	0.65	–
λ / eV	–	2.0
$E^{0'}$ / V	-0.59	-0.52
% MSAD	9.4 ± 2.3	20.3 ± 2.8

10.3.3 The one electron reduction of 2-methyl-2-nitropropane (MeNP)

Next, we consider the system MeNP + e $\rightleftharpoons$ $MeNP^{\bullet -}$. Cyclic voltammetry was next carried out on a 2 mM solution of 2-methyl-2-nitropropane in acetonitrile containing 0.1 M TBAP as supporting electrolyte. Again a wide range of scan rates was studied, from 10 mV s^{-1} to 10 V s^{-1}, which encompassed steady-state to fully transient voltammetric responses. The diffusion coefficients of MeNP and $MeNP^{\bullet -}$ were determined via fitting of double potential step chronoamperometric transients using the same procedure described above for Eu(III). The values for MeNP and $MeNP^{\bullet -}$ were both found to be 2.7×10^{-5} cm^2 s^{-1}, in excellent agreement with literature values. [36] There was no observed systematic shift in either $E^{0'}$ or k_0 with scan rate; thus ohmic drop was assumed to be negligible. Again, diffusion-migration simulations proved indistinguishable from diffusion-only simulations for the support ratio used in these experiments, as expected given that MeNP is uncharged.

The experimental voltammetry is shown for two different scan rates in Figure 10.2, along with best fit simulations for both Butler-Volmer and Marcus-Hush kinetics.

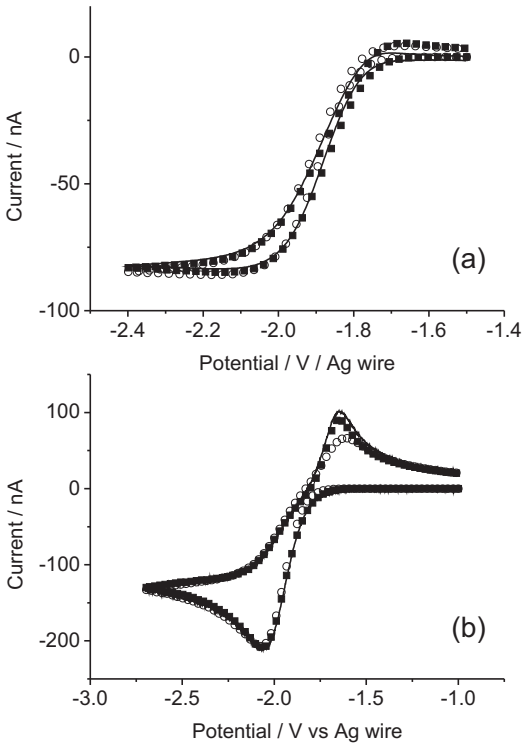


Figure 10.2: Comparison of experimental MeNP voltammetry (line) with best fit simulations using Butler-Volmer (■) and Marcus-Hush (○) kinetics. Parameters are given in Table 10.2. (a) 50 mV s^{-1} (b) 5000 mV s^{-1}.

Figure 10.2 shows that, as was the case for Eu(III), the voltammetry of MeNP was fitted very well using BV kinetics. The best fit values of k_0 and α were 3.2×10^{-3} cm s^{-1} and 0.38 respectively, both in close agreement with literature values. [20, 22, 37, 38] It can be seen that these simulations fit the experimental peak potentials and peak currents at high scan rates very closely and accurate reproduction of the steady-state current is also observed at low scan rate. This impressive agreement between simulation and experiment is reflected by the small MSAD value of 4.3%.

The best fit achieved using the MH model used $\lambda = 0.5$ eV and $k_0 = 3.2 \times 10^{-3}$ cm s^{-1} (Figure 10.2). These simulations yielded an MSAD value of 6.7% which is larger than was achieved by the BV fit. Almost perfect agreement is observed between simulation and experiment at high scan rate for the forward scan, but the simulated back peak is much smaller than experiment. At lower scan rates the MH fits are comparable to those produced by the BV model, but with a steady state current which is slightly larger than is observed experimentally.

This value of λ, however, is smaller than the theoretical outer sphere reorganisation energy alone,

calculated to be 1.6 eV using:

$$\lambda_{\mathrm{os}} = \frac{N_{\mathrm{A}} e^2}{8\pi\epsilon_0 r}\left(\frac{1}{\epsilon_{\mathrm{op}}} - \frac{1}{\epsilon_{\mathrm{s}}}\right) \tag{10.2}$$

using the spherical approximation of the Stokes-Einstein equation [39–42]

$$r = \frac{k_{\mathrm{B}} T}{6\pi\eta D} \tag{10.3}$$

where r is the molecular radius here treated as the solvodynamic radius according to Clegg et al, [40] ϵ_0 is the permittivity of free space, ϵ_{op} and ϵ_{s} are the optical and static frequency components of the dielectric permittivity of the solvent, η is the solvent viscosity and D the diffusion coefficient. N_{A}, e, k_{B} and T have their usual meanings.

From these equations λ_{os} for this system was found to be much larger than the value used to obtain the best fit. Voltammetry simulated using this larger value of 1.6 eV, which still assumes a negligible inner sphere contribution to λ, is shown in Figure 10.3. It can be seen that while the agreement between simulation and experiment for the back peak at high scan rates is improved by a larger peak current, the forward peak is now too large and fits less well than for the lower λ value. At lower scan rates the steady state current is also noticeably larger than the experimental value. The overall result is an increased MSAD value of 7.1%.

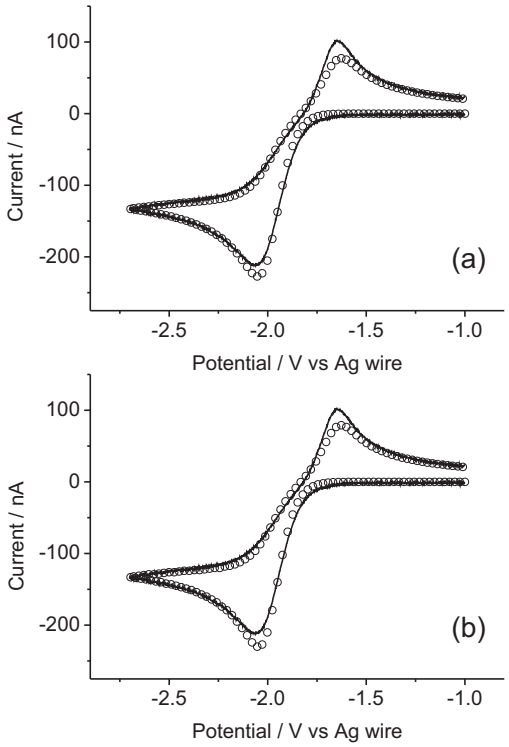


Figure 10.3: Comparison of experimental MeNP voltammetry (line) with simulations using Marcus-Hush kinetics (○), scan rate is 5000 mV s^{-1}. (a) $\lambda = 1.6$ eV (b) $\lambda = 2.5$ eV. Other parameters are given in Table 10.2.

Furthermore, DFT calculations [38] have shown that the *inner* sphere reorganisation for the reduction of MeNP has a value of approximately 0.9 eV, far from negligible. Further increasing λ to 2.5 eV, considering both inner and outer sphere reorganisation, results in an even higher overall MSAD value of 7.2% (Figure 10.3), demonstrating that simulations using MH kinetics with physically meaningful values of reorganisation energy may, in some cases, less accurately model the real physical process!

Table 10.2: Simulation parameters for the reduction of 2-methyl-2-nitropropane.

	Butler-Volmer	Marcus-Hush		
	Best fit	$\lambda_{\text{best fit}}$	λ_{os}	$\lambda_{\text{is}} + \lambda_{\text{os}}$
k_0 / cm s^{-1}	3.2×10^{-3}	3.2×10^{-3}	3.2×10^{-3}	3.2×10^{-3}
α	0.38	–	–	–
λ / eV	–	0.5	1.6	2.5
$E^{0'}$ / V (vs Ag)	-1.825	-1.83	-1.83	-1.83
% MSAD	4.3 ± 2.3	6.7 ± 3.4	7.1 ± 3.5	7.2 ± 3.6

The inability of the MH formalism to fit both experimental peaks simultaneously for any value of λ, which has been reported previously for this system, [20] is again not unexpected considering the fits for BV kinetics use a value of α which significantly deviates from $\frac{1}{2}$. This is a key indication that

when using simple three parameter models ($E^{0'}, k_0, \alpha$ in the case of BV kinetics or $E^{0'}, k_0, \lambda$) in the case of MH kinetics), while the Marcus-Hush model likely gives better physical insight, its application may not best *parameterise* voltammetric data in all cases.

A possible route to improving the ability of the MH model to parameterise experimental voltammetry would be to remove Chidsey's assumption [11] that the forward and back reactions have the same reorganisation energy. Through the use of non-symmetrised Marcus theory, [9] and the introduction of a second reorganisation energy (one for the forward reaction and another for the back reaction), it may be possible for the MHC model to better better parameterise electrochemical reactions while still giving physical insight into the underlying processes. It is also possible, however, that an additional parameter would only make fitting more difficult and raise possible questions of the uniqueness of sets of parameters which fit experimental data.

10.4 Conclusions

We have undertaken a comparison of the Butler-Volmer and Marcus-Hush kinetic formalisms using cyclic voltammetry at a microelectrode. We have shown that for both experimental systems studied, despite its limitations, the use of Butler-Volmer kinetics using literature values of k_0 and α afforded accurate fitting of the experimental data. Comparable fitting was also possible for some systems using Marcus-Hush kinetics, however in order to achieve this it was necessary to discard both literature and calculated values of reorganisation energy in favour of using λ purely as a further fitting parameter, yielding physically unrealistic values. Thus, as was found to be the case using pulse voltammetry, the Marcus-Hush formalism, in its current form, has proven less well suited for the *parameterisation* of solution-phase voltammetry than the Butler-Volmer model. That said, the Marcusian approach arguably remains more physically insightful.

As discussed by Marcus in his 1965 paper, [9] the effect of the forward and back reactions having different reorganisation energies will be for α to deviate from $\frac{1}{2}$ at zero overpotential. This could indicate that using this non-symmetrised formulation of Marcus theory, when applied to heterogeneous

electron transfer, could lead to a kinetic model which retains its physical insight whilst also accurately parameterising electrochemical data. [43] Some work has been done in this area, [44–48] but as yet there is no formulation which is as easily applied as the Marcus-Hush model considered in this work.

References

[1] T. Erdey-Grúz, M. Volmer, Z. Physik Chem. 150 (1930) 203–213.

[2] J.A.V. Butler, Trans. Faraday Soc. 28 (1932) 379–382.

[3] R.G. Compton, C.E. Banks, Understanding voltammetry, 2nd edn., Imperial College Press, London, 2010.

[4] R.A. Marcus, J. Chem. Phys. 24 (1956) 966–978.

[5] R.A. Marcus, J. Chem. Phys. 24 (1956) 979–989.

[6] R.A. Marcus, J. Chem. Phys. 26 (1957) 867–871.

[7] R.A. Marcus, J. Chem. Phys. 26 (1957) 872–877.

[8] R.A. Marcus, J. Phys. Chem. 67 (1963) 853–857.

[9] R.A. Marcus, J. Chem. Phys. 43 (1965) 679–701.

[10] J.R. Miller, L.T. Calcaterra, G.L. Closs, J. Am. Chem. Soc. 106 (1984) 3047–3049.

[11] C.E.D. Chidsey, Science 251 (1991) 919–922.

[12] J. Hale, J. Electroanal. Chem. 19 (1968) 315 – 318.

[13] J.F. Smalley, M.D. Newton, S.W. Feldberg, J. Electroanal. Chem. 589 (2006) 1–6.

[14] H.O. Finklea, L. Liu, M.S. Ravenscroft, S. Punturi, J. Phys. Chem. 100 (1996) 18852–18858.

[15] J. Hirst, F.A. Armstrong, Anal. Chem. 70 (1998) 5062–5071.

[16] P. Fristrup, M. Grubb, J. Zhang, H. Christensen, A. Hansen, J. Ulstrup, J. Electroanal. Chem. 511 (2001) 128–133.

[17] S.W. Feldberg, Anal. Chem. 82 (2010) 5176–5183.

[18] K.B. Oldham, J.C. Myland, J. Electroanal. Chem. 655 (2011) 65–72.

[19] J.N. Richardson, J. Harvey, R.W. Murray, J. Phys. Chem. 98 (1994) 13396–13402.

[20] E. Laborda, Y. Wang, M.C. Henstridge, F. Martinez-Ortiz, A. Molina, R.G. Compon, Chem. Phys. Lett. 512 (2011) 133–137.

[21] H. Elzanowska, Z. Galus, Z. Borkowska, J. Electroanal. Chem. 157 (1983) 251–268.

[22] D.A. Corrigan, D.H. Evans, J. Electroanal. Chem. 106 (1980) 287–304.

[23] S. Fletcher, T.S. Varley, Phys. Chem. Chem. Phys. 13 (2011) 5359–5364.

[24] J. Savéant, D. Tessier, Faraday Discuss. Chem. Soc. 74 (1982) 57–72.

[25] E.J.F. Dickinson, J.G. Limon-Petersen, N.V. Rees, R.G. Compton, J. Phys. Chem. C 113 (2009) 11157–11171.

[26] N.V. Rees, O.V. Klymenko, B.A. Coles, R.G. Compton, J. Electroanal. Chem. 534 (2002) 151–161.

[27] O.V. Klymenko, R.G. Evans, C. Hardacre, I.B. Svir, R.G. Compton, J. Electroanal. Chem. 571 (2004) 211–221.

[28] B. Timmer, M. Sluyters-Rehbach, J. Sluyters, J. Electroanal. Chem. 14 (1967) 181–191.

[29] W.F. Kinard, R.H. Philp, J. Electroanal. Chem. 25 (1970) 373–379.

[30] T. Rabockai, Electrochim. Acta 22 (1977) 489–490.

[31] S.R. Belding, E.I. Rogers, R.G. Compton, J. Phys. Chem. C 113 (2009) 4202–4207.

[32] S.R. Belding, J.G. Limon-Petersen, E.J.F. Dickinson, R.G. Compton, Angew. Chem. Int. Ed. 49 (2010) 9242–9245.

[33] A.N. Frumkin, Electrochim. Acta 9 (1964) 465–476.

[34] E.J.F. Dickinson, R.G. Compton, J. Electroanal. Chem. 661 (2011) 198–212.

[35] J.O. Bockris, S.U.M. Khan, D.B. Matthews, J. Res. Inst. Catalysis. Hokkaido Univ. 22 (1974) 1–21.

[36] J. Savéant, D. Tessier, J. Electroanal. Chem. 65 (1975) 57–66.

[37] D.H. Evans, A.G. Gilicinski, J. Phys. Chem. 96 (1992) 2528–2533.

[38] C. Kraiya, P. Singh, D.H. Evans, J. Electroanal. Chem. 563 (2004) 203–212.

[39] A.D. Clegg, N.V. Rees, O.V. Klymenko, B.A. Coles, R.G. Compton, ChemPhysChem 5 (2004) 1234–1240.

[40] A.D. Clegg, N.V. Rees, O.V. Klymenko, B.A. Coles, R.G. Compton, J. Am. Chem. Soc. 126 (2004) 6185–6192.

[41] A.D. Clegg, N.V. Rees, O.V. Klymenko, B.A. Coles, R.G. Compton, J. Electroanal. Chem. 580 (2005) 78–86.

[42] N.V. Rees, A.D. Clegg, O.V. Klymenko, B.A. Coles, R.G. Compton, J. Phys. Chem. B 108 (2004) 13047–13051.

[43] M.C. Henstridge, E. Laborda, N.V. Rees, R.G. Compton, Electrochim. Acta 84 (2012) 12–20.

[44] O.A. Petrii, R.R. Nazmutdinov, M.D. Bronshtein, G.A. Tsirlina, Electrochim. Acta 52 (2007) 3493 – 3504.

[45] H.X. Zhou, A. Szabo, J. Chem. Phys. 103 (1995) 3481–3494.

[46] D.V. Matyushov, G.A. Voth, J. Chem. Phys. 113 (2000) 5413–5424.

[47] D.W. Small, D.V. Matyushov, G.A. Voth, J. Am. Chem. Soc. 125 (2003) 7470–7478.

[48] D.V. Matyushov, J. Phys. Chem. B 110 (2006) 10095–10104.

Chapter 11 Quantitative Weaknesses of the Marcus-Hush Theory of Electrode Kinetics Revealed by Reverse Scan Square Wave Voltammetry: the Reduction of 2-Methyl-2-Nitropropane at Mercury Microelectrodes

The work presented in this chapter was carried out in collaboration with

- **E. Laborda, F. Martinez-Ortiz, A. Molina** and **M.C. Henstridge** (for the theory and modelling parts)

and has been published in:

E. Laborda, Y. Wang, M.C. Henstridge, F. Martinez-Ortiz, A. Molina, R.G. Compton, Chem. Phys. Lett. 512 (2011) 133–137

The Marcus-Hush and Butler-Volmer kinetic electrode models are compared experimentally by studying the reduction of 2-methyl-2-nitropropane in acetonitrile at mercury microelectrodes using Reverse Scan Square Wave Voltammetry. This technique is found to be very sensitive to the electrode kinetics and to permit critical comparison of the two models.

The Butler-Volmer model satisfactorily fits the experimental data whereas Marcus-Hush does not quantitatively describe this redox system.

11.1 Introduction

We consider a heterogeneous electrochemical reaction so that species O is reduced to species R at the surface of an electrode:

$$O + e^- \underset{k_{ox}}{\overset{k_{red}}{\rightleftharpoons}} R \tag{11.1}$$

For modelling the kinetics of the electron transfer between an electroactive species in solution and a metal electrode, different approaches has been developed, the Butler-Volmer (BV) [1, 2] and Marcus-Hush (MH) [3–7] models being the most commonly used for electrochemical studies.

The BV model has a simpler mathematical and conceptual background whereas Marcus-Hush provides better physical insights. In both models, the rate constants of reduction/oxidation of the electroactive species (k_{red}, k_{ox}) are function of two kinetic parameters, although the variation of these constants with the applied potential (E) is considered in different ways:

$$\mathrm{Butler-Volmer}\begin{cases} k_{\mathrm{red}}^{\mathrm{BV}} = k_{\mathrm{BV}}^{0} e^{-\alpha F(E-E_{\mathrm{f}}^{0})} \\ k_{\mathrm{ox}}^{\mathrm{BV}} = k_{\mathrm{BV}}^{0} e^{(1-\alpha)F(E-E_{\mathrm{f}}^{0})} \end{cases} \tag{11.2}$$

$$\mathrm{Marcus-Hush}\begin{cases} k_{\mathrm{red}}^{\mathrm{MH}} = k_{\mathrm{MH}}^{0} e^{-F(E-E_{\mathrm{f}}^{0})/2} f(E,\lambda) \\ k_{\mathrm{red}}^{\mathrm{MH}} = k_{\mathrm{MH}}^{0} e^{F(E-E_{\mathrm{f}}^{0})/2} f(E,\lambda) \end{cases} \tag{11.3}$$

with E_{f}^{0} being the formal potential, F the Faraday constant (96,485 C/mol), R the gas constant (8.314 J/mol K) and T the absolute temperature. The standard rate constant (k_0) is a common parameter in both treatments defined as the rate constant of the reduction/oxidation half-reactions at the formal potential. In the case of the Butler-Volmer formalism, the transfer coefficient (α) is a second kinetic parameter that shows if the transition state is reactant or product like. Within the Marcus-Hush formalism, $f(E,\lambda)$ is a function of the applied potential and the reorganization energy (λ), which is the energy required to adjust the configurations of the reactant and solvent to those of the equilibrium product state.

The Marcus-Hush model applied to electrode reactions predicts behaviour which contrasts with the classical Butler-Volmer treatment. Thus, according to the MH approach the value of the transfer coefficient is not constant but is dependent on the applied potential, which gives rise to curved Tafel plots. This fact has been corroborated experimentally for several redox systems. Savéant and Tessier first reported this behaviour from the reduction of nitro compounds at mercury electrodes in

different organic solvents [8]. More recently, Fletcher and Varley have reported curved Tafel slopes for the reduction of hexamminecobalt(III) at carbon microdisc electrodes [9]. In the context of the voltammetry of surface bound species Chidsey has also observed the curvature of the Tafel plot of electroactive ferrocene groups attached to a gold electrode through an alkanethiol monolayer [7].

In recent publications [10–13], the expected differences between the BV and MH formalisms have been theoretically evaluated for solution phase cyclic voltammetry and differential pulse voltammetries, revealing that significant discrepancies can be expected for slow charge transfer processes, small electrodes and fast scans. In particular, the response in Square Wave Voltammetry (SWV) is particularly sensitive to the kinetic model assumed due to the short pulse times usually employed.

According to the above, the study of sluggish electron transfer reactions using SWV is potentially very insightful for detecting possible differences between the BV and MH models and evaluating their relative suitability to characterise electrode kinetics. In addition, the SWV method offers good discrimination of the charging and background currents and well-defined responses, which are very valuable for quantitative studies [14] and [15].

In this work the one-electron reduction of 2-methyl-2-nitropropane (MeNP) at mercury microelectrodes in acetonitrile is considered [12, 16–18]:

$$\mathrm{MeNP} + \mathrm{e}^- \rightleftharpoons \mathrm{MeNP}^{\bullet -} \tag{11.4}$$

This redox system and other nitroalkanes are extensively employed in kinetic studies with the aim of examining the effects on the electron transfer of the applied potential, the nature of the supporting electrolyte and the molecular properties of the electroactive species [19]. The system is well characterised as diffusional and free of adsorption effects [19].

11.2 Experimental

11.2.1 Chemical reagents

2-Methyl-2-nitropropane (MeNP, Aldrich, 99%), tetra-n-butylammonium perchlorate (TBAP, Fluka, >99%), mercury(I) nitrate dihydrate ($Hg_2(NO_3)_2{\cdot}2H_2O$, Aldrich, >97%), nitric acid (HNO_3, Fischer scientific, 70%), ferrocene ($Fe(C_5H_5)_2$, Aldrich, 98%), acetonitrile (MeCN, Fischer scientific, dried and distilled, >99%) and nitrogen (N_2, BOC Gases) were used as received, without further purification.

11.2.2 Instrumental

The working electrode was a ca. 25 μm radius mercury hemisphere electrodeposited on a platinum (Pt) microdisk electrode made of 99.99% pure platinum wire (Goodfellow Cambridge Ltd, Cambridge). A gold foil counter electrode was introduced for all the measurements while a silver wire was used as the reference electrode.

11.2.3 Square wave voltammetry experiments

Square wave voltammograms were recorded between -1.2 and -2.6 V (vs. Ag wire). The potential step was 10 mV, the amplitude 25 mV and the measurements were operated over a range of different frequencies (f = 100, 200 and 300 Hz).

For the SWV experiments a 2 mM 2-methyl-2-nitropropane (MeNP) solution was made in acetonitrile with 100 mM TBAP as supporting electrolyte. The solutions were outgassed with N_2 before SWV experiments and a positive pressure of N_2 was maintained throughout.

The diffusion coefficient of MeNP was determined from transient chronoamperograms recorded with the hemispherical mercury electrode for 3 s by stepping the potential from -1.2 V vs. Ag wire (where no faradaic current is driven) to -2.5 V vs. Ag wire, where the reduction is fully diffusion-controlled. The diffusion coefficient was obtained by fitting of the theoretical and the experimental transients by inputting the values of the electrode radius, r_0, and bulk concentration according to the

following equation [21]:

$$I = 4FDc_{\text{bulk}}\left(\frac{1}{r_0} + \frac{1}{\sqrt{\pi Dt}}\right) \tag{11.5}$$

The result, $D_{\text{MeNP}} = 2.7 \times 10^{-5}$ cm^2 s^{-1}, is in good agreement with the literature values [12, 22].

11.2.4 Simulation details

The theoretical results corresponding to the Butler-Volmer and Marcus-Hush models were obtained by means of finite difference numerical methods with a homemade program [23].

This program employs an exponentially expanding grid with high expansion factors and four-point formulae for the discretisation of the spatial derivatives, which leads to very accurate results (four-figure accuracy) with only 8 points in the grid for planar electrodes and 26 points for spherical microelectrodes [23].

For the time-integration, the EXTRAP4 algorithm is used, which is very efficient for pulse techniques like Square Wave Voltammetry [24]. Thus, with only 5-time intervals in each potential step accurate results are obtained with very short computation times.

11.3 Characterisation of the electrode kinetics by SWV

For the characterisation of the electrode kinetics with SWV, the use of the 'forward' scan (that is, towards negative potentials in the case of a reduction process) can be problematical in the case of irreversible processes since the peak height and width are independent of the heterogeneous rate constant [14] and so the formal potential must be known to extract an unambiguous value of the standard rate constant from the SWV peak. In addition, it has been suggested [10] that the study of a single (reductive or oxidative) counterpart of the electrode reaction can lead to 'fictitious', erroneous fits of experimental and theoretical results, the study of both half-reactions being necessary to confirm the soundness of the kinetic formalism employed.

Hence, the analysis of the reverse scan in SWV (potential-time program shown in Figure 11.1a) is very suitable since both the reduction and oxidation half-reactions can be assessed in a single

scan [14, 15]. Under the appropriate conditions the voltammogram presents two peaks corresponding to the reduction (peak I in Figure 11.1a) and oxidation (peak II in Figure 1B) processes. The second peak is related to the remaining amount of product electrogenerated during the scan, and so it is promoted by fast scan rates, that is, large step potentials. From the values of the peak-to-peak separation and the ratio of the peak currents the values of the kinetic parameters, $\{k^0, \alpha\}$ or $\{k^0, \lambda\}$, can be extracted. Then, the formal potential is also accessible from the values of the peak potentials.

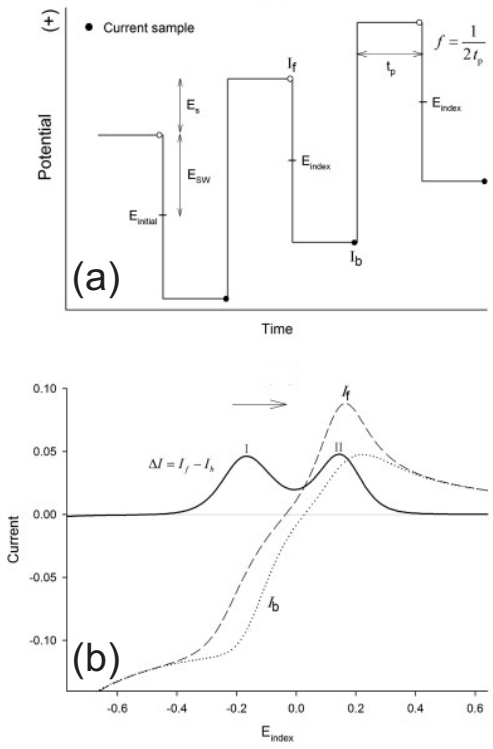


Figure 11.1: (a) Potential-time program and (b) forward, backward and net currents in Square Wave Voltammetry with reverse scan for a reduction process (scheme 11.1). A positive sign corresponds to oxidation currents.

In Figure 11.3, the experimental cyclic voltammogram (solid line) of a 2 mM 2-methyl-2-nitropropane (MeNP), 0.1 M TBAP acetonitrile solution at a mercury hemispherical electrode with $r_0 = 25$ μm is shown. As can be observed, a reductive peak is recorded in the forward scan at ca. -1.93 V (vs Ag wire) and in the backward scan the peak corresponding to the oxidation of the radical anion $MeNP^{\bullet -}$ is situated at ca. -1.54 V.

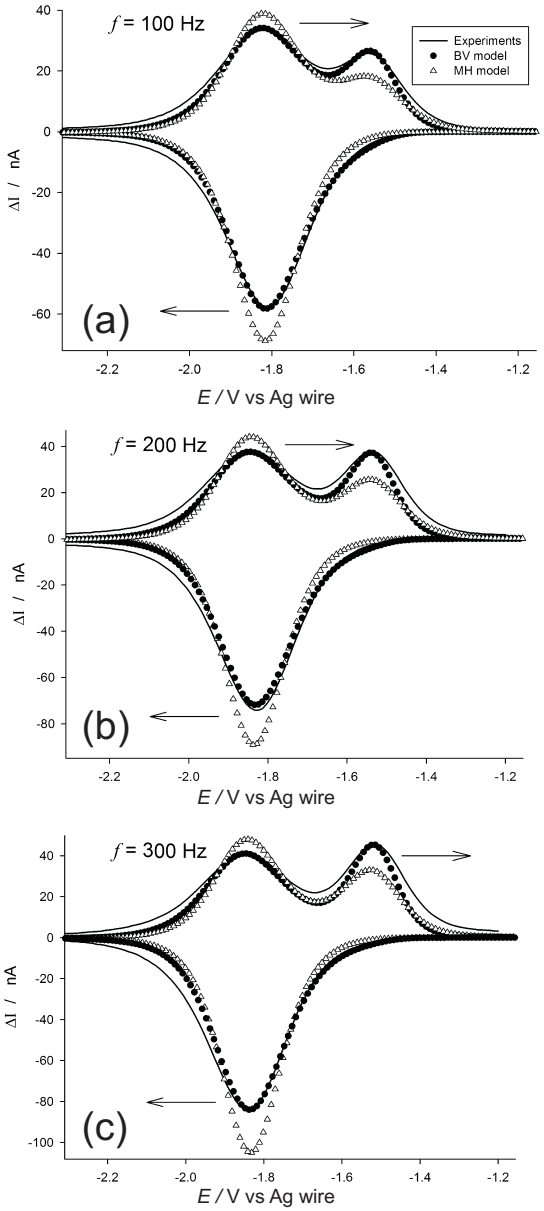


Figure 11.2: Experimental (solid line) and theoretical (points) SWV voltammograms obtained with Butler-Volmer (•) and Marcus-Hush (△) models. A positive sign corresponds to reverse scans. $E_{\text{initial}}^{\text{reverse}}$ = -2.6 V (vs Ag), E_{SW} = 25 mV, E_{S} = 10 mV. The values of the kinetic parameters and formal potential extracted in each case are given in Table 11.3. Test solution: 2 mM 2-methyl-2-nitropropane, 0.1 M tetra-*n*-butylammonium perchlorate in acetonitrile.

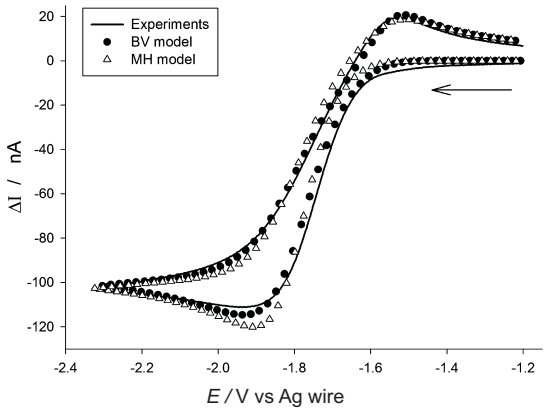


Figure 11.3: Experimental (solid line) and theoretical (points) cyclic voltammograms with Butler-Volmer (•) and Marcus-Hush (△) models $\nu = 500$ mV/s. The values of the kinetic parameters and formal potential used for simulations were the mean values extracted from SWV experiments (shown in Table 11.3). A positive sign corresponds to oxidation currents. Other experimental conditions as in Figure 11.2.

SWV experiments with different frequencies (f) were carried out in forward and reverse scan modes between -1.2 and -2.6 V (vs Ag), employing a 25 μm radius mercury electrode as the working electrode. The SWV parameters were optimised for obtaining two well-defined peaks in the reverse scan. This required the use of high frequencies ($f \geq 100$ Hz) and a value of the step potential $E_S = 10$ mV, which permits both fast experiments and a sufficient number of points in the voltammograms. The results are presented in Figure 11.2 (solid line), where a positive sign corresponds to reverse scan. As can be seen, the reductive and oxidative peaks are well resolved, the relative magnitude of the oxidative peak and the peak-to-peak separation increasing with frequency.

The theoretical reverse SWV voltammograms were fitted to the experimental data with $\{k^0, \alpha\}$ or $\{k^0, \lambda\}$ and the formal potential ($E^{0'}$) as fitting parameters, assuming both BV and MH models. As can be seen in Figure 11.2, with the Butler-Volmer formalism (•, Equation 11.2) excellent fits are obtained between experimental and theoretical SWV curves such that the magnitude and separation of the reduction and oxidation peaks are well described in all cases. The values of the kinetic parameters and the formal potential extracted at different frequencies (see Table 11.3) are consistent and they are in good agreement with those reported in the literature [12, 16–18]. Moreover, they also lead to an excellent description of the square wave voltammograms obtained with forward scans (Figure 11.2) and of cyclic voltammograms (see Figure 11.3). Tafel analysis of the cyclic voltammetry revealed a

linear region between -1.62 and -1.68 V, the slope of which corresponds to $\alpha = 0.39$.

Table 11.1: Parameters used for simulations

f /Hz	Butler-Volmer	Marcus-Hush
100	$k^0 = 3.1 \times 10^{-3}$ cm s^{-1} $\alpha = 0.40$ $E^{0'} =$ -1.652 V	$k^0 = 2.8 \times 10^{-3}$ cm s^{-1} $\lambda = 1.8$ eV $E^{0'} =$ -1.678 V
200	$k^0 = 2.9 \times 10^{-3}$ cm s^{-1} $\alpha = 0.39$ $E^{0'} =$ -1.647 V	$k^0 = 2.5 \times 10^{-3}$ cm s^{-1} $\lambda = 2.6$ eV $E^{0'} =$ -1.679 V
300	$k^0 = 2.8 \times 10^{-3}$ cm s^{-1} $\alpha = 0.39$ $E^{0'} =$ -1.638 V	$k^0 = 2.7 \times 10^{-3}$ cm s^{-1} $\lambda = 3.1$ eV $E^{0'} =$ -1.673 V
Mean Values	$\langle k^0 \rangle = (2.9 \pm 0.1) \times 10^{-3}$ cm s^{-1} $\langle \alpha \rangle = 0.393 \pm 0.006$ $\langle E^{0'} \rangle =$ -1.645 ± 0.007 V	$\langle k^0 \rangle = (2.7 \pm 0.2) \times 10^{-3}$ cm s^{-1} $\langle \lambda \rangle = 2.5 \pm 0.7$ eV $\langle E^{0'} \rangle =$ -1.677 ± 0.003 V

When the Marcus-Hush relationships ($\triangle$, Equation 11.3) are employed to describe the electrode kinetics, the simultaneous fit of both peaks was not possible for any $\{k^0, \lambda\}$ values. Thus, the standard rate constant obtained from the peak-to-peak separation gives rise to an oxidation peak significantly smaller than that obtained experimentally. The increase of the rate constant leads to a better description of the oxidation peak but also to the reduction of the peak-to-peak separation and an overestimation of the reduction peak current.

The values of the kinetic parameters corresponding to the least squared error in the peak currents of the reverse scan, and consistent with the peak-to-peak separation, are shown in Table 11.3. As can be seen in Figure 11.2, the quality of the fits of both forward and reverse voltammograms is not good and so the results extracted are not sound. Thus, in the reverse voltammograms the reductive peak is overestimated whereas the oxidative one and the peak-to-peak separation are underestimated. So, we can infer that the Marcus-Hush model is not able to describe simultaneously the reductive and oxidative counterparts and it is not appropriate for the study of the redox system considered. Nevertheless, very satisfactory fits of the forward SWV peak can be attained with Marcus-Hush (see Figure 11.4. This confirms the need to examine both the reductive and oxidative half-reactions in order to check the consistency of the kinetic model employed since the study of only the forward

reaction can lead to erroneous conclusions. From the comparison of Figure 11.2 and Figure 11.3 we can infer that the differences between the BV and MH models are more apparently revealed in SWV than in cyclic voltammetry.

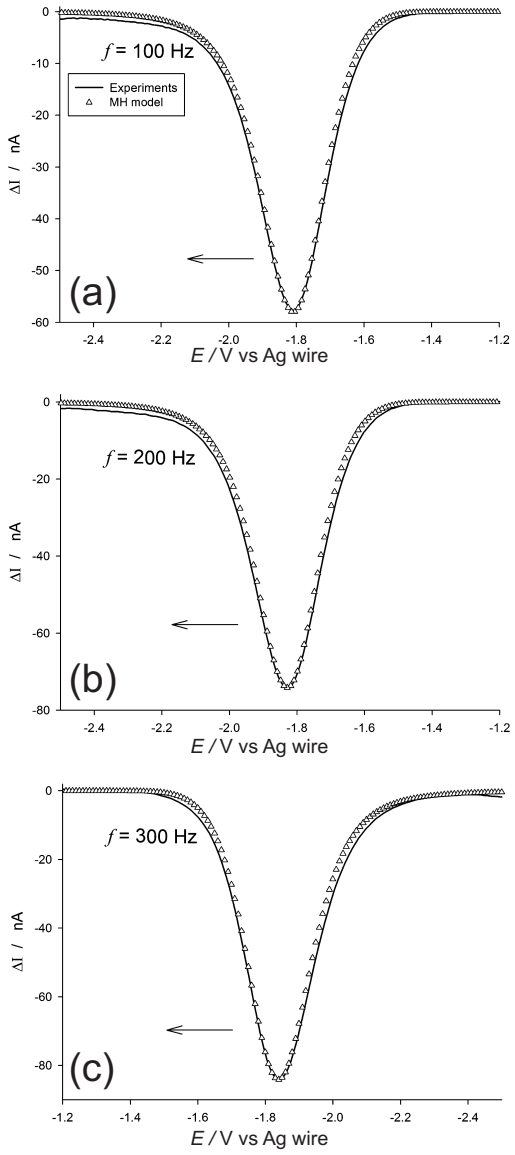


Figure 11.4: Experimental (solid line) and theoretical (points) SWV voltammograms in forward scan mode obtained with Marcus-Hush (△). E_{SW} = 25 mV, E_S = 10 mV. The values of the kinetic parameters and formal potential used for simulations were: $k^0 = 2.6 \times 10^{-3}$ cm s^{-1}, λ = 0.54 eV and E^0_f = -1.673 V (vs Ag wire). Other experimental conditions as in Figure 11.2.

Once the oxidative and reductive experimental peaks are well-fitted with Butler-Volmer with α = 0.39, the poor fits obtained with Marcus-Hush is not unexpected since the MH model cannot reproduce the BV results when the transfer coefficient are significantly different from 0.5, as in the present case [10–13].

These results complement recent experimental evidence [11, 12] indicating the inability of the MH model to describe properly the linear sweep voltammetry of redox systems in solution phase, in contrast with its successful description of surface bound redox systems [7, 25–28]. On the other hand, Butler-Volmer proves to be more suited for the parameterisation of the electrochemical response of this kind of systems, although this phenomenological theory does not provide the physical insights potentially accessible with Marcus-Hush theory.

In this chapter and other relative literatures [10–13], the Marcus-Hush formalism as developed by Chidsey [7] has been employed, which makes use of the symmetrized version of the Marcus theory [29]. This assumes a type of symmetry of the free energy curves of reactants and products which may not hold if the reorganization energies of the reduction and oxidation processes are different [30]. Thus the experimental deviations from the MH results here presented may indicate asymmetrical effects in the solvation of the electroactive species and the need for the use of the non-symmetrized Marcus theory [29].

This asymmetry, as well as the examination of analogous effects in other redox systems, will be considered in future work.

11.4 Conclusions

The suitability of the Butler-Volmer and Marcus-Hush approaches to model the electrode kinetics of diffusional systems has been assessed by studying the reduction of 2-methyl-2-nitropropane in acetonitrile at mercury microelectrodes.

Square Wave Voltammetry (SWV) with reverse scans has been employed since the response is significantly dependent on the kinetic model assumed and it is a very suitable method for kinetic studies of irreversible processes. Thus, under the appropriate conditions two peaks are obtained from which the examination of the reduction and oxidation half-reactions in the same scan is possible. The kinetic parameters and formal potential can be unambiguously determined from the values of the peak currents and potentials.

A good fitting of both reductive and oxidative peaks is obtained when using the Butler-Volmer model. The values extracted for the standard rate constant, the transfer coefficient and the formal potential are consistent under different experimental conditions and they are in good agreement with literature values.

On the other hand, the Marcus-Hush formalism does not lead to good fits to experimental data, which can be interpreted as an indication of the different reorganization energies of the reduction and oxidation processes and the need of considering the non-symmetrized Marcus theory. This indicates that Marcus-Hush is not appropriate for modelling the electrode reaction considered and it opens questions as to the ability of this approach to model quantitatively the electrode kinetics of diffusional redox systems, although of course the physical insights of the model are not in doubt.

References

[1] J.A.V. Butler, Trans. Faraday Soc. 19 (1924) 729–733.

[2] T. Erdey-Gruz, M. Volmer, Z. Physik. Chem. 150 (1930) 203–213.

[3] R.A. Marcus, J. Chem. Phys. 24 (1956) 966–978.

[4] R.A. Marcus, Annu. Rev. Phys. Chem. 15 (1964) 155.

[5] N.S. Hush, J. Chem. Phys. 28 (1958) 962–972.

[6] N.S. Hush, J. Electroanal. Chem. 470 (1999) 170–195.

[7] C.E.D. Chidsey, Science 251 (1991) 919–922.

[8] J.M. Savéant, D. Tessier, Disc. Faraday Soc. 74 (1982) 57–72.

[9] S. Fletcher, T.S. Varley, Phys. Chem. Chem. Phys. 13 (2011) 5359–5364.

[10] S.W. Feldberg, Anal. Chem. 82 (2010) 5176–5183.

[11] D. Suwatchara, M.C. Henstridge, N.V. Rees, R.G. Compton, J. Phys. Chem. C 115 (2011) 14876–14882.

[12] M.C. Henstridge, Y. Wang, J.G. Limon-Petersen, E. Laborda, R.G. Compton, Chem. Phys. Lett. 517 (2011) 29–35.

[13] E. Laborda, M. Henstridge, A. Molina, F. Martinez-Ortiz, R.G. Compton, J Electroanal. Chem. 660 (2011) 169–177.

[14] V. Mirčeski, Š. Komorsky-Lovrić, M. Lovrić, Square-Wave Voltammetry: Theory and Application, Springer, 2007.

[15] N. Fatouros, D. Krulic, J. Electroanal. Chem. 520 (2002) 1–5.

[16] C. Kraiya, P. Singh, D.H. Evans, J. Electroanal. Chem. 563 (2004) 203–212.

[17] D.A. Corrigan, D.H. Evans, J. Electroanal. Chem. 106 (1980) 287–304.

[18] D.H. Evans, A.G. Gilicinski, J. Phys. Chem. 96 (1992) 2528–2533.

[19] D.H. Evans, Chem. Rev. 108 (2008) 2113–2144.

[20] J. Mauzeroll, E.A. Hueske, A.J. Bard, Anal. Chem. 75 (2003) 3880–3889.

[21] R.G. Compton, C.E. Banks, Understanding Voltammetry, 2nd edn., Imperial College Press, London, 2011.

[22] J.M. Savéant, D. Tessier, J. Electroanal. Chem. 65 (1975) 57–66.

[23] F. Martinez-Ortiz, N. Zoroa, A. Molina, C. Serna, E. Laborda, Electrochim. Acta 54 (2009) 1042–1055.

[24] F. Martinez-Ortiz, A. Molina, E. Laborda, Electrochim. Acta 56 (2011) 5707–5716.

[25] J.F. Smalley, M.D. Newton, S.W. Feldberg, J. Electroanal. Chem. 589 (2006) 1–6.

[26] Q. Chi, J. Zhang, J.E.T. Andersen, J. Ulstrup, J. Phys. Chem. B 105 (2001) 4669–4679.

[27] J. Hirst, F.A. Armstrong, Anal. Chem. 70 (1998) 5062–5071.

[28] H.O. Finklea, D.D. Hanshew, J. Am. Chem. Soc. 114 (1992) 3173–3181.

[29] R.A. Marcus, J. Chem. Phys. 43 (1965) 679–701.

[30] O.A. Petrii, R.R. Nazmutdinov, M.D. Bronshtein, G.A. Tsirlina, Electrochim. Acta 52 (2007) 3493–3504.

Chapter 12 The Use of Differential Pulse Voltammetries to Discriminate Between the Butler-Volmer and the Simple Marcus-Hush Models for Heterogeneous Electron Transfer: The Electro-reduction of Europium (III) in Aqueous Solution

The work presented in this chapter was carried out in collaboration with

- **E. Laborda, F. Martinez-Ortiz, A. Molina** and **M.C. Henstridge** (for the theory and modelling parts)

Y. Wang, E. Laborda, M.C. Henstridge, F. Martinez-Ortiz, A. Molina, R.G. Compton, J. Electroanal. Chem. 668 (2012) 7–12

Differential multipulse voltammetry and square wave voltammetry are employed to critically compare and discriminate between the Butler-Volmer and Marcus-Hush kinetic formalisms of heterogeneous electron transfer. The reduction of europium (III) in aqueous solution is studied with mercury hemispherical microelectrodes.

By using these differential pulse techniques in reverse scan mode, both the reduction and oxidation half-reactions can be evaluated at the same time and are very appropriate for kinetic analysis due to the reduction of charging current and background effects and the sensitivity of the peak height to the electrode kinetics.

Numerical simulations using both theories are employed to fit the experimental voltammograms. The results show that the Butler-Volmer model parameterizes satisfactorily all the experimental data. Consistent values of the standard heterogeneous rate constant and the transfer coefficient are obtained with different techniques and different conditions of pulse times and frequency. In contrast, the Marcus-Hush model in its simple form does not yield a satisfactory description of the voltammograms of this redox couple in any case, which demands a critical revision of the kinetic approach.

12.1 Introduction

Over the years, the quantitative descriptions of the kinetics of heterogeneous electron transfer process have drawn much attention and effort from electrochemists. Different theoretical models have been developed ranging from the phenomenological Butler-Volmer approach [1, 2] to quantum mechanical models.

The classic Bulter-Volmer formalism describes the kinetics of the electron transfer process in a phenomenological way, giving rise to expressions for the heterogeneous rate constants easy to handle. Hence, considering a simple one-electron transfer process:

$$\mathrm{O} + \mathrm{e}^- \overset{E_\mathrm{f}^0, k^0}{\rightleftarrows} \mathrm{R} \tag{12.1}$$

where E_f^0 is the formal potential and k^0 the standard electrochemical rate constant. The BV approach establishes that for a one-electron process the heterogeneous rate constants , $k_\mathrm{red}^\mathrm{BV}$ and $k_\mathrm{ox}^\mathrm{BV}$, are given by:

$$k_\mathrm{red}^\mathrm{BV} = k_\mathrm{BV}^0 e^{-\alpha\eta} \tag{12.2}$$

$$k_\mathrm{ox}^\mathrm{BV} = k_\mathrm{BV}^0 e^{(1-\alpha)\eta} \tag{12.3}$$

where $\eta = F(E\text{-}E_\mathrm{f}^0)/RT$, α is the electron transfer coefficient, F the Faraday constant (96,485 C/mol), R the gas constant (8.314 J/mol K) and T the absolute temperature. Due to the simplicity of this model and the vast amount of data available in the literature, this is still the most commonly used kinetic treatment in electrochemistry.

On the other hand, since 1956 Marcus and other authors have developed microscopic models for electron transfer processes that enable us to rationalize the kinetics in terms of the properties of the system [3–6]. Their application to the case of interfacial processes (electrode reactions) is known as the Marcus-Hush formalism [7]. According to this, the expressions for the reduction and oxidation

rate constants are given by:

$$k_{\mathrm{red}}^{\mathrm{MH}} = k_{\mathrm{MH}}^{0} f_{\mathrm{red}}(\Lambda, \eta) \tag{12.4}$$

$$k_{\mathrm{ox}}^{\mathrm{MH}} = k_{\mathrm{MH}}^{0} f_{\mathrm{ox}}(\Lambda, \eta) \tag{12.5}$$

where f is a function of the applied potential and the reorganization energy (λ):

$$f_{\mathrm{red/ox}}(\Lambda, \eta) = \frac{I_{\mathrm{red/ox}}(\Lambda, \eta)}{I_{\mathrm{red/ox}}(\Lambda, 0)} \tag{12.6}$$

$$\Lambda = \frac{F\lambda}{RT} \tag{12.7}$$

$$I_{\mathrm{red/ox}}(\Lambda, \eta) = \int_{-\infty}^{+\infty} \frac{\exp\left[-\Delta G_{\mathrm{red/ox}}^{*}(\epsilon)\right]}{1 + \exp\left[\mp\epsilon\right]} d\epsilon \tag{12.8}$$

$$\Delta G_{\mathrm{red/ox}}^{*} = \frac{w_{\mathrm{r}} + w_{\mathrm{p}}}{2} + \frac{\lambda}{4} \pm \frac{\epsilon + \eta}{2} + \frac{[\pm(\epsilon + \eta) + w_{\mathrm{p}} - w_{\mathrm{r}}]^2}{4\Lambda} \tag{12.9}$$

where the upper sign refers to the reduction process and the lower one to the oxidation reaction.

Note that in the derivation of these expressions some approximations are assumed, mainly, equal reorganization energies for the forward and backward reactions and potential-independent electronic coupling and density of metallic states [7]. The possible need for the inclusion of work terms is considered in Equations 12.4 and 12.5 through the work terms in Equation 12.9, w_{r} and w_{p}, that represent the work required to bring the electroactive species from infinity to the location where the electron transfer takes place. The application of Marcus theory to real systems has been thoroughly investigated by Eberson [8] and procedures rigorously deduced in his book. On the basis of this, we infer that, in aqueous solution and under conditions of high electrolyte support, the work terms can be omitted. This is generally assumed when applying the Marcus theory to electrode reactions as can be concluded from Chidsey's seminal paper [7] and subsequent works [9–12]. Further, we note that the inclusion of work terms are rarely, if ever, considered in the application of Butler-Volmer theory in highly supported voltammetry. In order to compare the BV and MH models on equal bases, neglecting the work terms, in addition to the physical argument presented by Eberson, is

appropriate. On this basis, MH theory will below be seen to behave less well than BV theory. In this chapter, we analyze these deviations showing that the asymmetric MH theory adequately describes the voltammetry without the need for inclusion of work terms.

The reorganization energy, λ, is related to the energy required to distort the atomic configurations of the reactant and its solvation shell to those of the product. The λ value affects both the activation energy of the electron transfer (the greater the λ value, the greater the activation energy) and the standard heterogeneous rate constant k^0_{MH} (the greater the λ value, the smaller the standard rate constant). Consequently, through this parameter the kinetics of the electron transfer can be connected with the properties of the electroactive molecules.

As shown in Figure 12.1, the main difference between the BV and MH models is the variation of the heterogeneous rate constant with the applied potential ($\eta = F(E\text{-}E^0_{\mathrm{f}})/RT$). The divergence between the predictions of the two models increases with the applied overpotential. At very large overpotentials, from the MH model a limiting value for the rate constants is expected, in contrast to the BV model where a continuous increase *ad infinitum* is observed. For small overpotentials, the MH model coincides with BV for $\alpha = 0.5$. According to these results, differences between the two kinetic models are expected to be most obvious under kinetic-controlled conditions at large overpotentials. This behaviour can be studied with surface-bound species by means of potential-step experiments [7] and the MH approach has been successfully employed for the study of many surface-bound redox couples [13–22].

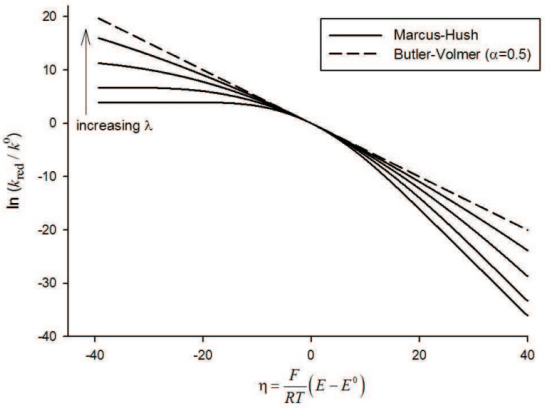


Figure 12.1: Plot of the variation of the reduction rate constant with the applied potential from the Butler-Volmer (dashed line) and Marcus-Hush (solid line) models.

Regarding solution-phase redox couples, Miller discussed the implication of the MH model by the approach of forming an adequately pinhole-free self-assembled monolayer on the electrode [23], and a discussion about the suitability of the MH model is outgoing [11, 12, 24–28]. When working with these systems, the electrochemical response at large overpotentials can be controlled by mass transport, which obviously impedes the assessment of the kinetics. Compton and coworkers have tackled this problem in recent publications [24–29] through the evaluation of the kinetics of slow electron transfer processes in voltammetric techniques with microelectrodes. Differential pulse voltammetries with short pulse times have shown to be very insightful for the examination of the electrode kinetics since the peak-shaped response obtained is very sensitive to the electrode kinetics [28, 29]. Moreover, these techniques reduce the distortion of the signal due to charging and background currents, and generate well-resolved peaks for quantitative determinations of kinetic parameters.

In this context, square wave voltammetry (SWV) has been applied to the study of the reduction of 2-methyl-2-nitropropane [28] and cyclooctatetraene [26] on mercury hemispherical microelectrodes. Due to their one-dimensional symmetry, the use of electrodes of spherical geometry simplifies, and makes faster, numerical simulations, being possible to include Ohmic drop and migration effects [30–34]. Moreover, given their small size, the charging current and Ohmic drop effects are greatly reduced.

The use of reverse scan SWV was found to be particularly useful since it examines the reduction and oxidation processes simultaneously. Thus, when the system is irreversible, two peaks are obtained,

the positions and heights of which permit the characterization of the electrode kinetics. In both redox processes studied to date with this technique, a better parameterization of the experimental results was achieved when the BV approach with $\alpha < 0.5$ was considered. On the other hand, with the MH approach the reductive and oxidative peaks could not be simultaneously fitted.

Analogously, the application of differential multipulse voltammetry (DMPV) [35] for kinetic studies is recommended [29, 36], although its experimental application in the present context has not been carried out hitherto. In this chapter, we fill this gap by studying the kinetics of reduction of Eu^{3+} in aqueous solutions at mercury microelectrodes with both DMPV and SWV:

$$Eu^{3+} + e^- \rightleftharpoons Eu^{2+} \tag{12.10}$$

For this system, very slow electron transfer has been reported with an α value considerably greater than 0.5, and no complications due to coupled chemical reactions or adsorption have been observed [34, 37, 38]. Therefore, this redox couple is an experimental system appropriate for the critical analysis of the Butler-Volmer and Marcus-Hush models, and the evaluation of the generality of the results previously obtained with electrochemical processes where $\alpha < 0.5$.

12.2 Experimental

12.2.1 Chemical Reagents

Europium (III) chloride hexahydrate ($EuCl_3 \cdot 6H_2O$, Aldrich, 99.99%), potassium chloride (KCl, Aldrich, >99%), tetra-*n*-butylammonium perchlorate (TBAP, Fluka, >99%), mercury(I) nitrate dihydrate ($Hg_2(NO_3)_2 \cdot 2H_2O$, Aldrich, ≥97%), nitric acid (HNO_3, Fischer scientific, 70%), ferrocene ($Fe(C_5H_5)_2$, Aldrich, 98%) and acetonitrile (MeCN, Fischer scientific, dried and distilled, >99 %) were used as received, without further purification.

12.2.2 Instrumental and Solutions

A computer-controlled μ-Autolab potentiostat (Eco-Chemie, Netherlands) was used to carry out all the electrochemical experiments. 50 and 25 μm radius platinum (Pt) microdisk electrodes made of 99.99 % pure platinum wire (Goodfellow Cambridge Ltd, Cambridge) were employed as working electrodes. It was polished using 1.0, 0.3 and 0.01 μm alumina-water slurry (Buehler, Illinois) on soft lapping pads before the deposition of mercury. A Ag/AgCl electrode was used for aqueous solutions. The counter electrode was a gold foil.

The calibration of the working electrodes followed the widely adopted method [39–42]. By recording the steady-state limiting current of a 2mM ferrocene acetonitrile solution with 0.1M TBAP at 293K, the radius of the electrode can be calculated by the following equation:

$$I_{\text{lim}} = -4nFr_{\text{d}}Dc_{\text{bulk}} \tag{12.11}$$

where i_{lim} is the steady-state limiting current, n is the number of electrons transfered, D is the diffusion coefficient, and c_{bulk} is the bulk concentration. A literature value of 2.3×10^{-9} m^2 s^{-1} for D was used [43].

The mercury hemispheres were electrodeposited on the Pt surface by setting the potential at -0.25 V vs. Ag wire in a solution containing 10mM $Hg_2(NO_3)_2$ solution (acidified by 0.5% of HNO_3) [44]. The size was controlled by monitoring the amount of charge, which was 1.704 mC corresponding to 17.68 nmol Hg for a 50 μm electrode radius. The size and shape of the electrode was confirmed by electrochemical and optical methods, as described in reference [26].

All experiments were performed in a thermostat Faraday cage maintained at 298 K. The solutions were degassed with N_2 for 30 minutes prior to each experiment to reduce the influence of O_2 reduction and N_2 pressure was maintained during the experiments.

12.2.3 Determination of diffusion coefficients by double potential step chronoamperometry

Transient chronoamperograms were measured on a 25 μm Pt disk electrode. The current was recorded for 3s by stepping the potential from open circuit to a value -0.85 V vs. Ag/AgCl corresponding to fully diffusion control, then back to -0.05 V vs. Ag/AgCl. To fit the first step, the expression developed by Shoup and Szabo [45] was applied, which allows the quantitative determination of the diffusion coefficient for the oxidized species Eu^{3+} ($D_{Eu^{3+}}$):

$$I = -4nFDc_{\text{bulk}}r_{\text{d}}f(\tau) \tag{12.12}$$

$$f(\tau) = 0.7854 + 0.8863\tau^{-\frac{1}{2}} + 0.2146\exp(-0.7823\tau^{-\frac{1}{2}}) \tag{12.13}$$

where the dimensionless time parameter, τ is given by:

$$\tau = \frac{4Dt}{{r_{\text{d}}}^2} \tag{12.14}$$

A computer simulation program (developed by Klymenko *et al.* [46]) was used to fit the second step by adopting the best fit $D_{Eu^{3+}}$ value from the first, the diffusion coefficient for Eu^{2+} ($D_{Eu^{2+}}$) being the only adjustable parameter.

$D_{Eu^{3+}}$ and $D_{Eu^{2+}}$ values were found to be (6.5 $\pm$ 0.2) $\times$ 10^{-10} m^2 s^{-1} and (9.0 $\pm$ 0.2) $\times$ 10^{-10} m^2 s^{-1}, which are in good agreement with the literature values [27, 37].

12.2.4 Voltammetric kinetic studies

The kinetics of reaction (12.10) was studied by means of differential multipulse voltammetry and square wave voltammetry. The potential-time programs applied in each case are shown in Figure 12.2 [35]. The main differences between these differential pulse techniques are the duration of the pulses and the sign of the pulse amplitude. Hence, in DMPV the pulse time (t_{p}) is usually shorter than the period between pulses (t_1), and the pulse amplitude is applied in the same sense of the scan. On the other hand, in SWV all the pulses have the same duration and the pulse amplitude is opposite

from the scan direction.

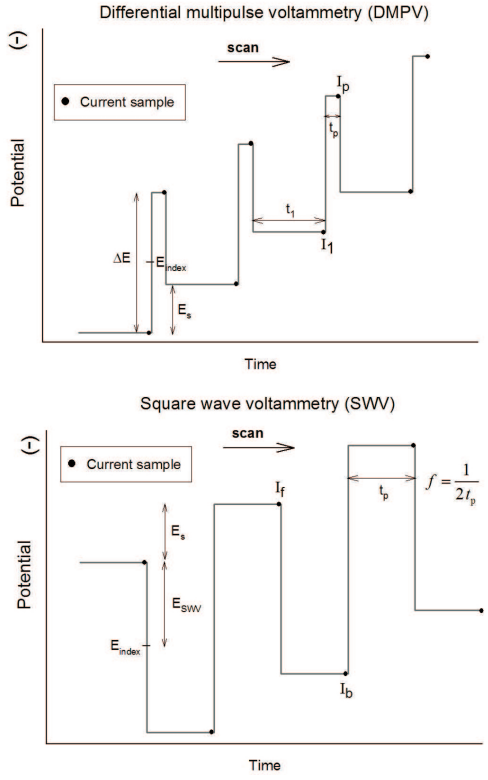


Figure 12.2: Potential-time programs applied in differential multipulse voltammetry (DMPV) and square wave voltammetry (SWV).

For the experiments, water solutions 1 mM in $EuCl_3$ and 0.4 M in KCl were employed. Under these conditions, with a support ratio of 400, diffusion-migration simulations [30–32] show that the contribution of migration to mass transport of the electroactive species was negligible (difference less than 1% in the current). The occurrence of Ohmic drop effects was also discarded from simulation [34] of the influence of the uncompensated resistance for the conditions of our solution with a resistivity *ca.* 0.17 $\Omega \cdot m$ [47].

Additional experiments in a range of supporting electrolyte concentrations between 0.1 M and 1.0 M were carried out to discount possible double layer effects [48]. Non-systematic variation was observed in the values of the kinetic parameters when varying the KCl concentration, which suggests the exclusion of possible Frumkin effects [49, 50].

In DMPV different modulation times between 8 and 20 ms were employed, with an unique interval time of 100 ms. The value of the pulse amplitude ΔE was 25 mV and the step potential E_s = 30

mV. Regarding SWV, the value of the frequency for the experiments ranged from 25 to 75Hz, with a pulse amplitude $E_{SWV} = 25$ mV and a step potential $E_s = 10$ mV. Both in SWV and DMPV, forward and reverse scans were recorded. The experimental results were fitted with a homemade simulation program [33] considering Butler-Volmer and Marcus-Hush models for modeling the electrode kinetics.

Cyclic voltammograms were also measured in a range of scan rates from 100 to 1000 mV s^{-1}. Experimental votammograms were fitted using the commercial electrochemical simulation program Digisim (version 3.0, BAS Technicol, USA [51–55]).

12.3 Results and discussion

As can be seen in Figure 12.2, the use of DMPV introduces a new parameter with respect to SWV. Besides the pulse amplitude, the step potential and the pulse time, it is possible to vary the relative duration of the pulses, t_1/t_p. The effect of this parameter on the response corresponding to reverse scans is analyzed in Figure 12.3 where the results obtained by numerical simulation for a reduction electrode process are plotted. When the electrode process is sluggish, the response in differential pulse techniques presents two peaks corresponding to the reduction ($I_{p,red}$) and oxidation ($I_{p,ox}$) half-reactions taking place at very different potentials [28, 56–59]. This is of great importance when studying the kinetics of electrode processes since both half-reactions must be simultaneously examined in order to assess the validity of any kinetic model [11]. The position and height of the peaks permit the determination of kinetic parameters [28]. The effect of the t_1/t_p value on the relative peak height is analyzed in Figure 12.3. At large electrodes (linear diffusion), the increase of the duration of the period between pulses gives rise to the relative increase of the oxidative peak (i.e., greater $I_{p,ox}/I_{p,red}$ values) due to the increase of the reversibility of the electrode reaction. At spherical electrodes, the t_1/t_p influence is more complex since it also affects the "effective" sphericity of the electrode [57–59] such that the longer the first pulse, the greater the diffusion of the electrogenerated species R towards the bulk solution. Consequently, a compromise value for t_1/t_p should be employed. Therefore, at large and medium-sized electrodes, optimizing the t_1/t_p value can help to enhance the magnitude of the

second peak in the reverse scan voltammogram in order to characterize the product of the electrode reaction.

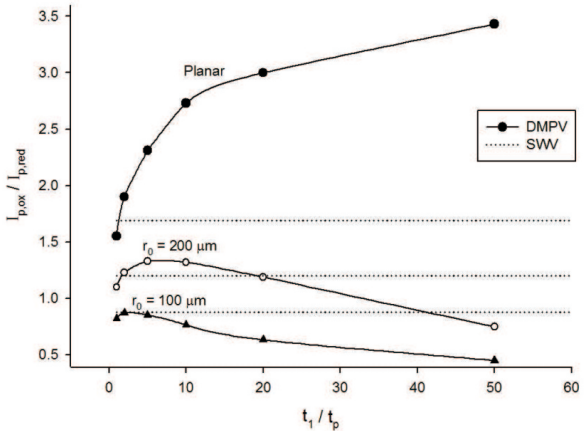


Figure 12.3: Influence of the t_1/t_p value on the relative height of the second peak in reverse DMPV and reverse SWV for spherical electrodes of different size. $k^0 = 10^{-4}$ cm/s, $\alpha = 0.5$, $t_\mathrm{p} = 10$ ms ($f = 50$ Hz), $\Delta E = 50$ mV, $E_{SWV} = 25$ mV, $E_\mathrm{s} = 10$ mV.

With respect to the separation between peaks, in general terms this diminishes as t_1/t_p increases such that both peaks are situated at less extreme overpotentials. This can be helpful to tune the position of the peaks for better resolution when other faradaic processes take place in the same potential region.

Taking into account the above indications, the experimental conditions were optimized to study the one-electron reduction of Eu^{3+} at hemispherical mercury microelectrodes with $r_0 = 50$ μm. As discussed above, in the case of small electrodes the time scale of the experiment should be reduced in order to prevent the depletion of the electrogenerated species by diffusion, that is, fast "formal" scan rates, $v = E_\mathrm{s}/t_\mathrm{p}$ [28, 56–59], should be employed. This involves the use of short pulse times (high frequencies) and large step potential values.

Experimental DMPV and SWV voltammograms are plotted in Figures 12.4 and 12.5, respectively. The simulated curves corresponding to the best fit with the BV and MH models are also shown. Cyclic voltammetry experiments were also performed and fitted for comparison (see Figure 12.6).

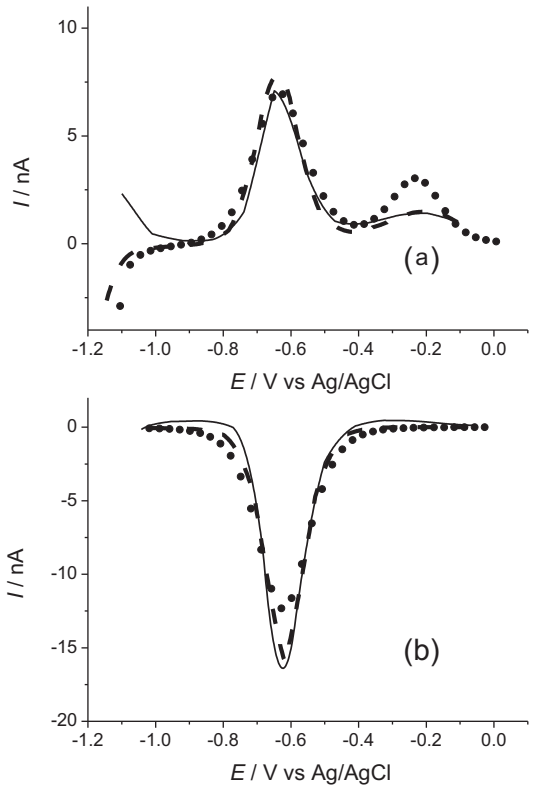


Figure 12.4: Experimental (–), best-fit BV theoretical (**- -**), and best-fit MH theoretical (•) differential multipulse voltammograms (a. for backward scan, b. for forward scan) for a 1 mM $EuCl_3$ solution with 0.4 M KCl as supporting electrolyte using the parameters from Table 12.1. The potential was scanned from -0.05 to -1.1 V vs. Ag/AgCl for forward scans and from -1.1 to -0.05 V vs. Ag/AgCl for backward scans. This example is under the condition of: modulation time = 10 ms, interval time = 100 ms, step potential = 30 mV, and modulation amplitude = 25 mV

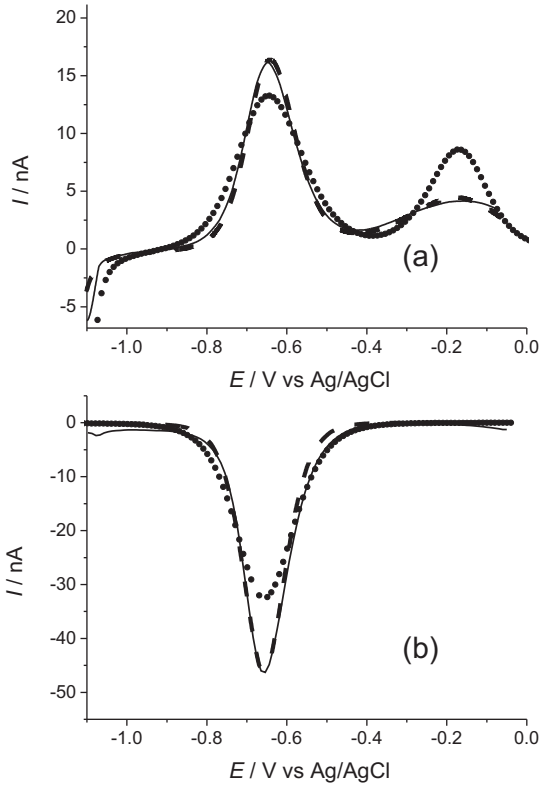


Figure 12.5: Experimental (–), best-fit BV theoretical (**- -**), and best-fit MH theoretical (•) square wave voltammograms (a. for backward scan, b. for forward scan) for a 1 mM $EuCl_3$ solution with 0.4 M KCl as supporting electrolyte using the parameters from Table 12.1. The potential was scanned from -0.05 to -1.1 V vs. Ag/AgCl for forward scans and from -1.1 to -0.05 V vs. Ag/AgCl for backward scans. This example is under the condition of: frequency = 50Hz, step potential = 10 mV, and modulation amplitude = 25 mV

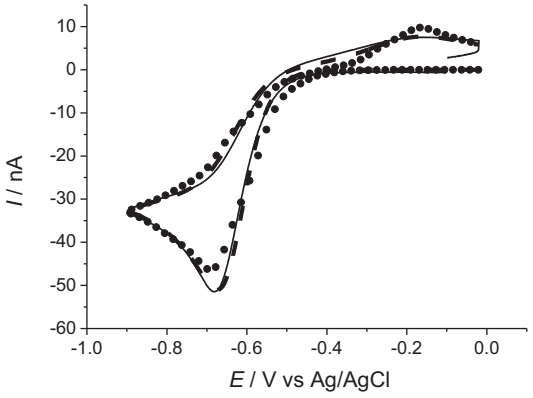


Figure 12.6: Experimental (–), best-fit BV theoretical (**- -**), and best-fit MH theoretical (•) cyclic voltammograms for a 1 mM $EuCl_3$ solution with 0.4 M KCl as supporting electrolyte using the parameters from Table 12.1. The potential was scanned from -0.05 to -0.9 and back to -0.05 V vs. Ag/AgCl at the scan rate of 250 mV s^{-1}.

The parameters extracted from the best fits of the DMPV and SWV voltammograms are included in Table 12.1. They are obtained from the fitting of the peak-to-peak separation and the relative heights of the peaks of the reverse scans. Hence, the peak-to-peak separation is mainly defined by

the standard heterogeneous rate constant (k^0) and from the peak currents the α or λ values can be determined.

Table 12.1: Kinetic parameters for the electro-reduction of Eu^{3+} in 1mM aque solution with 0.4 M KCl as supporting electrolyte on a *ca.* 50 μm radius Hg hemisphere electrode from the best-fit differential multi pulse, square wave, and cyclic voltammograms shown in Figure 12.6[a].

Parameter	Butler-Volmer	Marcus-Hush
	DMPV	
k^0 / m s^{-1}	1.9 ($\pm$ 0.3) $\times$ 10^{-6}	1.8 ($\pm$ 0.4) $\times$ 10^{-6}
α	0.68 ($\pm$ 0.01)	-
λ / eV	-	>10
	SWV	
k^0 / m s^{-1}	1.9 ($\pm$ 0.4) $\times$ 10^{-6}	1.2 ($\pm$ 0.1) $\times$ 10^{-6}
α	0.68 ($\pm$ 0.01)	-
λ / eV	-	>10
	CV	
k^0 / m s^{-1}	1.9 ($\pm$ 0.1) $\times$ 10^{-6}	1.2 ($\pm$ 0.1) $\times$ 10^{-6}
α	0.68 ($\pm$ 0.01)	-
λ / eV	-	15.5

[a] Error bars were calculated from the standard deviation of the best theoretical fits from voltammograms with different modulation times (for DMPV), frequencies (for SWV), and scan rates (for CV).

The experimental voltammograms can be satisfactorily fit with the BV model in all the techniques considered: DMPV, SWV and CV. Moreover, the parameters obtained are consistent and agree well with those reported in the literature (see Table 12.2).

Table 12.2: Literature values for the heterogeneous rate constants and electron transfer coefficients for the electro-reduction of Eu^{3+}.

Parameter	Literature Value	Method	Reference
k^0 / m s^{-1}	2.5 $\times$ 10^{-6}[a]	d.c. polarography	[37]
	1.7 $\times$ 10^{-6}[b]	DMPV	[34]
	0.93 $\times$ 10^{-6}[c]	Chrono-coulometry	[38]
α	0.60[a]	d.c. polarography	[37]
	0.69[b]	DMPV	[34]
	0.68[c]	Chrono-coulometry	[38]

[a] 1M $NaClO_4$, pH=3.
[b] 1M $NaClO_4$, pH=4.
[c] 0.5M $NaClO_4$.

On the other hand, the experimental results cannot be parameterized when the MH model is assumed. In DMPV and SWV, once the k^0 value is extracted from the peak-to-peak separation, the peak heights of reduction and oxidation cannot be fitted simultaneously with any λ value. The

MH curves shown in Figures 12.4, 12.5 and 12.6 correspond to the least squared error in the peak currents in consistency with the peak-to-peak separation, yielding meaningless λ values. As can be seen, the magnitude of the reduction peaks is underestimated by MH whereas it overestimates the height of the oxidative peaks. This situation is opposite to that found for the reduction of 2-methyl-2-nitropropane in acetonitrile [28] and cyclooctatetraene in DMSO [26], for which α values less than 0.4 were determined.

The above results join other recent experimental evidences [24–28] pointing out the inability of the MH model to describe the voltammetric response of solution-phase redox couples for which α values different from 0.5 are reported. These deviations may be indicating that some of the approximations assumed in Equations 12.4 and 12.5 do not apply for this redox system. Thus, the assumption of equal Gibbs energy curves of reactants and products [7] may not hold due to the change in charge that can affect the vibrational modes of the species as well as its interactions with the solvent [60, 61]. Hence, the use of the non-symmetrized models should be more adequate for these systems and this will be tackled in future work.

12.4 Conclusions

The kinetic analysis of the one-electron reduction of Eu^{3+} at mercury electrodes in aqueous solution has been performed by considering the Butler-Volmer (BV) and Marcus-Hush (MH) models. The most commonly used voltammetric techniques have been employed, namely, square wave voltammetry (SWV), differential multipulse votammetry (DMPV) and cyclic voltammetry (CV).

The use of differential pulse techniques (SWV and DMPV) in reverse scan mode has proven to be very appropriate for kinetic model discrimination. Besides the well-known advantage of pulse techniques for reducing background effects, reverse scan voltammograms enable to examine simultaneously the reactant and product species if the appropriate conditions are assured. The optimum technique parameters (step potential and pulse times) have been discussed for electrodes of different size.

The experimental voltammograms obtained for Eu^{3+} reduction have been fitted satisfactorily with

the BV model in all the techniques considered, obtaining the values $k^0 = 1.9 \times 10^{-6}$ m s^{-1} and $\alpha = 0.68$. These are very consistent in the different methods and are in good agreement with previous data in the literature.

Regarding the MH model, the reduction and oxidation peaks cannot be fitted simultaneously with any set of $\{k^0, \lambda\}$ values. In all cases, the results obtained from the MH approach in its simple version underestimate the magnitude of the reduction peak and overestimate that of the oxidation one. These results, together with other previous experimental deviations from the symmetric MH model, may indicate asymmetrical Gibbs energy curves for the electroactive species due to their different charge.

References

[1] J.A.V. Butler, Trans. Faraday Soc. 19 (1924) 729–733.

[2] T. Erdey-Gruz, M. Volmer, Z. Physik. Chem. 150 (1930) 203–213.

[3] R.A. Marcus, J. Chem. Phys. 24 (1956) 966–978.

[4] R.A. Marcus, Annu. Rev. Phys. Chem. 15 (1964) 155.

[5] N.S. Hush, J. Chem. Phys. 28 (1958) 962–972.

[6] N.S. Hush, J. Electroanal. Chem. 470 (1999) 170–195.

[7] C.E.D. Chidsey, Science 251 (1991) 919–922.

[8] L. Eberson, Electron transfer reactions in organic chemistry, Springer-Verlag, Berlin Heidelberg, 1987.

[9] Y. Liu, R. He, Q. Zhang, S. Chen, J Phys. Chem. C 114 (2010) 10812–10822.

[10] P.D. Tyma, M.J. Weaver, J. Electroanal. Chem. Interfacial. Electrochem. 111 (1980) 195–210.

[11] S.W. Feldberg, Anal. Chem. 82 (2010) 5176–5183.

[12] K.B. Oldham, J.C. Myland, J. Electroanal. Chem. 655 (2011) 65–72.

[13] R.J. Forster, L.R. Faulkner, J. Am. Chem. Soc. 116 (1994) 5444–5452.

[14] H.O. Finklea, D.D. Hanshew, J. Am. Chem. Soc. 114 (1992) 3173–3181.

[15] H.O. Finklea, L. Liu, M.S. Ravenscroft, S. Punturi, J. Phys. Chem. 100 (1996) 18852–18858.

[16] M.S. Ravenscroft, H.O. Finklea, J. Phys. Chem. 98 (1994) 3843–3850.

[17] J.N. Richardson, G.K. Rowe, M.T. Carter, L. Tender, L. Curtin, S. Peck, R. Murray, Electrochim. Acta 40 (1995) 1331–1338.

[18] G.K. Rowe, M.T. Carter, J.N. Richardson, R.W. Murray, Langmuir 11 (1995) 1797–1806.

[19] R.M. Haddox, H.O. Finklea, J. Phys. Chem. B 108 (2004) 1694–1700.

[20] N. Madhiri, H.O. Finklea, Langmuir 22 (2006) 10643–10651.

[21] B.R. Kozub, M.C. Henstridge, C. Batchelor-McAuley, R.G. Compton, ChemPhysChem 12 (2011) 2806–2815.

[22] M.C. Henstridge, C. Batchelor-McAuley, R. Gusmao, R.G. Compton, Chem. Phys. Lett. 517 (2011) 108–112.

[23] C.J. Miller, Physical Electrochemistry Principles, Methods, and Applications, Marcel Dekker, 1995.

[24] M.C. Henstridge, E. Laborda, N.V. Rees, R.G. Compton, Electrochim. Acta in press.

[25] D. Suwatchara, M.C. Henstridge, N.V. Rees, R.G. Compton, J. Phys. Chem. C 115 (2011) 14876–14882.

[26] D. Suwatchara, N.V. Rees, M.C. Henstridge, E. Laborda, R.G. Compton, J Electroanal. Chem. 665 (2012) 38–44.

[27] M.C. Henstridge, Y. Wang, J.G. Limon-Petersen, E. Laborda, R.G. Compton, Chem. Phys. Lett. 517 (2011) 29–35.

[28] E. Laborda, Y. Wang, M.C. Henstridge, F. Martinez-Ortiz, A. Molina, R.G. Compton, Chem. Phys. Lett. 512 (2011) 133–137.

[29] E. Laborda, M. Henstridge, A. Molina, F. Martinez-Ortiz, R.G. Compton, J Electroanal. Chem. 660 (2011) 169–177.

[30] J.G. Limon-Petersen, I. Streeter, N.V. Rees, R.G. Compton, J. Phys. Chem. C 113 (2009) 333–337.

[31] E.J.F. Dickinson, J.G. Limon-Petersen, N.V. Rees, R.G. Compton, J. Phys. Chem. C 113 (2009) 11157–11171.

[32] C. Amatore, E. Maisonhaute, G. Simonneau, J. Electroanal. Chem. 486 (2000) 141–155.

[33] F. Martinez-Ortiz, N. Zoroa, A. Molina, C. Serna, E. Laborda, Electrochim. Acta 54 (2009) 1042–1055.

[34] E. Laborda, E.I. Rogers, F. Martinez-Ortiz, A. Molina, R.G. Compton, Electrochim. Acta 55 (2010) 6577–6585.

[35] A. Molina, E. Laborda, F. Martinez-Ortiz, D.F. Bradley, D.J. Schiffrin, R.G. Compton, J. Electroanal. Chem. 659 (2011) 12–24.

[36] A. Molina, E. Laborda, E.I. Rogers, F. Martinez-Ortiz, C. Serna, J.G. Limon-Petersen, N.V. Rees, R.G. Compton, J. Electroanal. Chem. 634 (2009) 73–81.

[37] B. Timmer, M. Sluyters-Rehbach, J.H. Sluyters, J. Electroanal. Chem. 14 (1967) 181–191.

[38] M. Cetnarska, J. Stroka, J. Electroanal. Chem. Interfacial. Electrochem. 234 (1987) 263–275.

[39] Y. Wang, E.I. Rogers, R.G. Compton, J. Electroanal. Chem. 648 (2010) 15–19.

[40] Y. Wang, E.I. Rogers, S.R. Belding, R.G. Compton, J. Electroanal. Chem. 648 (2010) 134–142.

[41] Y. Wang, S.R. Belding, E.I. Rogers, R.G. Compton, J. Electroanal. Chem. 650 (2011) 196–204.

[42] Y. Wang, J. Limon-Petersen, R. Compton, J. Electroanal. Chem. 652 (2011) 13–17.

[43] M. Sharp, Electrochim. Acta 28 (1983) 301–308.

[44] J. Mauzeroll, E.A. Hueske, A.J. Bard, Anal. Chem. 75 (2003) 3880–3889.

[45] D. Shoup, A. Szabo, J. Electroanal. Chem. Interfacial Electrochem. 140 (1982) 237–245.

[46] O.V. Klymenko, R.G. Evans, C. Hardacre, I.B. Svir, R.G. Compton, J. Electroanal. Chem. 571 (2004) 211–221.

[47] R.B. McCleskey, J. Chem. Eng. Data 56 (2011) 317–327.

[48] R.G. Compton, C.E. Banks, Understanding Voltammetry, 2nd edn., Imperial College Press, 2011.

[49] A.N. Frumkin, Electrochimica Acta 9 (1964) 465–476.

[50] E.J.F. Dickinson, R.G. Compton, J. Electroanal. Chem. 661 (2011) 198–212.

[51] M. Rudolph, J. Electroanal. Chem. Interfacial. Electrochem. 314 (1991) 13–22.

[52] M. Rudolph, J. Electroanal. Chem. 338 (1992) 85–98.

[53] M. Rudolph, D.P. Reddy, S.W. Feldberg, Anal. Chem. 66 (1994) 589A–600A.

[54] M. Rudolph, J. Electroanal. Chem. 375 (1994) 89–99.

[55] W. Luo, S.W. Feldberg, M. Rudolph, J. Electroanal. Chem. 368 (1994) 109–113.

[56] V. Mirčeski, Š. Komorsky-Lovrić, M. Lovrić, Square-Wave Voltammetry: Theory and Application, Springer, 2007.

[57] N. Fatouros, D. Krulic, J. Electroanal. Chem. 520 (2002) 1–5.

[58] M. Zelic, Croat. Chem. Acta 79 (2006) 49–55.

[59] M. Lovrić, D. Jadreško, Electrochim. Acta 55 (2010) 948–951.

[60] J.T. Hupp, M.J. Weaver, J. Phys. Chem. 88 (1984) 6128–6135.

[61] R.A. Marcus, J. Chem. Phys. 43 (1965) 679–701.

Chapter 13 Giving Physical Insight into the Butler-Volmer Model of Electrode Kinetics: Application of Asymmetric Marcus-Hush Theory to the Study of the Electroreductions of 2-Methyl-2-Nitropropane, Cyclooctatetraene and Europium(III) on Mercury Microelectrodes

The work presented in this chapter was carried in collaboration with

- **E. Laborda, N. Rees, A. Molina, F. Martinez-Ortiz** and **M.C. Henstridge** (for the theory and modelling parts)
- **D. Suwatchara** (for the cyclooctatetraene experiments)

and has been published in:

M.C. Henstridge, E. Laborda, Y. Wang, D. Suwatchara, R.G. Compton, J. Electroanal. Chem. 672 (2012) 45–52

The asymmetric Marcus-Hush (MH) model for electrodekinetics is applied to the kinetic study of the electroreduction of 2-methyl-2-nitropropane in acetonitrile, cyclooctatetraene in dimethylsulfoxide and europium(III) in aqueous solution, using mercury microhemispheres as working electrodes. This kinetic model includes the possibility of the oxidative and reductive processes having different reorganization energies due to differences between the force constants of the electroactive species.

For each redox couple, the response obtained in cyclic and square wave voltammetries can be fitted satisfactorily with the four-parameter asymmetric MH model. From the fitting of the voltammograms the values of the kinetic parameters are extracted and analyzed in terms of physical properties of the electroactive species. A comparison of the asymmetric model against the simpler, phenomenological

Butler-Volmer (BV) approach is discussed, as well as a possible physical interpretation for the BV transfer coefficient.

13.1 Introduction

In recent works, the authors have evaluated the so called Marcus-Hush-Chidsey approach (here referred as the symmetric Marcus-Hush (MH) approach) through quantitative study of the voltammetric responses of several solution-phase systems using various techniques [1–7]. These include the electroreduction of 2-methyl-2-nitropropane in acetonitrile [4, 5], cyclooctatetraene in dimethylsulfoxide [3] and europium(III) in water solution [4, 7], which have been examined via cyclic, square wave and differential pulse voltammetries. Hemispherical mercury microelectrodes were employed under fully supported conditions which enabled the exclusion of possible effects due to ohmic drop and migration via numerical simulation [8–10].

For each of the above redox systems it was not possible to fit the experimental voltammetry satisfactorily when using the symmetric MH approach, however the empirical Butler-Volmer (BV) model permitted an adequate parameterisation of the experiments, employing a transfer coefficient (α) different from 0.5.

Other deviations from the symmetric MH model have been reported in the literature. Savéant and Tessier [11] observed that for the electroreduction of various nitrocompounds the value of a at the formal potential is smaller than 0.5. Additionally, asymmetric anodic and cathodic Tafel plots have been found for metal aquo-complexes in solution [12] and osmium [13, 14] and ferrocene [15–17] complexes attached to the electrode surface.

Marcus [18] and other authors [11, 12] have pointed out that these deviations may be due to differences between the force constants of the reactants and products, which are assumed equal in the symmetric MH model. As a consequence of the electron transfer, reactant and product species carry differing charges. The vibrational modes and interactions with the solvent can therefore differ significantly, resulting in differences in the reorganization energies of the oxidative and reductive processes.

For homogeneous electron transfer processes, different oxidative and reductive reorganization energies in one of the participating redox couples may be compensated by a corresponding difference in the other. By contrast, for reactions occurring at an electrode there is only one participating redox couple and so such compensation is less likely.

Accordingly, in a recent publication [19] we have made use of the asymmetric form of Marcus theory [18] to derive expressions for the oxidation and reduction rate constants of electrode processes that consider possible differences in the reorganization energies. The resulting asymmetric model can be parameterized in terms of four kinetic parameters: the formal potential, the standard heterogeneous rate constant, the reorganization energy, and the parameter β. This latter is related to the difference between the force constants of reactants and products, so that the symmetric model can be considered a particular case of the asymmetric one for which $\beta = 0$.

The theoretical study of the voltammetry of solution-phase redox systems using the asymmetric MH model has shown that this approach can account for the experimental deviations reported. Thus, asymmetric cathodic and anodic Tafel plots are expected when different reorganization energies occur, as well as α values which differ from 0.5 at the formal potential. Moreover, the asymmetric model has proved more flexible than the symmetric version when fitting voltammetry.

All of these aspects are examined experimentally in this chapter with the quantitative application of the asymmetric model to the electroreductions of 2-methyl-2-nitropropane in acetonitrile, cyclooctatetraene in dimethylsulfoxide and europium(III) in aqueous solution using mercury microhemisphere working electrodes:

$$\mathrm{MeNP} + \mathrm{e}^- \rightleftharpoons \mathrm{MeNP}^{\bullet -} \tag{13.1}$$

$$\mathrm{COT} + \mathrm{e}^- \rightleftharpoons \mathrm{COT}^{\bullet -} \tag{13.2}$$

$$\mathrm{Eu}^{3+} + \mathrm{e}^- \rightleftharpoons \mathrm{Eu}^{2+} \tag{13.3}$$

The quality of fitting and the uniqueness of the kinetic parameters extracted from cyclic and square wave voltammograms are discussed. Further, an approximate relationship is derived between

the transfer coefficient from Butler-Volmer and the ratio β/λ from the asymmetric Marcus-Hush model, suggesting the possibility of gaining real physical insight into an electrochemical system using the phenomenological Butler-Volmer model.

13.2 Experimental

13.2.1 Chemical Reagents

Cyclooctatetraene (COT, Aldrich, 98%), 2-methyl-2-nitropropane (MeNP, Aldrich, 99%), europium(III) chloride hexahydrate ($EuCl_3{\cdot}6H_2O$, Aldrich, 99.99%), mercury(I) nitrate dihydrate ($Hg_2(NO_3)_2 \cdot 2H_2O$, Aldrich, >97%), nitric acid (HNO_3, Fisher scientific, 70%), ferrocene ($Fe(C_5H_5)_2$, Aldrich, 98%), cobalt(III) sepulchrate trichloride ($[CoSep]Cl_3$, Aldrich, 95%), potassium nitrate (KNO_3, Aldrich, >99%), potassium chloride (KCl, Aldrich, >99%), acetonitrile (MeCN, Fisher Scientific, HPLC grade), N,N-dimethylformamide (DMF, Aldrich, anhydrous grade) and dimethylsulfoxide (DMSO, Alfa Aesar, >99%) were all used as received without further purificatio

Background electrolytes including tetraethylammonium perchlorate (TEAP, Fluka, Puriss grade), tetraethylammonium bromide (TEABr, BDH Chemicals, 98%), tetrabutylammonium perchlorate (TBAP, Fluka, Puriss grade) and tetrabutylammonium iodide (TBAI, Aldrich, >98%) were recrystallized from ethanol and dried in a dessicator for 48 h prior to use in order to remove adsorbed moisture and trace electroactive species.

13.3 Instrumental

Mercury hemispherical electrodes electrodeposited on platinum discs were used as working electrodes. A silver wire was employed as reference electrode for organic solvents and a saturated calomel electrode (SCE) for aqueous solutions. A platinum foil was used as counter electrode.

Microdisk electrodes of radii 25 and 50 μm were fabricated in-house by sealing Pt wire (Goodfellow Cambridge Ltd., UK) into a soda glass capillary. Mercury hemispheres were electrochemically deposited onto each microdisc by stepping to -0.25 V vs. Ag wire in a 5 mM $Hg_2(NO_3)_2$ solution

containing 0.1 M KNO_3 and acidified to 0.5% with HNO_3 [20].

The size of the hemispherical drop was initially controlled by the amount of charge passed, and then confirmed by both optical and electrochemical methods. Thus, visual measurement of the hemispheres was obtained through the use of JVC digital video camera TK-C921EG. In all cases, the mercury droplet was found to adopt the radius of its respective microdisk. The electrochemical characterization of the mercury hemispheres was also carried out through analysis of the limiting current chronoamperogram of an aqueous solution containing 2 mM [CoSep]Cl_3 and 0.1 M KNO_3. The value of the diffusion coefficient of [CoSep]Cl_3 employed for the calculations was $D = 6.3 \times 10^{-10}$ m^2 s^{-1} [3, 21, 22].

13.3.1 Experiments

The specific conditions for cyclic voltammetry (CV) and square wave voltammetry (SWV) experiments are given in each figure.

In all cases, the working solution was degassed with N_2 (BOC Gases) for at least 20 min before each experiment and a positive pressure of N_2 was maintained throughout. Measurements were carried out at 298 ± 0.2 K with stringent thermal control of the electrochemical cell through the use of an air heater-controller system.

The diffusion coefficients of the electroactive species were determined separately via double potential step chronoamperometry [25] in the case of MeNP and Eu(III). In the case of COT, the use of double step chronoamperometry was not feasible due to interference by a second reduction wave [3, 23]. The diffusion coefficient of the oxidized species (COT) was extracted via single pulse chronoamperograms and that of the reduced species (radical anion $COT^{\bullet -}$) was determined from the fitting of the cyclic voltammograms. The results obtained are included in Table 13.3.1.

Table 13.1: Values of the diffusion coefficients obtained for the electroactive species of each redox system under the experimental working conditions for cyclic and square wave voltammetry experiments.

Redox couple	Medium	D_{ox} (m^2 s^{-1})	D_{red} (m^2 s^{-1})
MeNP/$MeNP^{\bullet-}$	0.1 M TBAP, MeCN	2.7×10^{-9}	2.7×10^{-9}
COT/$COT^{\bullet-}$	0.1 M TEABr, DMSO	7.4×10^{-10}	6.5×10^{-10}
Eu(III)/Eu(II)	0.4 M KCl, H_2O	6.5×10^{-10}	9.0×10^{-10}

The occurrence of ohmic drop or migration effects are not considered following simulation [8–10] of the influence of the uncompensated resistance for the conditions of the working solutions.

13.3.2 Fitting details

The theoretical results corresponding to the Butler-Volmer and Marcus-Hush models were obtained by means of finite difference numerical methods using homemade programs.

Best fit parameters were sought for each model, $\{E^{0\prime}, k^0, \lambda\}$ for BV and $\{E^{0\prime}, k^0, \lambda, \beta\}$ for asymmetric MH, via minimization of the Mean Scaled Absolute Deviation (MSAD) for each voltammogram:

$$\%\text{MSAD} = \frac{1}{N} \sum_{N} \left| \frac{I_{\text{exp}} - I_{\text{sim}}}{I_{\text{exp}}} \right| \times 100 \tag{13.4}$$

where N is the number of data points, and I_{exp} and I_{sim} are the experimental and simulated signals, respectively. In order to avoid large contributions to the MSAD as a consequence of a very small signal value, only the points where I_{exp} is, at least, 10% of the peak current have been considered in the calculations. In the case of the electroreduction of COT in SWV, only the points around the SWV peak ($I_{\text{exp}} > 0.7 \times I_{\text{exp,peak}}$) were considered to avoid any distortion by the second wave.

13.4 Results and discussion

Experimental cyclic (CV) and square-wave (SWV) voltammetries for the electroreduction of systems 13.1, 13.2, and 13.3 were fitted using both the asymmetric Marcus-Hush model (Equations Appx VI.2, Appx VI.3, Appx VI.4, Appx VI.7, and Appx VI.8) and the phenomenological Butler-Volmer

model [24, 25], for which the reductive and oxidative rate constants are given by:

$$k_{\mathrm{red}}^{\mathrm{BV}} = k^0 e^{-\alpha\eta} \tag{13.5}$$

$$k_{\mathrm{ox}}^{\mathrm{BV}} = k^0 e^{(1-\alpha)\eta} \tag{13.6}$$

Voltammetry for each of the three redox systems is shown, along with the best fit of each kinetic model, in Figures 13.1, 13.2, 13.3, 13.4, 13.5, and 13.6.

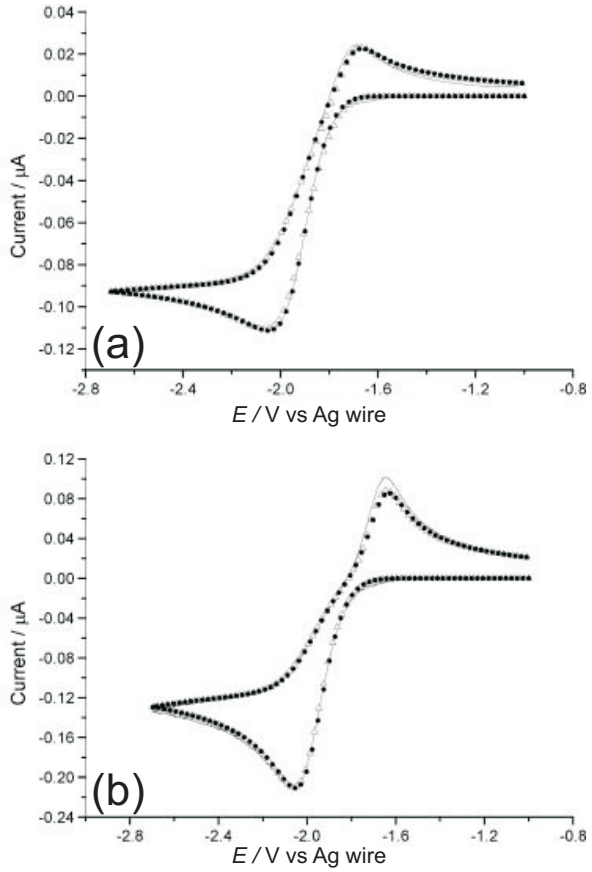


Figure 13.1: Experimental (solid line) and theoretical (points) CV voltammograms obtained with the asymmetric Marcus-Hush (•) and Butler-Volmer (△) models for the electroreduction of 2-methyl-2-nitropropane with a scan rate: (a) 500 and (b) 5000 mV s^{-1}. The values of the kinetic parameters considered for simulated results are given in Table 13.2. Working solution: 2 mM MeNP, 0.1 M TBAP in MeCN. A 25 μm radius mercury hemisphere was employed as working electrode.

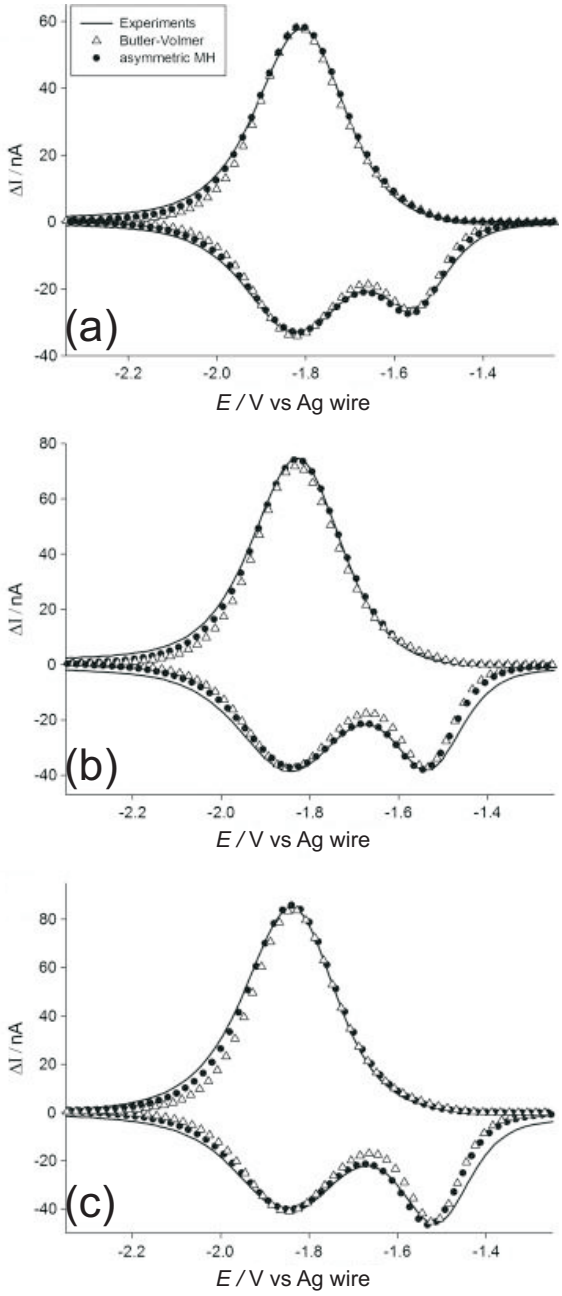


Figure 13.2: Experimental (solid line) and theoretical (points) SWV voltammograms obtained with the asymmetric Marcus-Hush (•) and Butler-Volmer (△) models for the electroreduction of 2-methyl-2-nitropropane at different frequencies: (a) 100, (b) 200 and (c) 300 Hz. E_{SW} = 25 mV, E_S = 10 mV. The values of the kinetic parameters considered for simulated results are given in Table 13.2. Working solution: 2 mM MeNP, 0.1 M TBAP in MeCN. A 25 μm radius mercury hemisphere was employed as working electrode.

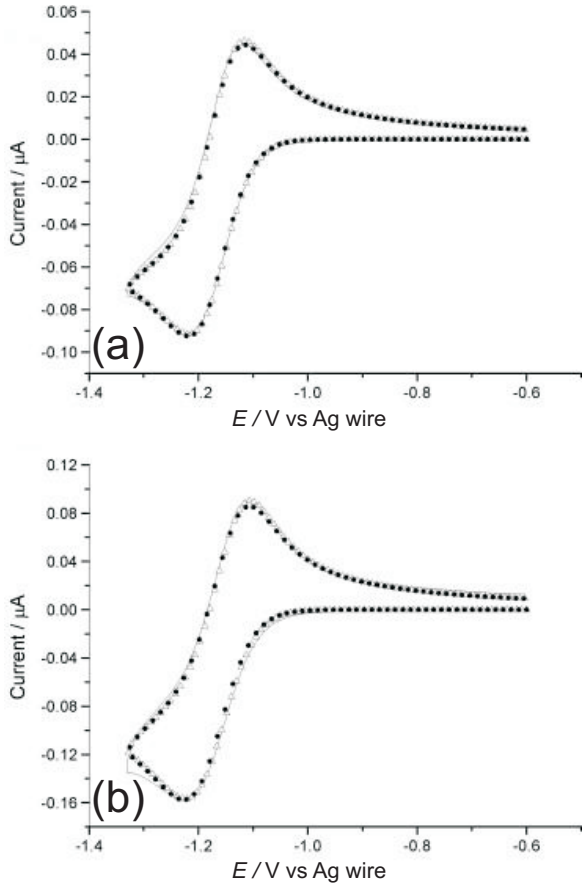


Figure 13.3: Experimental (solid line) and theoretical (points) CV voltammograms obtained with the asymmetric Marcus-Hush (•) and Butler-Volmer (△) models for the electroreduction of cyclooctatetraene with a scan rate: (a) 250 and (b) 1000 mV s^{-1}. The values of the kinetic parameters considered for simulated results are given in Table 13.2. Working solution: 1 mM COT, 0.1 M TEABr in DMSO. A 50 μm radius mercury hemisphere was employed as working electrode.

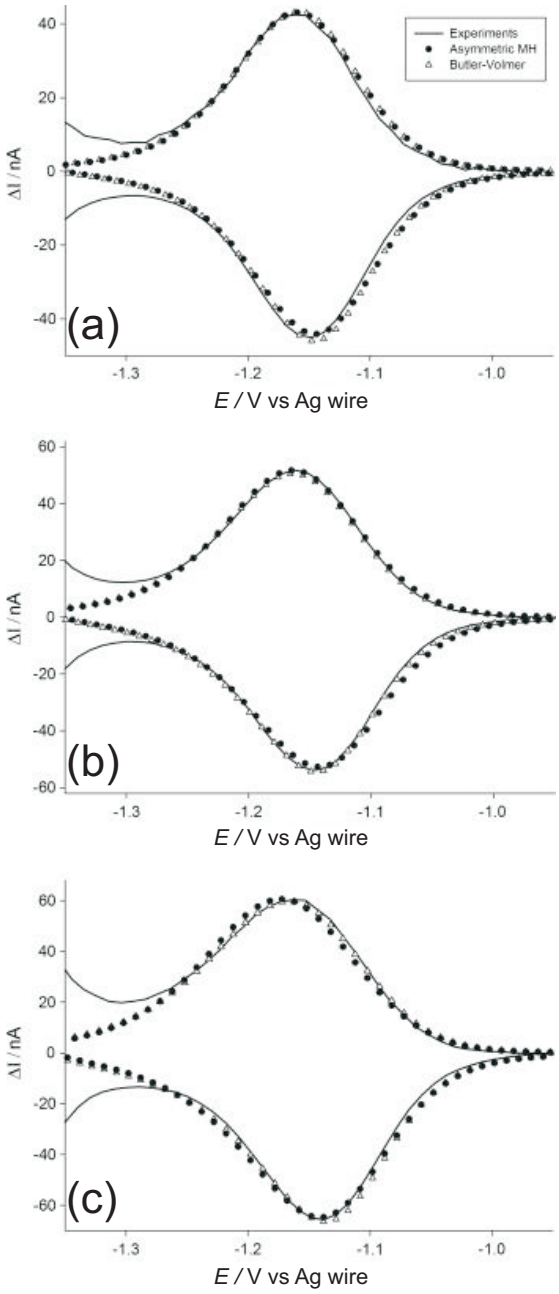


Figure 13.4: Experimental (solid line) and theoretical (points) SWV voltammograms obtained with the asymmetric Marcus-Hush (•) and Butler-Volmer (△) models for the electroreduction of cyclooctatetraene at different frequencies: (a) 25, (b) 50 and (c) 100 Hz. E_{SW} = 15 mV, E_S = 10 mV. The values of the kinetic parameters considered for simulated results are given in Table 13.2. Working solution: 1 mM COT, 0.1 M TEABr in DMSO. A 50 μm radius mercury hemisphere was employed as working electrode.

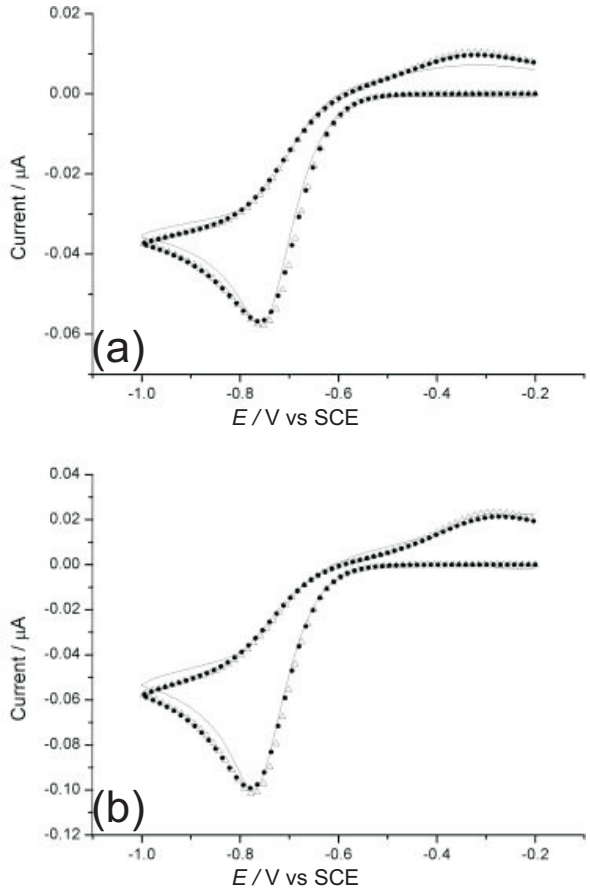


Figure 13.5: Experimental (solid line) and theoretical (points) CV voltammograms obtained with the asymmetric Marcus-Hush (•) and Butler-Volmer (△) models for the electroreduction of Eu(III) with a scan rate: (a) 250 and (b) 1000 mV $^{-1}$. The values of the kinetic parameters considered for simulated results are given in Table 13.2. Working solution: 1 mM $EuCl_3$, 0.4 M KCl in water. A 50 μm radius mercury hemisphere was employed as working electrode.

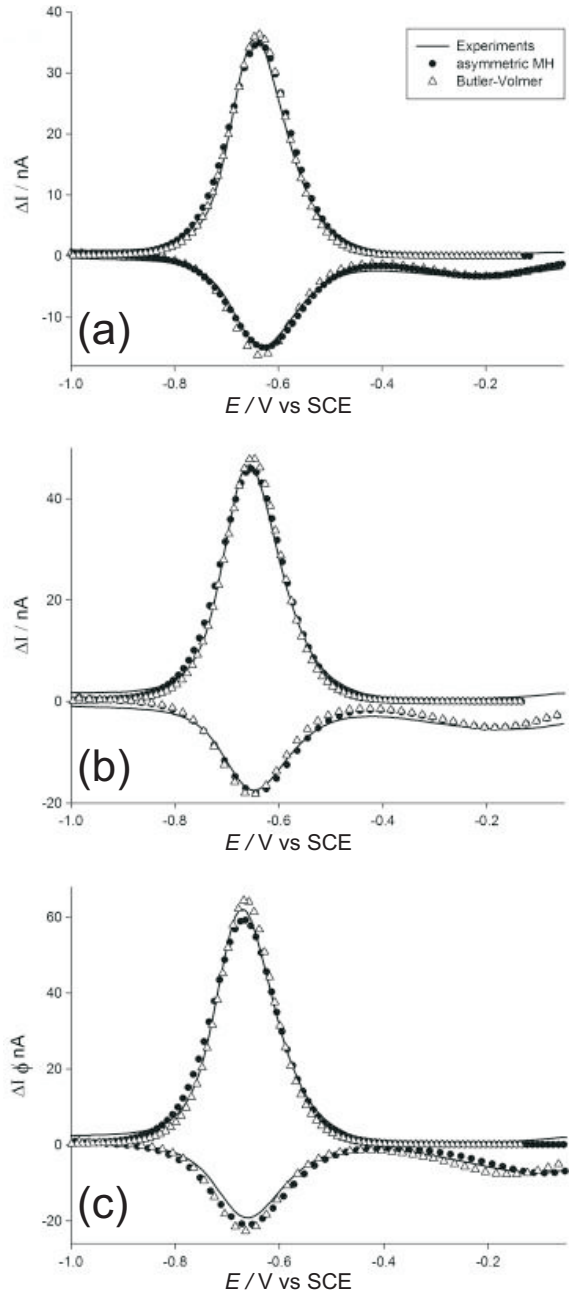


Figure 13.6: Experimental (solid line) and theoretical (points) SWV voltammograms obtained with the asymmetric Marcus-Hush (•) and Butler-Volmer (△) models for the electroreduction of Eu(III) at different frequencies: (a) 25, (b) 50 and (c) 100 Hz. E_{SW} = 25 mV, E_S = 10 mV. The values of the kinetic parameters considered for simulated redults are given in Table 13.2. Working solution: 1 mM $EuCl_3$, 0.4 M KCl in water. A 50 μm radius mercury hemisphere was employed as working electrode.

In previous publications [1, 2, 4, 5, 7], the authors have reported that the use of the symmetric MH kinetic formalism does not enable fitting of the voltammetric response for these redox systems. Once the value of the standard electrochemical rate constant (k^0) is determined from the separation of the reduction and oxidation peaks, the best fit in terms of MSAD gave rise to an overestimation

of the current for one peak and an underestimation of the other. However, as can be seen in Figures 13.1, 13.2, 13.3, 13.4, 13.5, and 13.6, both CV and SWV can be parameterized satisfactorily by using the classical BV model with $\alpha < 0.5$ for COT and MeNP, and $\alpha > 0.5$ for Eu(III). The best fit kinetic parameters obtained from the BV model, together with the average MSAD values, are given in Table 13.2.

Table 13.2: Kinetic parameters obtained from the fitting of cyclic and square wave voltammograms with the asymmetric Marcus-Hush (asymMH) and Butler-Volmer (BV) models. Error bars calculated from the standard deviation of the best fits at several scan rates or frequencies.

Redox couple	Kinetic model	Kinetic parameters	%MSAD	
			CV	SWV
MeNP/MeNP$^{\bullet-}$, 0.1 M TBAP, MeCN	BV	$k^0 = (3.0 \pm 0.2) \times 10^{-3}$ cm^{-1} s $\alpha = 0.38 \pm 0.01$	4 ± 2	9.6 ± 0.6
	AsymMH	$k^0 = (3.0 \pm 0.2) \times 10^{-3}$ cm^{-1} s $\beta/\lambda = -0.31 \pm 0.04$ $\lambda = 1.0 \pm 0.2$ eV	3 ± 1	5 ± 1
COT/COT$^{\bullet-}$, 0.1 M TEABr, DMSO	BV	$k^0 = (1.2 \pm 0.2) \times 10^{-2}$ cm^{-1} s $\alpha = 0.38 \pm 0.02$	7 ± 2	3.6 ± 0.7
	AsymMH	$k^0 = (1.1 \pm 0.3) \times 10^{-2}$ cm^{-1} s $\beta/\lambda = -0.22 \pm 0.07$	7 ± 2	4.3 ± 0.6
Eu(III)/Eu(II), 0.4 M KCl, H_2O	BV	$k^0 = (1.7 \pm 0.7) \times 10^{-4}$ cm^{-1} s $\alpha = 0.66 \pm 0.02$	9 ± 2	12 ± 4
	AsymMH	$k^0 = (1.7 \pm 0.5) \times 10^{-4}$ cm^{-1} s $\beta/\lambda = -0.55 \pm 0.04$	8 ± 3	10 ± 4

Figures 13.1, 13.2, 13.3, 13.4, 13.5, and 13.6 also show that satisfactory fitting of the experimental voltammetry is possible when using the asymmetric MH model, with $\{E^{0\prime}, k^0, \lambda, \beta\}$ as adjustable parameters. The quality of the fittings is seen to be comparable or, in some cases, superior to that obtained with the BV model. The asymmetric MH approach, however, carries the additional benefit of enabling rationalization of the kinetic parameters in terms of microscopic properties of the system, as will be discussed below.

Given that four parameters are adjusted in the fitting procedure with the asymmetric MH model, the uniqueness of the best-fit set of data may be questioned. In Figure 13.7, this is analyzed via

representative MSAD surfaces obtained as a function of the parameters λ and β/λ, with the k^0 value fixed at the best-fit value (see Table 13.2). For the electroreduction of MeNP (Figure 13.7a), a minimum in the MSAD surface is observed which enables the unambiguous definition of best-fit kinetic parameters. By contrast, for the cases of COT and Eu(III) a 'valley', rather than a minimum, is obtained. Thus, the MSAD is effectively the same (within 0.5%) in a region defined mainly by the ratio β/λ (see Figure 13.7b and c). In this situation, from the fitting of the voltammograms only an estimation of the optimum β/λ value can be extracted.

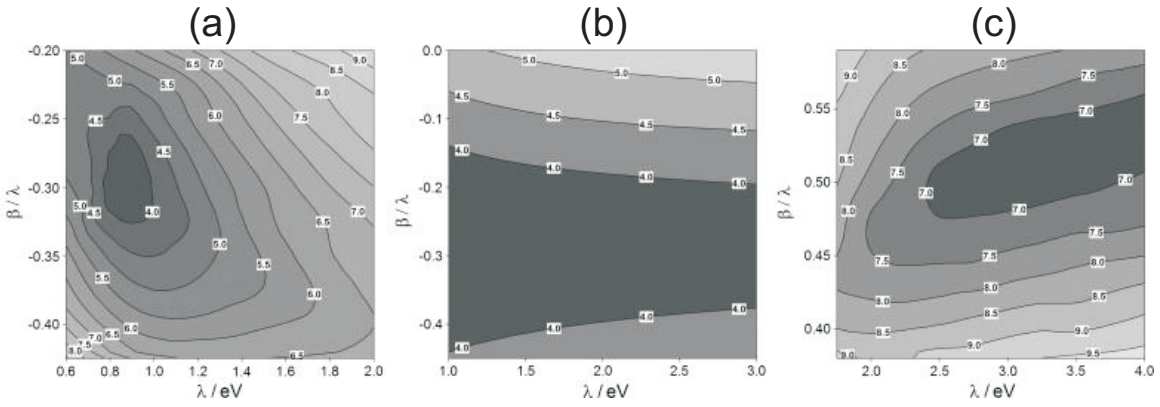


Figure 13.7: Representative MSAD surfaces corresponding to the fitting of the SWV voltammograms of the electroreduction of (a) MeNP, (b) COT and (c) Eu(III). Other conditions as in Figures 13.1, 13.2, 13.3, 13.4, 13.5, and 13.6.

The results obtained from electrochemical methods can be complemented with those from theoretical calculations to gain further information. For example, for the electroreduction of MeNP, the theoretical estimation of the inner-sphere reorganization energy yields a value of 0.84 eV [26]. Combined with the value β = -0.31 eV extracted from the voltammograms, one finds that $\langle I_s \rangle$ = -0.37, which involves that the average ratio of the force constants of the oxidized and reduced species is $f_s^{ox}/f_s^{red} = 0.46$ (see Equation Appx VI.12).

From the definition of β (Equation Appx VI.9), the ratio β/λ is seen to be directly related to the differences between the force constants through $\langle I_s \rangle$. According to the discussion above, this ratio is the key parameter defining the symmetry of the redox process, and so the voltammetric waveshape. Thus, a positive β/λ value indicates $f_s^{ox} > f_s^{red}$ and hence a tighter Gibbs energy curve for the

oxidized species. This gives rise to an increase of the reductive signal with respect to the oxidative signal [19]. The opposite effect is observed for negative β/λ values, which are associated with greater force constants of the reduced species. Clearly, the greater the absolute value of β/λ, the greater the differences in the force constants and then the greater the effects described above.

Applying this interpretation of the β/λ value to the experimental results, we observe that negative β/λ values are obtained for the electroreduction of COT and MeNP. In both cases the oxidized species is neutral and the reduced species is a radical anion. One would therefore expect the reduced species to interact more strongly with the solvent than the oxidized species and consequently the Gibbs energy curve is tighter for the reduced species [11]. By contrast, for the reduction of Eu(III), a positive β/λ value is determined. This can be understood taking into account that in this case the oxidized species carries a larger charge (+3) than the reduced one (+2).

The analysis of the MSAD in Figure 13.7 revealed some correlation between the ratio β/λ and the transfer coefficient in the BV model. Consequently, it is of interest to analyze the possible connection between these parameters in order to assign a physical interpretation to α. Figure 13.8 shows the variation of both oxidative and reductive rate constants with overpotential for a range of reorganisation energies with a constant ratio $\beta/\lambda = +0.4$. The value of can be seen to affect only the range of potentials over which the 'Tafel' plot is approximately linear. Thus, it is principally the ratio β/λ which determines the rate of variation of the rate constants with overpotential. In this way, the ratio β/λ acts in a similar fashion within the asymmetric Marcus-Hush model as does the transfer coefficient α in the Butler-Volmer model.

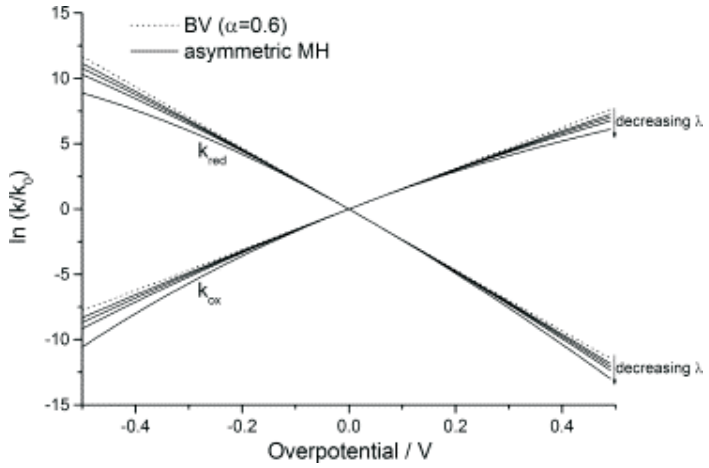


Figure 13.8: Effect of the reorganization energy (λ) on the evolution of the electrochemical rate constants with the applied overpotential according to the asymmetric Marcus-Hush model (solid line) for $\beta/\lambda = +0.4$. The results corresponding to the Butler-Volmer model for $\alpha = 0.6$ are also plotted (dotted line).

Within the symmetric MH model (i.e., $\beta = 0$) the rate constants have been shown [27] to tend towards those given by the Butler-Volmer model for $\alpha = 0.5$ as $\lambda^* \to \infty$. A treatment of the asymmetric Marcus-Hush model similarly shows that as $\lambda^* \to \infty$, the rate constants (given by Equations Appx VI.2 and Appx VI.3) tend towards those given by the Butler-Volmer model for $\alpha = \frac{1}{2} + \frac{1}{4}\frac{\beta}{\lambda}$. Accordingly, for the case considered in Figure 13.8 (i.e., $\beta/\lambda = +0.4$), we see that the MH curves tend to that for BV with $\alpha = 0.6$ as the reorganization energy increases.

While this relationship between andβ/λ is exact only in the limit $\lambda^* \to \infty$, the following relationship holds at the formal potential for all values of reorganization energy:

$$(\alpha)_{E=E^{0\prime}} = \frac{1}{2} + \gamma\frac{\beta}{\lambda} \tag{13.7}$$

Figure 13.9 shows the variation of the parameter γ with λ. While the value of γ deviates markedly from 0.25 for very small reorganisation energies, taking a typical experimental reorganisation energy of 2 eV yields $\gamma = 0.234$. Empirical fitting of the curve in Figure 13.9 yields the following relationship:

$$\gamma = \frac{1}{4} - \frac{1.267}{\lambda^* + 3.353} \tag{13.8}$$

which is accurate to within 0.1% for reorganisation energies greater than 0.5 eV.

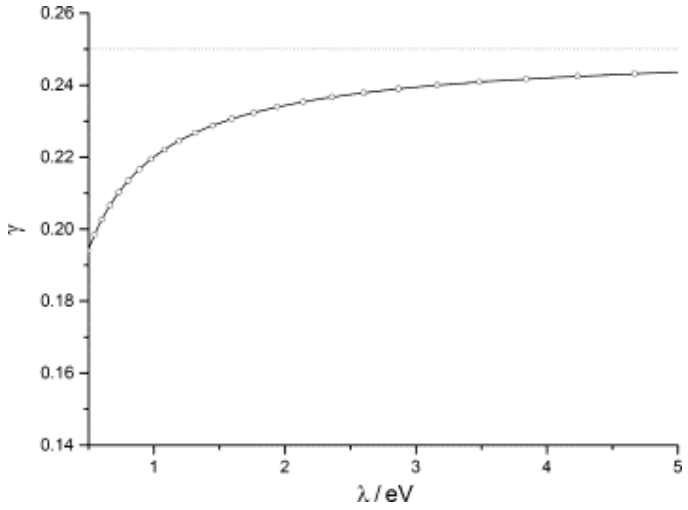


Figure 13.9: Variation of the parameter γ in Equation 13.7 with the value of the reorganization energy, λ.

The above expressions permit a precise estimation of β/λ once the value of the transfer coefficient at the formal potential is known. This is of importance since it permits an approximate physical interpretation for the great number of experimental systems for which the transfer coefficient is already known. In the same way, it justifies the use of a simpler Butler-Volmer like analysis of the electrode kinetics, complemented with the physical insights derived from the asymmetric MH model.

To conclude, α values different from 0.5 can be indicative of asymmetries of the reductionCoxidation processes. According to the asymmetric MH model, these are related to differences between the inner-shell force constants of the electroactive species, and they can be treated in a simple, general and analytical way (Equations Appx VI.7, Appx VI.8). Nevertheless, asymmetric effects may be described by other theories [28] and they may also arise from interactions outside the coordination shell (e.g., with the solvent), although their treatment can be more complex and needs computer simulations.

13.5 Conclusions

The asymmetric Marcus-Hush model has been applied to the quantitative study of three reduction processes on mercury hemispherical microelectrodes: electroreduction of 2-methyl-2-nitropropane (MeNP) in acetonitrile, cyclooctatetraene (COT) in dimethylsulfoxide and europium(III) in water solution.

The experimental voltammograms recorded in cyclic and square wave voltammetry for all these systems can be fitted satisfactorily using the Butler-Volmer (BV) model, as well as the asymmetric Marcus-Hush (MH) model. We have previously shown [1–7] that such fitting is not achievable when using the symmetric version.

Through the fitting of experimental data using the asymmetric MH model, values of the standard heterogeneous rate constant and the ratio β/λ are extracted, the latter being related to the differences between the force constants of the oxidized and reduced species. Thus, a positive value of β/λ is found for the redox couple Eu(III)/Eu(II), which indicates greater force constants in average for the oxidized species. By contrast, for the reductions of the neutral species MeNP and COT into their corresponding radical anions we obtain negative values of β/λ.

The effect of the ratio β/λ on the voltammograms has been shown to be analogous to that of the transfer coefficient (α) within the Butler-Volmer formalism. This enables the use of the α value of a given redox couple as an indicator of the differences between the oxidized and reduced species. Thus, the case $\alpha < 0.5$ is related to force constants of the reduced species greater than those of the oxidized one; the opposite situation applies for $\alpha > 0.5$. Moreover, simple relationships have been established to connect the parameters $(\alpha)_{E=E^{0\prime}}$ and β/λ. This enables a revision of the vast number of α data in terms of this physical interpretation, as well as the use of a simpler BV-like analysis of electrode kinetics while preserving the physical insights available from Marcus theory.

References

[1] M.C. Henstridge, E. Laborda, N.V. Rees, R.G. Compton, Electrochim. Acta in press.

[2] D. Suwatchara, M.C. Henstridge, N.V. Rees, R.G. Compton, J. Phys. Chem. C 115 (2011) 14876–14882.

[3] D. Suwatchara, N.V. Rees, M.C. Henstridge, E. Laborda, R.G. Compton, J. Electroanal. Chem. 665 (2012) 38–44.

[4] M.C. Henstridge, Y. Wang, J.G. Limon-Petersen, E. Laborda, R.G. Compton, Chem. Phys. Lett. 517 (2011) 29–35.

[5] E. Laborda, Y. Wang, M.C. Henstridge, F. Martinez-Ortiz, A. Molina, R.G. Compton, Chem. Phys. Lett. 512 (2011) 133–137.

[6] M.C. Henstridge, E. Laborda, E.J. Dickinson, R.G. Compton, J. Electroanal. Chem. 664 (2012) 73–79.

[7] Y. Wang, E. Laborda, M.C. Henstridge, F. Martinez-Ortiz, A. Molina, R.G. Compton, J. Electroanal. Chem. 668 (2012) 7–12.

[8] J.G. Limon-Petersen, I. Streeter, N.V. Rees, R.G. Compton, J. Phys. Chem. C 113 (2009) 333–337.

[9] E.J.F. Dickinson, J.G. Limon-Petersen, N.V. Rees, R.G. Compton, J. Phys. Chem. C 113 (2009) 11157–11171.

[10] C. Amatore, E. Maisonhaute, G. Simonneau, J. Electroanal. Chem. 486 (2000) 141–155.

[11] J.M. Savéant, D. Tessier, Disc. Faraday Soc. 74 (1982) 57–72.

[12] J.T. Hupp, M.J. Weaver, J. Phys. Chem. 88 (1984) 6128–6135.

[13] R.M. Haddox, H.O. Finklea, J. Phys. Chem. B 108 (2004) 1694–1700.

[14] N. Madhiri, H.O. Finklea, Langmuir 22 (2006) 10643–10651.

[15] A.L. Eckermann, J.A. Shaw, T.J. Meade, Langmuir 26 (2010) 2904–2913.

[16] G.A. Orlowski, H.B. Kraatz, Electrochim. Acta 51 (2006) 2934–2937.

[17] G.A. Orlowski, S. Chowdhury, H.B. Kraatz, Langmuir 23 (2007) 12765–12770.

[18] R.A. Marcus, J. Chem. Phys. 43 (1965) 679–701.

[19] E. Laborda, M. Henstridge, R.G. Compton, J. Electroanal. Chem. 667 (2012) 48–53.

[20] J. Mauzeroll, E.A. Hueske, A.J. Bard, Anal. Chem. 75 (2003) 3880–3889.

[21] T.J. Davies, B.A. Brookes, A.C. Fisher, K. Yunus, S.J. Wilkins, P.R. Greene, J.D. Wadhawan, R.G. Compton, J. Phys. Chem. B 107 (2003) 6431–6444.

[22] A. Molina, E. Laborda, E.I. Rogers, F. Martinez-Ortiz, C. Serna, J.G. Limon-Petersen, N.V. Rees, R.G. Compton, J. Electroanal. Chem. 634 (2009) 73–81.

[23] R.D. Allendoerfer, P.H. Rieger, J. Amer. Chem. Soc. 87 (1965) 2336–2344.

[24] A.J. Bard, L.R. Faulkner, Electrochemical Methods, Fundamentals and Applications, John Wiley & Sons, New York, 2001.

[25] R.G. Compton, C.E. Banks, Understanding Voltammetry, 2nd edn., Imperial College Press, London, 2011.

[26] C. Kraiya, P. Singh, D.H. Evans, J. Electroanal. Chem. 563 (2004) 203–212.

[27] S.W. Feldberg, Anal. Chem. 82 (2010) 5176–5183.

[28] S. Fletcher, J. Solid State Electrochem. 14 (2010) 705–739.

Part VI Overall Conclusions

This thesis presents several recent developments in electroanalytical chemistry.

First of all, chronoamperommetric techniques along with cyclic voltammetric methods were employed to study the diffusional behavious. Ferrocene and ferricenium ions were found that had similar diffusion coefficients, diffusional activation energies, and half-wave potentials in solutions with either TBAP or $TBAPF_6$ as supporting electrolyte, which suggested an insignificant ion-pairing effect. In aqueous solutions, the $[Ru(NH_3)_6]^{3+}/[Ru(NH_3)_6]^{2+}$ redox was studied, and a consistent diffusion coefficient ratio was found at around 0.71 supported by KCl or KNO_3, while at around 0.65 with K_2SO_4, suggesting a possible ion-pairing effect.

Secondly, electrochemistry in Room Temperature Ionic Liquids was investigated. The two-electron reduction of 1,4-benzoquinone in the ionic liquids, $[C_2mim][NTf_2]$ was studied. The diffusion coefficients for benzoquinone, its radical anion and dianion are different, enabling a quantitative determination of the comproportionation between benzoquinone and the dianion. In addition, the oxidation of hydroquinone in $[C_2mim][NTf_2]$ was also investigated suggesting a EC mechanism with a full profile of related kinetic and thermodynamic parameters.

Furthermore, quantitative analysis methods of weakly supported systems were reported. With the new insight of this technique, the mechanism of electro-reduction of 2-nitrobenzene in acetonitrile was suggested as a DISP1 process. 2,6-diphenylpyrylium ion in acetonitrile was found that had a signifi-

cant ion-pairing effect with BF_4^- resulting in unanticipated voltammetry. Therefore weakly-supported voltammogram was developed revealing mechanistic details of this EC_2 process. Additionally, pulse voltammetric techniques were applied to investigate the redox couples of cobaltocenium(I/0) in acetonitrile and cobalt(III/II)sepulchrate in aqueous solutions. The results had a good agreement with cyclic voltammetry enabling an alternative method for further studies.

Finally, electroanalytical techiques were also utilised to compare the Butler-Volmer and Marcus-Hush electron transfer kinetic formalisms. The fittings of theoretical and experimental cyclic votammograms were carried out for the electro-reductions of Eu^{3+} in aqueous solution and 2-methyl-2-nitropropane in acetonitrile at mercury hemispherical electrodes. Cyclic voltammetric technique showed that the Marcus-Hush model gave either less satisfactory fits than the Butlter-Volmer model, or a best-fit requiring unexpected reorganisation energy. Pulse voltammetric analysis further confirmed this conclusion. To preserve the physical insights of the Marcus theory, an asymmetric model with an additional parameter β related to the difference between the force constants of reactants and products was developed and compared with the simple Butler-Volmer approach.

In conclusion, further research on RTILs and weakly supported voltammetry is needed to fully understand electrode and charge transfer processes. In addition, new theories of the electron transfer kinetics are also needed as is rigorous measurement of transport properties.

Appendices

Appendix I: Theory for Chapter 5

The work presented in this appendix was carried out in collaboration with

- **S.R. Belding**

We consider the following reactions:

$$\mathrm{A} + \mathrm{e}^- \rightleftharpoons \mathrm{B} \quad (E^{0'}_{\mathrm{A|B}}) \quad k^0_{\mathrm{A|B}} \tag{Appx I.1}$$

$$\mathrm{B} + \mathrm{e}^- \rightleftharpoons \mathrm{C} \quad (E^{0'}_{\mathrm{B|C}}) \quad k^0_{\mathrm{B|C}} \tag{Appx I.2}$$

$$\mathrm{A} + \mathrm{C} \rightleftharpoons 2\mathrm{B} \quad K_{\mathrm{eqm}} \tag{Appx I.3}$$

at a microdisk electrode (Figure Appx I.1). The formal potentials, $E^{0'}_{\mathrm{A|B}}$ and $E^{0'}_{\mathrm{B|C}}$, will provide information about the equilibrium constant:

$$K_{\mathrm{eqm}} = \frac{k_{\mathrm{comp}}}{k_{\mathrm{disp}}} = \frac{[\mathrm{B}]^2}{[\mathrm{A}][\mathrm{C}]} \tag{Appx I.4}$$

and $\Delta G^{\circ}_{\mathrm{comp}}$ for the comproportionation reaction:

$$\Delta G^{\circ}_{\mathrm{comp}} = -RT\ln(K_{\mathrm{eqm}}) = -F(-E^{0'}_{\mathrm{B|C}} + E^{0'}_{\mathrm{A|B}}) \tag{Appx I.5}$$

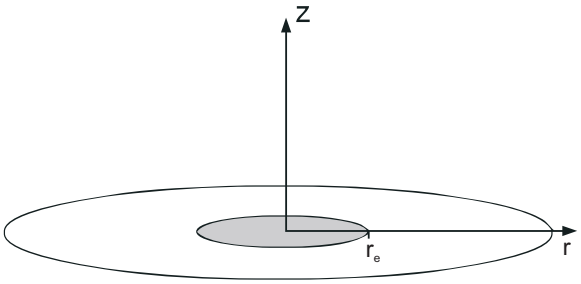


Figure Appx I.1: Circular disc electrode inlaid on an insulating support.

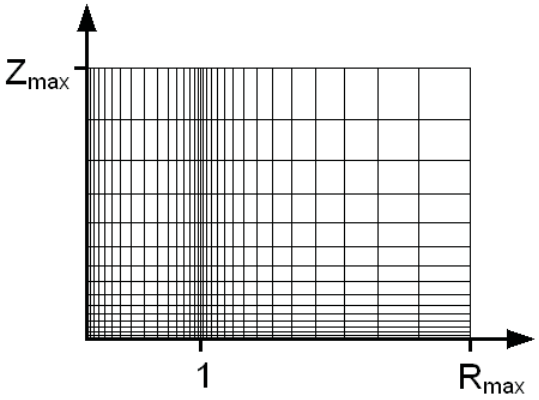


Figure Appx I.2: Discretised grid used in the simulations (some points have been removed for clarity).

Specifically, we consider the cases of cyclic voltammetry and chronoamperometry. These techniques are simulated by solving the following mass transport equations:

$$\frac{\partial c_{\mathrm{A}}}{\partial t} = D_{\mathrm{A}}\left(\frac{\partial^2 c_{\mathrm{A}}}{\partial r^2} + \frac{1}{r}\frac{\partial c_{\mathrm{A}}}{\partial r} + \frac{\partial^2 c_{\mathrm{A}}}{\partial z^2}\right) + k_{\mathrm{disp}}{c_{\mathrm{B}}}^2 - k_{\mathrm{comp}}c_{\mathrm{A}}c_{\mathrm{C}} \qquad \text{(Appx I.6)}$$

$$\frac{\partial c_{\mathrm{B}}}{\partial t} = D_{\mathrm{B}}\left(\frac{\partial^2 c_{\mathrm{B}}}{\partial r^2} + \frac{1}{r}\frac{\partial c_{\mathrm{B}}}{\partial r} + \frac{\partial^2 c_{\mathrm{B}}}{\partial z^2}\right) - 2\left(k_{\mathrm{disp}}{c_{\mathrm{B}}}^2 - k_{\mathrm{comp}}c_{\mathrm{A}}c_{\mathrm{C}}\right) \qquad \text{(Appx I.7)}$$

$$\frac{\partial c_{\mathrm{C}}}{\partial t} = D_{\mathrm{C}}\left(\frac{\partial^2 c_{\mathrm{C}}}{\partial r^2} + \frac{1}{r}\frac{\partial c_{\mathrm{C}}}{\partial r} + \frac{\partial^2 c_{\mathrm{C}}}{\partial z^2}\right) + k_{\mathrm{disp}}{c_{\mathrm{B}}}^2 - k_{\mathrm{comp}}c_{\mathrm{A}}c_{\mathrm{C}} \qquad \text{(Appx I.8)}$$

where all symbols are defined in Table Appx I.1. In both cyclic voltammetry and chronoamperometry, when $t > 0$, $z = 0$ and $r \leq r_{\mathrm{e}}$, the boundary conditions are the Butler-Volmer conditions describing species A and C and conservation of mass for species B:

$$
\begin{aligned}
D_{\mathrm{A}}\left(\frac{\partial c_{\mathrm{A}}}{\partial z}\right)_0 = \quad & k^0_{\mathrm{A|B}} c_{\mathrm{A},0} \exp\left(-\alpha_{\mathrm{A|B}} \frac{F(E-E^{0'}_{\mathrm{A|B}})}{RT}\right) \\
& -k^0_{\mathrm{A|B}} c_{\mathrm{B},0} \exp\left((1-\alpha_{\mathrm{A|B}}) \frac{F(E-E^{0'}_{\mathrm{A|B}})}{RT}\right) \\
D_{\mathrm{B}}\left(\frac{\partial c_{\mathrm{B}}}{\partial z}\right)_0 = \quad & -D_{\mathrm{A}}\left(\frac{\partial c_{\mathrm{A}}}{\partial z}\right)_0 - D_{\mathrm{C}}\left(\frac{\partial c_{\mathrm{C}}}{\partial z}\right)_0 \\
D_{\mathrm{C}}\left(\frac{\partial c_{\mathrm{C}}}{\partial z}\right)_0 = \quad & -k^0_{\mathrm{B|C}} c_{\mathrm{B},0} \exp\left(-\alpha_{\mathrm{B|C}} \frac{F(E-E^{0'}_{\mathrm{B|C}})}{RT}\right) \\
& +k^0_{\mathrm{B|C}} c_{\mathrm{C},0} \exp\left((1-\alpha_{\mathrm{B|C}}) \frac{F(E-E^{0'}_{\mathrm{B|C}})}{RT}\right)
\end{aligned}
$$

Table Appx I.1: Dimensional parameters.

Dimensional parameter	Definition
$\alpha_{\mathrm{X\|Y}}$	Transfer coefficient for $\mathrm{X} + \mathrm{e}^- \rightleftharpoons \mathrm{Y}$ / unitless
c_{X}	Concentration of species X / mol m^{-3}
$c_{\mathrm{X},0}$	Concentration of species X at the electrode surface / mol m^{-3}
c^*_{X}	Concentration of species X in bulk solution / mol m^{-3}
D_{X}	Diffusion coefficient of species X / $\mathrm{m}^2\ \mathrm{s}^{-1}$
E	Applied potential / V
$E^{0'}_{\mathrm{X\|Y}}$	Formal reduction potential for $\mathrm{X} + \mathrm{e}^- \rightleftharpoons \mathrm{Y}$ / V
${k^0}_{\mathrm{X\|Y}}$	Electrochemical rate constant for $\mathrm{X} + \mathrm{e}^- \rightleftharpoons \mathrm{Y}$ / m s^{-1}
k_{comp}	Rate constant for comproportionation / $\mathrm{m}^3\ \mathrm{mol}^{-1}\ \mathrm{s}^{-1}$
k_{disp}	Rate constant for comproportionation / $\mathrm{m}^3\ \mathrm{mol}^{-1}\ \mathrm{s}^{-1}$
i	Current / A
j	Flux across the electrode / mol $\mathrm{m}^2\ \mathrm{s}^{-1}$
r	Radial coordinate / m
t	Time / s
v	Scan-rate / V s^{-1}
z	Axial coordinate / m

The remaining boundary conditions are:

$t = 0$, all r, all z	$c_{\mathrm{A}} = c^*_{\mathrm{A}}$	$c_{\mathrm{B}} = 0$	$c_{\mathrm{C}} = 0$
$t > 0$, $r > r_{\mathrm{e}}$, $z = 0$	$\frac{\partial c_{\mathrm{A}}}{\partial z} = 0$	$\frac{\partial c_{\mathrm{B}}}{\partial z} = 0$	$\frac{\partial c_{\mathrm{C}}}{\partial z} = 0$
$t > 0$, all r, $z \to \infty$	$\frac{\partial c_{\mathrm{A}}}{\partial z} = 0$	$\frac{\partial c_{\mathrm{B}}}{\partial z} = 0$	$\frac{\partial c_{\mathrm{C}}}{\partial z} = 0$
$t > 0$, $r \to \infty$, all z	$\frac{\partial c_{\mathrm{A}}}{\partial r} = 0$	$\frac{\partial c_{\mathrm{B}}}{\partial r} = 0$	$\frac{\partial c_{\mathrm{C}}}{\partial r} = 0$
$t > 0$, $r = 0$, all z	$\frac{\partial c_{\mathrm{A}}}{\partial r} = 0$	$\frac{\partial c_{\mathrm{B}}}{\partial r} = 0$	$\frac{\partial c_{\mathrm{C}}}{\partial r} = 0$

Cyclic Voltammetry

In the cyclic voltammetry experiment, the applied potential, E, is swept from an initial value, E_i, to a more oxidising value, $E^{0'}$, and then back to a more reducing value. The value of E is therefore calculated at any time on the forward sweep using Equation (Appx I.9) and on the reverse sweep using Equation (Appx I.10), where v is the voltage scan-rate and t is the time:

$$E_\mathrm{forward} = E_\mathrm{i} - vt \tag{Appx I.9}$$

$$E_\mathrm{reverse} = 2E_\mathrm{f} - E_\mathrm{i} + vt \tag{Appx I.10}$$

Multiple Step Chronoamperometry

The applied potential, E, is stepped in the sequence indicated in Figure Appx I.3.

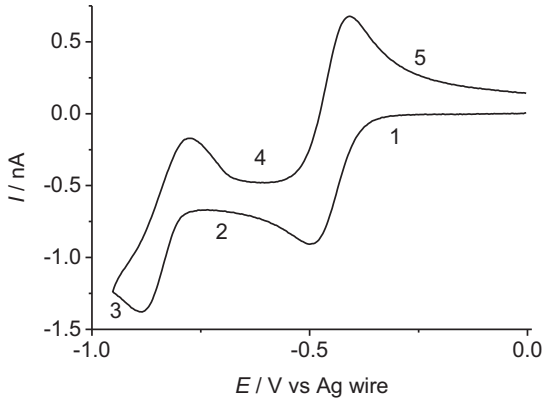


Figure Appx I.3: Cyclic voltammogram annotated with the potential step sequence used in the chronoamperometry experiments.

Computational Details

The problem is discretised using the Alternating Direct Implicit method [1, 2](ADI) and solved numerically using the iterative Newton-Raphson scheme [3]. The discretised spatial mesh is analogous to that reported by Gavaghan [4](Figure Appx I.2) and converged to within 0.5 %. All programs were written in C++ and compiled using a Borland compiler. The simulations were run on a desktop PC

with a processor speed of ≈ 3 GHz. Approximately 20-30 min of CPU time were required to simulate a single voltammogram.

References

[1] D. Britz, Digital Simulation in Electrochemistry, Springer-Verlag: New York, 2005.

[2] J. Heinze, J. Electroanal. Chem. 124 (1981) 73–86.

[3] W.H. Press, S.A. Teukolsky, W.T. Vetterling, B.P. Flannery (Eds.) Numerical Recipes: The Art of Scientific Computing, Cambridge University Press, 2007.

[4] D.J. Gavaghan, J. Electroanal. Chem. 456 (1998) 1–12.

[5] D. Shoup, A. Szabo, J. Electroanal. Chem. 140 (1982) 237–245.

Appendix II: Theory for Chapter 6

The work presented in this appendix was carried out in collaboration with

- **S.R. Belding**

We consider the reaction mechanism mentioned in Equation 6.28–6.31 at a microdisc electrode (see Figure Appx II.1). This mechanism is simulated numerically by solving the following mass transport equations:

$$\frac{\partial c_{\mathrm{QH_2}}}{\partial t} = D_{\mathrm{QH_2}} \left(\frac{\partial^2 c_{\mathrm{QH_2}}}{\partial r^2} + \frac{1}{r}\frac{\partial c_{\mathrm{QH_2}}}{\partial r} + \frac{\partial^2 c_{\mathrm{QH_2}}}{\partial z^2} \right) \tag{Appx II.1}$$

$$\frac{\partial c_{\mathrm{QH_2^{2+}}}}{\partial t} = D_{\mathrm{QH_2^{2+}}} \left(\frac{\partial^2 c_{\mathrm{QH_2^{2+}}}}{\partial r^2} + \frac{1}{r}\frac{\partial c_{\mathrm{QH_2^{2+}}}}{\partial r} + \frac{\partial^2 c_{\mathrm{QH_2^{2+}}}}{\partial z^2} \right) - k_{\mathrm{QH_2^{2+}|HNTf_2}} c_{\mathrm{QH_2^{2+}}} \tag{Appx II.2}$$

$$\frac{\partial c_{\mathrm{HNTf_2}}}{\partial t} = D_{\mathrm{HNTf_2}} \left(\frac{\partial^2 c_{\mathrm{HNTf_2}}}{\partial r^2} + \frac{1}{r}\frac{\partial c_{\mathrm{HNTf_2}}}{\partial r} + \frac{\partial^2 c_{\mathrm{HNTf_2}}}{\partial z^2} \right) + 2k_{\mathrm{QH_2^{2+}|HNTf_2}} c_{\mathrm{QH_2^{2+}}} \tag{Appx II.3}$$

$$\frac{\partial c_{\mathrm{Q}}}{\partial t} = D_{\mathrm{Q}} \left(\frac{\partial^2 c_{\mathrm{Q}}}{\partial r^2} + \frac{1}{r}\frac{\partial c_{\mathrm{Q}}}{\partial r} + \frac{\partial^2 c_{\mathrm{Q}}}{\partial z^2} \right) + k_{\mathrm{QH_2^{2+}|HNTf_2}} c_{\mathrm{QH_2^{2+}}} \tag{Appx II.4}$$

$$\frac{\partial c_{\mathrm{H^\bullet}}}{\partial t} = D_{\mathrm{H^\bullet}} \left(\frac{\partial^2 c_{\mathrm{H^\bullet}}}{\partial r^2} + \frac{1}{r}\frac{\partial c_{\mathrm{H^\bullet}}}{\partial r} + \frac{\partial^2 c_{\mathrm{H^\bullet}}}{\partial z^2} \right) - 2k_{\mathrm{H^\bullet|H_2}} c_{\mathrm{H^\bullet}} \tag{Appx II.5}$$

$$\frac{\partial c_{\mathrm{H_2}}}{\partial t} = D_{\mathrm{H_2}} \left(\frac{\partial^2 c_{\mathrm{H_2}}}{\partial r^2} + \frac{1}{r}\frac{\partial c_{\mathrm{H_2}}}{\partial r} + \frac{\partial^2 c_{\mathrm{H_2}}}{\partial z^2} \right) + k_{\mathrm{H^\bullet|H_2}} c_{\mathrm{H^\bullet}} \tag{Appx II.6}$$

where all symbols are defined in Table Appx II.1 and $k_{\mathrm{H^\bullet|H_2}}$. In cyclic voltammetry, when $t > 0$, $z = 0$ and $r \leq r_{\mathrm{e}}$, the boundary conditions are the Butler-Volmer conditions describing all the species, with conservation of mass for the remaining species:

$$
\begin{aligned}
D_{\mathrm{QH_2}}\left(\frac{\partial c_{\mathrm{QH_2}}}{\partial z}\right)_0 = \quad & k^0_{\mathrm{QH_2|QH_2^{2+}}} c_{\mathrm{QH_2},0} \exp\left(-\alpha_{\mathrm{QH_2|QH_2^{2+}}} \frac{F(E-E^{0'}_{\mathrm{QH_2|QH_2^{2+}}})}{RT}\right) \\
& -k^0_{\mathrm{QH_2|QH_2^{2+}}} c_{\mathrm{QH_2^{2+},0}} \exp\left((2-\alpha_{\mathrm{QH_2|QH_2^{2+}}}) \frac{F(E-E^{0'}_{\mathrm{QH_2/QH_2^{2+}}})}{RT}\right) \\
D_{\mathrm{QH_2^{2+}}}\left(\frac{\partial c_{\mathrm{QH_2^{2+}}}}{\partial z}\right)_0 = \quad & -k^0_{\mathrm{QH_2|QH_2^{2+}}} c_{\mathrm{QH_2},0} \exp\left(-\alpha_{\mathrm{QH_2|QH_2^{2+}}} \frac{F(E-E^{0'}_{\mathrm{QH_2|QH_2^{2+}}})}{RT}\right) \\
& +k^0_{\mathrm{QH_2|QH_2^{2+}}} c_{\mathrm{QH_2^{2+},0}} \exp\left((2-\alpha_{\mathrm{QH_2|QH_2^{2+}}}) \frac{F(E-E^{0'}_{\mathrm{QH_2|QH_2^{2+}}})}{RT}\right) \\
D_{\mathrm{HNTf_2}}\left(\frac{\partial c_{\mathrm{HNTf_2}}}{\partial z}\right)_0 = \quad & k^0_{\mathrm{HNTf_2|H^\bullet}} c_{\mathrm{HNTf_2},0} \exp\left(-\alpha_{\mathrm{HNTf_2|H^\bullet}} \frac{F(E-E^{0'}_{\mathrm{HNTf_2|H^\bullet}})}{RT}\right) \\
& -k^0_{\mathrm{HNTf_2|H^\bullet}} c_{\mathrm{H^\bullet},0} \exp\left((1-\alpha_{\mathrm{HNTf_2|H^\bullet}}) \frac{F(E-E^{0'}_{\mathrm{HNTf_2|H^\bullet}})}{RT}\right) \\
D_{\mathrm{Q}}\left(\frac{\partial c_{\mathrm{Q}}}{\partial z}\right)_0 = \quad & 0 \\
D_{\mathrm{H^\bullet}}\left(\frac{\partial c_{\mathrm{H^\bullet}}}{\partial z}\right)_0 = \quad & -k^0_{\mathrm{HNTf_2|H^\bullet}} c_{\mathrm{HNTf_2},0} \exp\left(-\alpha_{\mathrm{HNTf_2|H^\bullet}} \frac{F(E-E^{0'}_{\mathrm{HNTf_2|H^\bullet}})}{RT}\right) \\
& +k^0_{\mathrm{HNTf_2|H^\bullet}} c_{\mathrm{H^\bullet},0} \exp\left((1-\alpha_{\mathrm{HNTf_2|H^\bullet}}) \frac{F(E-E^{0'}_{\mathrm{HNTf_2|H^\bullet}})}{RT}\right) \\
D_{\mathrm{H_2}}\left(\frac{\partial c_{\mathrm{H_2}}}{\partial z}\right)_0 = \quad & 0
\end{aligned}
$$

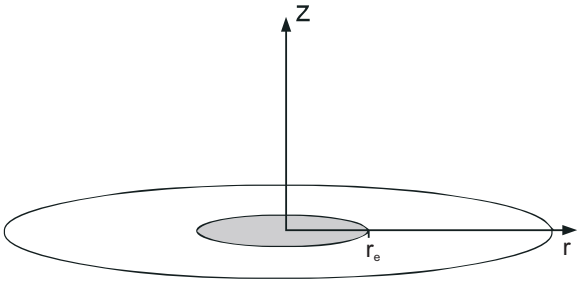


Figure Appx II.1: Circular disc electrode inlaid on an insulating support.

Table Appx II.1: Dimensional parameters.

Dimensional Parameter	**Definition**
$\alpha_{\mathrm{X/Y}}$	Transfer coefficient for $\mathrm{X} - e^- \rightleftharpoons \mathrm{Y}$ / unitless
c_{X}	Concentration of species X / mol m^{-3}
$c_{\mathrm{X},0}$	Concentration of species X at the electrode surface / mol m^{-3}
c^*_{X}	Concentration of species X in bulk solution / mol m^{-3}
D_{X}	Diffusion coefficient of species X / $\mathrm{m}^2\ \mathrm{s}^{-1}$
E	Applied potential / V
$E^{0'}_{\mathrm{X/Y}}$	Formal reduction potential for $\mathrm{X} - e^- \rightleftharpoons \mathrm{Y}$ / V
$k^0_{\mathrm{X/Y}}$	Electrochemical rate constant for $\mathrm{X} - e^- \rightleftharpoons \mathrm{Y}$ / m s^{-1}
i	Current / A
r	Radial coordinate / m
t	Time / s
v	Scan-rate / V s^{-1}
z	Axial coordinate / m

The remaining boundary conditions are:

$t = 0$, all r, all z	$c_{\mathrm{QH_2}} = c^*_{\mathrm{QH_2}}$	$c_{\mathrm{QH_2^{2+}}} = 0$	$c_{\mathrm{HNTf_2}} = 0$
	$c_{\mathrm{Q}} = 0$	$c_{\mathrm{H^\bullet}} = 0$	$c_{\mathrm{H_2}} = 0$
$t > 0$, $r > r_{\mathrm{e}}$, $z = 0$	$\frac{\partial c_{\mathrm{QH_2}}}{\partial z} = 0$	$\frac{\partial c_{\mathrm{QH_2^{2+}}}}{\partial z} = 0$	$\frac{\partial c_{\mathrm{HNTf_2}}}{\partial z} = 0$
	$\frac{\partial c_{\mathrm{Q}}}{\partial z} = 0$	$\frac{\partial c_{\mathrm{H^\bullet}}}{\partial z} = 0$	$\frac{\partial c_{\mathrm{H_2}}}{\partial z} = 0$
$t > 0$, all r, $z \to \infty$	$\frac{\partial c_{\mathrm{QH_2}}}{\partial z} = 0$	$\frac{\partial c_{\mathrm{QH_2^{2+}}}}{\partial z} = 0$	$\frac{\partial c_{\mathrm{HNTf_2}}}{\partial z} = 0$
	$\frac{\partial c_{\mathrm{Q}}}{\partial z} = 0$	$\frac{\partial c_{\mathrm{H^\bullet}}}{\partial z} = 0$	$\frac{\partial c_{\mathrm{H_2}}}{\partial z} = 0$
$t > 0$, $r \to \infty$, all z	$\frac{\partial c_{\mathrm{QH_2}}}{\partial r} = 0$	$\frac{\partial c_{\mathrm{QH_2^{2+}}}}{\partial r} = 0$	$\frac{\partial c_{\mathrm{HNTf_2}}}{\partial r} = 0$
	$\frac{\partial c_{\mathrm{Q}}}{\partial r} = 0$	$\frac{\partial c_{\mathrm{H^\bullet}}}{\partial r} = 0$	$\frac{\partial c_{\mathrm{H_2}}}{\partial r} = 0$
$t > 0$, $r = 0$, all z	$\frac{\partial c_{\mathrm{QH_2}}}{\partial r} = 0$	$\frac{\partial c_{\mathrm{QH_2^{2+}}}}{\partial r} = 0$	$\frac{\partial c_{\mathrm{HNTf_2}}}{\partial r} = 0$
	$\frac{\partial c_{\mathrm{Q}}}{\partial r} = 0$	$\frac{\partial c_{\mathrm{H^\bullet}}}{\partial r} = 0$	$\frac{\partial c_{\mathrm{H_2}}}{\partial r} = 0$

In the cyclic voltammetry experiment, the applied potential, E, is swept from an initial value, E_{i}, to a more oxidising value, $E^{0'}$, and then back to the initial value. The value of E is therefore calculated at any time on the forward sweep using Equation (Appx II.7) and on the reverse sweep using Equation (Appx II.8), where v is the voltage scan-rate and t is the time:

$$E_{\text{forward}} = E_{\text{i}} + vt \tag{Appx II.7}$$

$$E_{\text{reverse}} = 2E_{\text{f}} + E_{\text{i}} - vt \tag{Appx II.8}$$

Computational Details

The problem is discretised using the Alternating Direct Implicit method [1, 2](ADI) and solved numerically using the iterative Newton-Raphson scheme [3]. The discretised spatial mesh is analogous to that reported by Gavaghan [4](Figure Appx II.2) and converged to within 0.5 %. All programs were written in C++ and compiled using a Borland compiler. The simulations were run on a desktop PC with a processor speed of ≈ 3 GHz. Approximately 20-30 min of CPU time were required to simulate a single voltammogram.

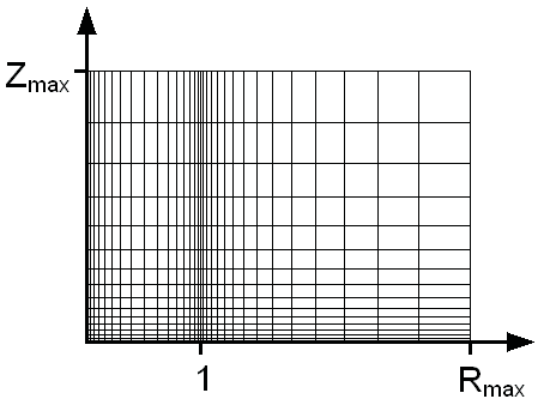


Figure Appx II.2: Discretised grid used in the simulations (some points have been removed for clarity).

References

[1] D. Britz, Digital Simulation in Electrochemistry, Springer-Verlag: New York, 2005.

[2] J. Heinze, J. Electroanal. Chem. 124 (1981) 73–86.

[3] W.H. Press, S.A. Teukolsky, W.T. Vetterling, B.P. Flannery (Eds.) Numerical Recipes: The Art of Scientific Computing, Cambridge University Press, 2007.

[4] D.J. Gavaghan, J. Electroanal. Chem. 456 (1998) 1–12.

[5] V.D. Parker, Electrochim. Acta 18 (1973) 519–524.

Appendix III: Theory for Chapter 7

The work presented in this appendix was carried out in collaboration with

- **E.O. Barnes**

Theory

The theory developed in this section can be applied to both routes of investigation in this chapter, namely studying the reaction of interest over a wide range of scan rates bridging the gap between convergent and linear diffusion, and investigations carried out at a wide range of support ratios.

We consider the following electrochemical reductions and coupled homogeneous reactions:

$$\mathrm{A} + \mathrm{e}^- \rightleftharpoons \mathrm{B}^- \qquad E^{0\prime}_{\mathrm{A/B}} \tag{Appx III.1}$$

$$\mathrm{B}^- \rightleftharpoons \mathrm{C} + \mathrm{Z}^- \qquad K_{\mathrm{eqm}} = \frac{k_{\mathrm{f}}}{k_{\mathrm{r}}} \tag{Appx III.2}$$

$$\mathrm{B}^- + \mathrm{C} \rightleftharpoons \mathrm{A} + \mathrm{P}^- \qquad K^{\mathrm{disp}}_{\mathrm{eqm}} = \frac{k^{\mathrm{disp}}_{\mathrm{f}}}{k^{\mathrm{disp}}_{\mathrm{r}}} \tag{Appx III.3}$$

$$\mathrm{C} + \mathrm{e}^- \rightleftharpoons \mathrm{P}^- \qquad E^{0\prime}_{\mathrm{C/P}} > E^{0\prime}_{\mathrm{A/B}} \tag{Appx III.4}$$

Two limiting mechanisms will be studied, the ECE mechanism in which reaction Appx III.3 is unimportant and species C is more easily reduced than species A, and the DISP1 mechanism where reaction Appx III.4 is unimportant and reaction Appx III.2 is rate limiting. A further mechanism, DISP2, occurs when reaction Appx III.4 is unimportant and reaction Appx III.3 is rate limiting, but this is not considered here. In both cases, fast electrode kinetics are assumed. Dissolved in the solution is an arbitrary amount of supporting electrolyte, $\mathrm{M}^+\mathrm{X}^-$, which is completely dissociated.

The flux of any species i at any point in solution is described by the Nernst-Planck equation:

$$\mathbf{J}_\mathrm{i} = -D_\mathrm{i}\left(\nabla C_\mathrm{i} + \frac{z_\mathrm{i}F}{RT}C_\mathrm{i}\nabla\phi\right) \tag{Appx III.5}$$

where the first term in parentheses describes diffusion and the second term migration. All symbols are defined in Table . This is combined with Fick's second Law:

$$\frac{\partial C_\mathrm{i}}{\partial t} = -\nabla\cdot\mathbf{J}_\mathrm{i} \tag{Appx III.6}$$

to give:

$$\frac{\partial C_\mathrm{i}}{\partial t} = D_\mathrm{i}\left[\nabla^2 C_\mathrm{i} + \frac{z_\mathrm{i}F}{RT}\left(C_\mathrm{i}\nabla^2\phi + \nabla C_\mathrm{i}\nabla\phi\right)\right] \tag{Appx III.7}$$

Additionally, the potential at every point in solution must satisfy the Poisson equation:

$$\nabla^2\phi = -\frac{\rho}{\epsilon_\mathrm{s}\epsilon_0} \tag{Appx III.8}$$

where ϵ_s is the dielectric constant of the solvent, ϵ_0 is the permittivity of free space, and ρ is the local charge density, given by:

$$\rho = F\sum_\mathrm{i} z_\mathrm{i}C_\mathrm{i} \tag{Appx III.9}$$

Together, these form the Nernst-Planck-Poisson system of equations, and in hemispherically symmetric space become:

$$\frac{\partial C_\mathrm{i}}{\partial t} = D_\mathrm{i}\left[\frac{\partial^2 C_\mathrm{i}}{\partial r^2} + \frac{2}{r}\frac{\partial C_\mathrm{i}}{\partial r} + \frac{z_\mathrm{i}F}{RT}\left(\frac{\partial C_\mathrm{i}}{\partial r}\frac{\partial\phi}{\partial r} + C_\mathrm{i}\frac{\partial^2\phi}{\partial r^2} + C_\mathrm{i}\frac{2}{r}\frac{\partial\phi}{\partial r}\right)\right] \tag{Appx III.10}$$

and

$$\frac{\partial^2\phi}{\partial r^2} + \frac{2}{r}\frac{\partial\phi}{\partial r} = -\frac{F}{\epsilon_s\epsilon_0}\sum_\mathrm{i} z_\mathrm{i}C_\mathrm{i} \tag{Appx III.11}$$

Table Appx III.1: Dimensional Parameters

Parameter	Description	Units
$\alpha_{i/j}$	Transfer coefficient of the i/j redox couple	Unitless
D_i	Diffusion coefficient of species i	$m^2\ s^{-1}$
C_i	Concentration of species i	mol
C_i^*	Bulk solution concentration of species i	mol
C_i^0	Concentration of species i at the electrode surface	mol
E	Applied potential	V
$E_{i/j}^{0'}$	Formal potential of i/j couple	V
ϵ_s	Dielectric constant (relative permittivity) of solvent	Unitless
ϵ_0	Permittivity of free space ($=8.854 \times 10^{-12}$)	$F\ m^{-1}$
F	Faraday constant (=96485)	$C\ mol^{-1}$
i	Current measured at working electrode	A
$\mathbf{J}_i$	Flux of species i	$mol\ m^{-2}\ s^{-1}$
$k_{i/j}^0$	Electrochemical rate constant of i/j redox couple	$m\ s^{-1}$
k_f	Forward rate constant for first chemical step	s^{-1}
k_r	Reverse rate constant for first chemical step	$m^3\ mol^{-1}\ s^{-1}$
k_f^{disp}	Forward rate constant for disproportionation chemical step	$m^3\ mol^{-1}\ s^{-1}$
k_r^{disp}	Reverse rate constant for disproportionation chemical step	$m^3\ mol^{-1}\ s^{-1}$
K_{eqm}	Equilibrium constant for first chemical step	$mol\ m^{-3}$
K_{eqm}^{disp}	Equilibrium constant for disproportination chemical step	Unitless
ν	Scan rate	$V\ s^{-1}$
R	Gas constant (=8.314)	$J\ K^{-1}\ mol^{-1}$
ϕ	Solution potential	V
ϕ_0	Solution potential at electrode surface	V
r_e	Electrode radius	m
t	time	s
z_i	Charge on species i	Unitless

The homogeneous kinetics are described by the rate equations:

$$\frac{\partial C_A}{\partial t} = nk_f^{disp} C_{B^-} C_C - nk_r^{disp} C_A C_{P^-} \quad \text{(Appx III.12)}$$

$$\frac{\partial C_{B^-}}{\partial t} = k_r C_C C_{Z^-} - k_f C_{B^-} - nk_f^{disp} C_{B^-} C_C + nk_r^{disp} C_A C_{P^-} \quad \text{(Appx III.13)}$$

$$\frac{\partial C_C}{\partial t} = k_f C_{B^-} - k_r C_C C_{Z^-} - nk_f^{disp} C_{B^-} C_C + nk_r^{disp} C_A C_{P^-} \quad \text{(Appx III.14)}$$

$$\frac{\partial C_{P^-}}{\partial t} = nk_f^{disp} C_{B^-} C_C - nk_r^{disp} C_A C_{P^-} \quad \text{(Appx III.15)}$$

$$\frac{\partial C_{Z^-}}{\partial t} = k_f C_{B^-} - k_r C_C C_{Z^-} \quad \text{(Appx III.16)}$$

where n is equal to zero in the ECE limit, and n is equal to 1 in the DISP1 limit.

The space-time evolution of the concentration of species i is given by summing the space-time evolution due to mass transport and homogeneous kinetics. These equations, subject to appropriate

boundary conditions, completely describe the system. Cyclic voltammograms can therefore be simulated by simultaneously solving this set of coupled partial differential equations, using the numerical Newton-Raphson method [1].

Dimensionless Parameters

In order to reduce the number of independent variables and simplify the equations, a number of dimensionless parameters are introduced, listed in Table . Substituting these dimensionless variables into the Nernst-Planck-Poisson system of equations gives:

$$\frac{\partial c_{\mathrm{i}}}{\partial \tau} = D'_{\mathrm{i}}\left[\frac{\partial^2 c_{\mathrm{i}}}{\partial R^2} + \frac{2}{R}\frac{\partial c_{\mathrm{i}}}{\partial R} + z_{\mathrm{i}}\left(\frac{\partial c_{\mathrm{i}}}{\partial R}\frac{\partial \theta_{\mathrm{sln}}}{\partial R} + c_{\mathrm{i}}\frac{\partial^2 \theta_{\mathrm{sln}}}{\partial R^2} + c_{\mathrm{i}}\frac{2}{R}\frac{\partial \theta_{\mathrm{sln}}}{\partial R}\right)\right] \qquad \text{(Appx III.17)}$$

and

$$\frac{\partial^2 \theta_{\mathrm{sln}}}{\partial R^2} + \frac{2}{R}\frac{\partial \theta_{\mathrm{sln}}}{\partial R} = -R_{\mathrm{e}}^2 \sum_{\mathrm{i}} z_{\mathrm{i}} c_{\mathrm{i}} \qquad \text{(Appx III.18)}$$

As a further simplification, Equation Appx III.18 can be substituted into Equation Appx III.17, rendering the discretization process easier:

$$\frac{\partial c_{\mathrm{i}}}{\partial \tau} = D'_{\mathrm{i}}\left[\frac{\partial^2 c_{\mathrm{i}}}{\partial R^2} + \frac{2}{R}\frac{\partial c_{\mathrm{i}}}{\partial R} + z_{\mathrm{i}}\left(\frac{\partial c_{\mathrm{i}}}{\partial R}\frac{\partial \theta_{\mathrm{sln}}}{\partial R} - c_{\mathrm{i}} R_{\mathrm{e}}^2 \sum_{\mathrm{i}} z_{\mathrm{i}} c_{\mathrm{i}}\right)\right] \qquad \text{(Appx III.19)}$$

Dimensionless parameters are also introduced to the homogeneous rate equations, giving:

$$\frac{\partial c_{\mathrm{A}}}{\partial \tau} = nK_{\mathrm{f}}^{\mathrm{disp}} c_{\mathrm{B^-}} c_{\mathrm{C}} - nK_{\mathrm{f}}^{\mathrm{disp}} c_{\mathrm{A}} c_{\mathrm{P^-}} \qquad \text{(Appx III.20)}$$

$$\frac{\partial c_{\mathrm{B^-}}}{\partial \tau} = K_{\mathrm{r}} c_{\mathrm{C}} c_{\mathrm{Z^-}} - K_{\mathrm{f}} c_{\mathrm{B^-}} - nK_{\mathrm{f}}^{\mathrm{disp}} c_{\mathrm{B^-}} c_{\mathrm{C}} + nK_{\mathrm{r}}^{\mathrm{disp}} c_{\mathrm{A}} c_{\mathrm{P^-}} \qquad \text{(Appx III.21)}$$

$$\frac{\partial c_{\mathrm{C}}}{\partial \tau} = K_{\mathrm{f}} c_{\mathrm{B^-}} - K_{\mathrm{r}} c_{\mathrm{C}} c_{\mathrm{F^-}} - nK_{\mathrm{f}}^{\mathrm{disp}} c_{\mathrm{B^-}} c_{\mathrm{C}} + nK_{\mathrm{r}}^{\mathrm{disp}} c_{\mathrm{A}} c_{\mathrm{P^-}} \qquad \text{(Appx III.22)}$$

$$\frac{\partial c_{\mathrm{P^-}}}{\partial \tau} = nK_{\mathrm{f}}^{\mathrm{disp}} c_{\mathrm{B^-}} c_{\mathrm{C}} - nK_{\mathrm{r}}^{\mathrm{disp}} c_{\mathrm{A}} c_{\mathrm{P^-}} \qquad \text{(Appx III.23)}$$

$$\frac{\partial c_{\mathrm{Z^-}}}{\partial \tau} = K_{\mathrm{f}} c_{\mathrm{B^-}} - K_{\mathrm{r}} c_{\mathrm{C}} c_{\mathrm{Z^-}} \qquad \text{(Appx III.24)}$$

where n = 0 in the ECE limit and n = 1 in the DISP1 limit.

Table Appx III.2: Dimensionless Parameters

Dimensionless Parameter	Definition
c_i	$\frac{C_\mathrm{i}}{C^*_\mathrm{A}}$
D'_i	$\frac{D_\mathrm{i}}{D_\mathrm{A}}$
j	$\frac{i}{2\pi r_e F D_\mathrm{A} C_\mathrm{A}}$
K_f	$\frac{r_\mathrm{e}^2}{D_\mathrm{A}} k_\mathrm{f}$
K_r	$\frac{r_\mathrm{e}^2 C^*_\mathrm{A}}{D_\mathrm{A}} k_\mathrm{r}$
$K_\mathrm{f}^\mathrm{disp}$	$\frac{r_\mathrm{e}^2 C^*_\mathrm{A}}{D_\mathrm{A}} k_\mathrm{f}^\mathrm{disp}$
$K_\mathrm{r}^\mathrm{disp}$	$\frac{r_\mathrm{e}^2 C^*_\mathrm{A}}{D_\mathrm{A}} k_\mathrm{r}^\mathrm{disp}$
$K^0_\mathrm{i/j}$	$\frac{r_e}{D_\mathrm{A}} k^0_\mathrm{i/j}$
θ_app	$\frac{F}{RT} E$
$\theta_\mathrm{f,i/j}$	$\frac{F}{RT} E^{0'}_\mathrm{A/B}$
θ_sln	$\frac{F}{RT}\phi$
θ_0	$\frac{F}{RT}\phi_0$
R	$\frac{r}{r_\mathrm{e}}$
R_e	$r_\mathrm{e}\sqrt{\frac{F^2 C^*_\mathrm{A}}{RT\epsilon_\mathrm{s}\epsilon_0}}$
σ	$\frac{F r_\mathrm{e}^2}{RT D_\mathrm{A}}\nu$
τ	$\frac{D_\mathrm{A}}{r_\mathrm{e}^2} t$

Boundary Conditions

Equations Appx III.18 to Appx III.24 are solved subject to appropriate boundary conditions describing a cyclic voltammetry experiment.

At R=1, (the electrode surface), Butler-Volmer kinetics are applied to electroactive species:

$$\begin{aligned} D'_\mathrm{A}\left(\frac{\partial c_\mathrm{A}}{\partial R}\right)_{\mathrm{R}=1} &= K^0_\mathrm{A/B} c^0_\mathrm{A} \exp\left[-\alpha_\mathrm{A/B}\left(\theta_\mathrm{app}-\theta_0-\theta_\mathrm{f}\right)\right] \\ &\quad -K^0_\mathrm{A/B} c^0_\mathrm{B} \exp\left[\left(1-\alpha_\mathrm{A/B}\right)\left(\theta_\mathrm{app}-\theta_0-\theta_\mathrm{f}\right)\right] \qquad \text{(Appx III.25)} \\ D'_\mathrm{C}\left(\frac{\partial c_\mathrm{C}}{\partial R}\right)_{\mathrm{R}=1} &= K^0_\mathrm{C/P} c^0_\mathrm{C} \exp\left[-\alpha_\mathrm{C/P}\left(\theta_\mathrm{app}-\theta_0-\theta_\mathrm{f}\right)\right] \\ &\quad -K^0_\mathrm{C/P} c^0_\mathrm{P} \exp\left[\left(1-\alpha_\mathrm{C/P}\right)\left(\theta_\mathrm{app}-\theta_0-\theta_\mathrm{f}\right)\right] \qquad \text{(Appx III.26)} \end{aligned}$$

and

$$D'_\mathrm{B}\left(\frac{\partial c_\mathrm{B}}{\partial R}\right)_{\mathrm{R}=1} = -D'_\mathrm{A}\left(\frac{\partial c_\mathrm{A}}{\partial R}\right)_{\mathrm{R}=1} \qquad \text{(Appx III.27)}$$

$$D'_\mathrm{P}\left(\frac{\partial c_\mathrm{P}}{\partial R}\right)_{\mathrm{R}=1} = -D'_\mathrm{C}\left(\frac{\partial c_\mathrm{C}}{\partial R}\right)_{\mathrm{R}=1} \qquad \text{(Appx III.28)}$$

where the dimensionless parameters $K^0_{\mathrm{i/j}}$, θ_{app}, θ_0 and θ_{f} are defined in Table .

In a cyclic voltammetry experiment, θ_{app} varies with time according to the expression:

$$\theta_{\mathrm{app}} = |-\sigma\tau + \theta_{\mathrm{s}} - \theta_{\mathrm{v}}| + \theta_{\mathrm{v}} \tag{Appx III.29}$$

where σ is the dimentionless scan rate:

$$\sigma = \frac{Fr_{\mathrm{e}}^2}{RTD_{\mathrm{A}}}\nu \tag{Appx III.30}$$

and θ_{s} and θ_{v} are respectively the start and vertex potentials.

Assuming the other species to be electrochemically inert and the electrode surface to be impermeable, a no flux boundary condition is applied to all other species at the electrode surface:

$$D'_{\mathrm{i}}\left(\frac{\partial c_{\mathrm{i}}}{\partial R}\right)_{R=1} = 0 \tag{Appx III.31}$$

This model assumes that the electric double layer is negligibly small compared to the extent of the diffusion layer, and therefore the electric field, which is equal to the potential gradient, at the electrode surface is vanishingly small. This is known as the 'zero-field approximation,' and past work [2] has shown this approximation is generally valid except for nanoelectrodes, where the diffusion layer is of comparable size to the electrical double layer [3]. This leads to the following boundary condition for the potential:

$$\left(\frac{\partial \theta_{\mathrm{sln}}}{\partial R}\right)_{R=1} = 0 \tag{Appx III.32}$$

The $R \to \infty$ boundary condition is approximated as $R_{\max} = 6\sqrt{D'_{\max}\tau_{\max}}$, [4–7] where $D'_{\max}$ is the maximum dimensionless diffusion coefficient in the system and $\tau_{\max}$ is the dimensionless taken to complete the cyclic voltammogram. At this boundary condition a no flux requirement is imposed on all species, i.e:

$$D'_{\mathrm{i}}\left(\frac{\partial c_{\mathrm{i}}}{\partial R}\right)_{R=R_{\max}} = 0 \tag{Appx III.33}$$

The potential in bulk solution is set such that electroneutrality is maintained outside the diffusion

layer. The Poisson equation in an electroneutral solution is:

$$\frac{\partial^2 \theta_{\mathrm{sln}}}{\partial R^2} = 0 \qquad \text{(Appx III.34)}$$

Solving this under the condition that $\theta \to 0$ as $\mathrm{R} \to \infty$ gives the boundary condition:

$$\theta_{\mathrm{sln,R=R_{max}}} + R_{\mathrm{max}} \left(\frac{\partial \theta_{\mathrm{sln}}}{\partial R} \right)_{R=R_{\mathrm{max}}} = 0 \qquad \text{(Appx III.35)}$$

Numerical methods

The Nernst-Planck-Poisson equations are solved using a finite difference method over an irregular grid of points, expanding in R away from the electrode. This grid corresponds to that used in previous work [8–11], with a region of extremely dense regular grid spacing close to the electrode that expands proportionally to R beyond some characteristic switching point R_{s}. Mathematically, the R position of a point R_{j} is defined as:

$$R < R_{\mathrm{s}} \qquad R_{\mathrm{j}} = R_{\mathrm{j-1}} + \gamma_{\mathrm{R}}(R_{\mathrm{s}} - 1) \qquad \text{(Appx III.36)}$$

$$R \geq R_{\mathrm{s}} \qquad R_j = R_{\mathrm{j-1}} + \gamma_{\mathrm{R}}(R_{\mathrm{j-1}} - 1) \qquad \text{(Appx III.37)}$$

where the point at the electrode surface, R_0, is equal to 1. A regular time grid was employed, where the number of discreet timesteps per unit θ_{app} is given by a parameter τ_{PT}. If the change in θ_{app} between two temporal grid points is given by Δ, then:

$$\tau_{\mathrm{PT}} = \frac{1}{\Delta} \qquad \text{(Appx III.38)}$$

Convergence studies at varying σ, c_{sup} and D'_{i} were used to find optimal grid parameters which for the majority of systems were: $\gamma_{\mathrm{R}} = 1 \times 10^{-2}$; $R_{\mathrm{s}} = R_0 + \left(2 \times 10^{-3}\right)$; $\tau_{\mathrm{PT}} = 50$.

The Nernst-Planck-Poisson equations are discretised in this simulation space according to the Crank-Nicolson method [12], which is characterised as stable and accurate for 1D simulations [13].

The resulting set of coupled non-linear simultaneous equations is solved using the iterative Newton-Raphson method. All simulations were programmed in C++ and run on various desktop computers (processors ranging from Intel Pentium 4, 3 GHz, to Intel Core2 Quad, 2.4 GHz; RAM ranging from 1-2 GB), with a typical running time of 30-40 minutes per voltammogram.

Theoretical Results

Fully Supported Voltammetry

Figure Appx III.1 shows working curves for ECE, DISP1 and DISP2 reaction mechanisms, which have been previously published and are well understood [14, 15]. The effective number of electrons transfered, n_{eff}, was calculated from the limiting current in simulated highly supported steady state voltammetry. As noted above, the value of n_{eff} approaches a common limiting value of one for very low K and two for very high K. For intermediate K, it can be seen that there are only slight differences between ECE and DISP1, and more significant differences between DISP2 and the other mechanisms, due to the changed rate determining step. This implies that steady state ECE and DISP1 voltammograms will be indistinguishable if slightly differing rate constants are appropriately chosen, and the mechanism cannot be unambiguously assigned.

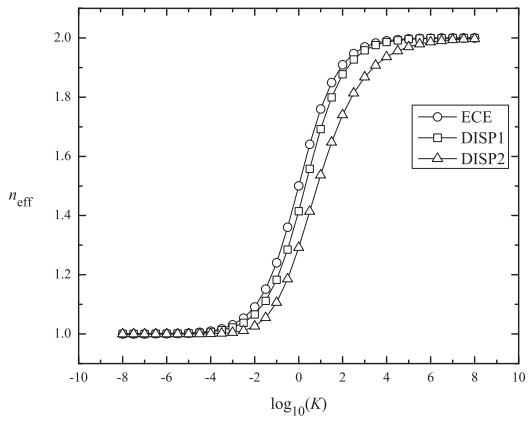


Figure Appx III.1: Working curves for ECE, DISP1 and DISP2 reactions at a hemispherical electrode, showing the effective number of electrons transfered under steady state conditions, (n_{eff}), against the decadic log of the dimensionless rate constant of the rate limting reaction in each case (reaction Appx III.2 for ECE and DISP1, reaction Appx III.3 for DISP2). Foe ECE and DISP1, $K = K_{\text{f}}$, for DISP2, $K = K_{\text{f}}^{\text{disp}}$.

Figure Appx III.2 shows simulated DISP1 voltammograms at a range of dimensionless scan rates,

with kinetic parameters equal to those obtained in the Experimental Results section below. Overlaid on these are simulated ECE voltammograms with parameters chosen such that the steady state voltammograms are indistinguishable from each other. It can be seen that at high values of σ the voltammograms are also near identical. In this limit the homogeneous kinetics are too slow to significantly impact the voltammetry, and we see essentially a reversible one electron reduction for each mechanism. At intermediate scan rates however, we see differences between the voltammograms on the reverse wave. A significant cross over effect is seen for the ECE case. Once the formal potential of the A/B couple has passed, species C can still be reduced since, as defined above, $E^{0\prime}_{\mathrm{C/P}} > E^{0\prime}_{\mathrm{A/B}}$. This means the measured current at the electrode surface will be more negative for ECE than DISP1 between these two formal potentials, and can cause the crossover effect seen here. This crossover effect may be used as a potential means of resolution between the mechanisms.

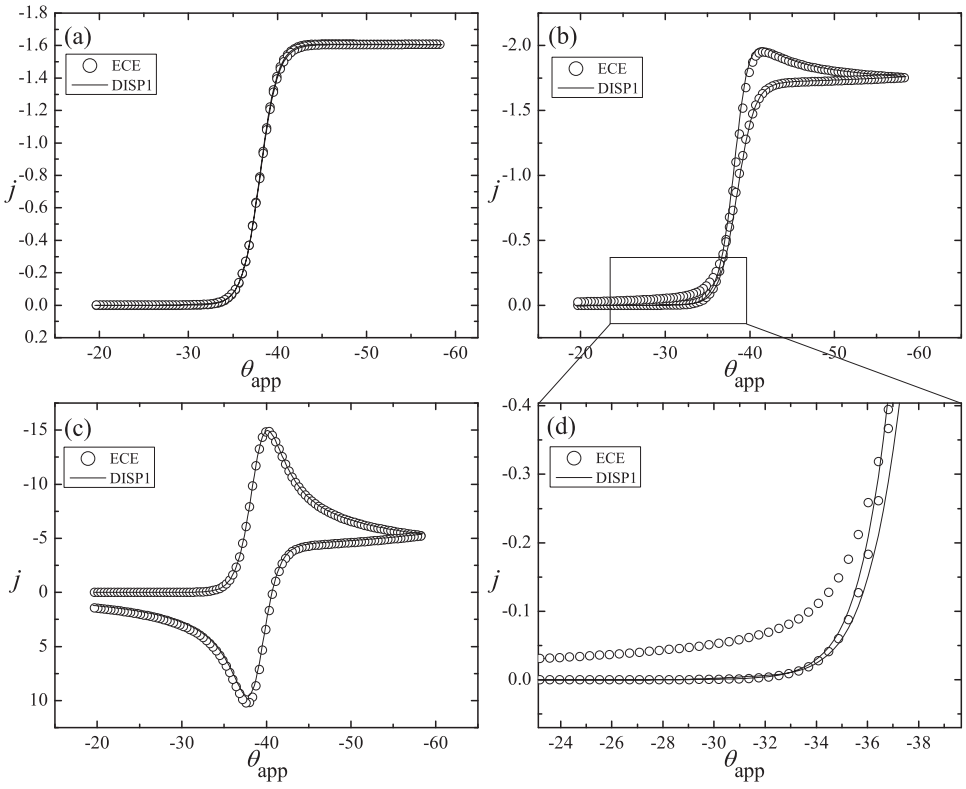


Figure Appx III.2: Simulated ECE voltammograms fitted to those of DISP1 simulated using kinetic parameters obtained in the Experimental Results section at high support for σ values of: (a) 1×10^{-3}, (b) 1, (c) 1×10^{3}. (d) shows part of (b) zoomed in for clarity. For the DISP1 mechanism, $K_{\mathrm{f}} = 4.637$, and for the ECE mechanism $K_{\mathrm{f}} = 2.371$, corresponding to dimensional k_{f} values of 23 s^{-1} and 11.76 s^{-1} respectively (where $r_{\mathrm{e}} = 25\mu$m and all diffusion coefficients are equal to 3.1×10^{-9} $\mathrm{m}^2\mathrm{s}^{-1}$).

The same procedure was then carried out in reverse, with ECE voltammograms being simulated

using experimentally obtained parameters, and DISP1 voltammograms being fitted to these. The results are shown in Figure Appx III.1. The same results are seen, with significant qualitative differences only apparent at intermediate scan rates where the crossover effect for ECE is noted.

Simulations were then carried out for ECE and DISP1 mechanisms where the chemical step is fast. Figure Appx III.3 shows simulated voltamograms for a DISP1 mechanism where reaction Appx III.2 is set as fast ($k_f = 1 \times 10^6 s^{-1}$). ECE voltammograms were simulated to fit those of DISP1 and overlaid. The procedure was again carried out in reverse, and ECE was simulated with a fixed value of $k_f = 1 \times 10^6 s^{-1}$, and DISP1 responses fitted to these. The same results are seen, shown in Figure Appx III.2. It can be seen that, in this limit of fast homogeneous kinetics, there is no difference between the two mechanisms at any value of σ investigated. When k_f is very fast, as in this case, as soon as species B is electrochemically produced at the electrode surface, it is converted to species C which is then immediately reduced, either via heterogeneous electron transfer or disproportionation. Once species B stops being produced, there is no species C at the electrode surface to contribute to a reductive current in the limit, and no distinguishing crossover effect is seen in the ECE limit.

In the case where k_f is an intermediate value compared to the timescale of the experiment, however, species B has time to diffuse away from the electrode surface before it is homogeneously converted to species C, which, in the ECE limit, must then diffuse back to the electrode in order to be reduced, leading to a crossover effect. When k_f is very fast, prohibitively high scan rates must be reached for the homogeneous kinetics to no longer appear instantaneous on the experimental timescale [16] and for this crossover effect to be seen.

When k_f is slow compared to the timescale of the experiment, as in Figure Appx III.2 (c), the chemical step is "outrun" and a simple reversible one electron reduction is observed, yielding no information on the nature of the mechanism.

Weakly Supported Voltammetry

The simulations carried out in the Fully Supported Voltammetry subsection above were repeated for a weakly supported system, where $c_{sup} = 0.1$. The same kinetic parameters were used in each case.

Figure Appx III.4 shows simulated voltammograms for DISP1 using experimentally obtained parameters, with ECE voltammograms fitted to these. The general effects of reducing the support ratio is illustrated in Figure Appx III.4 (c). The potential drop between the electrode and the solution causes the increased peak separation and reduced peak height. Notably, carrying out reactions in low concentrations of supporting electrolyte appears to yield no more information about the reaction mechanism than at high support; both mechanisms are affected by the support ratio in the same way. In the DISP1 case, the species being reduced are effectively 2 molecules of A, and in the ECE case the species are a molecule each of A and C. Since all these species are neutral, their mass transport properties will all be affected in an identical way as the support ratio is lowered, leading to no new means of discrimination on the forward sweep. On the reverse sweep, the only difference between the mechanisms is again the crossover effect in the ECE case, since the species being oxidized bear a single negative charge in both the ECE and DISP1 case, and so will behave in the same way in the presence of an electric field.

Figure Appx III.3 is analogous to Figure Appx III.4, except that now ECE voltammograms are simulated using experimentally obtained parameters, and DISP1 voltammograms are fitted to these. The same results are seen, with significant qualitative differences only seen at intermediate scan rates.

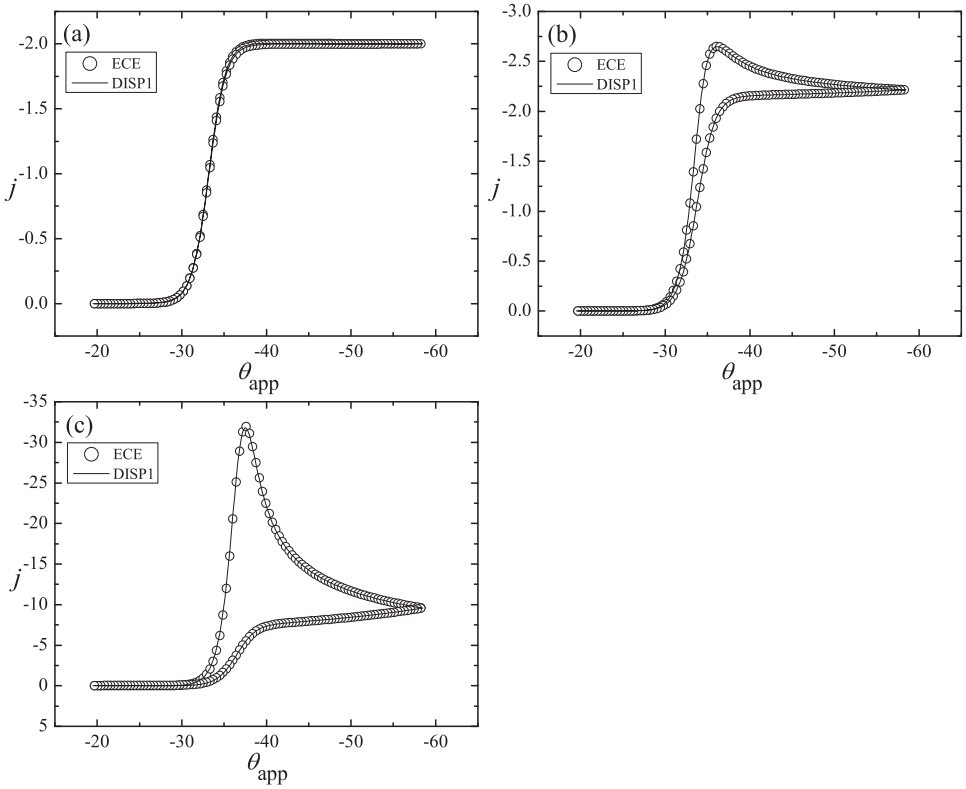


Figure Appx III.3: Simulated ECE voltammograms fitted to those of DISP1 where the chemical step is set as fast and irreversible, at high support for σ values of: (a) 1×10^{-3}, (b) 1, (c) 1×10^{3}. For the DISP1 mechanism, $K_{\mathrm{f}} = 2.016 \times 10^{5}$, and for the ECE mechanism $K_{\mathrm{f}} = 1.008 \times 10^{5}$, corresponding to dimensional k_{f} values of 1×10^{6} s^{-1} and 5×10^{5} s^{-1} respectively (where $r_{\mathrm{e}} = 25\mu\mathrm{m}$ and all diffusion coefficients are equal to 3.1×10^{-9} $\mathrm{m}^{2}\mathrm{s}^{-1}$). In each case, K_{r} is set equal to zero.

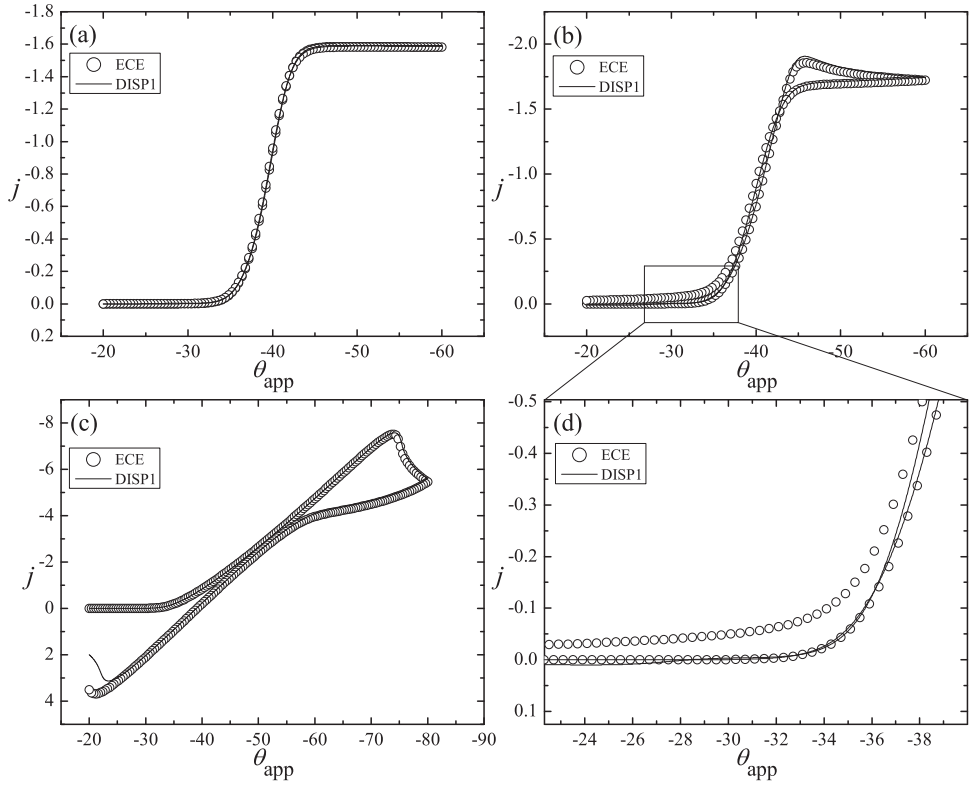


Figure Appx III.4: Simulated ECE voltammograms fitted to those of DISP1 simulated using kinetic parameters obtained in the Experimental Results section at low support ($c_{\mathrm{sup}} = 0.1$) for σ values of: (a) 1×10^{-3}, (b) 1, (c) 1×10^{3}. (d) shows part of (b) zoomed in for clarity. Kinetic parameters as in Figure Appx III.2.

The situation where the chemical step is fast and irreversible again yields no distinguishing features between ECE and DISP1 (Figures Appx III.4 and Appx III.5). As with the high support case, the homogeneous kinetics involved are too fast to be probed by cyclic voltammetry unless prohibitively high scan rates are reached.

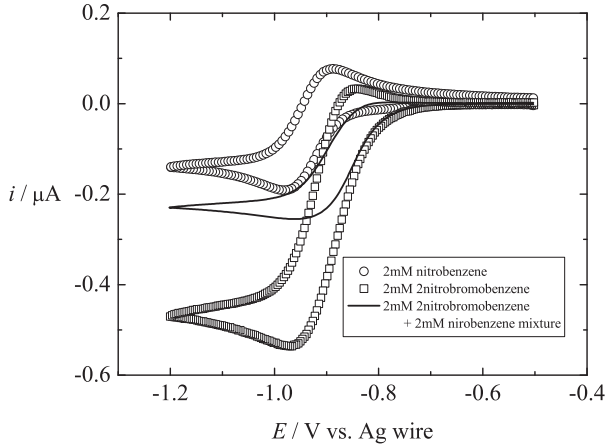


Figure Appx III.5: Cyclic voltammograms in acetonitrile on a Hg hemisphere electrode (25 μm radius) at scan rate of 500 mV s^{-1} in a 2 mM 2-nitrobromobenzene solution, a 2 mM nitrobenzene solution and a mixed solution of 2 mM 2-nitrobromobenzene and 2mM nitrobenzene, all supported by 100 mM TBAP.

References

[1] W.H. Press, S.A. Teukolsky, W. Vetterling, B.P. Flannery, Numerical Recipes: The Art of Scientific Computing, Cambridge University Press, Cambridge, 2007.

[2] I. Streeter, R.G. Compton, J. Phys. Chem. C 112 (2008) 13716–13728.

[3] E.J. Dickinson, R.G. Compton, Chem. Phys. Lett. 497 (2010) 178 – 183.

[4] D.J. Gavaghan, J. Electroanal. Chem. 456 (1998) 25–35.

[5] D.J. Gavaghan, J. Electroanal. Chem. 456 (1998) 13–23.

[6] D.J. Gavaghan, J. Electroanal. Chem. 456 (1998) 1–12.

[7] I.B. Svir, A.I. Oleinick, R.G. Compton, Radiotekhnika 116 (2001) 114.

[8] J.G. Limon-Petersen, I. Streeter, N.V. Rees, R.G. Compton, J. Phys. Chem. C 113 (2009) 333–337.

[9] J.G. Limon-Petersen, E.J.F. Dickinson, N.V. Rees, R.G. Compton, J. Phys. Chem. C 113 (2009) 15320–15325.

[10] J.G. Limon-Petersen, J.T. Han, N.V. Rees, E.J.F. Dickinson, I. Streeter, R.G. Compton, J. Phys. Chem. C 114 (2010) 2227–2236.

[11] S.R. Belding, J.G. Limon-Petersen, E.J.F. Dickinson, R.G. Compton, Angew. Chemie Int. Ed. 49 (2010) 9242–9245.

[12] J. Crank, E. Nicolson, Proc. Camb. Phil. Soc. 43 (1947) 50–67.

[13] M. Störzbach, J. Heinze, J. Electroanal. Chem. 346 (1993) 1 – 27.

[14] J.A. Alden, R.G. Compton, J. Phys. Chem. B 101 (1997) 9606–9616.

[15] C. Amatore, J. Saveant, J. Electroanal. Chem. 102 (1979) 21–40.

[16] C. Amatore, J. Savéant, J. Electroanal. Chem. 86 (1978) 227 – 232.

Appendix IV: Theory and UV Experiments for Chapter 8

The work presented in this appendix was carried out in collaboration with

- **E.O. Barnes**

We consider the following generic EC_2 electrochemical reduction, with an associated ion pairing equilibrium:

$$\mathrm{A^+ + e-} \rightleftharpoons \mathrm{B} \quad E^{0'}_{\mathrm{A/B}} \tag{Appx IV.1}$$

$$\mathrm{2B} \rightarrow \mathrm{C} \quad k_{\mathrm{dim}} \tag{Appx IV.2}$$

$$\mathrm{A^+ + X^-} \rightleftharpoons \mathrm{Z} \quad K_{\mathrm{eqm}} = \frac{k_{\mathrm{f}}}{k_{\mathrm{r}}} \tag{Appx IV.3}$$

where species X^- is both the counter ion for A^+ and the anion in the supporting electrolyte, M^+X^-, present in an arbitrary quantity. The mass transport of all species in the mechanism is quantified by the Nernst-Planck equation. For a generic species i in hemispherically symmetric space:

$$\frac{\partial C_{\mathrm{i}}}{\partial t} = D_{\mathrm{i}}\left[\frac{\partial^2 C_{\mathrm{i}}}{\partial r^2} + \frac{2}{r}\frac{\partial C_{\mathrm{i}}}{\partial r} + \frac{z_{\mathrm{i}}F}{RT}\left(\frac{\partial C_{\mathrm{i}}}{\partial r}\frac{\partial \phi}{\partial r} + C_{\mathrm{i}}\frac{\partial^2 \phi}{\partial r^2} + C_{\mathrm{i}}\frac{2}{r}\frac{\partial \phi}{\partial r}\right)\right] \tag{Appx IV.4}$$

which describes both diffusion and migration. All symbols are defined in Table . Dimensionless parameters (defined in Table) are introduced into this equation. Dimensionless parameters serve to reduced the number of independent variables and provide more general solution (by removing scaling effects of, for example, electrode size and concentration of electroactive species). Expressed in terms

Table Appx IV.1: Dimensional Parameters

Parameter	Description	Units
$\alpha_{i/j}$	Transfer coefficient of the i/j redox couple	Unitless
D_i	Diffusion coefficient of species i	$m^2\ s^{-1}$
C_i	Concentration of species i	mol
C_i^*	Bulk solution concentration of species i	mol
C_i^0	Concentration of species i at the electrode surface	mol
C_{sup}	Concentration of supporting electrolyte	mol
E	Applied potential	V
$E_{i/j}^{0'}$	Formal potential of i/j couple	V
E_s	Starting potential for cyclic voltammetry	V
E_v	Vertex potential for cyclic voltammetry	V
ϵ_s	Dielectric constant (relative permittivity) of solvent	Unitless
ϵ_0	Permittivity of free space ($\approx 8.854 \times 10^{-12}$)	$F\ m^{-1}$
F	Faraday constant (≈ 96485)	$C\ mol^{-1}$
I	Current measured at working electrode	A
$k_{i/j}^0$	Electrochemical rate constant of i/j redox couple	$m\ s^{-1}$
k_f	Forward rate constant ion pairing equilibrium	s^{-1}
k_r	Reverse rate constant ion pairing equilibrium	$m^3\ mol^{-1}\ s^{-1}$
k_f^{dim}	Rate constant for the dimerisation step	$m^3\ mol^{-1}\ s^{-1}$
K_{eqm}	Equilibrium constant for the ion pairing step	$mol\ m^{-3}$
Λ_i	Molar conductivity of species i	$S\ m^2\ mol^{-1}$
R	Gas constant (≈ 8.314)	$J\ K^{-1}\ mol^{-1}$
ϕ	Solution potential	V
ϕ_0	Solution potential at electrode surface	V
r_e	Electrode radius	m
t	time	s
v	Scan rate	$V\ s^{-1}$
z_i	Charge on species i	Unitless

of these parameters, the Nersnt-Plank equation becomes:

$$\frac{\partial c_i}{\partial \tau} = D_i' \left[\frac{\partial^2 c_i}{\partial R^2} + \frac{2}{R}\frac{\partial c_i}{\partial R} + z_i \left(\frac{\partial c_i}{\partial R}\frac{\partial \theta}{\partial R} + c_i \frac{\partial^2 \theta}{\partial R^2} + c_i \frac{2}{R}\frac{\partial \theta}{\partial R} \right) \right] \tag{Appx IV.5}$$

In addition to mass transport, the space time evolution of each species is dependent on the homogeneous kinetics involved in the mechanism. In dimensionless parameters, the space time evolution of all species are given by:

Table Appx IV.2: Dimensionless Parameters

Dimensionless Parameter	Definition
c_i	$\frac{C_\mathrm{i}}{C_\mathrm{A}^*}$
c_sup	$\frac{C_\mathrm{sup}}{C_\mathrm{A}^*}$
D_i'	$\frac{D_\mathrm{i}}{D_\mathrm{A}}$
j	$\frac{I}{2\pi r_\mathrm{e} F D_\mathrm{A} C_\mathrm{A}}$
K_f	$\frac{r_\mathrm{e}^2 C_\mathrm{A}^*}{D_\mathrm{A}} k_\mathrm{f}$
K_r	$\frac{r_\mathrm{e}^2}{D_\mathrm{A}} k_\mathrm{r}$
$K_\mathrm{f}^\mathrm{dim}$	$\frac{r_\mathrm{e}^2 C_\mathrm{A}^*}{D_\mathrm{A}} k_\mathrm{f}^\mathrm{disp}$
$K_\mathrm{i/j}^0$	$\frac{r_e}{D_\mathrm{A}} k_\mathrm{i/j}^0$
θ_app	$\frac{F}{RT} E_\mathrm{app}$
$\theta_\mathrm{f,i/j}$	$\frac{F}{RT} E_\mathrm{A/B}^{0'}$
θ_s	$\frac{F}{RT} E_\mathrm{s}$
θ_v	$\frac{F}{RT} E_\mathrm{v}$
θ	$\frac{F}{RT} \phi$
θ_0	$\frac{F}{RT} \phi_0$
R	$\frac{r}{r_\mathrm{e}}$
R_e	$r_\mathrm{e}\sqrt{\frac{F^2 C_\mathrm{A}^*}{RT\epsilon_\mathrm{s}\epsilon_0}}$
σ	$\frac{F r_\mathrm{e}^2}{RT D_\mathrm{A}} v$
τ	$\frac{D_\mathrm{A}}{r_\mathrm{e}^2} t$

$$\frac{\partial c_\mathrm{A}}{\partial \tau} = D_\mathrm{A}' \left[\frac{\partial^2 c_\mathrm{A}}{\partial R^2} + \frac{2}{R}\frac{\partial c_\mathrm{A}}{\partial R} + \left(\frac{\partial c_\mathrm{A}}{\partial R}\frac{\partial \theta}{\partial R} + c_\mathrm{A}\frac{\partial^2 \theta}{\partial R^2} + c_\mathrm{A}\frac{2}{R}\frac{\partial \theta}{\partial R} \right) \right] - K_\mathrm{f} c_\mathrm{A} c_\mathrm{X} + K_\mathrm{r} c_\mathrm{Z}$$

$$\frac{\partial c_\mathrm{B}}{\partial \tau} = D_\mathrm{B}' \left[\frac{\partial^2 c_\mathrm{B}}{\partial R^2} + \frac{2}{R}\frac{\partial c_\mathrm{B}}{\partial R} \right] - 2K_\mathrm{dim} c_\mathrm{B}^2$$

$$\frac{\partial c_\mathrm{C}}{\partial \tau} = D_\mathrm{C}' \left[\frac{\partial^2 c_\mathrm{C}}{\partial R^2} + \frac{2}{R}\frac{\partial c_\mathrm{C}}{\partial R} \right] + K_\mathrm{dim} c_\mathrm{B}^2$$

$$\frac{\partial c_\mathrm{X}}{\partial \tau} = D_\mathrm{X}' \left[\frac{\partial^2 c_\mathrm{X}}{\partial R^2} + \frac{2}{R}\frac{\partial c_\mathrm{X}}{\partial R} - \left(\frac{\partial c_\mathrm{X}}{\partial R}\frac{\partial \theta}{\partial R} + c_\mathrm{X}\frac{\partial^2 \theta}{\partial R^2} + c_\mathrm{X}\frac{2}{R}\frac{\partial \theta}{\partial R} \right) \right] - K_\mathrm{f} c_\mathrm{A} c_\mathrm{X} + K_\mathrm{r} c_\mathrm{Z}$$

$$\frac{\partial c_\mathrm{Z}}{\partial \tau} = D_\mathrm{B}' \left[\frac{\partial^2 c_\mathrm{Z}}{\partial R^2} + \frac{2}{R}\frac{\partial c_\mathrm{Z}}{\partial R} \right] + K_\mathrm{f} c_\mathrm{A} c_\mathrm{X} - K_\mathrm{r} c_\mathrm{Z}$$

$$\frac{\partial c_\mathrm{M}}{\partial \tau} = D_\mathrm{M}' \left[\frac{\partial^2 c_\mathrm{M}}{\partial R^2} + \frac{2}{R}\frac{\partial c_\mathrm{M}}{\partial R} + \left(\frac{\partial c_\mathrm{M}}{\partial R}\frac{\partial \theta}{\partial R} + c_\mathrm{M}\frac{\partial^2 \theta}{\partial R^2} + c_\mathrm{M}\frac{2}{R}\frac{\partial \theta}{\partial R} \right) \right]$$

The additional terms after the Nernst-Planck equation describe the homogeneous kinetics, and the dimensionless rate constants K_dim, K_f and K_r are defined in Table .

To complete the model, the dimensionless solution potential θ must be defined throughout the solution. This employs Poisson's equation, which in dimensionless parameters is given by:

$$\frac{\partial^2 \theta}{\partial R^2} + \frac{2}{R}\frac{\partial \theta}{\partial R} = -R_\mathrm{e}^2 \sum_\mathrm{i} z_\mathrm{i} c_\mathrm{i} \qquad \text{(Appx IV.6)}$$

in hemispherically symmetric space.

The mass transport equations, along with the Poisson equation, must be solved simultaneously over the simulation space, defined as $1 \leq R \leq R_{\max}$ where $R = 1$ is the electrode surface. $R_{\max}$ is defined as [1–4]:

$$R_{\max} = 6\sqrt{D'_{\max}\tau_{\max}} \tag{Appx IV.7}$$

where $D'_{\max}$ is the largest dimensionless diffusion coefficient in the system, and $\tau_{\max}$ is the dimensionless time taken to complete the cyclic voltammogram.

The boundary conditions for the chemical species are given by:

$\tau = 0$, all R	$c_{\mathrm{A}} = 1$	$c_{\mathrm{B}} = 0$	$c_{\mathrm{C}} = 0$
	$c_{\mathrm{Z}} = 0$	$c_{\mathrm{X}} = 1 + c_{\mathrm{sup}}$	$c_{\mathrm{M}} = c_{\mathrm{sup}}$
$\tau > 0$, $R = R_{\max}$	$\frac{\partial c_{\mathrm{A}}}{\partial R} = 0$	$\frac{\partial c_{\mathrm{B}}}{\partial R} = 0$	$\frac{\partial c_{\mathrm{C}}}{\partial R} = 0$
	$\frac{\partial c_{\mathrm{Z}}}{\partial R} = 0$	$\frac{\partial c_{\mathrm{X}}}{\partial R} = 0$	$\frac{\partial c_{\mathrm{M}}}{\partial R} = 0$
$\tau > 0$, $R = 1$	$D'_{\mathrm{A}}\frac{\partial c_{\mathrm{A}}}{\partial R} = K^0_{\mathrm{A/B}}c^0_{\mathrm{A}}\exp\left[-\alpha_{\mathrm{A/B}}\left(\theta_{\mathrm{app}} - \theta^{\ominus}_{\mathrm{f,A/B}} - \theta_0\right)\right]$		
	$-K^0_{\mathrm{A/B}}c^0_{\mathrm{B}}\exp\left[\alpha_{\mathrm{A/B}}\left(\theta_{\mathrm{app}} - \theta^{\ominus}_{\mathrm{f,A/B}} - \theta_0\right)\right]$		
	$D'_{\mathrm{B}}\frac{\partial c_{\mathrm{B}}}{\partial R} = D'_{\mathrm{A}}\frac{\partial c_{\mathrm{A}}}{\partial R}$		$\frac{\partial c_{\mathrm{C}}}{\partial R} = 0$
	$\frac{\partial c_{\mathrm{Z}}}{\partial R} = 0$	$\frac{\partial c_{\mathrm{X}}}{\partial R} = 0$	$\frac{\partial c_{\mathrm{M}}}{\partial R} = 0$

The Butler-Volmer boundary conditions for species A and B contain a θ_0 term in the exponent. This represents the solution potential at $R = 1$, which reduces the potential felt by the electroactive species from the measured applied potential, θ_{app}.

The boundary condition for solution potential at $R_{\max}$ is obtained by assuming the solution to be electroneutral at this point, *i.e* $\Sigma z_{\mathrm{i}} c_{\mathrm{i}} = 0$. Substituting this into the Poisson equation gives:

$$\left(\frac{\partial^2\theta}{\partial R^2}\right)_{R=R_{\max}} + \frac{2}{R}\left(\frac{\partial\theta}{\partial R}\right)_{R=R_{\max}} = 0 \tag{Appx IV.8}$$

This equation can be integrated to obtain a boundary condition, subject to the condition that $\theta \to 0$

as $R \to \infty$, giving:

$$\theta_{R=R_{\max}} + R_{\max}\left(\frac{\partial\theta}{\partial R}\right)_{R=R_{\max}} = 0 \qquad \text{(Appx IV.9)}$$

The solution potential boundary condition at the electrode surface ($R = 1$) makes use of the zero field approximation. Within this approximation, the double layer that forms at the electrode surface is assumed to negligible in extent when compared to the diffusion layer. This infinitely small double layer fully compensates the charge on the electrode surface, meaning there is no overall electric field and hence no potential gradient at this point, *i.e*:

$$\left(\frac{\partial\theta}{\partial R}\right)_{R=1} = 0 \qquad \text{(Appx IV.10)}$$

This approximation removes the need to model the double layer, thus greatly simplifying the problem, and has been shown to be appropriate for electrodes above the nano scale [5].

Finally, the variation of applied potential with time must be defined. This is given by:

$$\theta_{\text{app}} = |-\sigma\tau + \theta_{\text{s}} - \theta_{\text{v}}| + \theta_{\text{v}} \qquad \text{(Appx IV.11)}$$

where θ_{s} and θ_{v} are the dimesionless start and vertex potentials, and σ and τ are dimensionless scan rate and time, defined in Table .

The dimensional current is calculated from the dimensionless flux of species A at the electrode surface:

$$I = 2\pi F r_{\text{e}} C^*_{\text{A}} D_{\text{A}} j^0_{\text{A}} \qquad \text{(Appx IV.12)}$$

where

$$j^0_{\text{A}} = \left(\frac{\partial c_{\text{A}}}{\partial R}\right)_{R=1} \qquad \text{(Appx IV.13)}$$

Numerical Methods

The NPP equations and boundary conditions are discretised using the finite difference method. Discretisation requires that we define appropriate spatial and temporal grids. This investigation uses grids that have been established previously, and demonstrated to be appropriate [6–10]. The spatial grid employed is non-regular, and has a series of dense, regularly spaced points close to the electrode surface, but which expands proportionally with R beyond some characteristic switching point, R_s. This set up is appropriate since the steepest concentration and potential gradients will occur near the electrode surface. At R values further from the electrode surface, all parameters being calculated tend towards constant bulk values, and gradients approach zero. It is therefore in the interest of computational efficiency that spatial grid points become less dense further from the electrode surface. The spatial grid can be defined mathematically in the following way:

$$R_j = \begin{cases} R_{j-1} + \gamma_{\mathrm{R}}(R_s - 1) & \text{if } R < R_s, \\ R_{j-1} + \gamma_{\mathrm{R}}(R_{j-1} - 1) & \text{if } R \geq R_s. \end{cases} \qquad \text{(Appx IV.14)}$$

where γ_{R} is an expansion coefficient. The first spatial point, R_0, is at the electrode surface and is equal to 1.

The temporal grid uses is a regular array of points, and is defined by a parameter θ_{div}, which is the number of temporal steps per unit of dimensionless potential swept out. Mathematically:

$$\tau_{\mathrm{k+1}} = \tau_{\mathrm{k}} + \frac{1}{\sigma\theta_{\mathrm{div}}} \qquad \text{(Appx IV.15)}$$

where τ_0 is set equal to zero.

As the grids defined above become more and more dense, the solution obtained by the simulation will converge on an accurate answer, assuming that any error in one step does not become amplified in subsequent steps [11]. However, the denser the grids, the longer the simulation will take. Optimal grid

parameters providing accurate results in reasonable computation times were obtained *via* convergence studies. The parameters used gave a result within ±0.2% of a fully converged value. These parameters were found to be: $\gamma_{\mathrm{R}} = 10^{-2}$; $R_{\mathrm{s}} = 1 + \left(2 \times 10^{-3}\right)$; $\theta_{\mathrm{div}} = 50$. During each time step, the correct solution is obtained iteratively using the Newton-Raphson method [12]. The step was ended when the dimensionless potential and dimensionless concentrations lay within $\pm 1 \times 10^{-4}$ of the correct solution.

The simulation of systems involving both diffusion and migration are approximately 100 times slower than those involving diffusion alone. The total time, t_{total}, required to simulate a voltammogram is given by:

$$t_{\mathrm{total}} = \text{number of timesteps} \times \text{number of iterations per timestep} \times \text{time to solve matrix} \tag{Appx IV.16}$$

In this study, and others [5, 6, 13], the number of timesteps required for diffusion-migration and for diffusion-only simulations are found to be equal. The number of iterations per timestep is slightly higher for diffusion-migration owing to the highly non-linear nature of the discretised equations. Therefore, as a first approximation, the total time for diffusion-migration and for diffusion-only is:

$$t_{\mathrm{total}} \propto \text{time to solve matrix} \tag{Appx IV.17}$$

The time taken to solve a matrix is given by:

$$t_{\mathrm{timetosolvematrix}} \propto \text{rows} \times \text{diagonals}^2 \tag{Appx IV.18}$$

The number of rows are given by:

$$\text{rows} = \text{species} \times \text{spatial points} \tag{Appx IV.19}$$

Owing to the nature of the migration term and the need to fit it into the matrix, the number of

diagonals required by diffusion-migration is given by:

$$\text{diagonals} = 4 \times \text{species} + 1 \tag{Appx IV.20}$$

For diffusion-only:

$$\text{diagonals} = 2 \times \text{species} + 1 \tag{Appx IV.21}$$

Therefore:

$$t_{\text{totaldiff}-\text{mig}} \propto \text{species} \times \text{spatial points} \times (4 \times \text{species} + 1)^2 \tag{Appx IV.22}$$

$$t_{\text{totaldiff}-\text{only}} \propto \text{species} \times \text{spatial points} \times (2 \times \text{species} + 1)^2 \tag{Appx IV.23}$$

For diffusion-only, there are 4 species (A, B, C & Z) while for diffusion-migration, there are 7 species (A, B, C, Z, M, X & potential). In general, the number of spatial points required for a diffusion-only cyclic voltammogram is of the order 100. In contrast, simulations which model both diffusion and migration require a number of spatial points of the order 1000 in order to attain satisfactory convergence [5, 6]. This is requirement is derived from the low diagonal dominance of the discretised equations in the matrix compared to the diffusion-only case [14]. Therefore:

$$\frac{t_{\text{totaldiff}-\text{mig}}}{t_{\text{totaldiff}-\text{only}}} \approx \frac{\text{species} \times \text{spatial points} \times (4 \times \text{species} + 1)^2}{\text{species} \times \text{spatial points} \times (2 \times \text{species} + 1)^2} \tag{Appx IV.24}$$

$$\frac{t_{\text{totaldiff}-\text{mig}}}{t_{\text{totaldiff}-\text{only}}} \approx 100 \tag{Appx IV.25}$$

Accordingly, a simple diffusion-only programs takes of the order 5-10 seconds; the corresponding diffusion-migration problem takes approximately 10–20 minutes.

Estimation of the Diffusion Coefficient of BF_4^- in Acetonitrile

The diffusion coefficient of the BF_4^- ion in acetonitrile at 298 K was estimated from the reported [15] value of the molar conductivity of the ion in this solvent (96.8 S cm^2 mol^{-1}). The Nernst-Einstein Equation:

$$D_\mathrm{i} = \Lambda_\mathrm{i} \frac{RT}{z_\mathrm{i}^2 F^2} \qquad \text{(Appx IV.26)}$$

can then be used to estimate a value of $D_{BF_4^-} \approx 2.57 \times 10^{-5}$ cm^2 mol^{-1}.

UV/Visible spectrometric measurements of ion-pairing

UV/Visible spectrometric measurements were made on solutions as follows: (i) $0 < c_{DPP^+ClO_4^-} \leq$ 0.15mM; (ii) $0 < c_{DPP^+BF_4^-} \leq 0.15$mM; (iii) 0.1mM $DPP^+BF_4^-$ in the presence of varying $c_{NBu_4BF_4}$ up to 0.4M. The data was fitted to the simple ion-pairing model:

$$DPP^+ + BF_4^- \rightleftharpoons DPP^+ \cdot BF_4^- \qquad K_\mathrm{eqm} \qquad \text{(Appx IV.27)}$$

The absorption at 275nm seen for low concentrations of $DPP^+ClO_4^-$ or $DPP^+BF_4^-$ (<0.2mM) where there is no ion-pairing showed that the extinction coefficient for the non-ionpaired DPP^+ cation (ϵ_{DPP^+}) is 1.23×10^3 m^2 mol^{-1}. Measurements were then made for a range of $c_{BF_4^-}$ and the absorbance (A) found. The data were analysed (shown in Figure Appx IV.1) according to:

$$A = \frac{(\epsilon_{DPP^+} + \epsilon_{IP} K_\mathrm{eqm} c_{BF_4^-}) l c_{DPP^+}}{1 + K_\mathrm{eqm} c_{BF_4^-}} \qquad \text{(Appx IV.28)}$$

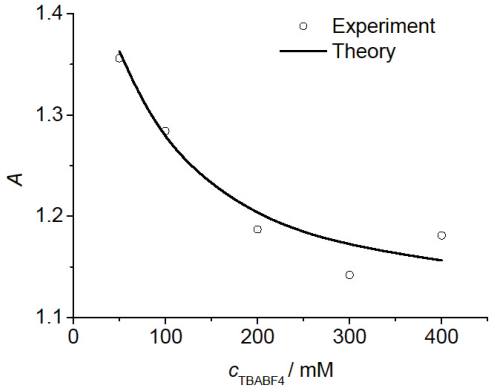


Figure Appx IV.1: Experimental and fitted plots of A versus $c_{\mathrm{BF}_4^-}$. The theoretical model is described by Equation Appx IV.28.

where ϵ_{IP} is the extinction coefficient of the ion pair salt and l the width of the solution. A was found to decrease with increasing additions of BF_4^- concentration with $\epsilon_{\mathrm{IP}} = 1.11 \times 10^3$ m^2 mol^{-1} and $K_{\mathrm{eqm}} = 0.035$ m^3 mol^{-1}.

References

[1] D.J. Gavaghan, J. Electroanal. Chem. 456 (1998) 25–35.

[2] D.J. Gavaghan, J. Electroanal. Chem. 456 (1998) 13–23.

[3] D.J. Gavaghan, J. Electroanal. Chem. 456 (1998) 1–12.

[4] I.B. Svir, A.I. Oleinick, R.G. Compton, Radiotekhnika 116 (2001) 114.

[5] I. Streeter, R.G. Compton, J. Phys. Chem. C 112 (2008) 13716–13728.

[6] E.J.F. Dickinson, J.G. Limon-Petersen, N.V. Rees, R.G. Compton, J. Phys. Chem. C 113 (2009) 11157–11171.

[7] J.G. Limon-Petersen, I. Streeter, N.V. Rees, R.G. Compton, J. Phys. Chem. C 113 (2009) 333–337.

[8] J.G. Limon-Petersen, E.J.F. Dickinson, N.V. Rees, R.G. Compton, J. Phys. Chem. C 113 (2009) 15320–15325.

[9] J.G. Limon-Petersen, J.T. Han, N.V. Rees, E.J.F. Dickinson, I. Streeter, R.G. Compton, J. Phys. Chem. C 114 (2010) 2227–2236.

[10] E.O. Barnes, Y. Wang, J.G. Limon-Petersen, S.R. Belding, R.G. Compton, J. Electroanal. Chem. 659 (2011) 25–35.

[11] D. Britz, Digital Simulation in Electrochemistry, Springer-Verlag, Heidelberg, 2005.

[12] W.H. Press, S.A. Teukolsky, W. Vetterling, B.P. Flannery, Numerical Recipes: The Art of Scientific Computing, Cambridge University Press, Cambridge, 2007.

[13] S.R. Belding, J.G. Limon-Petersen, E.J.F. Dickinson, R.G. Compton, Angew. Chemie Int. Ed. 49 (2010) 9242–9245.

[14] O.V. Klymenko, C. Amatore, I. Svir, Anal. Chem. 79 (2007) 6341–6347.

[15] H. Wang, J. Wang, S. Zhang, Y. Pei, K. Zhuo, Chem. Phys. Chem. 10 (2009) 2516–2523.

Appendix V: Theory for Chapter 10

The work presented in this appendix was carried out in collaboration with

- **M.C. Henstridge**

Theory

We consider the redox reaction $\mathrm{A} + \mathrm{e} \rightleftharpoons \mathrm{B}$ taking place in solution at a hemispherical electrode. For this system the appropriate mass transport equation, neglecting migration, [1] is therefore:

$$\frac{\partial c_i}{\partial t} = D_i \left[\frac{\partial^2 c_i}{\partial r^2} + \frac{2}{r} \frac{\partial c_i}{\partial r} \right] \qquad \text{(Appx V.1)}$$

where c_i (mol cm^{-3}) and D_i (cm^2 s^{-1}) are respectively the concentration and diffusion coefficient, t (s) is time and r (cm) is radial distance from the centre of the hemisphere of radius r_e. This equation is solved numerically using the backwards implicit finite difference method [2] over an expanding grid of points subject to the following:

$$t = 0 \qquad r \geq r_\mathrm{e} \qquad c_\mathrm{A} = c_\mathrm{A}^* \, , \; c_\mathrm{B} = 0 \qquad \text{(Appx V.2)}$$

$$t > 0 \qquad r \to \infty \qquad c_\mathrm{A} = c_\mathrm{A}^* \, , \; c_\mathrm{B} = 0 \qquad \text{(Appx V.3)}$$

$$t > 0 \qquad r = r_\mathrm{e} \qquad D_\mathrm{A} \frac{\partial c_\mathrm{A}}{\partial r} = k_\mathrm{red} \, c_\mathrm{A} - k_\mathrm{ox} \, c_\mathrm{B} \qquad \text{(Appx V.4)}$$

$$t > 0 \qquad r = r_\mathrm{e} \qquad D_\mathrm{A} \frac{\partial c_\mathrm{A}}{\partial r} = -D_\mathrm{B} \frac{\partial c_\mathrm{B}}{\partial r} \qquad \text{(Appx V.5)}$$

where c_A^* (mol cm^{-3}) is the bulk concentration of A and k_red and k_ox (cm s^{-1}) are the rate constants for reduction and oxidation respectively, which are defined differently within the Butler-Volmer and Marcus-Hush formalisms.

Within the Butler-Volmer model these rate constants are given by:

$$k_{\mathrm{red}}^{\mathrm{BV}} = k_0 \exp\left[-\alpha\,\theta\right] \tag{Appx V.6}$$

$$k_{\mathrm{ox}}^{\mathrm{BV}} = k_0 \exp\left[+\beta\,\theta\right] \tag{Appx V.7}$$

where k_0 (cm s^{-1}) is the standard electrochemical rate constant, α and β are transfer coefficients and θ is a dimensionless potential, defined thus:

$$\theta = \frac{F}{RT}(E - E^{0'}) \tag{Appx V.8}$$

where E (V) is potential, $E^{0'}$ (V) is the formal potential and F, R and T have their usual meanings. Within the Marcus-Hush formalism for electron transfer at a metallic electrode [3–5] these rate constants are given by:

$$k_{\mathrm{red}}^{\mathrm{MH}} = k_0 \exp\left[-\frac{\theta}{2}\right] \frac{I(\Lambda,\theta)}{I(\Lambda,0)} \tag{Appx V.9}$$

$$k_{\mathrm{ox}}^{\mathrm{MH}} = k_0 \exp\left[+\frac{\theta}{2}\right] \frac{I(\Lambda,\theta)}{I(\Lambda,0)} \tag{Appx V.10}$$

where Λ is a dimensionless reorganisation energy, defined thus:

$$\Lambda = \frac{F}{RT}\lambda \tag{Appx V.11}$$

in which λ (eV) is the reorganisation energy and the integral

$$I(\Lambda,\theta) = \int_{-\infty}^{\infty} \frac{\exp\left[\frac{-(\epsilon-\theta)^2}{4\Lambda}\right]}{2\cosh\left[\frac{\epsilon}{2}\right]} d\epsilon \tag{Appx V.12}$$

in which ϵ is an integration variable, is evaluated numerically using the trapezium rule. It should be noted that in the limit of very high reorganisation energy (i.e. $\Lambda \to \infty$) the ratio of integrals in Equations Appx V.9 and Appx V.10 tends to unity. Thus in this limit the Marcus-Hush rate constants

are reduced to their Butler-Volmer equivalents for the case when $\alpha = \frac{1}{2}$.

In this work we consider cyclic voltammetry, thus the potential applied at the electrode varies as a function of time according to:

$$E(t) = |E_1 - \sigma t - E_2| + E_2 \qquad \text{(Appx V.13)}$$

where E_1 and E_2 (V) are the starting and vertex potentials respectively and σ (V s^{-1}) is the scan rate.

Rate constants are calculated at each timestep and the resulting set of simultaneous equations, which can be formulated as a diagonal matrix, is then solved using the Thomas algorithm. [2]

Both the Butler-Volmer and Marcus-Hush program variants were written in C++ and run on a desktop PC. Due to the inherent extra calculation required in numerically evaluating the integral in Equation 12.8 when calculating the rate constants for the Marcus-Hush model, these simulations were slower than those for the Butler-Volmer model, taking approximately twice the time to run. However for both programs typical simulation times were below five seconds.

Theoretical Results

Values of the Marcus-Hush oxidative rate constant calculated from Equation Appx V.10 are shown in Figure Appx V.1 for a range of λ values, the Butler-Volmer rate constants for $\alpha = \frac{1}{2}$ is also shown for comparison. The limiting value of rate constant predicted by the Marcus-Hush model can clearly be seen. For very small values of λ this plateau is reached at fairly low overpotentials, but with increasing λ the limiting rate constant increases, as does the overpotential required to reach it. Figure Appx V.1 also demonstrates graphically that in the limit of $\lambda \to \infty$, Marcus-Hush kinetics yields rate constants equal to those of Butler-Volmer kinetics for $\alpha = \frac{1}{2}$ for the same overpotential, assuming equal k_0 values.

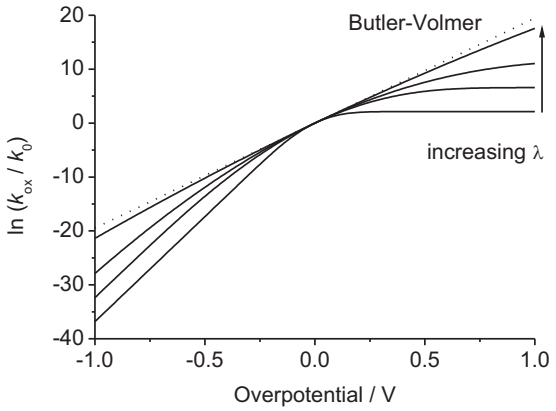


Figure Appx V.1: Plot of potential vs ln (k_{ox}/k_0) for Butler-Volmer, $\alpha = \frac{1}{2}$ (dotted line) and Marcus-Hush (solid lines) for λ values 0.1, 0.5, 1.0 and 5.0 eV.

In order to differentiate between the two kinetic formalisms voltammetrically there must be an appreciable difference in rate constants while the current is still under kinetic control. This is because the diffusion-limited current is inherently independent of the rate constant. As can be seen in Figure Appx V.1 the two models yield almost indistinguishable rate constants for potentials in the vicinity of $E^{0'}$, indeed at $E = E^{0'}$ the rate constants are exactly equal. For small reorganisation energies up to around 1 eV the two models begin to significantly diverge at overpotentials of the order of 50–100 mV, although as reorganisation energy increases so does the overpotential required for an observable difference in rate constants. Thus an experimental system must give a kinetically controlled current at an appreciable overpotential. For a totally reversible system the peak potential is approximately 29 mV, [6] beyond which the current is under diffusional control. Therefore for a diffusion-only system, without employing extremely high scan rates, it is only redox systems with significantly irreversible electrode kinetics that will enable differentiation between the Butler-Volmer and Marcus-Hush kinetic models.

The effect α and λ have on typical cyclic voltammetry when deviating from the $\alpha = \frac{1}{2}$ (or $\lambda \to \infty$) limit is shown in Figure Appx V.2. Decreasing λ is seen to broaden and shorten both forward and back peaks. Within the BV formalism, however, when α deviates from $\frac{1}{2}$ one peak is see to become broadened relative to the $\alpha = \frac{1}{2}$ case, while the other peak becomes "sharper" since $\alpha + \beta = 1$.

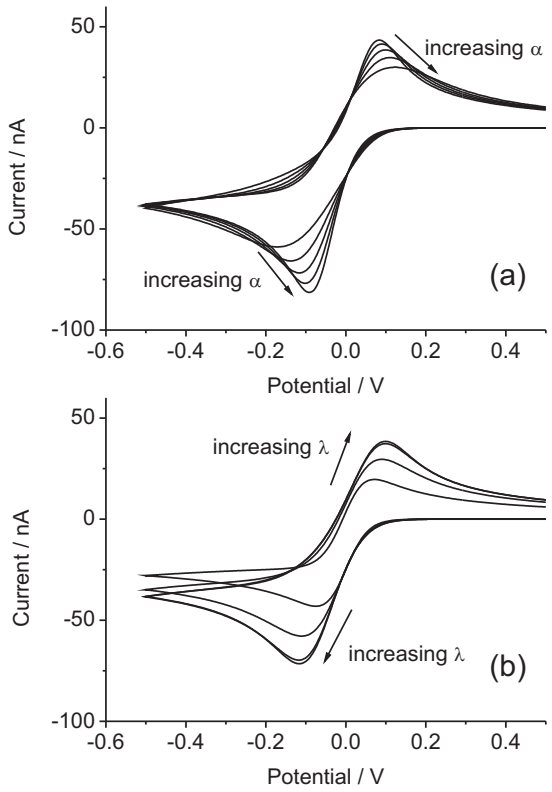


Figure Appx V.2: Theoretical voltammetry simulated at 5 V s^{-1} for a 25 μm hemisphere, $k_0 = 10^{-2}$ cm s^{-1}, $D_A = D_B = 10^{-5}$ cm^2 s^{-1} (a) using Butler-Volmer kinetics with $\alpha = 0.3$, 0.4, 0.5, 0.6 and 0.7 (b) using Marcus-Hush kinetics with $\lambda = 0.01$, 0.1, 1 and 10.

Excepting the case of steady-state voltammetry, where the current is always limited by the rate of mass transport, it is therefore not possible to exactly reproduce voltammetry simulated using BV kinetics with $\alpha \neq \frac{1}{2}$ by using MH kinetics, regardless of the value of λ used. Equally, BV kinetics cannot precisely replicate voltammetry which is simulated using MH kinetics with a small reorganisation energy, no matter the value of α. Thus if a set of experimental data is fitted very accurately using one of either BV or MH kinetics (excepting the limiting cases discussed previously), the other model will likely yield a poor fit.

References

[1] E.J.F. Dickinson, J.G. Limon-Petersen, N.V. Rees, R.G. Compton, J. Phys. Chem. C 113 (2009) 11157–11171.

[2] L. Lapidus, G.F. Pinder, Numerical solution of partial differential equations in science and engineering, Wiley, New York, 1982.

[3] C.E.D. Chidsey, Science 251 (1991) 919–922.

[4] S.W. Feldberg, Anal. Chem. 82 (2010) 5176–5183.

[5] K.B. Oldham, J.C. Myland, J. Electroanal. Chem. 655 (2011) 65–72.

[6] R.G. Compton, C.E. Banks, Understanding voltammetry, 2nd edn., Imperial College Press, London, 2010.

Appendix VI: Theory for Chapter 13

The work presented in this appendix was carried out in collaboration with

- **E. Laborda** and **M.C. Henstridge**

We consider the one-electron reduction of solution-phase species Ox at the surface of an electrode:

$$\mathrm{Ox} + \mathrm{e}^- \underset{k_{\mathrm{ox}}}{\overset{k_{\mathrm{red}}}{\rightleftharpoons}} \mathrm{Red} \qquad \text{(Appx VI.1)}$$

where k_{red} and k_{ox} are the rate constants for reduction and oxidation respectively.

After considering the continuum of electronic levels of the electrode [1–4], the following general relationships are obtained for the heterogeneous rate constants:

$$k_{\mathrm{red}} = k^0 \frac{I_{\mathrm{red}}(\eta, \lambda^*)}{I_{\mathrm{red}}(0, \lambda^*)} \qquad \text{(Appx VI.2)}$$

$$k_{\mathrm{ox}} = k^0 \frac{I_{\mathrm{ox}}(\eta, \lambda^*)}{I_{\mathrm{ox}}(0, \lambda^*)} \qquad \text{(Appx VI.3)}$$

where $\lambda^* = F\lambda/RT$ is the dimensionless reorganization energy, $\eta = F(E - E^{0'})$ the dimensionless overpotential, and $I(\eta, \lambda^*)$ is an integral of the form:

$$I_{\mathrm{red/ox}}(\eta, \lambda^*) = \int_{-\infty}^{\infty} \frac{\exp\left[-\Delta G^{\neq}_{\mathrm{red/ox}}(\chi)\right]}{1 + \exp(\mp\chi)} d\chi \qquad \text{(Appx VI.4)}$$

where $\chi = F(\epsilon - E)/RT$ is an integral variable, $\mathrm{E}^0_{\mathrm{f}}$ the formal potential, E the applied potential, F the Faraday constant (96,485 C/mol), R the gas constant (8.314 J/mol K) and T the absolute temperature. Where two signs appear, the upper sign refers to the reductive process; the lower one to the oxidative reaction.

According to the symmetric form of Marcus theory, where the Gibbs energy curves are assumed to have the same curvature (i.e., equal reorganization energies), the activation energy, $-\Delta G^{\neq}_{\mathrm{sys}}(\chi)$ for the reductive and oxidative processes is given by:

$$\Delta G^{\neq}_{\mathrm{sys,red}}(\chi) = \frac{\lambda^*}{4}(1 + \frac{\eta + \chi}{\lambda^*})^2 \qquad \text{(Appx VI.5)}$$

$$\Delta G^{\neq}_{\mathrm{sys,ox}}(\chi) = \frac{\lambda^*}{4}(1 - \frac{\eta + \chi}{\lambda^*})^2 \qquad \text{(Appx VI.6)}$$

by substituting Equations Appx VI.5 and Appx VI.6 into Equation Appx VI.4, the Marcus-Hush formulation for electrode reactions as used by Chidsey is obtained [2–4].

As discussed above, it is of great interest to consider the use of the asymmetric form of the Marcus model, where the values of the inner-shell force constants differ. From the equations presented in Appendix IV of Ref. [5], the following expressions for the activation energies of the reduction and oxidation processes were obtained [6]:

$$\Delta G^{\neq}_{\mathrm{sys,red}}(\chi) = \frac{\lambda^*}{4}(1 + \frac{\eta + \chi}{\lambda^*})^2 + \beta^*(\frac{\eta + \chi}{4\lambda^*})\left\{1 - (\frac{\eta + \chi}{\lambda^*})^2\right\} + \frac{\beta^{*2}}{16\lambda^*} \qquad \text{(Appx VI.7)}$$

$$\Delta G^{\neq}_{\mathrm{sys,ox}}(\chi) = \frac{\lambda^*}{4}(1 - \frac{\eta + \chi}{\lambda^*})^2 + \beta^*(\frac{\eta + \chi}{4\lambda^*})\left\{1 - (\frac{\eta + \chi}{\lambda^*})^2\right\} + \frac{\beta^{*2}}{16\lambda^*} \qquad \text{(Appx VI.8)}$$

where $\beta^* = F\beta/RT$ The parameter β accounts for the divergence of the curvatures of the Gibbs energy curves and is given by:

$$\beta = \lambda_{\mathrm{i}} \langle I_{\mathrm{s}} \rangle = \lambda_{\mathrm{i}} \frac{\sum_{\mathrm{s}} k_{\mathrm{s}} (\Delta q^0_{\mathrm{s}})^2 I_{\mathrm{s}}}{\sum_{\mathrm{s}} k_{\mathrm{s}} (\Delta q^0_{\mathrm{s}})^2} \qquad \text{(Appx VI.9)}$$

with λ_{i} being the inner-sphere reorganization energy:

$$\lambda_{\mathrm{i}} = \frac{1}{2} \sum_{\mathrm{s}} k_{\mathrm{s}} (\Delta q^0_{\mathrm{s}})^2 \qquad \text{(Appx VI.10)}$$

Δq^0_{s} the difference of the equilibrium values for the sth normal mode coordinate of reactants and products, and k_{s} and I_{s} symmetric and antisymmetric combinations of the force constants of the sth

mode of reactants and products, f_s^{ox} and f_s^{red}, respectively:

$$k_s = \frac{2 f_s^{ox} f_s^{red}}{f_s^{ox} + f_s^{red}} \tag{Appx VI.11}$$

$$I_s = \frac{f_s^{ox} - f_s^{red}}{f_s^{ox} + f_s^{red}} \tag{Appx VI.12}$$

According to the above definitions, the $\langle I_s \rangle$ parameter is related to the differences between the inner-shell force constants of oxidized and reduced species such that its absolute value increases from 0 to 1 with the disparity of their values.

In the case of very large differences occurring between the force constants of the oxidized and reduced species, $\langle I_s \rangle$ is very large and the results obtained from Equations Appx VI.7 and Appx VI.8 should be considered cautiously, as discussed in Ref. [6].

The general, asymmetric MH model employed here enables the parameterisation of voltammetry and the estimation of differences in the force constants without previous information about the experimental system. However, when very large differences occur, significant errors in the peak currents can be expected. For $|\langle I_s \rangle| \approx 0.5$ errors greater than 5% are observed only when the peaks are situated at very large overpotentials (i.e., very sluggish electrode reactions): $|\eta_{peak}| > 20$. For $|\langle I_s \rangle| = 0.6$, the error in the peak current is found to exceed 5% for $|\eta_{peak}| > 3$. The accurate description of these extreme situations ($|\langle I_s \rangle| > 0.6$, that is, force constants differing in a factor greater than 4) requires the particularization of the solution to the specific redox couple under scrutiny and, therefore, prior structural insight to the electroactive species under study.

References

[1] A.J. Bard, L.R. Faulkner, Electrochemical Methods, Fundamentals and Applications, John Wiley & Sons, New York, 2001.

[2] C.E.D. Chidsey, Science 251 (1991) 919–922.

[3] S.W. Feldberg, Anal. Chem. 82 (2010) 5176–5183.

[4] K.B. Oldham, J.C. Myland, J. Electroanal. Chem. 655 (2011) 65–72.

[5] R.A. Marcus, J. Chem. Phys. 43 (1965) 679–701.

[6] E. Laborda, M. Henstridge, R.G. Compton, J. Electroanal. Chem. 667 (2012) 48–53.